分类号_____ 密级

UDC _____ 编号

中国科学院地球化学研究所

博士后研究工作报告

稻田生态系统铁硫循环对汞生物地球化学过程的影响

刘 江

工作完成日期：2020 年 06 月— 2023 年 08 月

报告提交日期：2023 年 08 月

中国科学院地球化学研究所

2023 年 08 月

稻田生态系统铁硫循环对汞生物地球化学过程的影响

Influences of iron and sulfur cycling on the biogeochemical processes of mercury in rice paddy systems

博 士 后 姓 名: 刘江

流动站（一级学科）名称: 环境科学与工程

专业（二级学科）名称: 环境科学

合 作 导 师: 孟博

研究工作起始时间： 2020 年 06 月

研究工作期满时间： 2023 年 08 月

中国科学院地球化学研究所

2023 年 08 月

本报告获得以下项目资助

- 国家自然科学基金委优秀青年科学基金项目（42022024）
- 国家自然科学基金委重点基金项目（41931297）
- 中国科学院“西部之光”交叉团队项目—重点实验室合作研究专项
- 国家自然科学基金委青年科学基金项目（42107442）

目录

摘要

汞（Hg）作为一种毒性很强的重金属污染物，其有机形态的甲基汞（MeHg）毒性最强，能够穿过胎盘屏障与血脑屏障，对人体产生神经毒性。申请人课题组前期研究发现，水稻是迄今为止唯一的甲基汞富集农作物，并且食用稻米是我国南方内陆居民甲基汞暴露的主要途径。因此，汞污染区水稻甲基汞污染问题引起了国际社会的广泛关注。一直以来，微生物介导下无机汞的甲基化过程是汞的生物地球化学循环研究和关注的重点。该过程是受多种生物（如微生物的群落结构、活性与丰度等）与非生物因素（如生物可利用汞的含量、电子供体与受体、温度、光照、pH等）影响的复杂生物地球化学过程。铁和硫作为生命组成元素，广泛分布于环境中。由于铁和硫元素自身的多价态属性，其能够敏感地响应环境中氧化还原条件的变化。稻田土壤的干湿交替过程促进了铁和硫的氧化还原反应。此外，微生物主导的硫酸盐还原和铁还原均为目前已知的无机汞生物甲基化的主要途径。目前，尽管有学者研究了环境中铁-硫的相互作用，但对于稻田生态系统铁硫循环对汞生物地球化学过程的影响了解较少。为此，本研究以稻田土壤为研究对象，从铁硫循环出发，探究铁硫循环对汞形态转化及分布的影响。取得如下主要研究结果：

（1）稻田土壤中甲基汞的生成取决于汞的生物有效性和参与汞甲基化过程的微生物活性及其群落结构。铁-硫的氧化还原循环与汞的环境行为高度耦合，并对汞的赋存形态产生影响。然而在铁硫循环过程中生成这些汞形态的生物有效性如何？能否参与汞甲基化过程仍不明确。基于此，本研究采用单一富集稳定汞同位素示踪技术，通过人工合成稻田土壤中普遍存在汞形态，包括溶解态汞（$^{198}Hg(NO_3)_2$）、有机质结合态汞（NOM-^{199}Hg(II)）、纳米颗粒态硫化汞（nano-^{202}HgS）以及硫化亚铁吸附态汞（≡FeS-^{200}Hg(II)），以探究上述汞形态在稻田土壤中的生物有效性。研究发现，nano-^{202}HgS 和 NOM-^{199}Hg(II)的甲基化反应速率常数与 $^{198}Hg(NO_3)_2$ 相似，是能够参与甲基化反应的重要汞形态。≡FeS-^{200}Hg(II)的甲基化速率常数在所有位点中均为最低，表明稻田土壤中新生成的 FeS 是溶解态 Hg 的汇，且几乎不能被甲基化。在不同汞浓度梯度的稻田土壤中，汞甲基化率随汞浓度的增加而下降，并且，稻田土壤汞浓度梯度引

起的甲基化速率的差异（10^3~10^4 倍）远远大于同一位点间不同汞形态之间的差异（1~5 倍）。此外，我们还发现，除了稻田土壤中汞的来源、土壤理化性质等因素外，不同位点间微生物群落结构及其活性的差异很可能是造成其甲基化速率存在巨大差异的主要原因。

（2）由于稻米中的甲基汞全部来自于稻田土壤中无机汞的甲基化过程，因此厘清稻田土壤中不同形态汞的转化过程尤为重要。大气硫沉降以及含硫肥料施加影响着稻田土壤中硫元素的氧化还原循环，而硫元素的氧化还原循环如何影响稻田土壤中汞的形态转化尚不清楚。因此，本研究采用不同形态汞同位素示踪技术，通过合成无机汞同位素示踪剂（$^{200}Hg^{II}$），甲基汞同位素示踪剂（$Me^{198}Hg$）以及零价汞同位素示踪剂（$^{202}Hg^0$），分别示踪稻田土壤中汞的甲基化、去甲基化、还原以及氧化过程。另外，通过外源添加两种含硫化合物（硫酸盐和硫代硫酸盐），探究硫氧化还原循环对汞形态转化的影响。研究发现，除常规已知的无机汞甲基化和甲基汞去甲基化过程外，稻田土壤中还存在微生物介导的无机汞暗还原、零价汞的甲基化以及甲基汞的暗还原过程。在淹水的稻田土壤中，不同形态汞（Hg^{II}，MeHg 和 Hg^0）之间的相互转化并非独立过程，而是微生物介导的耦合过程。由于存在无机汞的微生物暗还原以及零价汞的甲基化过程，因此值得进一步关注稻田土壤中汞的氧化还原过程及其对净甲基汞积累的影响。外源硫输入对汞形态转化的影响机制存在两个方面，（1）影响参与汞形态转化的微生物群落结构和（2）影响汞的化学形态。本研究发现，土壤中硫输入主要通过影响微生物群落结构而进一步影响汞形态转化。

（3）新沉降汞较稻田土壤中的存量汞更易于被甲基化。然而，对新沉降汞的生物地球化学过程的认识较少，铁硫循环是否影响新沉降汞在稻田土壤中的形态分布及生物有效性尚不了解。因此，本研究采用单一富集稳定汞同位素示踪技术，添加 $^{200}Hg^{II}$ 模拟新沉降汞，结合汞的连续提取技术，探究稻田土壤中新沉降汞的形态分布特征以及再分配过程。研究发现，“新”汞主要与土壤有机质结合在一起，以有机质结合态汞的形态存在，其次为残渣态汞、铁/锰氧化物结合态汞、溶解与可交换态汞和碳酸盐结合态汞。在水稻生长过程中，以溶解与可交换态汞、碳酸盐结合态汞、有机质结合态汞和残渣态汞形态存在的“新”汞向铁/锰氧化物结合态汞转化。微生物驱动的土壤有机质矿化作用以及氧化还原条件改变驱动的铁氧化物形态转化共同影响着稻田土壤中“新”汞的地球化学形态分馏。弱结晶型或者无定形铁氧化物与内源性有机

质构成的复合体系控制着稻田土壤中新沉降汞的形态。

关键词：稻田土壤、汞形态转化、铁硫循环、氧化还原、单一富集稳定汞同位素示踪技术

ABSTRACT

Methylmercury (MeHg), the organic form of mercury (Hg), is a broad public concern due to its neurotoxicity, bioaccumulation and biomagnification in food chains. Previous studies have reported that rice consumption is the major pathway for human MeHg exposure in inland China, especially in Hg contaminated regions. Multiple biological, physical and chemical factors determine net Hg methylation, including microbial community structure and function, Hg speciation, temperature, pH, redox, or natural organic matter (NOM) quality and quantity. Among those factors, the speciation and bioavailability of Hg is considered one of the most important factors controlling net MeHg production. Iron and sulfur was widely distributed in the nature environments. Due to the nature of multi-valence state, iron and sulfur could respond to the redox changes sensitively. Wetting and drying rotations in rice paddy soils promoted the redox cycling of iron and sulfur. In addition, sulfate reducing bacteria and iron reducing bacteria mediated Hg methylation are major pathways for the production of MeHg. Currently, understandings for the role of iron and sulfur cycling on Hg biogeochemical processes in rice paddy ecosystems are limited. In this study, therefore, rice paddy soil was selected as the object, and influences of iron and sulfur cycling on the biogeochemical processes of mercury in rice paddy systems were studied. The major results from this study are as follows:

(1) MeHg production, a microbially driven process, depends on both the chemical speciation of inorganic divalent mercury, Hg^{II}, that determines mercury bioavailability for methylation. Here, we conducted incubation experiments using a multi-isotope tracer technique including $^{198}Hg(NO_3)_2$, natural organic matter bond Hg^{II} (NOM-^{199} Hg^{II}), ferrous sulfide sorbed Hg^{II} (≡FeS-^{200} Hg^{II}), and nanoparticulate mercuric sulfide (nano-^{202}HgS), to investigate the relative importance of geochemically diverse yet relevant Hg^{II} species on mercury methylation in paddy soils across a Hg concentration gradient. We show that methylation rates for all Hg^{II} species tested decreased with increasing mercury concentrations, and that methylation rates using NOM-^{199} Hg^{II} and nano-^{202}HgS as substrates were similar or greater than rates obtained using the labile $^{198}Hg(NO_3)_2$ substrate. ≡FeS-^{200} Hg^{II} yielded the lowest methylation rate in all sites, and thus the formation of FeS is likely a sink for labile $^{198}Hg(NO_3)_2$ in sulfide-rich paddy soils. Moreover, the variability in the methylation data for

a given site (1 to 5-fold variation depending on the Hg species) was smaller than what was observed across the mercury concentration gradient (10^3 to 10^4 fold variation between sites). These findings emphasize that at broad spatial scales, site-specific characteristics, such as microbial community structure, need to be taken into consideration, alongside the nature of the Hg substrate available for methylation, to determine net MeHg production.

(2) An understanding of Hg transformation processes in paddy soils is urgently needed in order to control Hg contamination of human food and related health impacts. Sulfur (S)-regulated Hg transformation is one important process that controls Hg cycling in agricultural fields. In this study, Hg transformation processes, such as methylation, demethylation, oxidation and reduction, and their responses to S input (sulfate and thiosulfate) in paddy soils with a Hg contamination gradient, were elucidated simultaneously using a multi-compound specific isotope labelling technique ($^{200}Hg^{II}$, $Me^{198}Hg$ and $^{202}Hg^0$). In addition to Hg^{II} methylation and MeHg demethylation, this study revealed that microbially mediated reduction of Hg^{II}, methylation of Hg^0, and oxidative demethylation-reduction of MeHg occurred under dark conditions; these processes served to transform Hg between different species (Hg^0, Hg^{II}, and MeHg) in flooded paddy soils. Rapid redox recycling of Hg species contributed to Hg speciation resetting, which promoted the transformation between Hg^0 and MeHg by generating bioavailable Hg^{II} to fuel methylation. Sulfur input also likely affected the microbial community structure and functional profile of Hg^{II} methylators and, therefore, influenced Hg^{II} methylation.

(3) The newly deposited Hg is more readily methylated to MeHg than native Hg in paddy soil. However, the biogeochemical processes of the newly deposited Hg in soil are still unknown. How iron and sulfur cycling influenced Hg transformation is not clear. In this study, a field experimental plot together with a stable Hg isotope tracing technique was used to demonstrate the geochemical fractionation (i.e., partitioning and redistribution) of the newly deposited Hg in paddy soils during the rice-growing period. Our results showed that the majority of Hg tracer (^{200}Hg) was partitioned as organic matter bound ^{200}Hg (84.6–89.4%), followed by residual ^{200}Hg (7.6–8.1%), Fe/Mn oxides bound ^{200}Hg (2.8–7.2%), soluble and exchangeable ^{200}Hg (0.05–0.2%), and carbonates bound ^{200}Hg (0.04-0.07%) in paddy soils.

Coupling of poorly crystalline Fe (oxyhydr)oxides and autochthonous dissolved organic matter played a predominant role in controlling the redistribution of the newly deposited Hg among geochemical fractions (i.e., fraction changes). The expected aging processes of the newly deposited Hg were absent, potentially explaining the high bioavailability of these Hg in paddy soil.

KEY WORDS: Paddy soil; Hg transformation; iron and sulfur cycling; redox; enriched Hg isotope labeling

论文原创性声明和使用授权说明

本人声明所呈交的博士后出站报告是我个人和合作导师指导下进行的研究工作及取得的研究成果。尽我所知，除文中特别加以标注和致谢的地方外，论文中不包含其他人已经发表或撰写过的研究成果，也不包含为获得中国科学院地球化研究所或其他教育机构和科研单位的学位或证书而使用过的材料。与我一同工作的同志对本研究所做的任何贡献均已在论文中作了明确说明并表示了谢意。

签名：_____日期：____年___月___日

关于博士后出站报告使用授权说明

本人完全了解中国科学院地球化学研究所有关保留、使用博士后出站报告的规定，即中国科学院地球化学研究所有权保留送交博士后出站报告的复印件，允许博士后研究报告被查阅和借阅；中国科学院地球化学研究所可以公布博士后研究报告的全部或部分内容，可以采用影印、缩印或其他复制手段保存研究报告。

□公开 开保密(__年)(保密的论文在解密后应遵守此规定)

博士后签名：

合作导师签名：

日期：___年____月 ____日

第1章 绪论

1.1 研究背景

汞（Hg）作为一种毒性很强的重金属污染物，能够随大气进行长距离传输（Ariya et al., 2015）。环境中的汞通常以无机和有机的形式存在，其有机形态的甲基汞（MeHg）毒性最强，能够穿过胎盘屏障与血脑屏障，对人体产生神经毒性（Clarkson, 1997）。2013 年旨在控制与削减全球人为汞排放和使用的国际公约《关于汞的水俣公约》获得通过，并在2017年正式生效。因此，深入开展环境汞研究不仅是我国环境保护的需要，也是我国履行国际汞公约的重大需求（冯新斌等，2020）。

1.1.1 汞的生物地球化学循环

在自然生态系统中，不同生物地球化学过程可以驱动 Hg 形态的转化。在大气环境中，气态 Hg(0)不仅能跨区域传输，还可在大气氧化剂（·OH、H_2O_2、O_3等）的驱动下发生氧化，典型表现为极地地区春季大气中 Hg^0 急剧下降，即大气 Hg 亏损现象（AMDEs）（谢周清等，2004）。Hg^0 被氧化后，大气中的活性气态汞与颗粒态汞浓度升高，它们均可参与 Hg 的大气沉降，且表现出较快的干沉降速率（冯新斌等，2009）。此外，大气液相中的 Hg^{II} 能够利用含甲基的物质进行非生物甲基化，使得大气湿沉降成为地表 MeHg 的重要来源（Gårdfeldt et al., 2003; Hammerschmidt et al., 2007）。土壤环境中的 Hg 主要来自于母岩的风化和大气沉降，其中可以进行迁移转化的 Hg 主要以 Hg(II)的形式与土壤颗粒结合。土壤中的汞离子（Hg2+）能够与 Lewis 软碱（如卤化物和硫化物）形成较强的共价键，能够与 Lewis 硬碱（如氟）形成较弱的共价键（Skyllberg, 2011）。受土壤侵蚀、淋溶、植物活化与吸收等作用，土壤中的 Hg 又会进入水体与生物体内。此外，土壤环境还是 Hg 甲基化的重要场所，尤其是在缺氧或厌氧的湿地和沉积物系统中。

水生生态系统是 Hg 进行生物地球化学循环较为活跃的区域，除不同形态 Hg 可以随水力作用跨流域迁移外，Hg^0 与 Hg^{II} 间的氧化还原、溶解态 Hg^0 的挥发、Hg^{II} 与配体的络合、无机 Hg^{II} 的甲基化与 MeHg 的去甲基化、Hg 的生物积累与放大等过程共同构成了 Hg 在水生生态系统的生物地球化学过程。具体来说，水体中的无机汞能够在生物和非生物驱动下进行氧化还原。当光照强度较高时，水体中的 Hg^{II} 可以通过光致还

原转化为 Hg^0（Zhang and Lindberg, 2001; Poulain et al., 2004; Driscoll et al., 2013; 冯新斌等，2009），通常包括两个过程：（1）水体中具有电子转移能力的溶解性有机质接受光照后吸收能量；（2）吸收能量后的活性有机质将 Hg(II)还原为 Hg^0（Ariya et al., 2015）。在缺少光照的环境中，一些含铁矿物（Wiatrowski et al., 2009; Bone et al., 2014）和具有还原基团的腐殖质（Jiang et al., 2014; 2015）同样能够介导非生物的 Hg^{II} 还原。除 Hg(II)的还原外，紫外光照射（特别是 UV-B）能够将 Hg^0 氧化，且 NO_3^-（Sun et al., 2015）和 Cl^-（Garcia et al., 2005）的存在均能促进 Hg^0 的非生物光致氧化。在微生物和藻类作用下，无机汞会受到光能营养型和化能营养型生物的驱动进行氧化还原反应（Ariya et al., 2015）。水体中 Hg^0 的生成及其向大气挥发，能够降低水体中的 Hg 浓度，表现为水生生态系统的脱毒机制之一。水体中被氧化的 Hg^{II} 作为 Lewis 软酸，几乎不会以游离 Hg^{2+} 的形式存在，而是以 $Hg(OH)^+$ 和 $Hg(OH)_2$ 等形态存在。在水生生态系统中，淡水水体中的 Hg^{II} 形态受溶解性有机质（DOM）影响；厌氧水体中的 Hg^{II} 形态受无机硫化物（HS^- 和 S_2^-）和硫醇（R-SH）影响；生物体中的 Hg^{II} 形态受 R-SH 和含 R-SH 的蛋白质影响（Zhang et al., 2004; Lemes and Wang, 2009; Wang and Zhang, 2013）。水生生态系统中无机汞可以在生物或非生物作用下发生甲基化（Ullrich et al., 2001; Celo et al., 2006; Merritt and Amirbahman, 2009; Driscoll et al., 2013; 刘金铃和丁振华，2007）。其中，生物甲基化主要在硫酸盐还原菌（Compeau and Bartaha, 1985; Choi et al., 1993）、铁还原菌（Fleming et al., 2006）和产甲烷菌（Hamelin et al., 2011）的参与下进行，而非生物甲基化主要发生在富含有机质的湖泊中（Ullrich et al., 2001）。在缺氧水体，特别是分层水体中的厌氧滞水层和沉积物的氧化还原界面均可以进行无机汞的微生物甲基化（Zhang et al., 2009; Feyte et al., 2012）。在微生物作用下，生成的 MeHg 可以进行还原去甲基化和氧化去甲基化（Lu et al., 2016; Du et al., 2019）；在光照作用下，可以进行光致去甲基化（Kim and Zoh, 2013; Sun et al., 2013）。甲基化与去甲基化同时进行，二者的共同作用决定了水生生态系统的净 MeHg 含量，其含量变化反映出 MeHg 在不同生态系统中的“源-汇”特征。

1.1.2 弄清稻田土壤甲基汞生成过程是降低稻米甲基汞污染的基本前提

课题组前期研究发现，水稻是迄今为止唯一的甲基汞富集农作物（Qiu et al., 2008; Meng et al., 2010; 2011; Zhang et al., 2010a），并且食用稻米是我国南方内陆居民甲基汞暴露的主要途径（Feng et al., 2008; Li et al., 2012; Zhang et al., 2010b）。因此，汞污染区

水稻甲基汞污染问题引起了国际社会的广泛关注。近年来，申请人课题组针对稻田生态系统各环境介质中汞的分布特征、污染状况、主要来源等开展了系统的研究工作，取得了一些初步认识：1）稻田土壤中存在活跃的甲基化作用，是稻米富集甲基汞的主要原因（即稻米中的甲基汞主要来源于土壤）（Meng et al., 2010; 2014; Zhao et al., 2016a; Qin et al., 2020）。2）稻田土壤中无机汞的甲基化过程和甲基汞的去甲基化过程共同决定了甲基汞的浓度（Zhao et al., 2016b）。3）硫酸盐还原与铁的异化还原过程是稻田土壤汞甲基化过程的重要代谢途径（Rothenberg and Feng, 2012; Zhao et al., 2016b）；产甲烷菌作用的产甲烷过程促进了甲基汞的去甲基化作用（Wu et al., 2020）。因此，弄清稻田土壤甲基汞的生成过程是汞污染稻田土壤修复的前提，是降低人体通过食用稻米导致的甲基汞暴露风险的先决条件。目前，国内外学者针对稻田生态系统汞的生物地球化学过程开展了大量的研究工作（Rothenberg and Feng, 2012; Liu et al., 2018; Li et al., 2019; Wang et al., 2019; 2021; Du et al., 2021）。但是，稻田土壤甲基汞的生成过程及其影响因素非常复杂，其相关机理还不清楚。

1.1.3 铁硫循环在汞甲基化过程中扮演重要角色

一直以来，微生物介导下无机汞的甲基化过程是汞的生物地球化学循环研究和关注的重点。该过程是受多种生物（如微生物的群落结构、活性与丰度等）与非生物因素（如生物可利用汞的含量、电子供体与受体、温度、光照、pH等）影响的复杂生物地球化学过程（Li et al., 2019; Tang et al., 2020; Zhao et al., 2020）。除异化铁还原、硫酸盐还原和产甲烷等过程与汞甲基化高度耦合外，还原性硫与汞存在较强的亲和力（Skyllberg, 2008），可以通过改变汞生物有效性的方式，影响汞甲基化过程。基于这两点认识，目前针对铁硫循环对汞甲基化的影响已经开展了大量研究（图 1），主要表现在以下两个方面：1）影响汞的形态与赋存状态，进而改变汞的生物有效性；2）影响汞甲基化微生物的群落结构与活性。针对第一个方面，研究发现还原性硫与溶解性有机质虽然能与汞形成难溶性的沉淀或大分子配合物而降低汞的生物有效性（Ravichandran, 2004），但也能与汞形成溶解态的络合物、胶体或纳米尺度的颗粒物而增加汞的生物有效性（Skyllberg, 2008; Graham et al., 2013; Zhang et al., 2012; 2014）。例如，Zhang et al. (2012, 2014)研究发现，汞与硫化物生成的纳米颗粒态硫化汞（nano-HgS）仍能够被甲基化。溶解性有机质的存在减缓了硫化汞团聚体的生成，增加了纳米硫化汞体系的稳定性，进一步增加了汞的生物有效性（Graham et al., 2013），细胞膜

上的胞外聚合物（EPS）也具有与 DOM 相似的作用（Zhang et al., 2020）。另外，还原环境中生成的铁硫矿物能够以吸附或共沉淀的方式将汞固定在矿物表面，降低其生物有效性（Jeong et al., 2007; Bower et al., 2008; Wang et al., 2020）。还有研究报道，还原性的铁、硫与有机质还能将二价汞还原为零价汞而减少可参与甲基化反应的汞（Gu et al., 2011; Zheng et al., 2012; Bone et al., 2014; Han et al., 2020）。针对第二个方面，铁和硫元素的氧化-还原过程为汞甲基化过程提供了重要的电子受体/供体，促进了铁还原菌与硫酸盐还原菌生长。溶解性有机质不仅能够介导微生物参与的电子传递过程，还为微生物生长提供了必要碳源。可见，铁硫循环是汞形态转化过程的重要控制因素（Skyllberg et al., 2021），在汞甲基化过程中扮演着非常重要的角色（Rothenberg and Feng, 2012; Li et al., 2019）。

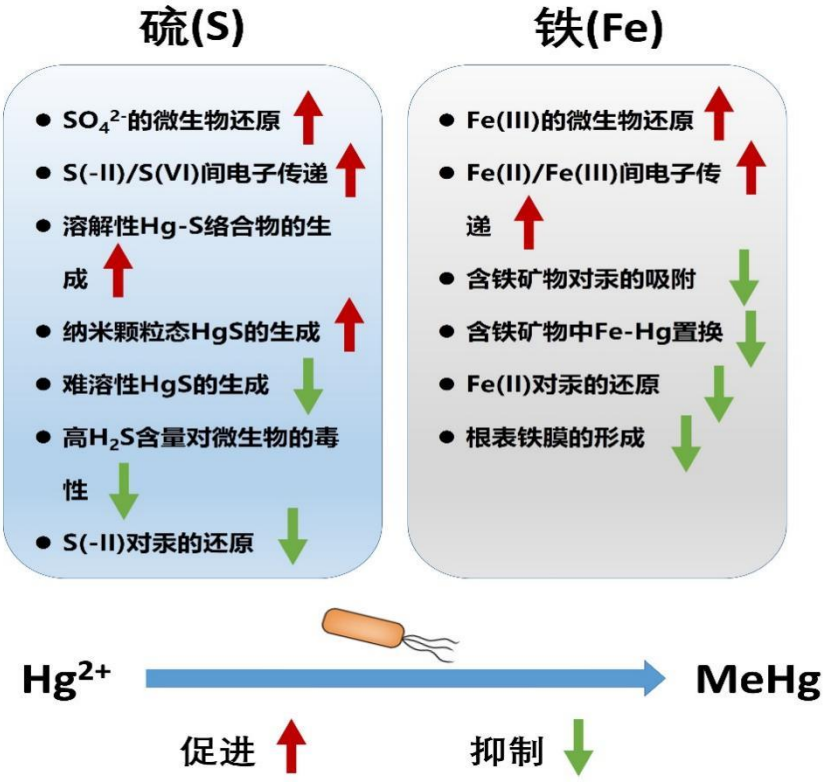

图 1-1 铁硫循环对汞甲基化过程存在的潜在影响

1.2 研究内容

（1）铁硫循环影响稻田土壤中参与甲基化反应的汞形态

以不同汞浓度梯度稻田土壤为研究对象，采用单一富集稳定汞同位素示踪技术，通过人工合成稻田土壤中普遍存在汞形态，包括溶解态汞（$^{198}Hg(NO_3)_2$）、有机质结合态汞（NOM-$^{199}Hg(II)$）、纳米颗粒态硫化汞（nano-^{202}HgS）以及硫化亚铁吸附态汞（≡FeS-$^{200}Hg(II)$），以探究上述汞形态在稻田土壤中的生物有效性，明确铁硫循环形成的典型汞形态能否参与甲基化反应。

（2）汞和硫的氧化还原循环影响稻田土壤中甲基汞的积累

以不同汞浓度梯度稻田土壤为研究对象，采用单一富集稳定汞同位素示踪技术，通过合成无机汞同位素示踪剂（$^{200}Hg^{II}$），甲基汞同位素示踪剂（$Me^{198}Hg$）以及零价汞同位素示踪剂（$^{202}Hg^{0}$），分别示踪稻田土壤中汞的甲基化、去甲基化、还原以及氧化过程。另外，通过外源添加两种含硫化合物（硫酸盐和硫代硫酸盐），探究不同形态硫添加及其氧化还原循环对汞形态转化的影响。

（3）铁氧化物-有机质复合体系控制稻田土壤中新沉降汞的地球化学形态分馏

以稻田土壤为研究对象，采用单一富集稳定汞同位素示踪技术，添加 $^{200}Hg^{II}$ 模拟新沉降汞，结合汞的连续提取技术，铁形态分级以及有机质形态分级等手段，探究稻田土壤中新沉降汞的形态分布特征以及再分配过程。明确稻田土壤中的铁氧化物如何影响汞的生物有效性。

第 2 章 铁硫循环影响稻田土壤中参与甲基化反应的汞形态

2.1 本章引言

淹水的稻田土壤作为一种间歇性的湿地系统，是汞（Hg）甲基化微生物理想的栖息地（Gilmour et al., 2013; Parks et al., 2013; Podar et al., 2015; Liu et al., 2018）。前期大量工作已经证实，稻米中的甲基汞（MeHg）来源于稻田土壤中无机汞的原位甲基化过程（孟其义等，2018；Meng et al., 2010, 2014; Zhao et al., 2016b; Qin et al., 2020; Liu et al., 2021）。因此，稻田土壤是汞甲基化研究的热点区域（Rothenberg and Feng, 2012）。众所周知，汞甲基化过程受多种生物、物理和化学因素的影响，如微生物群落结构、汞的形态、温度、pH、氧化还原状态、天然有机质等（Bravo and Cosio, 2020; Regnell and Watras, 2018）。其中，汞的形态及其生物有效性是影响净 MeHg 生成的重要因素之一（Hsu-kim et al., 2013; Wang et al., 2014; Regnell and Watras, 2018; Li et al., 2019）。湿地土壤中汞的形态是多种多样的，其中较为典型的汞形态包括与无机离子（如 HS^-）结合的溶剂态汞（Jonsson et al., 2012; Liem-Nguyen et al., 2016; Zhu et al., 2018）；与溶解性有机质（DOM）结合的汞（Jonsson et al., 2012; Liem-Nguyen et al., 2016; Mazrui et al., 2016; Zhu et al., 2018）；纳米颗粒态的硫化汞（HgS）（Zhang et al., 2012, 2014; Tian et al., 2021）以及吸附在硫化亚铁表面的汞（Jonsson et al., 2012）。可见，铁硫循环对于汞的形态具有重要的作用。然而，铁硫循环作用下形成的不同形态汞在稻田土壤中的生物有效性如何？其对于甲基汞生成的贡献如何？仍不清楚。这给稻田土壤汞污染防治与修复工作带来了极大的挑战。因此，本研究采用稳定汞同位素示踪技术，分别合成了溶解态汞（$^{198}Hg(NO_3)_2$）、有机结合态汞（NOM-^{199}Hg(II)）、硫化亚铁吸附态汞（≡FeS-^{200}Hg(II)）和纳米颗粒硫化汞（nano-^{202}HgS），定量识别不同形态汞在稻田土壤中的甲基化过程，揭示上述汞形态在甲基化过程中的生物有效性，并厘清汞浓度梯度对汞甲基化过程的影响。

2.2 材料与方法

2.2.1 研究区与样品采集

本实验选取三处 Hg 浓度差异较大的水稻田，其分别为位于贵州省铜仁市万山区

的废弃汞矿区稻田（四坑，SK）、土法炼汞区稻田（垢溪，GX）和贵州省贵阳市花溪区背景区稻田（HX）。其中，四坑为废弃汞矿区，该区域稻田土壤受汞矿渣堆积的污染；垢溪为土法炼汞区，该区域稻田土壤受土法炼汞活动影响，大气中汞浓度较高，而汞的大气沉降是该区域稻田土壤主要的汞污染源（Zhao et al., 2016b）；花溪区稻田土壤未受到汞污染影响。

前期研究发现，在水稻生长的第 50~60 天时，稻田土壤中净 MeHg 生成量较高，Hg 甲基化较为活跃（Zhao et al., 2016a, b）。因此，在该时期采集稻田土壤样品和对应上覆水样品。采集 1~5 cm 表层淹水土壤，装满至 500 mL 聚丙烯采样瓶中，不留空气。对应上覆水样品使用 250 mL 注射器，也采集至 500 mL 聚丙烯采样瓶中。所有土样与水样均使用 Parafilm®封口膜密封后，双层自封袋包装，保存于低温冷藏箱中，并在 24 小时内运回至实验室中。每个研究区稻田各采集三份稻田土壤与上覆水样品。本研究供试土壤的基础理化指标如表 2-1 所示。

表 2-1 水稻生长期稻田土壤中不同形态铁的含量

研究区稻田土壤	背景区 (HX)	土法炼汞区 (GX)	废弃汞矿区 (SK)
土壤			
总汞 THg (mg kg^{-1})	0.27 ±0.10 c	3.34 ±0.97 b	48.9 ±9.78 a
甲基汞 MeHg (μg kg^{-1})	0.37 ±0.23 c	6.56 ±2.28 a	2.50 ±0.49 b
MeHg/THg (%)	0.14 ±0.10 a	0.19 ±0.04 a	0.0051 ±0.002 b
土壤有机质 SOM (%)	7.47 ±0.27 a	4.11 ±0.19 b	3.28 ±0.30 c
酸碱性 pH	7.52	7.51	7.53
硫酸盐 SO_4^{2-} (mg kg^{-1})	486 ±41.5 b	489 ±21 b	1039 ±121 a
铵盐 NH_4^+ (mg kg^{-1})	3.55 ±0.30 b	5.86 ±0.95 a	1.69 ±0.07 c
硝酸盐 NO_3^- (mg kg^{-1})	5.67 ±0.87 b	3.18 ±0.55 c	22.3 ±0.88 a
土壤机械组成			
黏粒 (%)	34.0 ±0.0 a	30.7 ±2.3 a	15.3 ±1.2 b
粉粒 (%)	33.0 ±4.2 a	34.7 ±2.3 a	36.7 ±2.3 a
砂粒 (%)	33.0 ±4.2 b	34.7 ±4.6 b	48.0 ±3.5 a
土壤孔隙水			
硫酸根 SO_4^{2-} (mg L^{-1})	0.23 ±0.09 b	1.28 ±0.16 a	0.83 ±0.02 ab
硫化物 S(-II) (mg L^{-1})	0.025 ±0.004b	0.059 ±0.002 a	0.018 ±0.007b
硝酸根 NO_3^- (mg L^{-1})	N.D.	0.025 ±0.008 b	0.086 ±0.034 a
亚硝酸根 NO_2^- (mg L^{-1})	0.009 ±0.003b	0.21 ±0.03 a	N.D.
铵根 NH_4^+ (mg L^{-1})	35.7 ±2.21 b	25.3 ±3.39 c	60.5 ±11.9 a
亚铁离子 Fe^{2+} (mg L^{-1})	0.48 ±0.04 a	0.93 ±0.22 a	1.15 ±0.47 a
铁离子 Fe^{3+} (mg L^{-1})	0.76 ±0.03 a	0.38 ±0.06 b	0.69 ±0.15 a

注：不同小写字母表明同一指标在不同位点间差异显著（$p < 0.05$）

2.2.2 同位素示踪剂的制备与表征

本研究使用 ^{198}Hg（纯度 95.3 ± 0.15 %）、^{199}Hg（纯度 92.6 ± 0.15 %）、^{200}Hg（纯度 98.2 ± 0.15 %）和 ^{202}Hg（纯度 99.2 ± 0.15 %）四种无机汞同位素以及一种甲基汞同位素（$Me^{198}Hg$）；其中，无机汞同位素用于示踪甲基化过程，而甲基汞同位素示踪去甲基化过程。所有汞稳定同位素均购自美国 ISOFLEX 公司。人工制备得到四种不同形态的无机汞同位素，分别为溶解态汞（$^{198}Hg(NO_3)_2$）、有机结合态汞（NOM-

^{199}Hg(II)）、硫化亚铁吸附态汞（≡FeS-^{200}Hg(II)）和纳米颗粒硫化汞（nano-^{202}HgS）。具体的制备方法如下文：

^{198}Hg(NO$_3$)$_2$：将 ^{198}Hg^0 溶解于浓硝酸中（纯度≥ 99.9%），制备得到 ^{198}Hg(NO$_3$)$_2$ 储备液（20（μg mL^{-1}）），并使用超纯水（Milli-Q，Millipore，美国）稀释得到浓度为 1（μg mL^{-1}）的工作液。

NOM-^{199}Hg(II)：在厌氧手套箱中（PLAS-LABS，美国）将购买自国际腐殖质协会的标准腐殖质样品 Suwannee River NOM 与 ^{199}Hg(II)均匀混合，超声几秒钟后低温（4 ºC）静置 5 天（Jonsson et al., 2012）。制备得到的 NOM-^{199}Hg(II)浓度为 2.95（μg Hg mL^{-1}）。

≡FeS-^{200}Hg(II)：将 Fe(NH$_4$)$_2$(SO$_4$)$_2$ 和 N$_2$S·9H$_2$O 在厌氧手套箱中溶解于脱氧超纯水，制备得到 FeS(s)（14.9（mg mL^{-1}）。将制备得到的 FeS(s)润洗三次，以洗去残留的硫化物。随后将 ^{200}Hg(II)加入含 FeS(s)的脱氧超纯水中，制备得到浓度为 23.8（μg Hg mL^{-1}）的≡FeS-^{200}Hg(II)（Jonsson et al., 2012）。

Nano-^{202}HgS：在配制的 N$_2$S·9H$_2$O 溶液中加入 ^{202}Hg(II)、购买自国家腐殖质协会的腐殖酸标准样品 Suwannee River humic acid（浓度 10（mg C L^{-1}））、0.1 M NaNO$_3$、4 mM HEPES 缓冲液（pH 7.5），以稳定 HgS 纳米颗粒物。将该悬浮液在厌氧手套箱中常温静置一周，随后多次过滤至粒径小于 0.1 μm（Zhang et al., 2012），得到 nano-^{202}HgS，浓度为 10.03（μg mL^{-1}）。

Me^{198}Hg：采用甲基钴胺素为甲基供体合成得到 Me^{198}Hg（Rodríguez Martín-Doimeadios et al., 2002）。制备得到的 Me^{198}Hg 储备液浓度 3.77（μg mL^{-1}）。

制备得到的≡FeS-^{200}Hg(II)和 Nano-^{202}HgS 使用透射电镜（TEM）（Tecnai G2 F20 S-TWIN, FEI，美国）与 X 射线能量色散谱（EDX）（EDAX，美国）进行表征，表征结果如图 2-1 和图 2-2。

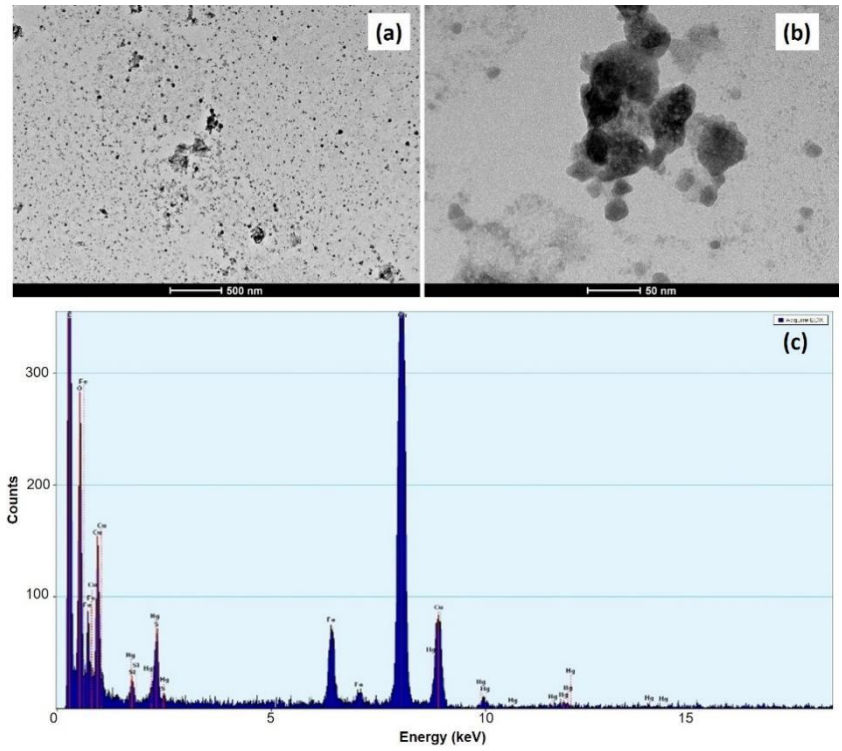

注：（a）500 nm TEM 图像；（b）50 nm TEM 图像（c）EDX 能谱表明样品中存在 Fe、S 和 Hg 元素

图 2-1 TEM-EDX 表征制备得到的≡FeS-^{200}Hg(II)

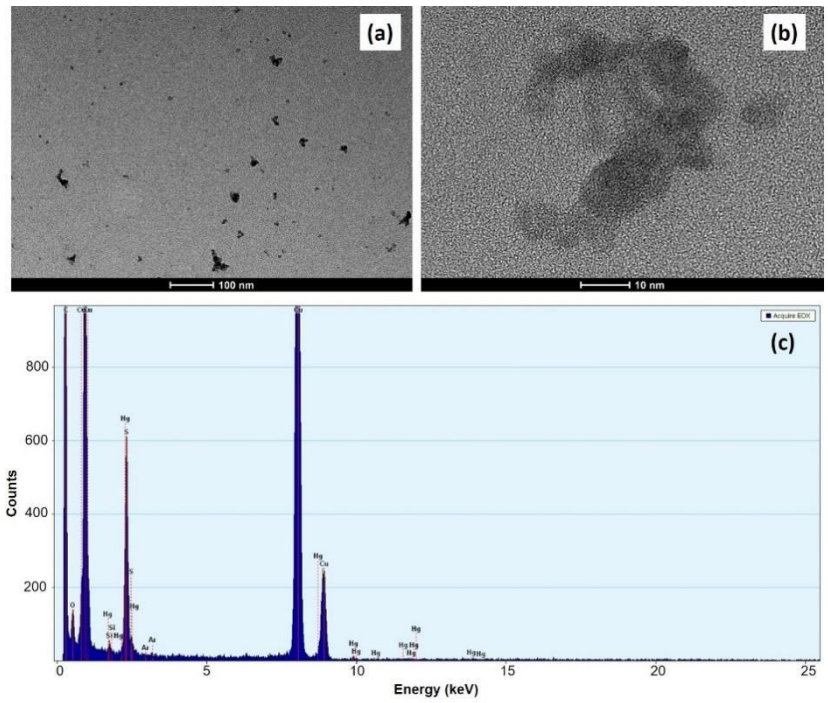

注：（a）100 nm TEM 图像；（b）10 nm TEM 图像（c）EDX 能谱表明样品中存在 S 和 Hg 元素

图 2-2 TEM-EDX 表征制备得到的 Nano-^{202}HgS

2.2.3 培养实验设计

在厌氧手套箱中，将采集自同一位点的稻田土壤与上覆水样品移至 2 L 烧杯中。使用特氟龙镊子挑出岩石颗粒与植物残体后，将稻田土壤与上覆水均匀混合为含水率为 75%的泥浆样品。随后将均匀的泥浆样品分装入 100 mL 血清瓶中，每瓶分装泥浆 50 mL。根据每个研究区稻田土壤总汞（THg）和 MeHg 的本底值，按照 THg 含量的 10%以及 MeHg 含量的 100%分别加入之前制备的无机汞与甲基汞示踪剂（Gilmour et al., 1998; Zhao et al., 2016a; Wu et al., 2020）。随后，将血清瓶完全密封，并在黑暗环境中厌氧培养两天。由于用于示踪去甲基化的示踪剂（$Me^{198}Hg$）所用汞同位素与 $^{198}Hg(NO_3)_2$ 一致，均为 ^{198}Hg。因此，甲基化过程与去甲基化过程分为两个培养试验，分别示踪，其中系列 A 为甲基化实验（设置 48 个培养瓶），系列 B 为去甲基化实验（设置 48 个培养瓶）（如图 2-3 所示）。分别在培养的第 0、0.25、0.5、1 和 2 天进行破坏性取样，每个采样点每次随机选取三个平行（共 9 个培养瓶 = 3 个平行 × 三个研究区）。取 30 mL 泥浆样品至 50 mL 离心管中，经过离心后分析上清液中 pH、总硫化物（[S(-II)]）、硫酸盐、[Fe^{2+}]和[Fe^{3+}]浓度以及土壤 DOM 含量。取少量泥浆样品装于 1.5 mL 冻存管中并-80 ºC 保存，用于提取 DNA 样品。其余泥浆样品加入 1 mL 6 N HCl 酸化后，-20 ºC 保存保存，用于分析汞同位素。所有的取样工作，均在厌氧手套箱中进行，以避免采样过程对样品的氧化。

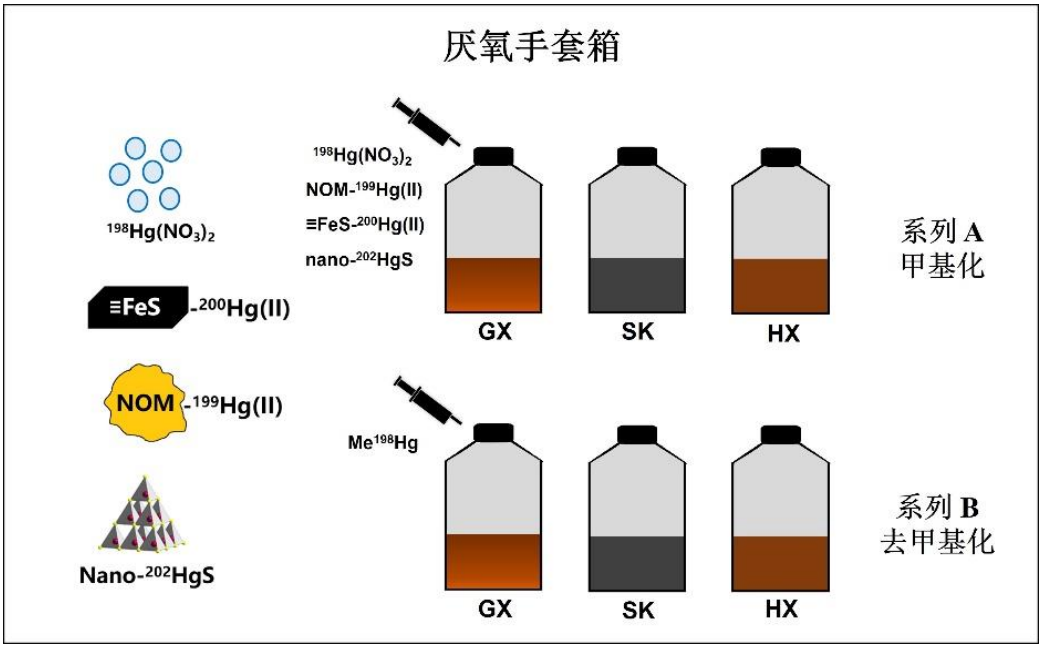

图 2-3 实验设计示意图

2.2.4 分析方法

使用气相色谱-电感藕合等离子体质谱（GC-ICP-MS）测定土壤样品中经过无机汞示踪剂甲基化生成的甲基汞同位素（$Me^{198}Hg$、$Me^{199}Hg$、$Me^{200}Hg$、$Me^{202}Hg$）含量。采用高通量 16s rRNA 基因测序的方法对三个采样区原始土壤样品，进行微生物群落多样性分析。16s rRNA 基因的扩增引物为 341F-805R （341F：5'-CCTACGGGNGGCWGCAG-3'；805R：5’-GACTACHVGGGTATCTAATCC-3’）。基于 Illumina PE250 测序平台对经过扩增和纯化的 DNA 进行测序，并对经过处理后的序列进行同源性分析，将相似度大于 97%的序列聚类为一个操作分类单元（OTU）。基于 OTU 进行 Alpha 多样性和 Beta 多样性计算，包括菌群丰度（*Chao1*）与多样性（*Shannon*）指标和主坐标分析（PCoA）。此外，针对汞甲基化功能基因 *hgc*AB 进行荧光定量 PCR 分析，所用因为为 ORNL-HgcAB-uni-F/R 以及对应不同进化枝的 Clade-specific hgcA in Deltaproteobacteria (ORNL-Delta-HgcA-F/R)（Christensen et al., 2016; Liu et al., 2019）。

2.2.5 计算方法与质量控制

根据添加无机汞甲基化生成的甲基汞同位素计算甲基化率（MeHg/Hg(II) (%)），根据添加的甲基汞同位素的消耗量计算去甲基化率（MeHg demethylation (%)），计算公式如下：

$$\text{甲基化率 (\%)} = \frac{[Me^{i}Hg]}{[^{i}Hg(II)]_{spiked}} \times 100\% \qquad \text{（公式 2-1）}$$

$$\text{去甲基化率 (\%)} = \frac{[Me^{198}Hg]_{spiked} - [Me^{198}Hg]}{[Me^{198}Hg]_{spiked}} \times 100\% \qquad \text{（公式 2-2）}$$

其中，$[Me^{i}Hg]$ 是通过添加的无机汞同位素甲基化生成的 MeHg；$[^{i}Hg(II)]_{spiked}$ 是添加的无机通同位素示踪剂；$[Me^{198}Hg]_{spiked}$ 是添加的甲基汞同位素示踪剂；i 等于 198、199、200 和 202。

对应甲基化率和去甲基化率，进一步计算甲基化速率常数（K_m）和去甲基化速率常数（K_d）（Hintelmann et al., 1995, 2000），计算方法如下式：

$$K_m = \frac{[Me^{i}Hg]_{tj} - [Me^{i}Hg]_{t0}}{[^{i}Hg(II)] \times t} \qquad \text{（公式 2-3）}$$

$$K_d = \frac{\ln([Me^{198}Hg]_{t0}) - \ln([Me^{198}Hg]_{tj})}{t} \qquad \text{（公式 2-4）}$$

其中，$[Me^{i}Hg]_{t0}$ 和$[Me^{i}Hg]_{tj}$ 分别为初始阶段（t_0）和不同取样时间点（t_j）时甲基

化生成的 MeHg 的含量；*t* 为培养时间；*j* 为 0.25、0.5、1 和 2 天。

本研究使用 ERMCC580（[MeHg] = 75.5 ± 3.7（μg kg^{-1}））为 MeHg 分析时的标准物质。通过测定发现，ERMCC580 的回收率为 111 ± 8.86 %，范围为 99 %至 125 %。此外，计算培养开始与末期的同位素质量平衡，同位素总量的回收率达 100.0 ± 3.59 %（图 2-4），表明培养实验过程中不存在同位素损失或者污染。

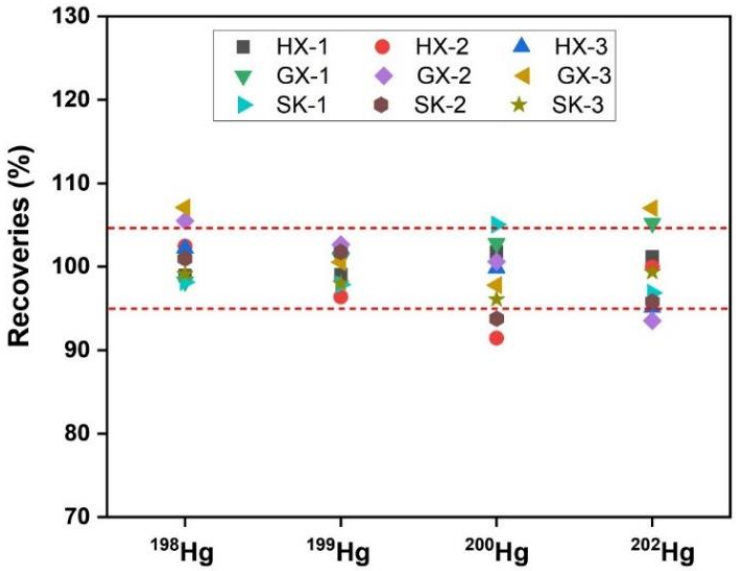

注：HX、GX、SK 分别为花溪、垢溪和四坑采样点

图 2-4 培养初期与末期汞同位素质量平衡

2.3 不同形态汞同位素示踪剂的甲基化与去甲基化

图 2-5 所示为添加不同形态无机汞同位素示踪剂后，不同采样点稻田土壤的甲基化率（MeHg/Hg(II)）和甲基化速率常数（K_m）。可以看出，除≡FeS-^{200}Hg(II)外，其他形态的无机汞均有显著的甲基化作用；并且 MeHg/Hg(II)随稻田土壤 Hg 含量的增加而显著降低，其中花溪背景区（HX，[THg] = 0.27（mg kg^{-1}））、土法炼汞区（GX，[THg] = 3.34（mg kg^{-1}））和废弃汞矿区（SK，[THg] = 48.93（mg kg^{-1}））稻田土壤的 MeHg/Hg(II)分别为 2~5%、0.3~0.35%和 0.002~0.005%（表 2-1 和图 2-5）。甲基化速率常数（K_m）的在不同位点间的变化趋势与甲基化率一致。

在背景区稻田土壤培养末期，$^{198}Hg(NO_3)_2$ 的 MeHg/Hg(II)最高（4.85 ± 0.13 %），然后依次是 NOM-^{199}Hg(II)、Nano-^{202}HgS 和≡FeS-^{200}Hg(II)（$p < 0.05$）。在中度汞污染的土法炼汞区稻田土壤培养末期，NOM-^{199}Hg(II)的 MeHg/Hg(II)最高，其次是 $^{198}Hg(NO_3)_2$ 和 Nano-^{202}HgS，但二者差异不显著。汞浓度最高的废弃汞矿区与土法炼

汞区相似，NOM-^{199}Hg(II)的 MeHg/Hg(II)最高，其次是 Nano-^{202}HgS（$p < 0.05$）。背景区和废弃汞矿区土壤培养实验中，MeHg/Hg(II)随时间的变化趋势是先增加后逐步达到平衡；而土法炼汞区土壤中 MeHg/Hg(II)表现出持续的增加趋势。

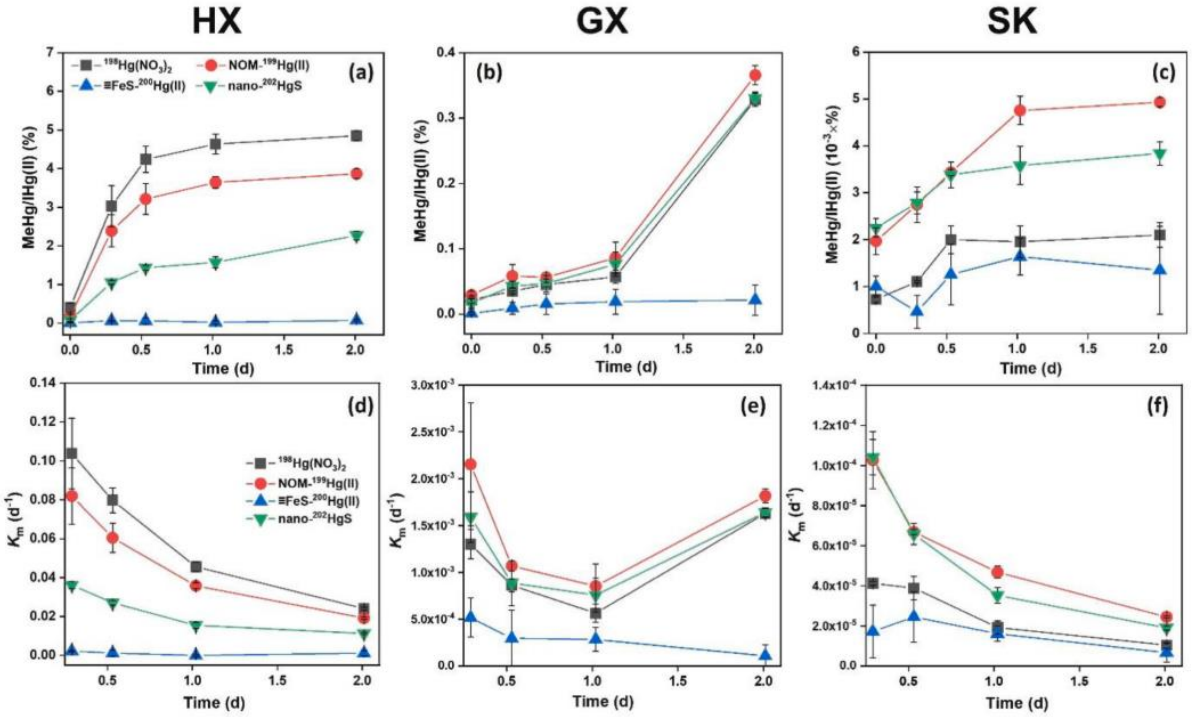

图 2-5 甲基化率与甲基化速率常数

在本研究中，培养前期不同形态无机汞的 K_m 值较高，随后表现出下降的趋势，这与 Gilmour 等人（2018）在纯培养体系中得到的结果一致。背景区和废弃汞矿区稻田土壤中不同形态无机汞示踪剂的 K_m 随时间的增长持续降低；而土法炼汞区稻田土壤中不同无机汞的 K_m 表现出先降低后增加的趋势，且在培养末期的 K_m 与初期接近（除≡FeS-^{200}Hg(II)）。

图 2-6 所示为甲基汞示踪剂（Me^{198}Hg）的去甲基化率及去甲基化速率常数（K_d）。在培养末期，HX、GX 和 SK 的去甲基化率分别为 44.26 ± 6.79 %、47.03 ± 6.45 %和 80.99 ± 3.86 %。SK 和 HX 的 K_d 随培养时间的变化趋势较为相似，分别从 2.28 ± 0.18（d^{-1}）和 1.38 ± 0.17 （d^{-1}）逐步下降至 0.84 ± 0.12（d^{-1}）（$p < 0.05$）和 0.31 ± 0.04（d^{-1}）（$p < 0.05$）。GX 的 K_d 则在培养的第一天内迅速从 1.03 ± 0.59（d^{-1}）下降至 0.33 ± 0.06（d^{-1}），并在随后的培养中保持稳定。

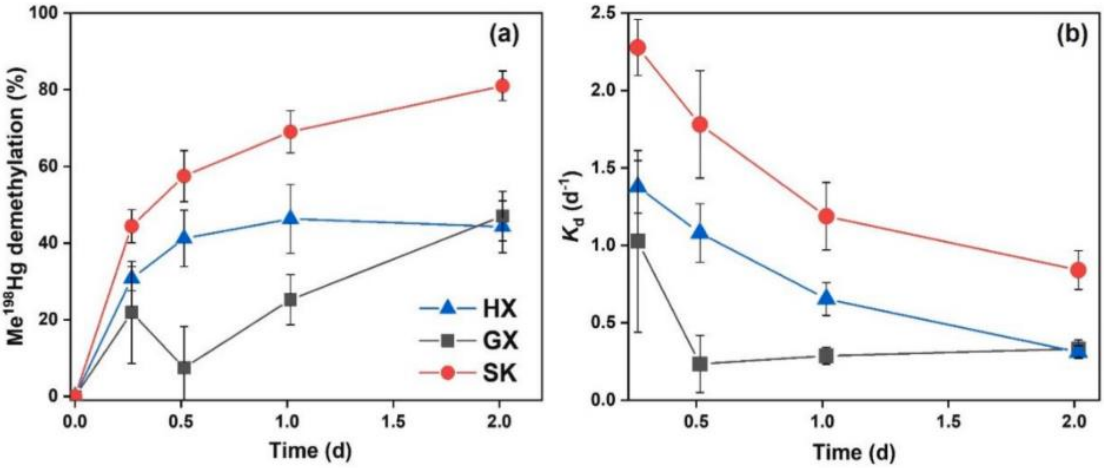

图 2-6 去甲基化率与去甲基化速率常数

2.4 稻田土壤中可参与甲基化作用的汞形态识别

纳米颗粒态 HgS 广泛存在于缺氧或者有氧的环境中（Enescu et al., 2016; Manceau et al., 2018; Zhang et al., 2020），并且有研究报道纳米颗粒态 HgS 能够被甲基化（凌倩倩等，2020；Zhang et al., 2012, 2014; Zhang et al., 2020; Deonarine and Hsu-Kim, 2009; Slowey, 2010; Gerbig et al., 2011; Graham et al., 2012; Tian et al., 2021）。纳米颗粒态 HgS 粒径的大小决定了其生物有效性，其中粒径越小的纳米颗粒态 HgS 可能生成更多的 MeHg（Zhang et al., 2012）。在本研究中，通过制备合成的 nano-^{202}HgS 的粒径为 10 nm 左右（图 2-2），这与 Zhang 等人（2012）制备的纳米颗粒态 HgS 粒径相似（3.2~20 nm），能够进行跨膜运输并被甲基化。值得注意的是，尽管 nano-^{202}HgS 能够被甲基化，NOM 对于 nano-^{202}HgS 的作用仍不可忽略。本研究在制备 nano-^{202}HgS 时，加入了一定量的 NOM，用与稳定纳米尺度 HgS 结构的稳定性（Slowey, 2010; Gerbig et al., 2011; Graham et al., 2012; Ravichandran et al., 1999; Pham et al., 2014）。有学者发现，胞外聚合物（EPS）也具有与 NOM 相似的功能（Zhang et al., 2020）。

在之前的研究中，学者通常认为天然有机质（NOM）的存在会与 Hg 形成大分子量的亲水性 Hg-NOM 复合物（Hsu-kim et al., 2013; Chiasson-Gould et al., 2014），从而降低 Hg 的生物有效性，进而抑制 MeHg 的生成（Barkay et al., 1997; Ravichandran, 2004）。然而，本研究发现，NOM-^{199}Hg(II)在厌氧的稻田土壤培养中，能够有效地生成 Me^{199}Hg，并且相较其他形态无机汞产生更多的 MeHg。由于土壤 DOM 的含量在培养周期内几乎未发生变化（图 2-7），说明实验土壤为微生物的代谢提供了充足的碳源，使得微生物甲基化过程并未受到碳源不足的影响。既然碳源的量并不是本研究影响甲

基化过程的主要因素，那么土壤中天然存在的 DOM 可能通过与不同形态 Hg 的相互作用，从而改变不同形态汞的生物有效性（吴丰昌等，2008）。有学者通过淋溶实验发现（Gai et al., 2016），与腐殖酸结合的 Hg(II)较溶解态的 Hg-Cl/-OH 络合物、Hg^0 和纳米颗粒态 HgS 具有更强的迁移性（mobility）。此外，还有学者指出，Hg(II)与 NOM 的结合能够显著减少 Hg(II)在土壤固相上的分配（Johs et al., 2019）。Zhu 等人（2018）利用在 Nätraån 河口沉积物进行甲基化培养实验发现，NOM-^{202}Hg(II)的 K_m 甚至接近于 $^{201}Hg(NO_3)_2$，说明 NOM-^{202}Hg(II)的是生物有效态的 Hg。在使用模式菌株 *Desulfovibrio desulfuricans* ND132 进行的纯培养实验中，Biswas 等人（2011）也发现 NOM-Hg(II)具有较高的生物有效性，且该实验所用的 NOM 和本研究一致，均为国际腐殖质协会的 SRNOM。基于文献报道和本研究数据，我们得到 NOM-^{199}Hg(II)这一汞形态具有较高的移动性与生物有效性，在稻田土壤中能够被甲基化。

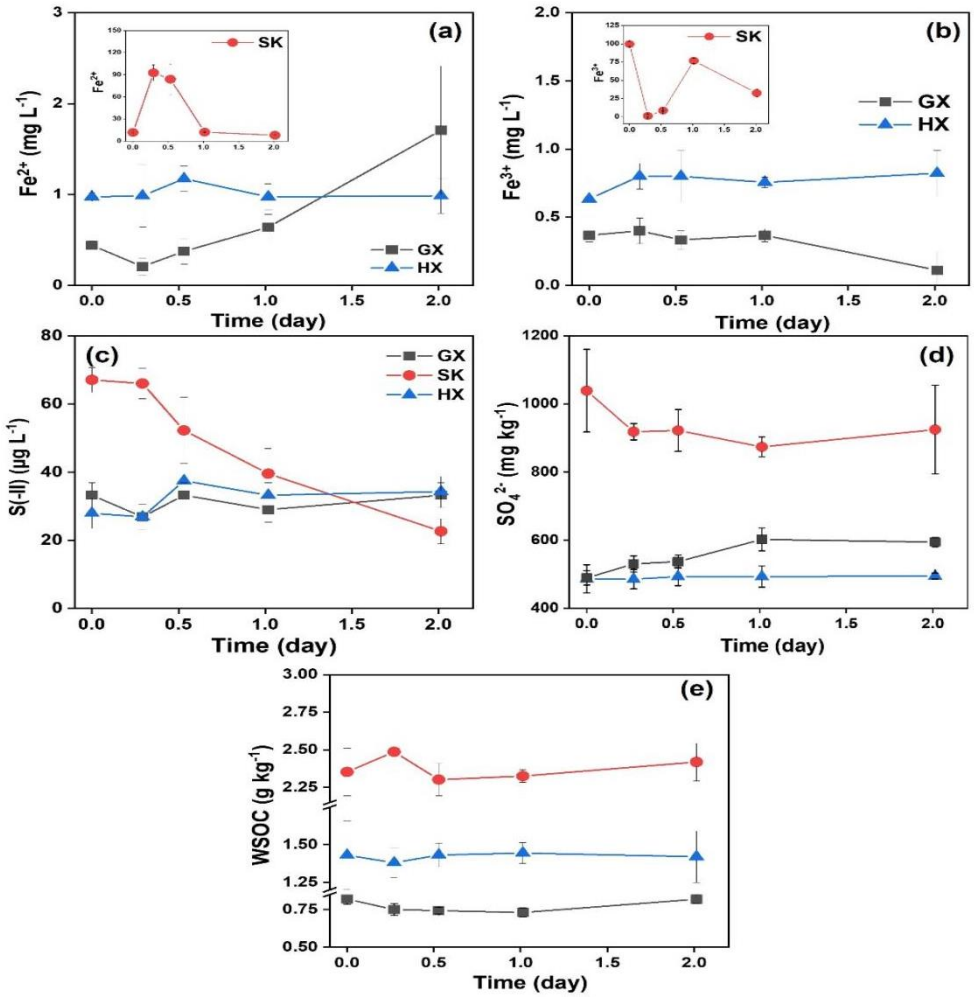

图 2-7 培养期间初期 Fe^{2+}、Fe^{3+}、S(-II)、SO_4^{2-} 以及土壤 DOM 含量

有学者发现地下水系统中存在的 FeS 对 Hg 具有较高的选择性，能够迅速与 Hg 结

合，从而抑制 Hg 的甲基化作用（Wang et al., 2020）。Skyllberg 等人（2021）在瑞典高纬度湖泊沉积物中也发现，FeS 的生成控制着 Hg 的化学形态。在本研究中，培养实验开始后，SK 土壤中表现出 Fe^{3+}含量的迅速下降以及 S(-II)的快速积累（图 2-7），这表明在本实验体体系中可能有 FeS 的生成。这部分新生成的 FeS 既能够通过表面吸附的方式结合 $^{198}Hg(NO_3)_2$，还能够通过 Fe-Hg 置换的方式生成 HgS（Wolfenden et al., 2005; Jeong et al., 2007; Skyllberg and Drott, 2010）。此外，较高的 S(-II)浓度会促进 MeHg 的非生物去甲基化（Jonsson et al., 2016；West et al., 2020），这可能是 SK 去甲基化率高于 GX 和 HX 的原因之一。

2.5汞浓度梯度对稻田土壤中汞甲基化和去甲基化的影响

在本研究中，我们发现随稻田土壤 Hg 含量的升高，无机汞的甲基化率与甲基化速率常数显著降低；特别是，不同形态无机汞在同一研究就位点的差异（相差 1~5 倍）远小于不同位点之间（相差 1000~10000 倍）的差异（图 2-8）。这一发现表明，在更大的区域尺度上，不同位点稻田土壤自身的特异性对于 Hg 甲基化过程的影响大于同一位点参与甲基化的不同 Hg 形态。

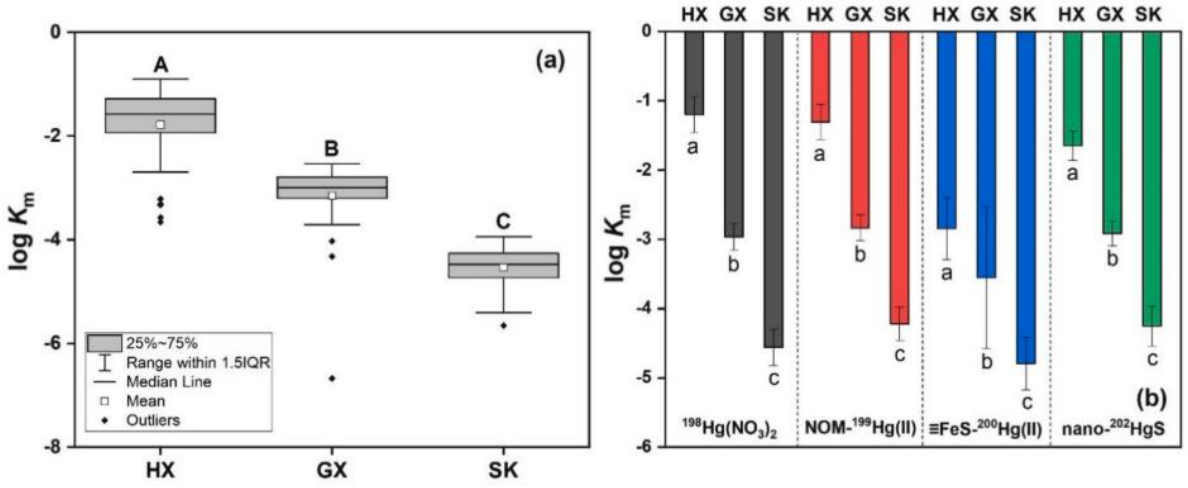

注：（a）将四种无机汞形态合并在一起；（b）不同无机汞形态在不同位点的平均 K_m。HX、GX、SK 分别为花溪、垢溪和四坑采样点

图 2-8 不同位点间经对数变换后的甲基化速率常数

然而，不同位点间 Hg 甲基化过程以及净 MeHg 积累的差异可能归咎于：（1）Hg 污染的来源以及 Hg 形态的差异；（2）不同位点间土壤物理化学性质的差异；（3）参

与 Hg 甲基化过程微生物群落结构的差异；（4）MeHg 去甲基化过程的差异。

2.5.1 汞污染的来源以及汞形态的差异

在本研究的背景区（HX），不存在 Hg 污染源，然而稻田土壤中的 THg 含量（0.27 ± 0.10（mg kg^{-1}））依旧显著高于全国背景值（0.058（mg kg^{-1}））。这是因为贵州省地处环太平洋汞矿化带上，土壤中 Hg 含量来自于地质背景（Qiu et al., 2008）。本研究中发现的 K_m 随时间的变化趋势与 Jonsson 等人（2012）采用河口沉积物进行的甲基化模拟实验一致，并且符合一级动力学模型（图 2-9），这表明不存在 Hg 污染的稻田土壤中，无机汞生物有效性由高到低的顺序为：$Hg(NO_3)_2$ > NOM-Hg(II) > Nano-HgS > ≡FeS-Hg(II)，且甲基化活性在 24 小时内最强，随后逐步降低。

土法炼汞区（GX），由于存在土法炼汞活动，大气中的 Hg^0 浓度显著高于背景区大气（Zhao et al., 2016a）。此外，该区域稻田土壤中的 MeHg 含量（4.16~9.93（μg kg^{-1}））以及 MeHg/THg 的比例（0.19 %）也为三个采样区中最高的（表 2-1）。有研究法发现新沉降的 Hg 更易于被甲基化从而转化为 MeHg（Zhao et al., 2016a），这可能是受大气 Hg 沉降影响区域 MeHg 含量较高的原因。除此之外，通过连续提取法对 Hg 形态进行分级后发现，有机结合态 Hg 是 GX 稻田土壤中主要的汞形态，结合本研究 NOM-^{199}Hg(II)较高的甲基化率与甲基化速率常数，我们推测一部分有机质结合态的 Hg 也能够参与甲基化反应。同时，一部分通过大气沉降进入稻田土壤的 Hg 可能会形成纳米颗粒态 HgS（Manceau et al., 2018），而这部分 Hg 也具有较高的生物有效性。

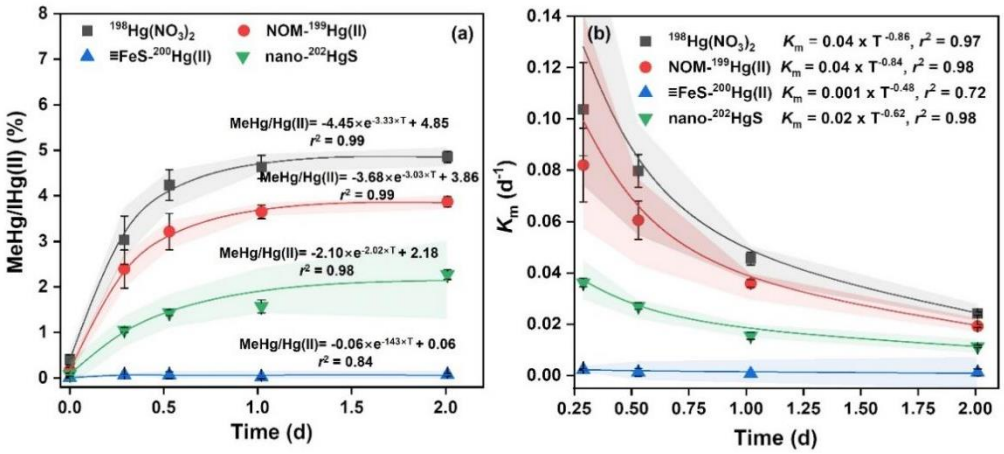

注：（a）甲基化率；（b）甲基化速率常数

图 2-9 背景区稻田土壤甲基化率和甲基化速率常数的动力学拟合

由于长期的汞矿开采活动以及尾矿的堆积，废弃汞矿区（SK）稻田土壤的 THg

含量最高，达 35.11~59.96（mg kg^{-1}）；但其甲基化速率常数最低。通过连续提取法对该区域土壤中 Hg 的形态进行分级发现，残渣态是主要 Hg 形态（陆本琦等，2021）；采用同步辐射技术对土壤中 Hg 的化学形态进行分析发现，β-HgS 的比例高达 67.4~72.0%，为主要 Hg 形态（Yin et al., 2016）。并且，本研究通过添加不同形态无机汞发现，SK 稻田土壤中添加的 $^{198}Hg(NO_3)_2$ 可能被土壤固相迅速固定，从而降低了其生物有效性。然而，固相分配对于 NOM-^{199}Hg(II)和 nano-^{202}HgS 的影响较小，这是因为 NOM-^{199}Hg(II)和 nano-^{202}HgS 率先与 NOM 以及硫化物进行预平衡，从而减少了固相吸附对其潜在的影响。动力学拟合进一步说明 NOM-^{199}Hg(II)和 Nano-^{202}HgS 的甲基化过程符合一级动力学过程，而 $^{198}Hg(NO_3)_2$ 的甲基化存在限速步骤（图 2-10）。

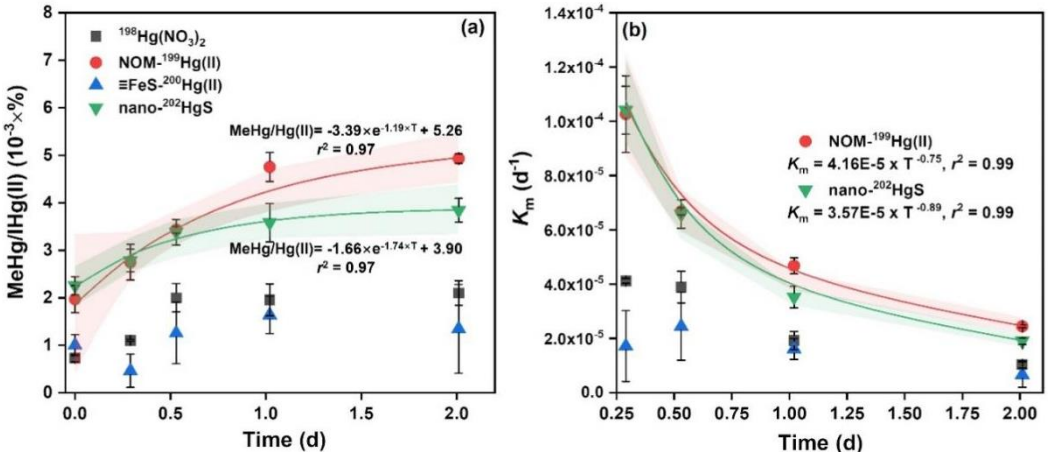

注：（a）甲基化率；（b）甲基化速率常数

图 2-10 废弃汞矿区稻田土壤甲基化率和甲基化速率常数的动力学拟合

2.5.2 土壤物理化学性质的差异

本研究所选的三个采样区均位于中国南方喀斯特区域，并且土壤类型和土壤质地均较为相似（表 2-1）。此外，三个位点土壤 pH 值几乎一致，不存在差异。通过 X 射线衍射分析可以看出，三种稻田土壤的矿物学组成也是相似的。因此，土壤理化性质的差异可能并不是造成无机汞甲基化存在巨大差异的原因。

2.5.3 微生物群落结构的差异

众所周知，Hg的甲基化与去甲基化过程是微生物主导的生物地球化学过程（胡海燕等，2011）。然而，Hg 对于微生物而言，是一种毒性物质。在许多研究中，学者甚至利用无机汞作为消毒剂，以实现灭菌的效果。因此，不同浓度的 Hg 深刻影响着稻

田土壤中微生物的群落结构和功能。通过主坐标分析（PCoA）发现，本研究中所选三个采样点的微生物群落结构完全不同（图 2-11）。进一步通过微生物群落的 α-多样性分析可以看出，废弃汞矿区稻田土壤中微生物可能受到高 Hg 污染的胁迫，因而群落结构的多样性水平较低。通过荧光定量 PCR 分析发现，废弃汞矿区土壤中汞甲基化功能基因的相对丰度也较土法炼汞区和背景区低（图 2-12）。上述结果表明，不同位点间微生物群落结构及其活性的差异很可能是造成其甲基化速率存在巨大差异的主要原因，且值得进一步关注。

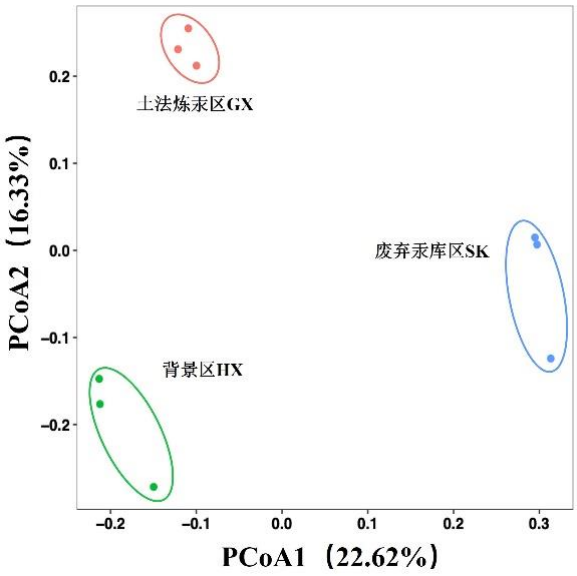

注：HX、GX、SK 分别为花溪、垢溪和四坑采样点

图 2-11 土壤微生物群落的主坐标分析

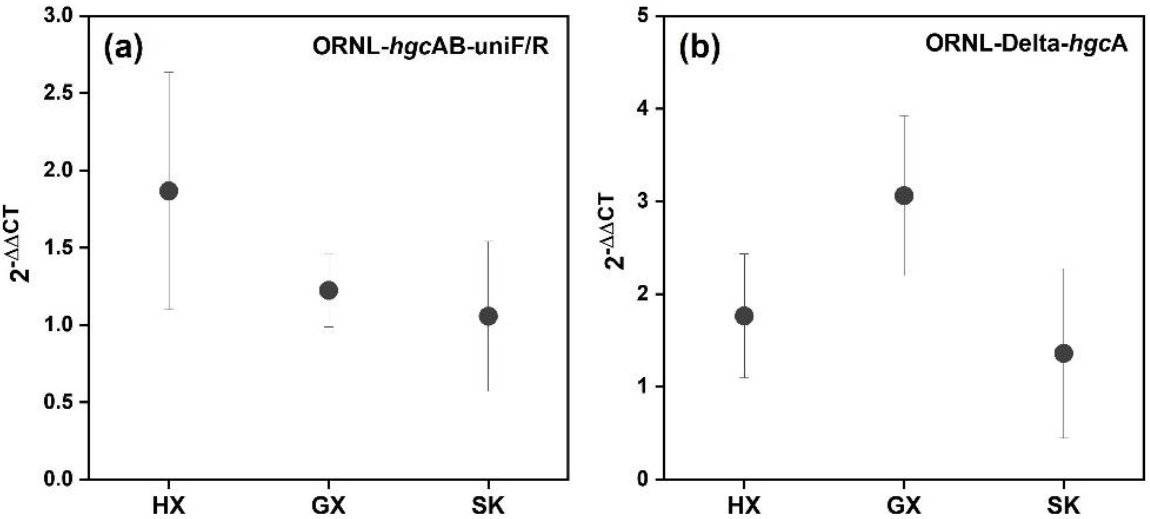

注：HX、GX、SK 分别为花溪、垢溪和四坑采样点

图 2-12 汞甲基化功能基因的相对表达量

2.5.4 去甲基化过程的差异

稻田土壤中净 MeHg 的生成受无机汞的甲基化与甲基汞的去甲基化共同作用影响（刘金玲和丁振华，2007；Wu et al., 2020; Zhou et al., 2020）。本研究中，废弃汞矿区稻田土壤中 $Me^{198}Hg$ 示踪剂的去甲基化率以及去甲基化速率常数在三个采样点之间均为最高的（图 2-6）；结合其无机汞示踪剂的甲基化率以及甲基化速率常数最低，因此 SK 即使 THg 含量最高，其 MeHg 含量也低于土法炼汞区稻田土壤。这说明，高 Hg 浓度土壤中可能存在某种促进 MeHg 去甲基化的机制，值得进一步研究。

2.6 本研究对汞污染稻田土壤修复的启示

目前，已经有学者为Hg污染的稻田土壤提出了不同的修复手段（Wang et al., 2012; Eckley et al., 2020），然而这些手段主要针对传统认为的生物有效态 Hg 的形态，如溶解与可交换态汞（Qian et al., 2003; Piao et al., 2006）。本研究发现，NOM-Hg(II)和 nano-HgS 在甲基化过程中具有与 $Hg(NO_3)_2$ 相似甚至更高的甲基化率和甲基化速率常数。这一发现说明之前对于能够参与汞甲基化反应的汞形态认识不足，而在稻田土壤中，NOM-Hg(II)和 nano-HgS 的甲基化过程被低估了。有学者也指出，仅仅利用溶解态 Hg 来评估 MeHg 的生成是不充分的（Jonsson et al., 2012; Zhang et al., 2012, 2014; Mazrui et al., 2016）。特别是，前期有研究发现贵州万山汞矿区土壤与植被中广泛存在着纳米颗粒态的 HgS（Manceau et al., 2018），而这部分 Hg 甲基化后产生的环境风险却没有被关注过。因此，在制定汞污染稻田土壤修复策略时，全面考察汞的形态及其生物有效性是非常有必要的。

2.7 本章小结

本部分内容采用多种稳定汞同位素示踪技术，发现 NOM-Hg(II)以及 nano-HgS 与 $Hg(NO_3)_2$ 在甲基化过程中具有相似甚至更高的甲基化率与甲基化速率常数，说明 NOM-Hg(II)和 nano-HgS 也是稻田土壤中能够参与甲基化反应的汞形态。≡FeS-Hg(II)几乎不能被甲基化，并且稻田土壤中新生成的 FeS 可能会显著降低 $Hg(NO_3)_2$ 的生物有效性。在不同汞浓度梯度的稻田土壤中，汞甲基化率随汞浓度的增加而下降，并且，稻田土壤汞浓度梯度引起的甲基化速率的差异（10^3~10^4 倍）远远大于同一位点

间不同汞形态之间的差异（1~5 倍）。此外，我们还发现，除了稻田土壤中汞的来源、土壤理化性质等因素外，不同位点间微生物群落结构及其活性的差异很可能是造成其甲基化速率存在巨大差异的主要原因，且值得进一步关注。在汞污染稻田土壤修复过程中，仅仅考虑溶解态汞这一汞形态是远远不够的，鉴于有机质结合态汞与纳米颗粒态硫化汞这类广泛存在于稻田土壤中的汞形态仍然具有较高的生物有效性，应引起人们的高度关注。

第 3 章 汞和硫的氧化还原循环影响稻田土壤中甲基汞的积累

3.1 本章引言

稻田土壤中不同形态汞（Hg）的相互转化过程，例如汞的甲基化，去甲基化，氧化和还原等过程，对于汞的生物积累与人体暴露风险至关重要。然而，现有研究主要聚焦于无机汞（Hg^{II}）的甲基化，和甲基汞（MeHg）的去甲基化作用（Zhao et al., 2016a, 2016b; Li et al., 2019; Wu et al., 2020），对于 Hg 的氧化还原过程了解较少。特别是 Hg 的氧化还原过程对甲基化和甲基化过程是否存在影响，以及存在何种影响尚不明确；这使得我们缺少对于稻田土壤中 Hg 形态转化过程的全面认识。另外，稻田这类湿地生态系统中 Hg 的循环往往与硫（S）的循环关系密切（Rothenberg and Feng, 2012; Skyllberg et al., 2021）。一方面，硫酸盐的还原以及硫化物的再氧化过程中产生的还原性硫配体控制着汞的化学形态及其生物有效性（Drott et al., 2013; Liem-Nguyen, 2017; Skyllberg et al., 2021）。另一方面，硫酸盐还原菌作用下的硫酸盐还原过程同样为自然环境中 Hg 甲基化的重要途径（Compeau and Bartha, 1985）。因此，在很长时间以来，大气硫沉降被认为是影响湿地生态系统 MeHg 生成的重要因素之一（Coleman Wasik et al., 2012）。然而，由于近年来大气硫沉降量的减少，在部分农田中表现出硫素缺乏的现象（Hinckley et al., 2020; Feinberg et al., 2021）。在我国，二氧化硫的排放量从 2011 年的 21.85 Tg S/年已经降低至 3.18Tg S/年（统计年鉴，2021），相应的硫肥施用量也呈现出逐年上升的趋势（Li et al., 2019）。在美国，农业含硫肥料的施用量在 2017 年时，已经超过了 3.3 Tg S/年，并且还有继续上升的趋势（Feinberg et al., 2021）。可见，含硫肥料的添加已经逐步成为驱动农田生态系统硫循环的新动力。因此，农田土壤中含硫肥料添加对 Hg 形态转化的影响值得进一步关注。目前，针对稻田土壤中硫输入影响汞形态转化的研究较少，且研究结果各异（Wang et al., 2016; Li et al., 2019; 2022; Lei et al., 2021）。并且，现有研究结论主要基于汞含量的变化，缺少对不同形态硫添加下汞形态转化过程的精确刻画。基于此，本章节内容采用不同形态汞同位素示踪技术（Multi-compound specific Hg isotope labeling technique），通过合成无机汞同位素示踪剂（$^{200}Hg^{II}$），甲基汞同位素示踪剂（$Me^{198}Hg$）以及零价汞同位素示踪剂（$^{202}Hg^{0}$），分别示踪稻田土壤中汞的甲基化、去甲基化、还原以及氧化过程。另外，

通过外源添加两种含硫化合物（硫酸盐和硫代硫酸盐），探究硫氧化还原循环对汞形态转化的影响。

3.2 材料与方法

3.2.1 样品采集

本部分内容的研究区域与第二章节一致，同样选取三处 Hg 浓度差异较大的水稻田，其分别为位于贵州省铜仁市万山区的废弃汞矿区稻田（四坑，SK）、土法炼汞区稻田（垢溪，GX）和贵州省贵阳市花溪区背景区稻田（HX）。其中，四坑为废弃汞矿区，该区域稻田土壤受汞矿渣堆积的污染；垢溪为土法炼汞区，该区域稻田土壤受土法炼汞活动影响，大气中汞浓度较高，而汞的大气沉降是该区域稻田土壤主要的汞污染源（Zhao et al., 2016b）；花溪区稻田土壤未受到汞污染影响。采集稻田土壤样品和对应上覆水样品。采集 1~5 cm 表层淹水土壤，装满至 500 mL 聚丙烯采样瓶中，不留空气。对应上覆水样品使用 250 mL 注射器，也采集至 500 mL 聚丙烯采样瓶中。所有土样与水样均使用 Parafilm®封口膜密封后，双层自封袋包装，保存于低温冷藏箱中，并在 24 小时内运回至实验室中。每个研究区稻田各采集三份稻田土壤与上覆水样品。

3.2.2 同位素示踪剂的制备

分别合成无机汞同位素示踪剂（$^{200}Hg^{II}$），甲基汞同位素示踪剂（$Me^{198}Hg$）以及零价汞同位素示踪剂（$^{202}Hg^{0}$）。通过测定 $Me^{200}Hg$ 和 $Me^{202}Hg$ 的生成示踪无机汞（Hg^{II} 和 Hg^{0}）的甲基化过程；通过测定 $Me^{198}Hg$ 的消耗，示踪 MeHg 的去甲基化过程；通过测定 $^{200}Hg^{0}$ 和 $^{198}Hg^{0}$ 的生成示踪汞的还原过程；通过测定 $^{202}Hg^{0}$ 的消耗，示踪汞的氧化或者固相分配过程。单一富集稳定汞同位素购买于 ISOFLEX 公司。本研究所用同位素组成如下：^{198}Hg (^{198}Hg 98.52 ± 0.15%, ^{196}Hg 0.10 ± 0.02%, ^{199}Hg 0.11 ± 0.02%, ^{200}Hg 0.59 ± 0.02%, ^{201}Hg 0.47 ± 0.05%, ^{202}Hg 0.16 ± 0.02%, ^{204}Hg < 0.05%), ^{200}Hg (^{200}Hg 98.09 ± 0.2%, ^{196}Hg 0.11 ± 0.05%, ^{198}Hg 0.43 ± 0.05%, ^{199}Hg 0.31 ± 0.05%, ^{201}Hg 0.32 ± 0.05%, ^{202}Hg 0.53 ± 0.05%, ^{204}Hg 0.21 ± 0.05%), and ^{202}Hg (^{202}Hg 98.68 ± 0.02%, ^{196}Hg 0.04%, ^{198}Hg 0.15 ± 0.02%, ^{199}Hg 0.23 ± 0.02%, ^{200}Hg 0.43 ± 0.2%, ^{201}Hg 0.34 ± 0.02%, ^{204}Hg 0.13 ± 0.02%)。$^{200}Hg^{II}$、$Me^{198}Hg$ 和 $^{202}Hg^{0}$ 示踪剂的合成方法如下：

$^{200}Hg^{II}$：将 $^{200}Hg^{0}$（metal）溶解于浓硝酸中（纯度≥ 99.9%），制备得到 $^{200}Hg^{II}$ 储备液（20（μg mL^{-1}）），并使用超纯水（Milli-Q，Millipore，美国）稀释得到浓度为 1（μg mL^{-1}）的工作液。

$Me^{198}Hg$：采用甲基钴胺素为甲基供体合成得到 $Me^{198}Hg$（Hintelmann, 2000；Rodríguez Martín-Doimeadios et al., 2002）。制备得到的 $Me^{198}Hg$ 储备液保存于异丙醇中（每 100 μL $Me^{198}Hg$ 储备液加入 10 mL 异丙醇）

$^{202}Hg^{0}$：采用 Wang et al. (2015)中的方法，制备得到 $^{202}Hg^{0}$ 饱和溶液。首先，将 $^{202}Hg^{0}$（metal）氧化溶解于浓硝酸中，并稀释制备得到浓度为 100 μg L^{-1} 的 $^{202}Hg^{II}$ 标准溶液。随后，使用蠕动泵将 $^{202}Hg^{II}$ 标准溶液缓慢泵入含有 10 mL $SnCl_2$ (20%, *w/v*)的 50 mL 反应瓶中，还原生成 $^{202}Hg^{0}$。使用超纯氮气体为载气，将还原生成的 $^{202}Hg^{0}$ 以 5 mL min^{-1} 的流速缓慢吹至 510 mL 超纯水中，制备得到 $^{202}Hg^{0}$ 饱和溶液，避光冷藏储存并平衡 24 小时。通常，$^{202}Hg^{0}$ 饱和溶液的浓度约为 3μg L^{-1}。在使用前测定 $^{202}Hg^{0}$ 饱和溶液浓度，并稀释至 1 ng mL^{-1}。

3.2.2 培养实验设计

在厌氧手套箱中，将采集自同一位点的稻田土壤与上覆水样品移至 2 L 烧杯中。使用特氟龙镊子挑出岩石颗粒与植物残体后，将稻田土壤与上覆水均匀混合为含水率为 75%的泥浆样品。随后将均匀的泥浆样品分装入 100 mL 血清瓶中，每瓶分装泥浆 30 mL。共设实验处理 4 个：硫酸盐（Na_2SO_4）添加处理、硫代硫酸盐（$Na_2S_2O_3$）添加处理、高温高压灭菌处理和对照处理。根据万山稻田土壤总硫含量背景（~200 mg kg^{-1}, Yin et al., 2018），设置 2 mg S/瓶的 S 添加量，且保持不同含硫处理中的硫添加量一致。分别在每个培养瓶中加入 $^{200}Hg^{II}$、$Me^{198}Hg$ 以及 $^{202}Hg^{0}$，加入量根据每个研究区稻田土壤总汞（THg）和 MeHg 的本底值确定（Gilmour et al., 1998; Zhao et al., 2016a; Wu et al., 2020），如表 3-1 所示。随后，立即将血清瓶完全密封，缓慢摇匀后，在黑暗环境中厌氧培养两天。

表 3-1 同位素示踪剂添加量

位点	THg*	[$^{200}Hg^{II}$]	体积	$^{200}Hg^{II}$	[$Me^{198}Hg$]	体积	$Me^{198}Hg$	[$^{202}Hg^{0}$]	体积	$^{202}Hg^{0}$
	mg kg^{-1}	μg mL^{-1}	mL	μg	ng mL^{-1}	mL	ng	ng mL^{-1}	mL	ng
HX	0.15 ± 0.003	0.4	0.5	0.2	50	0.1	5	1	10	10
GX	17.2 ± 1.7	4	0.5	2	50	1	50	1	10	10
SK	609 ± 7	60	0.5	30	50	0.4	20	1	10	10

注：THg*为不同位点的背景总汞含量。[$^{200}Hg^{II}$]、[$Me^{198}Hg$]和[$^{202}Hg^{0}$]和分别为同位素示踪剂稀释液浓度。

3.2.3 培养实验样品采集

分别在培养的第 0、12、24 和 48 小时进行破坏性取样，每个采样点每次随机选取三个平行（共 9 个培养瓶 = 3 个平行 × 三个研究区）。在破坏性采样之前，使用曝气-金管富集的方法率先进行 Hg^0 样品的采集。由于采样过程持续 2 小时，因此 Hg^0 样品的实际培养时间为 2、14、26 和 50 小时。采样时，将全新的不锈钢针头没如泥浆，使用经过金管预净化的高纯无汞氩气以 300 mL min^{-1} 的流速曝气 20 min，以确保所有可以吹出的 Hg^0（purgeable Hg^0）全部富集至金管上。当采集完所有样品的 purgeable Hg^0 后，将培养瓶转移至厌氧手套箱中进行破坏性取样。用于分析 MeHg 同位素的泥浆样品采集至 50 mL 离心管（JET, BIOFIL, 中国）中，1 mL 6 N HCl 酸化后，-20 ºC 保存（Gray et al., 2014; Liu et al., 2022）。取少量泥浆样品装于 1.5 mL 冻存管（Nalgene®, Thermo Fisher, 美国）中并-80 ºC 保存，用于提取 DNA 样品。其余泥浆样品采集至 50 mL 离心管中，离心过滤分离得到上清液后分析总硫化物（[S(-II)]）、[SO_4^{2-}]、[Fe^{2+}]、[Fe^{3+}]、[NO_3^-]和[NH_4^+]。

3.2.4 测定方法

使用电感藕合等离子体质谱（ICP-MS）测定稻田泥浆中生成零价汞同位素（$^{198}Hg^0$、$^{200}Hg^0$ 和 $^{202}Hg^0$）的含量。将将已富集至镀金石英砂管中的零价汞同位素加热脱附，在氩载气下进入 ICP-MS（Agilent 7700X，美国）进行检测，得到零价汞同位素组成，并计算得到零价汞总量。使用气相色谱-电感藕合等离子体质谱（GC-ICP-MS）测定泥浆样品中甲基汞同位素（$Me^{198}Hg$、$Me^{200}Hg$ 和 $Me^{202}Hg$）的含量。采用外标法进行质量控制（Hintelmann et al., 1995; Li et al., 2010; Meng et al., 2018），所用外标（MeHg 和 $Hg(NO_3)_2$）来自于 Brooks Rand™；其中 Hg^0 的外标为经过氯化亚锡还原

$Hg(NO_3)_2$ 的得到，本部分内容所用外标的同位素组成与天然同位素组成一致（本实验外标同位素比值 MeHg: $^{198}Hg/^{199}Hg = 0.59 \pm 0.006$, $^{200}Hg/^{199}Hg = 1.37 \pm 0.014$, $^{201}Hg/^{199}Hg = 0.78 \pm 0.0083$, and $^{202}Hg/^{199}Hg = 1.76 \pm 0.020$; Hg^0: $^{198}Hg/^{199}Hg = 0.59 \pm 0.004$, $^{200}Hg/^{199}Hg = 1.38 \pm 0.009$, $^{201}Hg/^{199}Hg = 0.79 \pm 0.005$, and $^{202}Hg/^{199}Hg = 1.78 \pm 0.015$; 天然丰度比值: $^{198}Hg/^{199}Hg = 0.59$, $^{200}Hg/^{199}Hg = 1.37$, $^{201}Hg/^{199}Hg = 0.78$, and $^{202}Hg/^{199}Hg = 1.76$, Blum and Bergquist, 2007）。[SO_4^{2-}]和[NO_3^-]采用离子色谱（ICS90, DIONEX, 美国）。[S(-II)]采用亚甲基蓝比色法测定（Cline, 1969）。[Fe^{2+}]和[Fe^{3+}]采用菲啰嗪比色法测定（Viollier et al., 2000）。[NH_4^+]采用靛酚蓝分光光度法测定。土壤溶解性有机质（DOM）采用风干土壤样品，以水土比 10:1 进行提取：以 200 rpm 的转速在水平振荡器振荡 16 小时后，离心，过滤（0.45-μm 混合醋酸纤维滤膜，Whatman，美国）。DOM 的浓度使用总有机碳分析仪测定（TOC-L, Shimadzu, 日本）测定，并用溶解性有机碳（DOC）表示。DOM 的紫外吸收光谱和荧光光谱采用 Aqualog®光谱仪（Jobin Yvon, Horiba, 日本）测定。为降低光谱分析过程中内滤效应带来的影响，本研究在进行 DOM 光谱分析前，将所有样品的 DOC 含量均稀释至 10 mg L^{-1} 以下（Jiang et al., 2018）。泥浆样品的 DNA 采用 FastDNA® 试剂盒（MP Biomedicals, Irvine, 美国）进行提取，并使用 Qubit™ 4 荧光仪（Qubit™ 4, Thermo Scientific, 美国）对提取得到的 DNA 浓度进行测定（Pu et al., 2022）。采用定量 PCR 法（ABI 7500, Applied Biosystems, 美国）测定汞甲基化功能基因（*hgcA*）、汞还原酶基因（*merA*）、有机汞裂解酶基因（*merB*）、硫酸盐还原基因（*dsrB*）和硫氧化基因（*soxB*）的丰度。扩增个引物与扩增条件如表 3-2 所示。

表 3-2 qPCR 引物与扩增条件

基因	引物名称	引物序列 (5'-3')	扩增条件	参考文献
hgcA	Delta-F Delta-R	GCCAACTACAAGMTGASCTWC CCSGCNGCRCACCAGACRTT	94°C for 3 min; 40 cycles of 95°C for 15 s, 65°C for 10 s, 65°C for 10 s; 72°C for 4 min	Christensen et al., 2016
merA	A7s-n-F A5-n-R	CGATCCGCAAGTGGCIACBGT ACCATCGTCAGRTARGGRAAVA	94°C for 2 min; 35 cycles of 94°C for 10 s and 60°C for 1 min	Schaefer et al., 2004
merB	Box-F Box-R	CGAGAAGGAACATCAGAATCCG CGCTTGTGGCAAAGAAAAGGTG	94°C for 2 min; 35 cycles of 94°C for 10 s and 60°C for 1 min	Schaefer et al., 2004
dsrB	DSRp2060-F DSR4-R	CAACATCGTYCAYACCCAGGG GTGTAGCAGTTACCGCA	95°C for 30 s; 40 cycles of 95°C for 5 s, 55°C for 34 s, 72°C for 34 s; 72°C for 4 min	Zhou et al., 2020
soxB	soxB693-F soxB1164-B	ATCGGNCARGCNTTYCCNTA AARTTNCCNCGNCGRTA	95°C for 5 min; 35 cycles of 95°C for 30 s and 55°C for 30 s, 72°C for 30 s; 72°C for 7 min	Meyer et al., 2007

采用 *hgcA* 基因测序和宏基因组测序的方法，识别汞甲基化微生物群落结构，所有测序数据均上传至 National Centre for Biotechnology Information (NCBI, https://www.ncbi.nlm.nih.gov/)。*hgcA* 基因测序和宏基因组测序上传数据编号分别为 PRJNA950218 和 PRJNA950935。

3.2.4 计算方法与质量控制

由于本研究添加了 ^{198}Hg、^{200}Hg 和 ^{202}Hg，因此我们采用未添加的 ^{199}Hg 信号（天然组成）来计算背景 Hg 含量。然而，由于所有添加的同位素并非 100%富集纯度，可能带入其他同位素的干扰（Hintelmann et al., 1995; Qvarnström and Frech, 2002）。因此，我们采用了基于数据矩阵的去卷积分析法计算体系内的同位素组成（Qvarnström and Frech, 2002）：

$$\sum S_{199} = R_{199/199,x} \times S_{199,x} + R_{199/198,a} \times S_{198,a} + R_{199/200,b} \times S_{200,b} + R_{199/202,c} \times S_{202,c}$$

（公式 3-1）

$$\sum S_{198} = R_{198/199,x} \times S_{199,x} + R_{198/198,a} \times S_{198,a} + R_{198/200,b} \times S_{200,b} + R_{198/202,c} \times S_{202,c}$$

（公式 3-2）

$$\sum S_{200} = R_{200/199,x} \times S_{199,x} + R_{200/198,a} \times S_{198,a} + R_{200/200,b} \times S_{200,b} + R_{200/202,c} \times S_{202,c}$$

（公式 3-3）

$$\sum S_{202} = R_{202/199,x} \times S_{199,x} + R_{202/198,a} \times S_{198,a} + R_{202/200,b} \times S_{200,b} + R_{202/202,c} \times S_{202,c}$$

（公式 3-4）

其中，$\sum S_i$ 是测定得到的 ^{i}Hg 同位素信号 (i = 198、199、200 和 202)；$R_{i/j}$ 是测定得到的 ^{i}Hg/^{j}Hg 比值；S_i 是经过校正的 ^{i}Hg 信号；x 表示具有天然组成的背景 Hg（ambient Hg）；a 表示配制的 Me^{198}Hg 标液；b 表示配制的 ^{200}Hg^{II} 标液；c 表示配制的 ^{202}Hg^{0} 标液。

由于本研究添加的 ^{198}Hg、^{200}Hg 和 ^{202}Hg 示踪剂里面所含的 ^{199}Hg 含量非常低，分别仅占 0.11 ± 0.02%、0.31 ± 0.05%和 0.23 ± 0.02%，在在单一添加同位素的试验中，可以忽略这部分同位素的贡献。因此，可以将基于数据矩阵的去卷积分析法简化为下述方法:

Ambient Hg = ^{199}Hg measured/16.94%　　（公式 3-5）

^{198}Hg $_{ambient}$ = ^{199}Hg $_{measured}$/16.94% × 10.04%　　（公式 3-6）

^{198}Hg $_{enriched}$ = ^{198}Hg $_{measured}$-^{198}Hg $_{ambient}$　　（公式 3-7）

^{200}Hg $_{ambient}$ = ^{199}Hg $_{measured}$/16.94% × 23.14%　　（公式 3-8）

^{200}Hg $_{enriched}$ = ^{200}Hg $_{measured}$-^{200}Hg $_{ambient}$　　（公式 3-9）

^{202}Hg $_{ambient}$ = ^{199}Hg $_{measured}$/16.94% × 29.73%　　（公式 3-10）

^{202}Hg $_{enriched}$ = ^{202}Hg $_{measured}$-^{202}Hg $_{ambient}$　　（公式 3-11）

其中，^{i}Hg $_{ambient}$ (i = 198, 200, 202)和 ^{i}Hg $_{enriched}$ (i = 198, 200, 202)分别表示背景 Hg 和添加部分的 Hg 同位素；^{i}Hg $_{measured}$ (i = 198, 199, 200, 202)为通过 ICP-MS 测定得到的 ^{i}Hg (i = 198, 199, 200, 202)信号。10.04%、16.94%、23.14%和 29.73%为 ^{198}Hg、^{199}Hg、^{200}Hg 和 ^{202}Hg 的天然组成（Blum and Bergquist, 2007）。

另外，我们对比采用上述经过简化的方法与基于数据矩阵的去卷积分析法得到的背景 199Hg 的含量，发现两种方法基于 233 个数据的变异系数仅为 0.30 ± 0.17%（图 3-1）。因此，我们继续沿用了上述简化的方法计算背景汞含量。

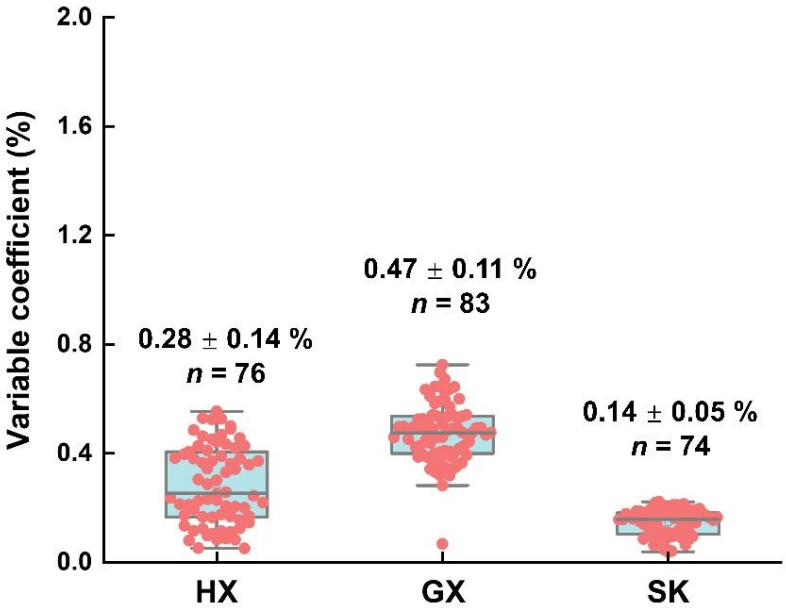

图 3-1 采用简化方法计算与基于数据矩阵的去卷积分析法得到背景 ^{199}Hg 含量的变异系数

根据添加无机汞甲基化生成的甲基汞同位素计算甲基化率（MeHg/Hg(II) (%)）对应甲基化速率常数（K_m）；根据添加的甲基汞同位素的消耗量计算去甲基化率（MeHg demethylation (%)）对应去甲基化速率常数（K_d）的方法同第 2 章介绍一致。在此基础上，本研究由于补充了汞的还原部分，因此采用 Zhu et al. (2018)介绍的方法进一步计算了可吹出 Hg0 的生成率以及挥发速率常数（K_v）：

$$\text{Purgeable } {}^{200}Hg^0/{}^{200}Hg^{II}\ (\%) = \frac{[{}^{200}Hg^0]}{[{}^{200}Hg^{II}]_{spiked}} \times 100\% \quad \text{（公式 3-12）}$$

$$\text{Purgeable } {}^{198}Hg^0/Me^{198}Hg\ (\%) = \frac{[{}^{198}Hg^0]}{[Me^{198}Hg]_{spiked}} \times 100\% \quad \text{（公式 3-13）}$$

$$K_v\text{-}{}^{200}Hg^{II} = \frac{[{}^{200}Hg^0]_{tj}}{[{}^{200}Hg^{II}]_{spiked} \times t} \quad \text{（公式 3-14）}$$

$$K_v\text{-}Me^{198}Hg = \frac{[{}^{198}Hg^0]_{tj}}{[Me^{198}Hg]_{spiked} \times t} \quad \text{（公式 3-15）}$$

其中，$[{}^{i}Hg^0]_{tj}$ 表示可吹出 Hg^0 的在不同时间点（t_j）的绝对质量（i = 198 和 200；j = 2, 14, 26 和 50 小时）；

另外，添加 $^{202}Hg^0$ 后测定得到的可吹出 $^{202}Hg^0$（purgeable $^{202}Hg^0$）的消耗量反映了 $^{202}Hg^0$ 的氧化或者固相分配作用，因此其氧化或固定率计算如下：

$$^{202}Hg^0 \text{ oxidation/immobilization } (\%) = \frac{[{}^{202}Hg^0]_{spiked} - [{}^{202}Hg^0]_{purgeable}}{[{}^{202}Hg^0]_{spiked}} \times 100\% \quad \text{（公式 3-16）}$$

本研究使用 ERMCC580（[MeHg] = 75.5 ± 3.7（μg kg^{-1}））为 MeHg 分析时的标准

物质。通过测定发现，ERMCC580 的回收率为 85.2 ± 9.07%，范围为 76.2%至 108.4%。

3.3 主要氧化还原元素与土壤 DOM 的变化特征

3.3.1 HS^{-}–SO_4^{2-}、NH_4^{+}–NO_3^{-}和 Fe^{2+}–Fe^{3+}的变化特征

如图 3-2 所示，培养试验泥浆液相中 NH_4^{+}的浓度较 NO_3^{-}浓度高 2~3 个数量级。NO_3^{-}浓度最高值出现在灭菌处理中。在来两个 S 添加处理中，对比对照处理 Fe^{2+}占总铁的比例均高于 Fe^{3+}（$p < 0.05$, 图 3-3）。如图 3-4 所示，Na_2SO_4 和 $Na_2S_2O_3$ 处理中的 SO_4^{2-}含量变化趋势在位点 HX 和 SK 相似，且 HS^{-}在所有位点的含量均较 SO_4^{2-}低 3 个数量级。

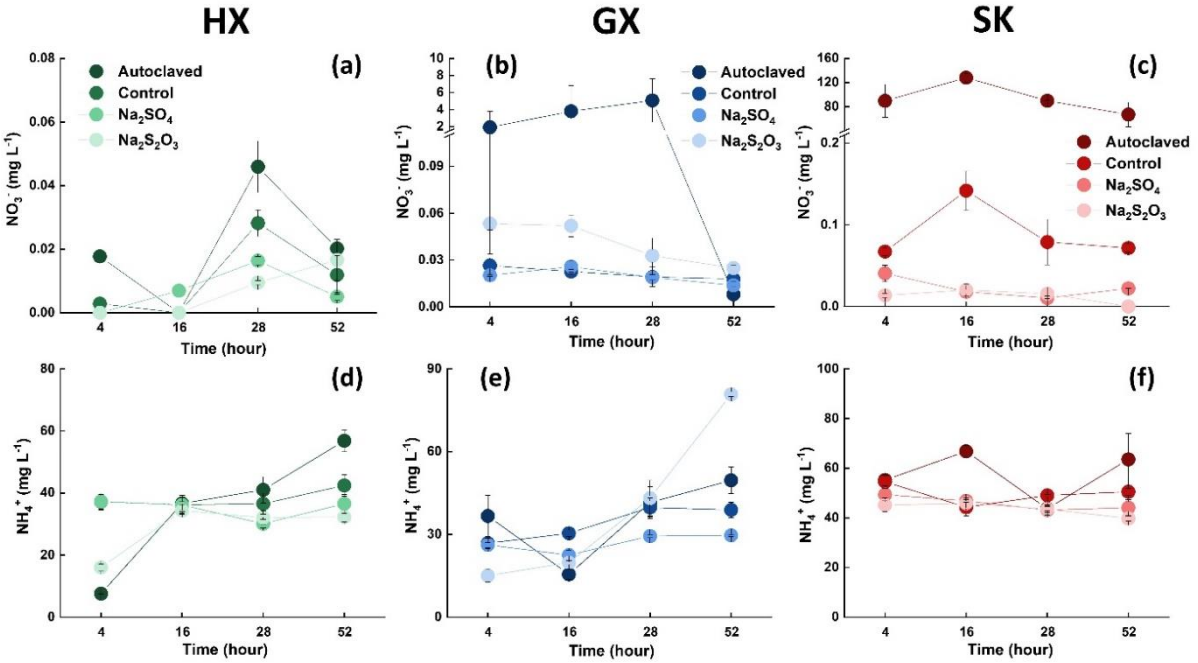

图 3-2 NH_4^{+}和 NO_3^{-}在不同位点随培养时间的变化

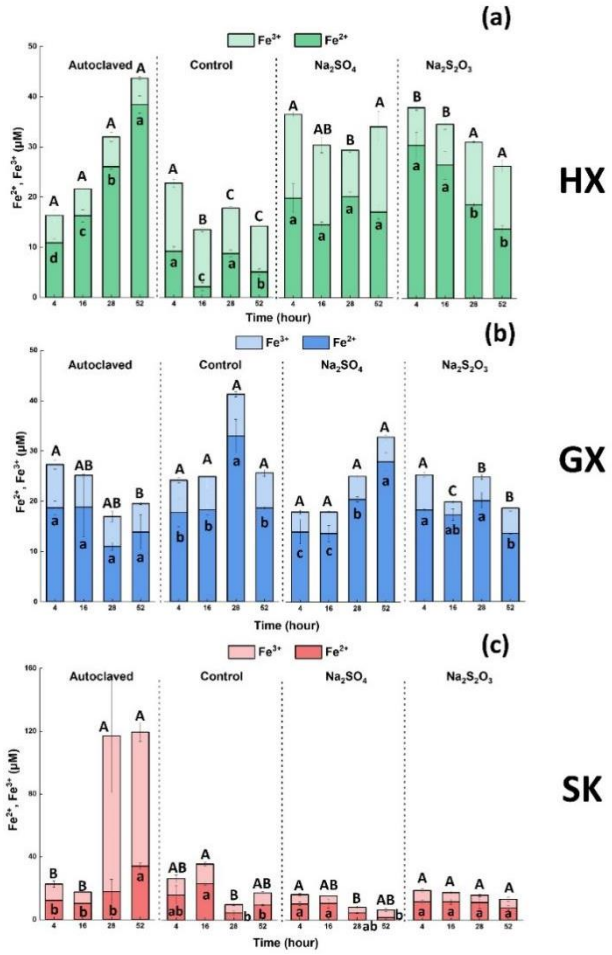

图 3-3 Fe^{2+}和 Fe^{3+}在不同位点随培养时间的变化

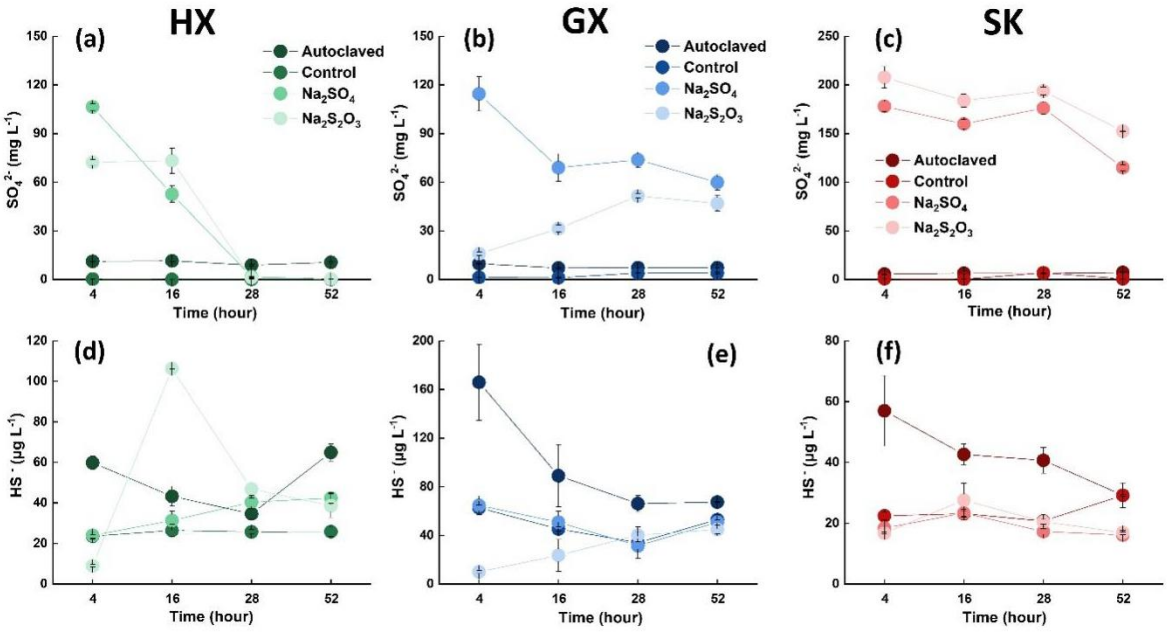

图 3-4 HS^-和 SO_4^{2-}在不同位点随培养时间的变化

3.3.2 DOM 含量与组成结构变化

DOM 的含量采用溶解性有机碳（DOC）来表示。从图 3-5 可知，DOC 值仅在不同位点间存在差异，然而同一位点不同处理之间的 DOC 不存在显著差异，这说明 S 添加并未改变稻田土壤中 DOC 的含量。

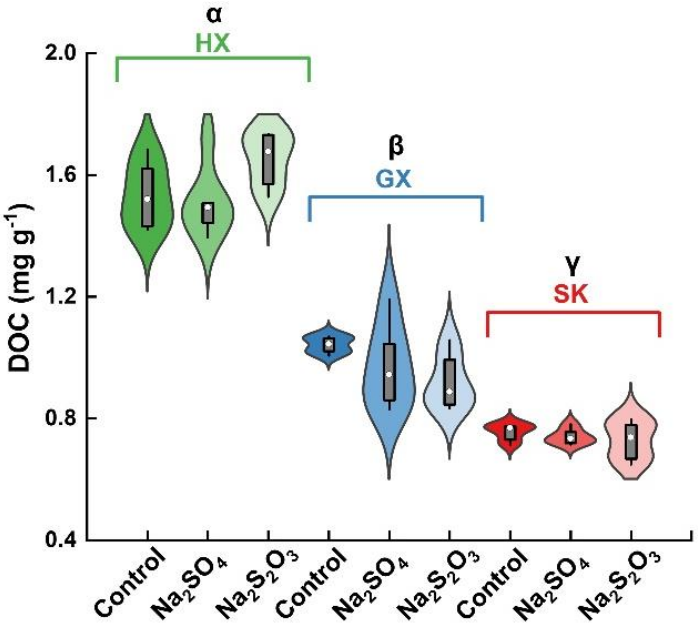

图 3-5 不同位点和处理中 DOC 的含量

本研究采用 DOM 的紫外吸收光谱和荧光光谱来反映 DOM 的组成和结构特征。同 DOC 类似，$SUVA_{254}$、275-295 波长紫外光谱斜率（$S_{275\text{-}295}$）、355 nm 波长吸光系数（a(355)）、荧光峰强、腐殖化指数（HIX）和自生源指数（BIX）等指标在不同处理间几乎不存在显著差异（图 3-6）。仅在 SK 位点，荧光峰 A 和 C 在 S 添加处理中显著高于对照处理。在位点 GX，荧光峰 B 和 T 在 S 添加处理中又显著低于对照处理（图 3-6）。

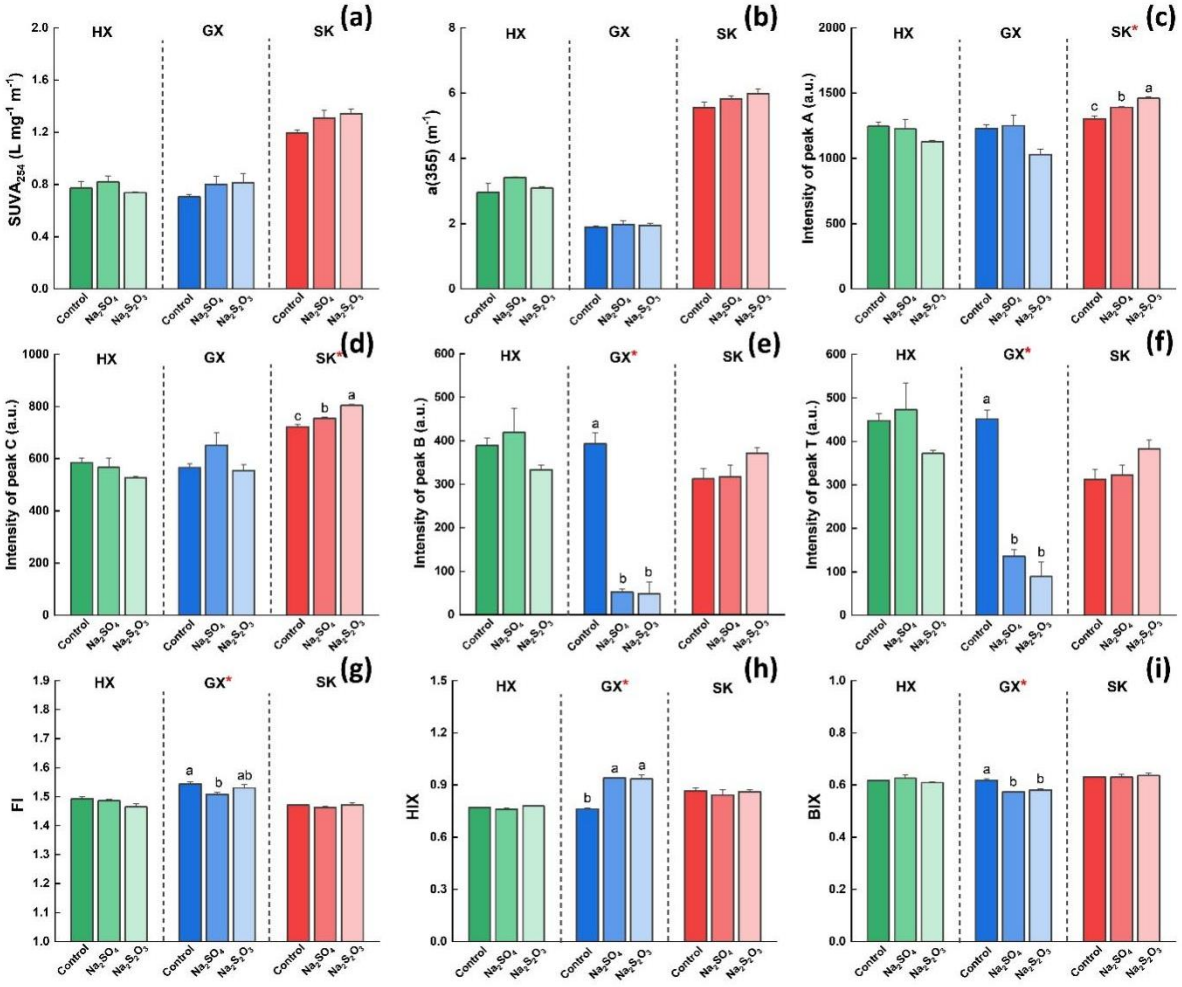

图 3-6 不同弄位点和处理中 DOM 的紫外吸收光谱和荧光光谱特征

3.4 功能基因定量与汞甲基化微生物群落结构

3.4.1 *hgcA*, *merA*, *merB*, *dsrB* 和 *soxB* 基因的丰度特征

本研究分别对汞甲基化基因（*hgcA*）、汞还原酶基因（*merA*）、有机汞裂解酶基因（*merB*）、硫酸盐还原基因（*dsrB*）和硫氧化基因（*soxB*）分别进行定量分析。研究发现，培养样品中 *mer* 操作子功能基因（*merA* 和 *merB*）均低于检出限（$C_T > 31$）。灭菌样品中 *hgcA*, *dsrB* 和 *soxB* 基因的丰度均显著低于非灭菌处理（$p < 0.05$, 图 3-7）。在位点 GX，对照处理中的 *hgcA* 基因的丰度高于 S 添加处理。然而，在位点 SK，S 添加处理中的 *hgcA* 基因丰度高于对照处理。由图 3-7 可见，位点 GX 和 SK 的 *hgcA* 和 *dsrB* 含量变化趋势一致。在所有位点中，$Na_2S_2O_3$ 处理的 *soxB* 基因丰度均高于 Na_2SO_4 处理。

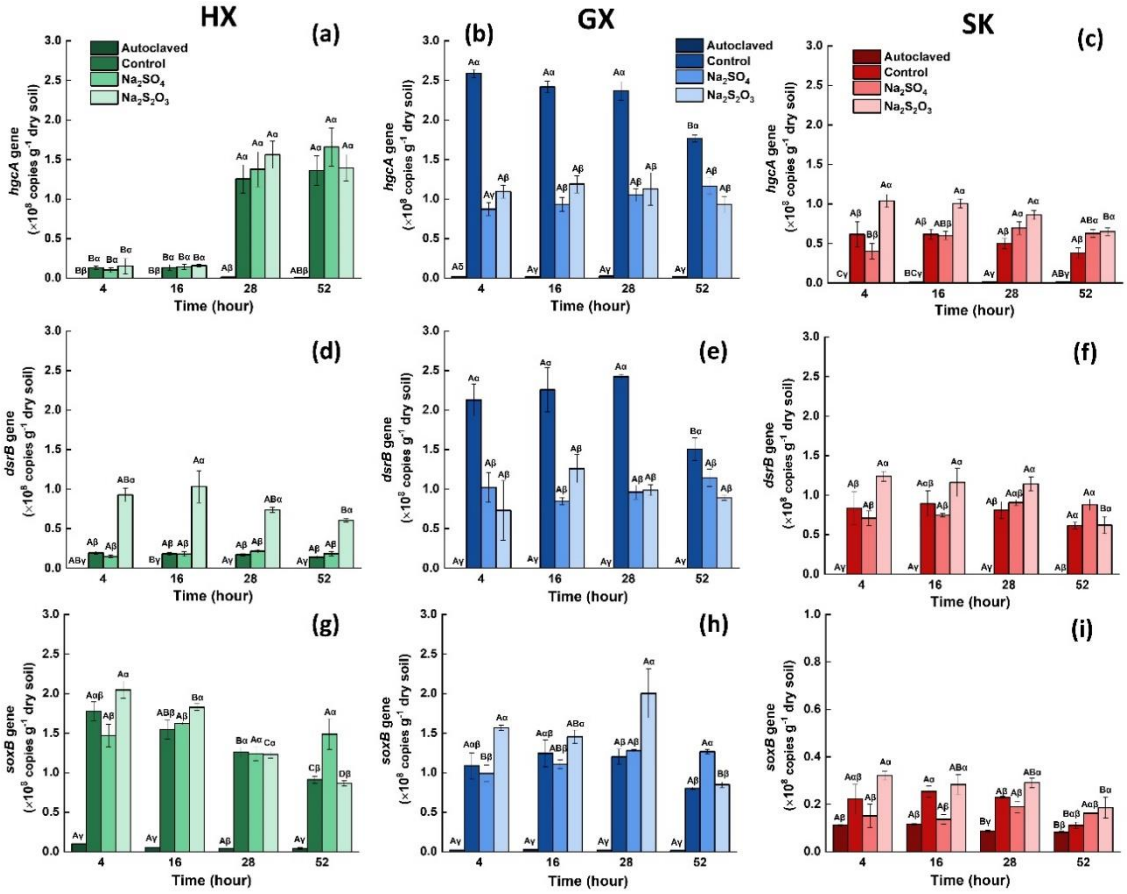

图 3-7 不同位点和处理中 *hgcA*、*dsrB* 和 *soxB* 基因的丰度

3.4.2 汞甲基化微生物群落结构

本研究分别时候用 *hgcA* 基因的扩增子测序技术和宏基因组技术揭示汞甲基化卫生女巫群落结构。通过 *hgcA* 基因的扩增子测序，发现 HX 和 GX 位点的 S 添加处理中属于硫酸盐还原菌（SRB）类的汞甲基化微生物的相对丰度为对照处理的 1.04-1.56 和 1.27-1.82 倍，并且主要识别得到的 SRB 甲基化微生物为 *Peptococcaceae*、*Desulfovibrionaceae* 和 *Desulfobulbaceae*（图 3-8）。进一步，在宏基因组数据中筛选携带有 hgcA 基因的 SRB 汞甲基化微生物，发现 S 添加处理显著增加了位点 HX 的汞甲基化微生物的丰度。

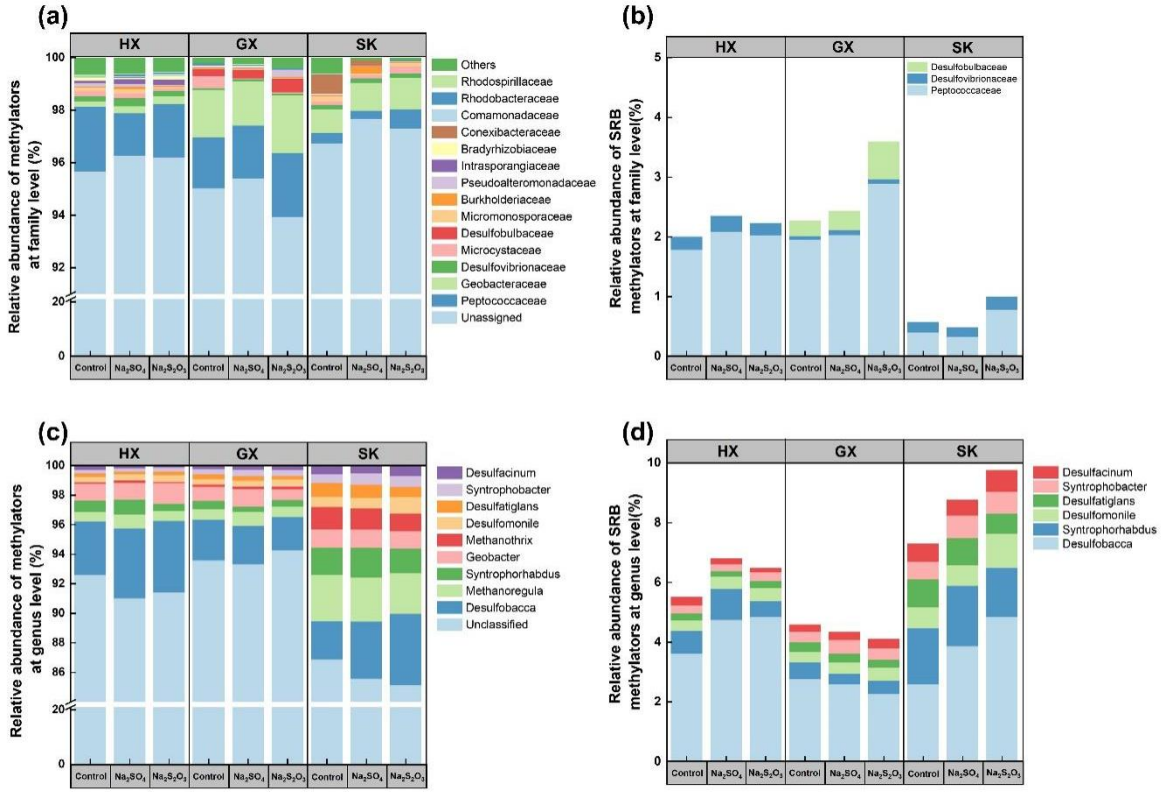

图 3-8 不同位点和处理中汞甲基化微生物群落结构。

（a）和（b）为 hgcA 基因扩增子测序；（c）和（d）为宏基因组测序。

3.5 稻田土壤中的汞形态转化过程

3.5.1 $^{200}Hg^{II}$ 和 $^{202}Hg^{0}$ 甲基化生成 $Me^{200}Hg$ 和 $Me^{202}Hg$

甲基化速率常数 K_m-$^{200}Hg^{II}$ (d^{-1})和 K_m-$^{202}Hg^{0}$ (d^{-1})分别表示示踪剂 $^{200}Hg^{II}$ 和 $^{202}Hg^{0}$ 的甲基化过程。由图 3-9 所示，所有位点 K_m-$^{200}Hg^{II}$ 的变化趋势一致，即 4 至 16 小时内迅速下降，随后缓慢下降。然而，不同位点间 K_m-$^{200}Hg^{II}$ 值存在数量级的差异。HX、GX 和 SK 位点 K_m-$^{200}Hg^{II}$ 的最大值均出现在 4 小时，分别为 $0.29 \pm 0.01\ d^{-1}$（在 Na_2SO_4 处理中）、$0.048 \pm 0.006\ d^{-1}$（Na_2SO_4 和 $Na_2S_2O_3$ 处理一致）、$0.0015 \pm 0.00002\ d^{-1}$（在对照处理中）。$Me^{200}Hg$ 的生成率以及其含量变化由图 3-10 和 3-11 所示。相比较对照处理，硫添加处理显著促进了位点 HX 和 GX 中 $Me^{200}Hg$ 的生成。另外，在位点 GX，$Na_2S_2O_3$ 处理中 $Me^{200}Hg$ 的生成多于 Na_2SO_4 处理。

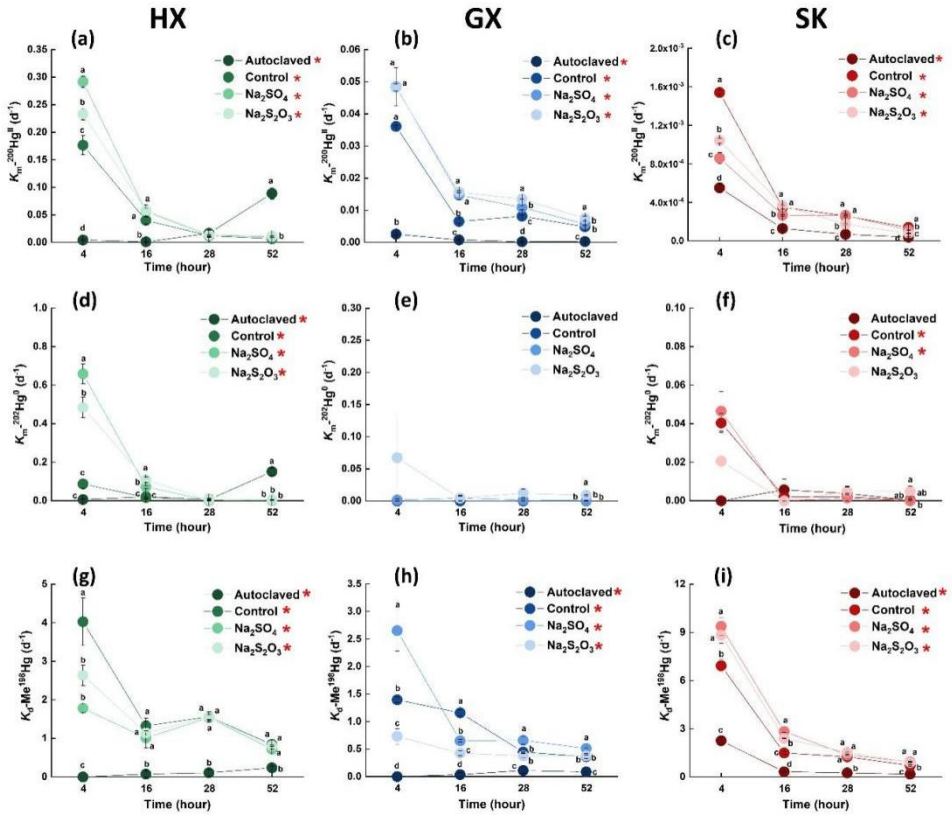

图 3-9 不同位点和处理中的汞甲基化速率常数与去甲基化速率常数

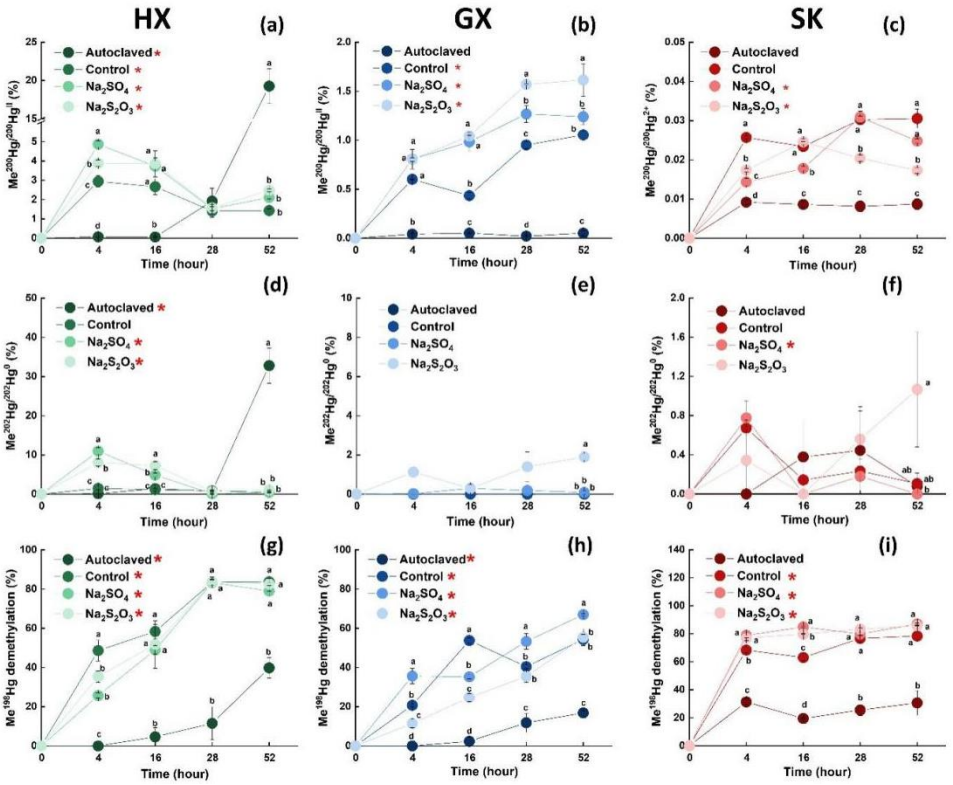

图 3-10 不同位点和处理中的甲基汞生成率与去甲基化率

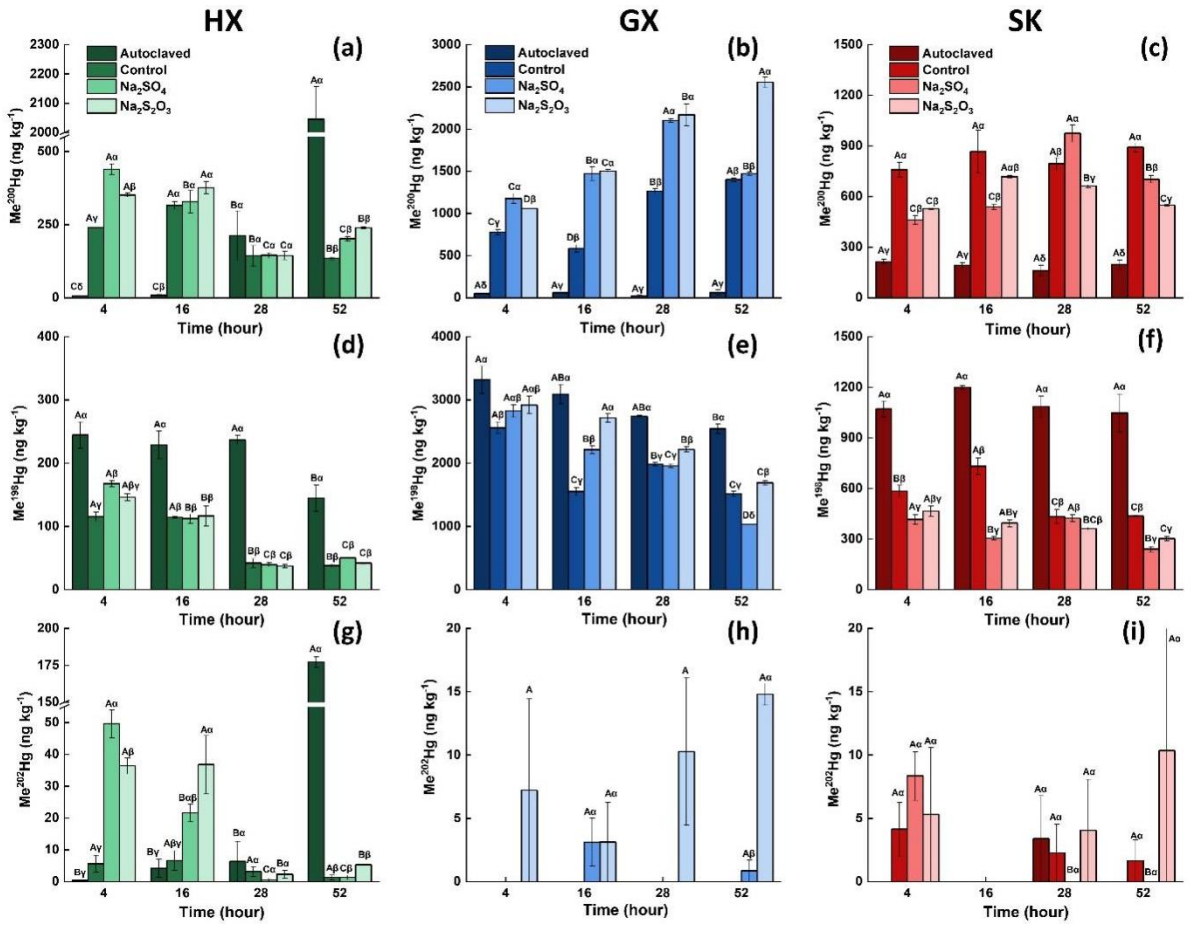

图 3-11 不同位点和处理中的甲基汞同位素的含量

同时，本研究依然检测到添加 $^{202}Hg^0$ 示踪剂后存在 $Me^{202}Hg$ 的生成，表明也能够 $^{202}Hg^0$ 参与甲基化反应并生成甲基化汞。在 HX 位点，K_m-$^{202}Hg^0$ 的最大值为 0.66 ± 0.05 d^{-1}，出现在 4 小时的 Na_2SO_4 处理中，其次为 $Na_2S_2O_3$ 处理的 0.49 ± 0.05 d^{-1}（图 3-9）。与之对应 Na_2SO_4 和 $Na_2S_2O_3$ 处理中 $^{202}Hg^0$ 向 $Me^{202}Hg$ 的转化率分别为 10.98 ± 0.85%和 8.08 ± 0.89%（图 3-10）。在位点 GX 和 SK，$Na_2S_2O_3$ 处理较其他处理产生了更多的 $Me^{202}Hg$。

3.5.2 $Me^{198}Hg$ 的去甲基化

除灭菌处理以外，其他所有处理添加的 $Me^{198}Hg$ 示踪剂均表现出不同程度的降低，表明存在微生物作用下的去甲基化过程。在 HX 位点，对照、Na_2SO_4 和 $Na_2S_2O_3$ 处理的 K_d-$Me^{198}Hg$ 不存在显著差异。在位点 GX 和 SK，S 添加处理较对照处理促进了去甲基化过程，表现为 K_d-$Me^{198}Hg$ 的增加（图 3-9）。

3.5.3 $^{200}Hg^{II}$ 和 $Me^{198}Hg$ 还原生成 $^{200}Hg^{0}$ 和 $^{198}Hg^{0}$

挥发速率常数 K_v-$^{200}Hg^{II}$ (d^{-1})和 K_v-$Me^{198}Hg$ (d^{-1})反映了添加示踪剂 $^{200}Hg^{II}$ 和 $Me^{198}Hg$ 生成可吹出 $^{200}Hg^{0}$ 和 $^{198}Hg^{0}$ 的速率（图 3-12）。由生成可吹出 $^{200}Hg^{0}$ 的绝对质量可知（图 3-13），非灭菌组的 $^{200}Hg^{0}$ 显著高于灭菌组，说明黑暗环境中 Hg 的还原是微生物作用下完成的形态转化过程。然而，$^{200}Hg^{0}$ 和 $^{198}Hg^{0}$ 的产率（即 $^{200}Hg^{0}/^{200}Hg^{II}$ (%)和 $^{198}Hg^{0}/Me^{198}Hg$ (%)）均比起生成 MeHg 的产率低 1~2 个数量级（图 3-10 和图 3-14）。在培养实验初期（2 小时），对照处理的 K_v-$^{200}Hg^{II}$ 高于 Na_2SO_4 和 $Na_2S_2O_3$ 添加处理。在位点 GX，S 添加处理的 $^{200}Hg^{0}$ 生成量在所有时间点均显著低于对照处理；然而在 HX 位点，S 添加处理的 $^{200}Hg^{0}$ 生成量仅在前 14 小时低于对照处理。

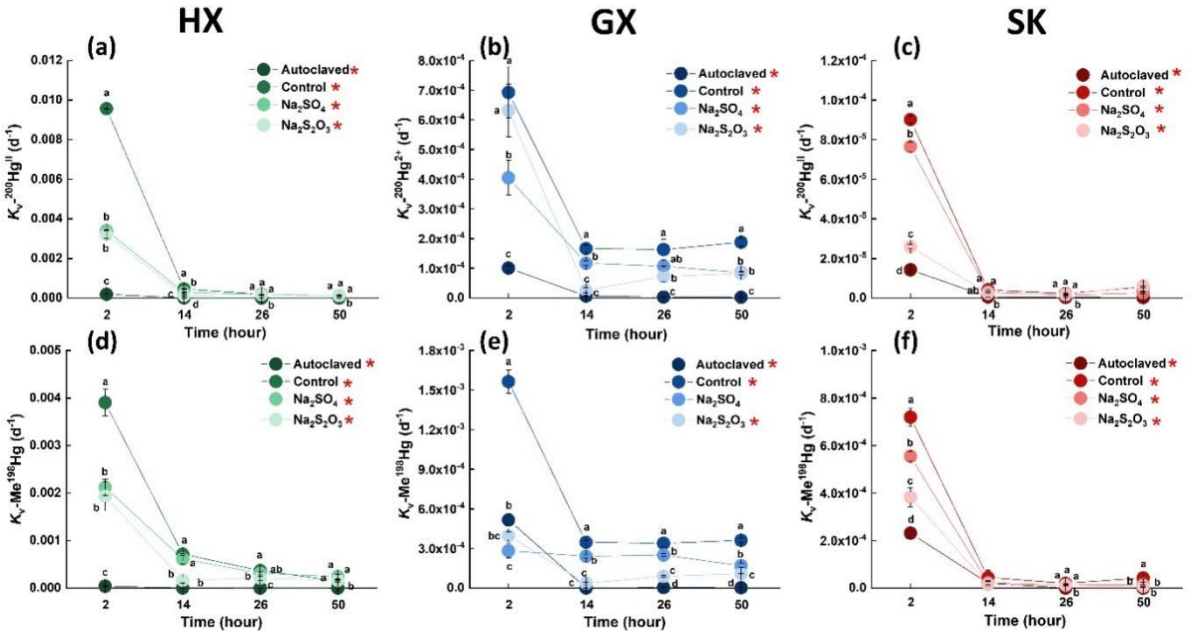

图 3-12 不同位点和处理中的汞挥发速率常数

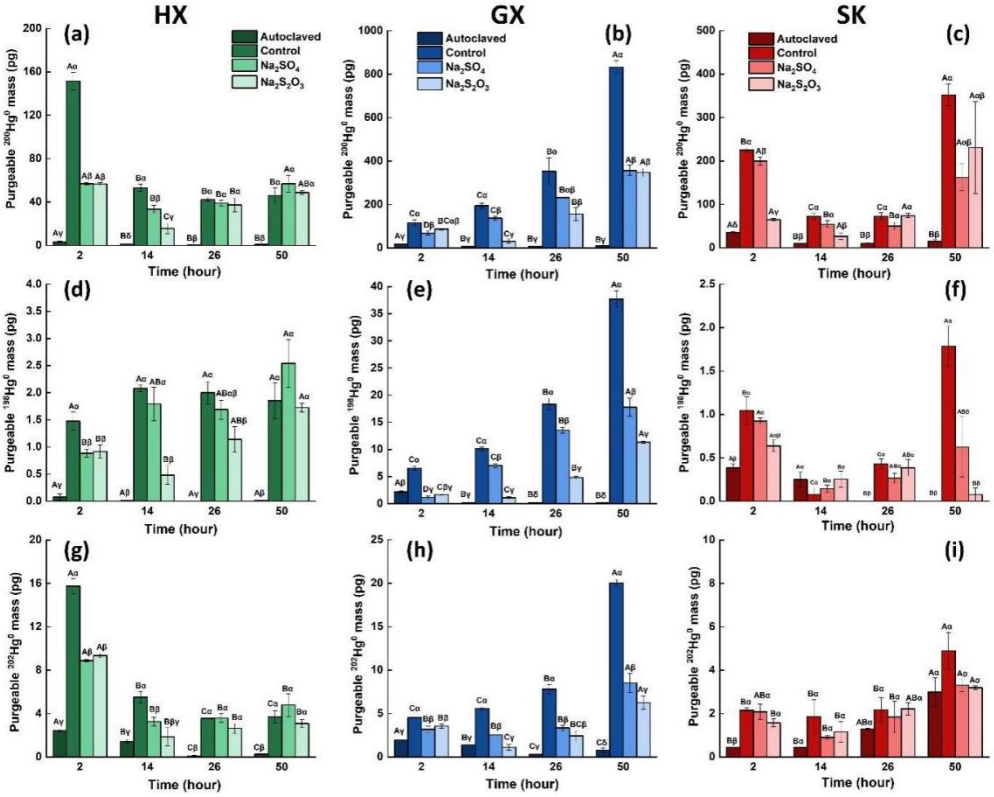

图 3-13 不同位点和处理中的零价汞同位素的绝对含量

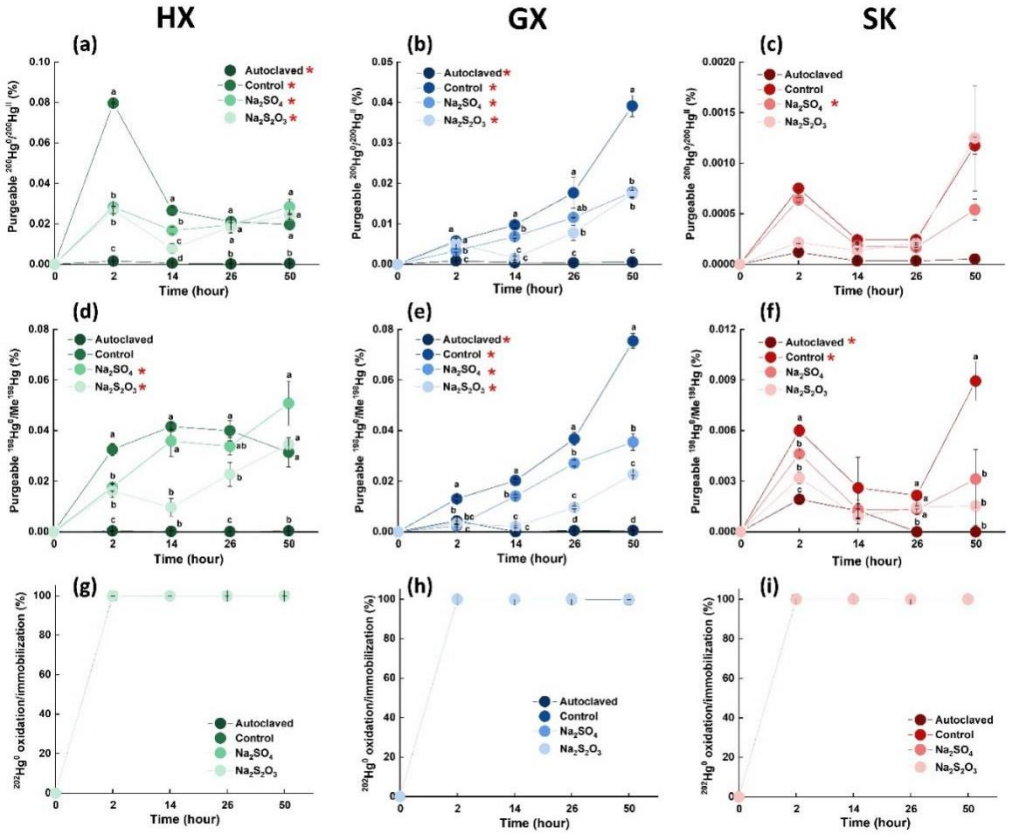

图 3-14 不同位点和处理中的可吹出零价汞的生成率

K_v-$Me^{198}Hg$ 与 K_v-$^{200}Hg^{II}$ 的变化趋势在所有位点相似，即其在 2 小时的对照处理中显著高于同时期的 S 添加处理（图 3-12）。在位点 GX，$Na_2S_2O_3$ 处理较 Na_2SO_4 处理产生的 $^{198}Hg^0$ 较少。值得一提的是，由于合成的 $Me^{198}Hg$ 纯度不可能达到 100%，那么一部分 $^{198}Hg^0$ 的产生可能来源于合成 $Me^{198}Hg$ 时残余的 $^{198}Hg^{II}$，而并非 $Me^{198}Hg$。因此，本研究进一步计算了本实验中 $Me^{198}Hg$ 的合成纯度。计算方法如下：

$$\text{Purity of } Me^{198}Hg\ (\%) = \frac{[Me^{198}Hg]}{[THg]} \times 100\% \qquad \text{（公式 3-16）}$$

通过计算可知，本实验中 $Me^{198}Hg$ 的合成纯度为 83.2%，其余 16.8%仍为 $^{198}Hg^{II}$，通过将这一部分无机汞带入转化率的计算：

$$\text{Recalibrated } ^{198}Hg^0\ (pg) = [^{198}Hg^0] - [^{198}Hg^{II}] \times \frac{[^{200}Hg^0]}{[^{200}Hg^{II}]} \qquad \text{（公式 3-17）}$$

$$[^{198}Hg^{II}] = \frac{[Me^{198}Hg]_{spiked}}{\text{Purity of } Me^{198}Hg} - [Me^{198}Hg]_{spiked} \qquad \text{（公式 3-18）}$$

我们得出，在位点 HX、GX 和 SK 中，生成的 $^{198}Hg^0$ 中分别有 86.4 ±11.6、89.4 ±10.4 和 97.1 ±3.4%来自于 $Me^{198}Hg$。上述校正计算在以往的研究中往往被忽视，可能导致对于甲基汞生成零价汞的高估。本研究通过校正，进一步明确了甲基汞生成零价汞的产率。

3.5.4 $^{202}Hg^0$ 的氧化或固相分配

$^{202}Hg^0$ 示踪剂添加后的消耗表明一部分 $^{202}Hg^0$ 又可吹出的 Hg（purgeable Hg^0）转变为了不可吹出的 Hg（non-purgeable Hg^0），而这一转化可能由 Hg^0 的氧化以及其在固相上的固定有关。本研究中，几乎所有的 $^{202}Hg^0$ 示踪剂在 2 小时内就被迅速氧化或者固定（图 3-14）。另外，在位点 HX 和 GX，S 添加处理较对照处理显著降低了 $^{202}Hg^0$ 的含量（图 3-13）。

3.5.5 稻田土壤中的汞形态转化过程

对比不同汞同位素示踪剂在对照处理和灭菌处理中的相互转化即可反映稻田土壤中汞的甲基化、去甲基化、还原、氧化/固相分配等转化过程。由图 3-11 可知，灭菌处理中 $Me^{200}Hg$ 的生成量显著低于非灭菌处理，表明稻田土壤中 Hg 的甲基化过程为微生物驱动的生物过程，非生物甲基化过程如果存在，也可以忽略。另外，$^{200}Hg^{II}$ 的甲基化过程受汞浓度梯度影响，K_m-$^{200}Hg^{II}$ 随稻田土壤中 Hg 浓度含量的升高而下降，这与我们之前的研究结果一致（Wu et al., 2020; Liu et al., 2022）。微生物组成的差异是

造成这一结果的原因（Wu et al., 2020; Liu et al., 2022）。因为（1）不同位点间土壤质地与性质差异较小；（2）汞胁迫下使得稻田土壤中的微生物群落结构进行重塑，改变了汞甲基化微生物或者其他与汞甲基化过程相关微生物的组成和丰度（Liu et al., 2018; Pu et al., 2022）。此外，在位点 SK，我们还发现虽然其 DOM 含量较低，但是其芳香性较位点 HX 和 GX 更强（更高的 $SUVA_{254}$）。此外，本研究还发现 K_m-$^{200}Hg^{II}$ 与不同位点代表 DOM 腐殖化程度的指标之间存在显著的负相关关系（表 3-3），这进一步说明，腐殖化程度更高的 DOM 会抑制微生物介导的 Hg 甲基化过程。通常来说，分子量较低，腐殖化程度较低，芳香性较低的 DOM（如小分子有机酸、糖类、蛋白等）较腐殖化程度更高的 DOM 更易于被微生物利用，进而进行汞的甲基化过程（Bravo et al., 2017）。

表 3-3 Hg 形态转化速率常数与 DOM 含量与光谱特征之间的相关性系数

	DOC	Peak A	Peak C	HIX	a(355)	$SUVA_{254}$	$S_{275\text{-}295}$
K_m-$^{200}Hg^{II}$	0.78**	-0.58*	-0.75**		-0.49*	-0.77**	0.55*
K_m-$^{202}Hg^0$	0.53*	-0.52*	-0.56*				
K_d-$Me^{198}Hg$					0.52*		
K_v-$Me^{198}Hg$	0.81**	-0.63**	-0.74**		-0.60**	-0.88**	0.69**
K_v-$^{200}Hg^{II}$	0.88**	-0.63**	-0.80**	-0.55*	-0.49*	-0.87**	0.76**

本研究发现 HX 位点的灭菌处理在培养后期表现出活跃的 Hg 甲基化现象，表现为现在增加的 $Me^{200}Hg$ 以及增加的 *hgcA* 基因丰度，这表明高温高压灭菌方法在培养后期可能会出现微生物复苏的现象，这一高温高压灭菌方法的不确定性同样有文献报道（Tuominen et al., 1994; Wu et al., 2020）。为进一步验证微生物的复苏，我们进行了一个测试灭菌后微生物培养的涂板试验。即使用高温高压灭菌后的样品接种至含有培养基（R2A 琼脂，Solarbio® 中国）的平板上，37°C 培养 24 小时。随后观察是否存在微生物（图 3-15）。并未发现有微生物的复苏，表明这部分微生物可能为无法培养（no countable）微生物。值得一提的是，当 HX 位点培养末期微生物复苏后，$^{200}Hg^{II}$ 和 $^{202}Hg^0$ 生成速率常数高度耦合（图 3-16），这暗示 $^{202}Hg^0$ 和 $^{200}Hg^{II}$ 均能够被甲基化，并且这二者的甲基化过程高度耦合。

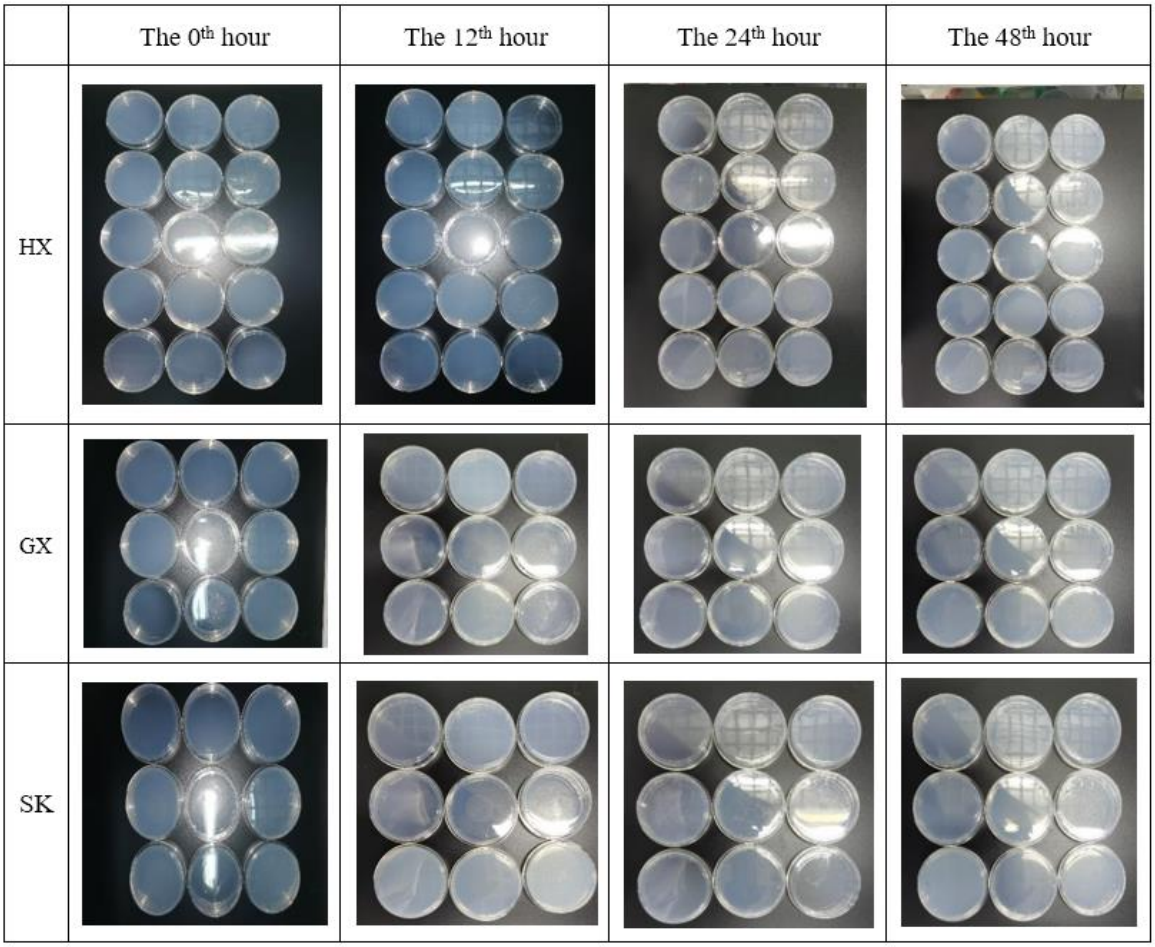

图 3-15 高温高压灭菌后微生物接种验证实验

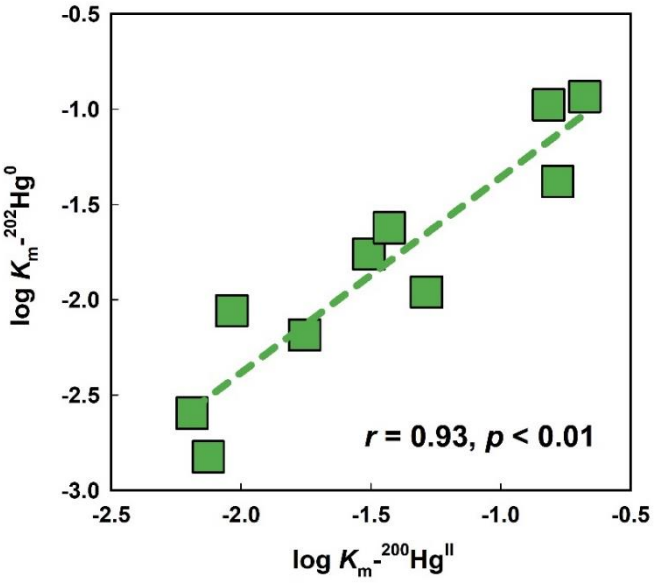

图 3-16 HX 灭菌处理中 logK_m-$^{200}Hg^{II}$ *versus* logK_m-$^{202}Hg^0$

之前有研究发现，Hg^0 在能够率先被氧化，然后进一步被甲基化（Colombo et al., 2014），并且这一过程在 *Desulfovibrio desulfuricans* ND132 菌（Colombo et al., 2013; Hu et al., 2013）和 *Geobacter sulfurreducens* PCA 菌（Hu et al., 2013; Lin et al., 2014）的纯培养实验中均得到验证。另外，在本研究中，超过 99%的 $^{202}Hg^0$ 在很短的时间内就会被氧化或者固相固定。虽然这部分不可吹出的 Hg 既能够以 Hg^0 的方式，又能够以 Hg^{II} 的方式与颗粒物结合（Wang et al., 2015）。但当有 DOM 或者一些厌氧微生物的存在下时，Hg^0 通常会被迅速地氧化为 Hg^{II}（Colombo et al., 2013; Hu et al., 2013; Zheng et al., 2012; Poulain et al., 2019）。并且也有研究指出，即使与颗粒物结合的 Hg^{II} 也能够参与甲基化反应，并生成 MeHg（Zhang et al., 2019; Xiang et al., 2022）。之前的研究发现微生物能够氧化 Hg^0（Colombo et al., 2013; Hu et al., 2013），然而本研究发现即使在灭菌处理，$^{202}Hg^0$ 也能够在很短的时间内被氧化或者固相固定，这表明非生物氧化同样是氧化 Hg^0 的重要途径。因此，本研究中高度相关的 $^{200}Hg^{II}$ 和 $^{202}Hg^0$ 甲基化过程表明 $^{202}Hg^0$ 率先被氧化，然后被微生物甲基化，且被氧化后的 $^{202}Hg^{II}$ 其甲基化过程与 $^{200}Hg^{II}$ 一致。

除上文所述的氧化和甲基化过程共变化以外，我们还发现 Hg^{II} 的还原过程和甲基化过程表现出共变化的关系。传统观念认为，由于 Hg 的还原过程与甲基化过程都需要生物有效态的 Hg^{II}，因此这两个过程存在竞争的关系；然而，当发现 Hg^0 也能参与甲基化过程以后（Colombo et al., 2013; Hu et al., 2013），人们的认识逐步拓宽。在本研究当中，未发现 Hg 的还原与甲基化的竞争关系，相反 $^{200}Hg^{II}$ 甲基化速率常数（K_m-$^{200}Hg^{II}$）与 $^{200}Hg^{II}$ 还原速率常数（K_v-$^{200}Hg^{II}$）呈现出显著的正相关关系（图 3-17）。Lu et al.（2016）报道一株携带有 *merA* 和 *merB* 基因的铁还原菌（FeRB）能够同时将 Hg^{II} 甲基化并通过还原去甲基化作用生成 Hg^0。在本研究中，$^{200}Hg^{II}$ 的甲基化过程与 $Me^{198}Hg$ 的去甲基化过程之间并无显著的相关关系，并且 *merA* 和 *merB* 基因未检出。这表明 Lu 等报道的甲基化耦合还原去甲基化过程并未发生在本研究中。相反，其他途径的 Hg 还原过程可能为 Hg^0 产生的主要途径，例如细胞色素 C 介导的 Hg 还原过程以及细菌发酵生长过程中伴随的 Hg 还原过程（Hu et al., 2013; Grégoire and Poulain, 2018）。其中，细胞色素 C 介导的 Hg 还原过程依赖于胞外电子传递，而细菌发酵生长过程中伴随的 Hg 还原过程依赖于可用于发酵反应的碳源（Shi et al., 2009; Grégoire et al., 2018; Grégoire and Poulain, 2018）。

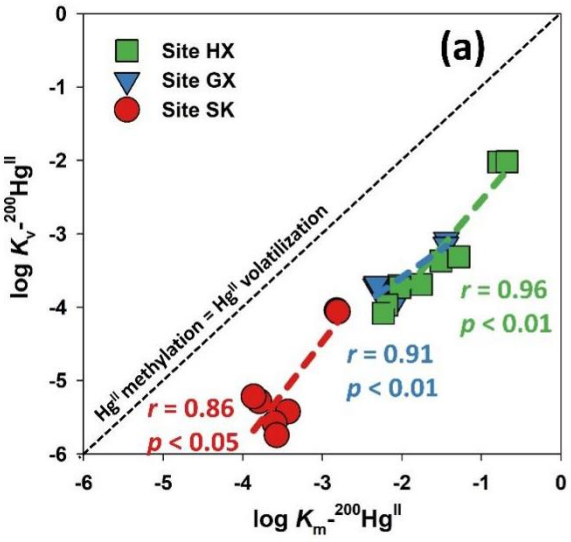

图 3-17 不同位点对照处理中 log K_m-$^{200}Hg^{II}$ *versus* logK_v-$^{200}Hg^{II}$

然而，$^{200}Hg^{II}$的还原量较其甲基化量低 1~2 个数量级（图 3-10 和图 3-13），表明在缺少光照的稻田土壤中 Hg 的甲基化过程较其还原过程更为主要。另外，由于还原生成的 $^{200}Hg^0$ 会被迅速氧化为 $^{200}Hg^{II}$，从而进一步被甲基化。因此，稻田土壤中 Hg 的迅速氧化还原循环可能通过提供生物有效态 Hg^{II} 的方式促进甲基化过程。当然，必须指出在长时间尺度下且土壤 Hg 含量较低的情况下，Hg 的还原及其向大气的排放势必会降低土壤中的 Hg 含量，并限制 Hg 的甲基化过程。

本研究，我们添加 Me^{198}Hg 示踪剂，并且检测捕捉到了 $^{198}Hg^0$ 的信号，表明存在 MeHg 向 Hg^0 转化的过程。但是该过程的转化率较 MeHg 的去甲基化率低 3~4 个数量级（图 3-10 和图 3-13）。由于介导 Hg 还原去甲基化的 *merA* 和 *merB* 基因（Begley et al., 1986; Barkay and Gu, 2022）丰度低于检测限，因此 MeHg 向 Hg^0 转化的过程并非还原去甲基化过程。那么，不依赖于 *mer* 操纵子的氧化去甲基化过程可能是本研究中 MeHg 去甲基化的机制（Zhou et al., 2020）。有研究指出，氧化去甲基化过程为一类非特异性的共代谢过程，其能够产生 Hg^{II} 和 CO_2，并且常见于厌氧环境中（Oremland et al., 1991; Barkay and Gu, 2022）。在本研究中，K_v-Me^{198}Hg 和 K_v-$^{200}Hg^{II}$ 的共变化关系（图 3-18）以及 $^{198}Hg^0$ 净含量和 $^{200}Hg^0$ 净含量之间的共变化关系（图 3-19），表明添加 Me^{198}Hg 生成 $^{198}Hg^0$ 的过程为一个两步式反应，即 Me^{198}Hg 先氧化去甲基化生成 $^{198}Hg^{II}$，随后进一步还原为 $^{198}Hg^0$。

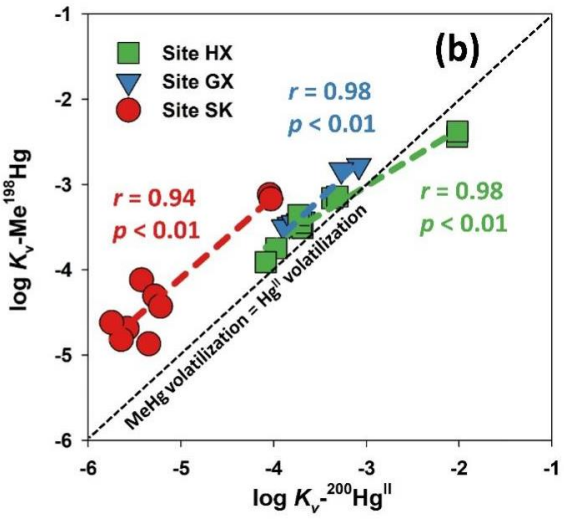

图 3-18 不同位点对照处理中 logK_v-$^{200}Hg^{II}$ *versus* logK_v-$Me^{198}Hg$

从图 3-18 中可以看出，所有数据点均分布在 logK_v-$Me^{198}Hg$: logK_v-$^{200}Hg^{II}$ = 1:1 附近，表明控制 $Me^{198}Hg$ 去甲基化和 $^{200}Hg^{II}$ 还原的作用机制相似。另外，所有位点中 $^{200}Hg^0$ 和 $^{202}Hg^0$ 的净含量之间同样存在共变化的关系（图 3-19），表明无论添加何种同位素示踪剂（$^{200}Hg^{II}$、$Me^{198}Hg$ 以及 $^{202}Hg^0$），其生成 Hg^0 的机制均相似。这说明，Hg 形态转化中生成 Hg^{II} 是 Hg 甲基化和还原的前提。

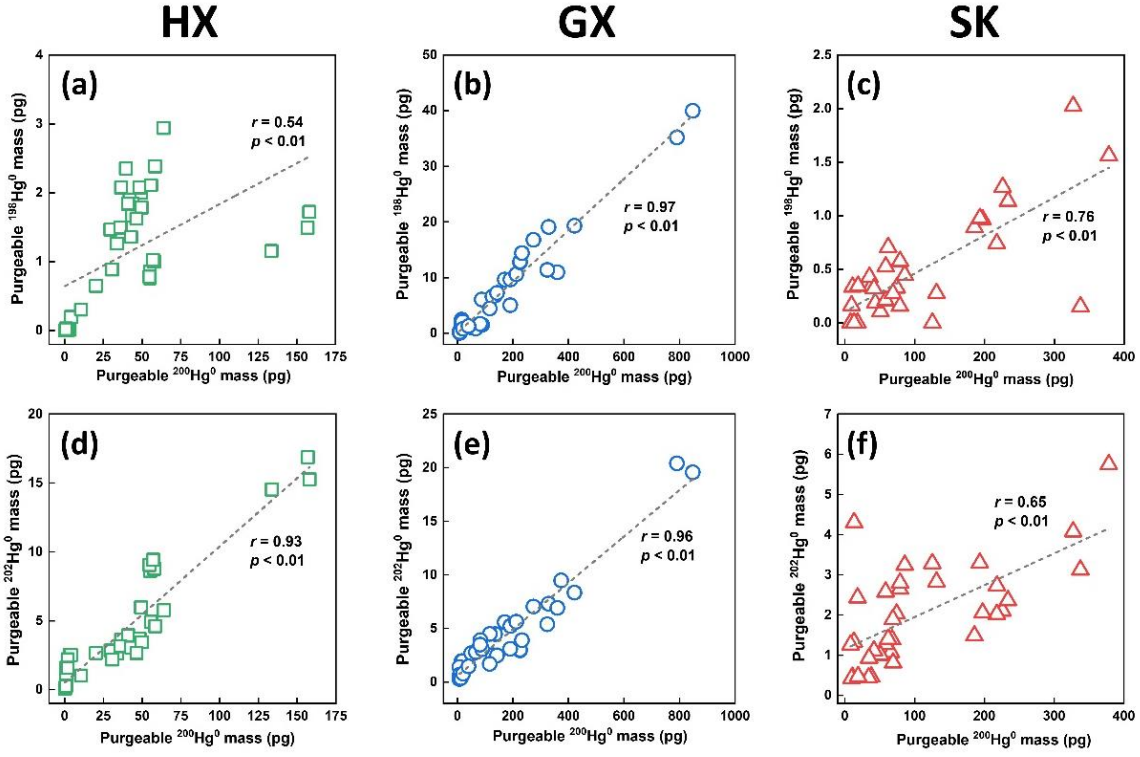

图 3-19 $^{198}Hg^0$, $^{200}Hg^0$ 和 $^{202}Hg^0$ 含量之间的共变化关系

此外，我们还发现反应 DOM 腐殖化程度的指标（peak A、peak C 和 $SUVA_{254}$）与 K_v-$Me^{198}Hg$ 和 K_v-$^{200}Hg^{II}$ 均与之间存在显著的负相关关系，但是却和 K_d-$Me^{198}Hg$ 不存在相关关系（表 3-3）。这表明，DOM 中腐殖化程度高的部分会抑制 Hg^{II} 的还原。铁在固相和液相的分配同样影响着 Hg 的形态转化过程。本研究中，K_m-$^{200}Hg^{II}$ 或 K_v-$^{200}Hg^{II}$ 均与不同形态铁存在显著的相关关系（表 3-4）。有研究指出，铁氧化物的还原溶解会释放之前被吸附固定的 Hg^{II}，从而提高 Hg 的生物有效性（Wang et al., 2021; Liu et al., 2022）。然而，铁氧化物向铁硫化物的转化过程又会降低 Hg 的生物有效性（Liu et al., 2022; Skyllberg et al., 2021）

表 3-4 Hg 形态转化速率常数与铁形态之间的相关性系数

	Fe^{2+}	Fe^{3+}	Fe^{2+}+Fe^{3+}
logK_m-$^{200}Hg^{II}$	0.45**	0.40*	0.53**
logK_m-$^{202}Hg^{0}$			0.40*
logK_d-$Me^{198}Hg$			
logK_v-$Me^{198}Hg$	0.37*	0.50**	0.48**
logK_v-$^{200}Hg^{II}$	0.40**	0.47**	0.52**

3.6 硫酸盐和硫代硫酸盐添加对稻田土壤中的汞形态转化过程的影响

我们发现当外源硫添加后，其对汞甲基化/去甲基化以及氧化还原的影响不仅与添加的 S 形态有关，还与不同位点有关（图 3-9 和图 3-12）。由于不同 S 形态影响 Hg 形态转化过程的差异，我们提出两个问题：（1）外源 S 添加如何影响汞形态转化过程？（2）硫酸盐和硫代硫酸盐是否通过相同的途径影响汞形态转化？为回答上述两个问题，我们展开下列讨论。

3.6.1 硫添加影响汞形态转化：汞生物有效性驱动还是微生物驱动？

汞的生物有效性和参与汞形态转化的微生物群落结构是影响自然环境中汞形态转化过程最为重要的两个因素（Hsu-Kim et al., 2013; Bravo and Cosio, 2020）。然而，这两个因素在汞形态转化过程中的作用究竟孰重孰轻尚不明确。近期，有研究指出 S 添加通过增加 Hg 的迁移性，从而促进了 MeHg 的生成，而并非改变参与 Hg 甲基化过程的微生物群落结构（Li et al., 2019; Lei et al., 2021）。在本研究中，我们发现在不同 Hg 浓度梯度稻田中，汞的生物有效性和微生物群落结构在汞甲基化中扮演着不同的角色。

在低 Hg 和中等 Hg 浓度的位点 HX 和 GX，添加 Na_2SO_4 和 $Na_2S_2O_3$ 促进 $Me^{200}Hg$ 的生成但抑制了 $^{200}Hg^0$ 的生成，表明 S 添加促进 $^{200}Hg^{II}$ 的甲基化作用，但抑制 $^{200}Hg^{II}$ 的还原作用（$p < 0.05$, 图 3-9 至图 3-14）。假如 Hg 的生物有效性增加，那么 S 添加不仅会促进 Hg 的甲基化，也会促进 Hg 的还原，特别在汞甲基化和汞还原存在共变化的关系时。并且，Hg 甲基化微生物和 Hg 还原微生物利用 Hg^{II} 的难易程度应该相似。这说明，Hg生物有效性增加可能不是造成这一现象的原因。在我们之前的研究中发现，SRB 是位点 HX 和 GX 的主要 Hg 甲基化微生物类群（Wu et al., 2020）。因此，添加 Na_2SO_4 和 $Na_2S_2O_3$ 均能够通过氧化或歧化的方式为 SRB 提供 SO_4^{2-}（Jørgensen, 1990; Schippers, 2004; Zopfi et al., 2008），进而促进硫酸盐还原介导的 Hg 甲基化过程。在本研究中，我们还发现在位点 HX，硫添加处理不仅增加了 SO_4^{2-} 的含量还增加了 *dsrB* 基因的丰度。在位点 GX，我们发现 *dsrB* 基因的丰度与 *hgcA* 基因的丰度存在显著的相关关系（图 3-20）。

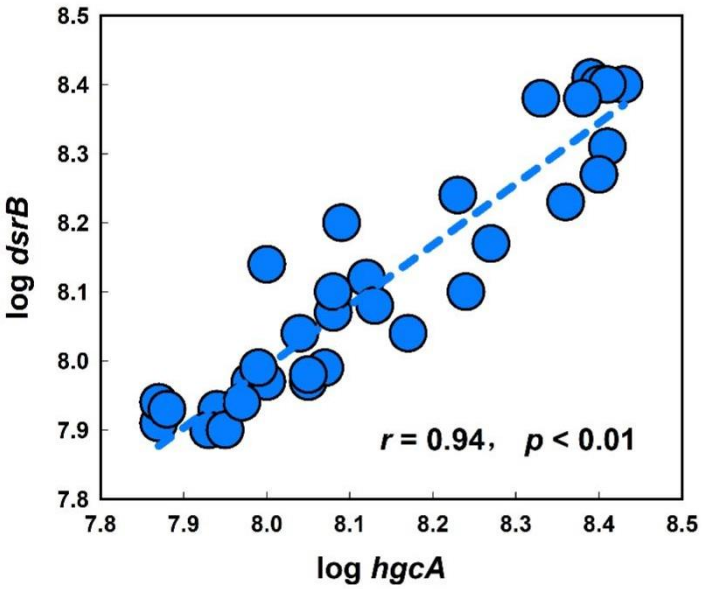

图 3-20 位点 GX 中 log *hgcA versus* log *dsrB*

通过 hgcA 基因的扩增子测序和宏基因组测序，我们也发现位点 HX 和 GX 硫添加处理中的 SRB 型 Hg 甲基化微生物的丰度较对照处理更高，这表明添加 Na_2SO_4 和 $Na_2S_2O_3$ 促进了 SRB 型 Hg 甲基化微生物的活性。另外，我们还发现 SRB 型 Hg 甲基化微生物中 *Desulfomonile* 的丰度与 $\log K_m$-$^{200}Hg^{II}$ 显著正先关（图 3-21），表明 *Desulfomonile* 可能是本研究中占主导地位的 Hg 甲基化微生物。

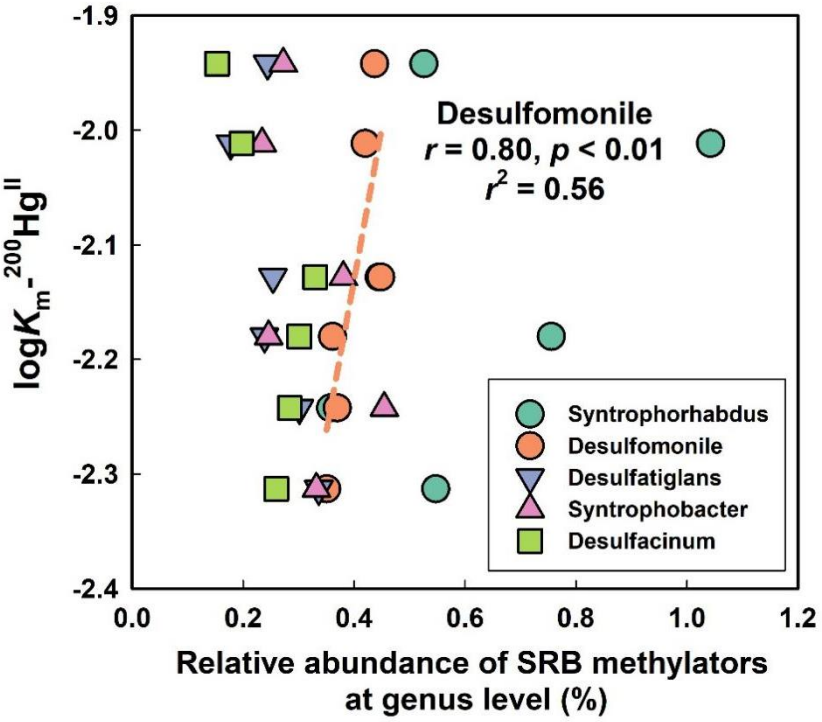

图 3-21 位点 HX 和 GX 中不同 SRB 型 Hg 甲基化微生物丰度 *versus* log K_m-$^{200}Hg^{II}$

在高汞浓度位点 SK，添加 Na_2SO_4 和 $Na_2S_2O_3$ 抑制了 Hg^{II} 的甲基化和 Hg^{II} 的还原，但促进了 MeHg 的去甲基化（图 3-9 至图 3-14）。在之前，我们发现位点 SK 灭菌处理中的 NO_3^- 浓度较位点 HX 和 GX 高 1~3 个数量级，表明在位点 SK 存在非常剧烈的 NO_3^- 异化还原作用（Yuan et al., 2022）。然而，NO_3^- 的大量还原会消耗参与 Hg^{II} 甲基化过程（如硫酸盐还原、铁还原和产甲烷过程）的电子供体，以及还原 Hg^{II} 的电子供体（Todorova et al., 2009; Strickman and Mitchell, 2018; Zhang et al., 2018）。本研究中发现的高 SO_4^{2-} 浓度，低 HS^- 浓度，低 Fe^{2+} 浓度均可证明电子供体的消耗。此外，之前的研究发现产甲烷菌可能是位点 SK 的主要甲基化微生物（Wu et al., 2020）。在本研究中，携带有 *hgcA* 基因的产甲烷菌 *Methanothrix* 和 *Methanoregula* 在 SK 的丰度也高于位点 HX 和 GX（图 3-8）。因此，SO_4^{2-} 的添加可能会增加 SRB 和产甲烷菌对于底物的竞争，并且甲烷产生较 SO_4^{2-} 还原更难发生，需要更低的 Eh（Kögel-knabner et al., 2010）。在前文中，我们发现 MeHg 的去甲基化主要为氧化去甲基化，而 SRB 同样为参与氧化去甲基化的微生物类群之一（Marvin-DiPasquale et al., 2000; Barkay and Gu, 2022），因此通过 SO_4^{2-} 添加促进 SRB 的活性，可能同样会促进 MeHg 的去甲基化。综上，外源 S 添加通过促进 Hg 甲基化微生物活性的方式促进 Hg 的甲基化过程。

3.6.2 硫酸盐 vs 硫代硫酸盐

众所周知，硫酸盐是 S 循环中的末端电子受体（Terminal electron acceptor），而硫代硫酸盐则为 S 氧化还原循环中的重要中间产物（Jørgensen, 1990; Zopfi et al., 2008; Orem et al., 2011; Santana et al., 2021）。

有文献报道 Hg^{II} 能够与 $S_2O_3^{2-}$结合生成生物有效态的 Hg-S_2O_3 络合物（如 $Hg(S_2O_3)_2^{2-}$和 $Hg(S_2O_3)_3^{4-}$）（Wang et al., 2012; 2014; Vázquez-Rodríguez et al., 2015; Liu et al., 2019），并因此促进 Hg 甲基化过程。然而，我们发现添加的 $Na_2S_2O_3$ 并不稳定，且 $S_2O_3^{2-}$会转化为 SO_4^{2-}（图 3-4）。另外，我们通过水化学平衡软件（Visual MINTEQ）计算发现（图 3-22），当存在硫化物（HS^-）时，Hg 的化学形态以 Hg-S 络合物为主（HgS_2H^-，$Hg(SH)_2^0$ 和 HgS_2^{2-}），Hg-S_2O_3 络合物作用可以忽略不计。

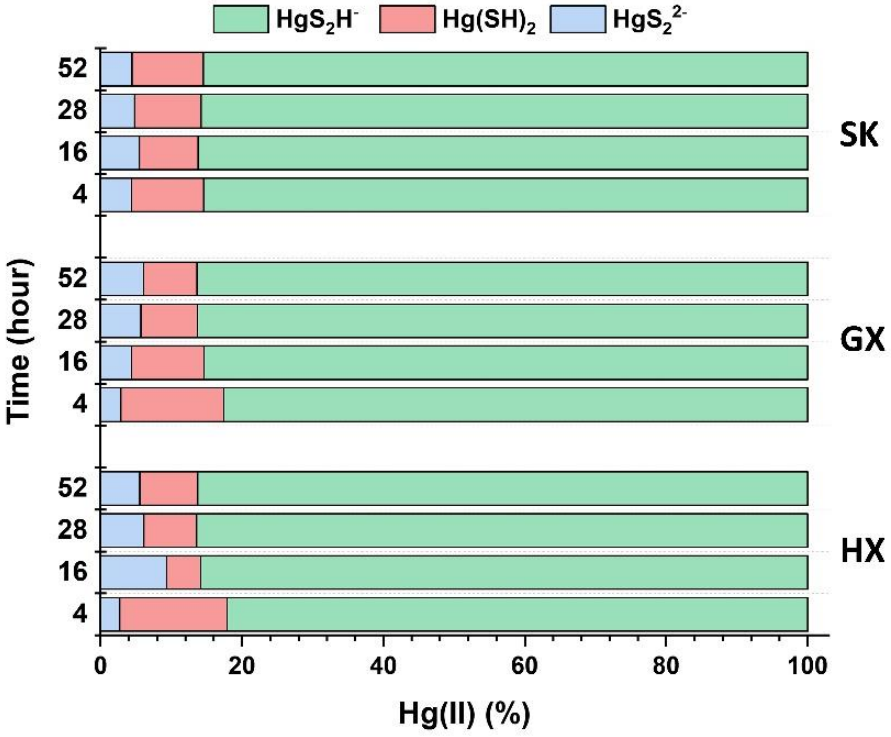

图 3-22 $Na_2S_2O_3$ 处理中 Hg^{II} 的化学形态分布

除 Na_2SO_4 和 $Na_2S_2O_3$ 添加对 Hg 化学形态的影响外，$Na_2S_2O_3$ 处理中 SO_4^{2-}的缓释作用可能是 $Na_2S_2O_3$ 处理较 Na_2SO_4 处理促进 Hg 甲基化的机制。在 Na_2SO_4 添加处理中，SO_4^{2-}的还原迅速进行，表现为 SO_4^{2-}的迅速消耗。然而在 $Na_2S_2O_3$ 添加处理中，$S_2O_3^{2-}$的氧化以及 $S_2O_3^{2-}$发生歧化反应生成 SO_3^{2-}和 S^0（Schippers, 2004），均减慢了

SO_4^{2-}的供给速度。并且上述反应均为无机发酵反应，其与外源的氧化剂和还原剂无关（Jørgensen et al., 2004）。在本研究中，位点 GX 中 SO_4^{2-}的生成速率低于位点 HX 和 SK，表明 GX 土壤中 $S_2O_3^{2-}$的氧化较慢。此外，我们还发现 $Na_2S_2O_3$ 添加处理较 Na_2SO_4 添加处理中的硫氧化功能基因 *soxB* 的丰度更高，且 *soxB* 基因的丰度与[HS^-]呈显著负相关；说明 $S_2O_3^{2-}$的氧化能够补充 SO_4^{2-}的供给。这意味着硫氧化微生物在 SRB 介导的 Hg 甲基化过程中同样扮演着重要的作用。

综上，$S_2O_3^{2-}$和 SO_4^{2-}影响的汞甲基化机制不尽相同，其都是通过提供 SO_4^{2-}，促进 SRB 的活性而促进 Hg 甲基化作用。但是 SO_4^{2-}生成的动力学速率以及微生物利用 SO_4^{2-}的速率却不同，这导致了 $Na_2S_2O_3$ 处理较 Na_2SO_4 处理产生更多 MeHg。

3.7 本章小结

除大家熟知的 Hg^{II} 甲基化和 MeHg 去甲基化过程外，本研究直接证明了微生物介导的 Hg^{II}暗还原作用，Hg^0的氧化/固相分配，Hg^0的甲基化，以及从 MeHg 生成 Hg^0的过程（图 3-23）。上述过程中，除 Hg^0 的氧化/固相分配为非生物过程外，其余转化过程均为微生物参与的生物过程。土壤中硫输入主要通过影响微生物群落结构而进一步影响汞形态转化。

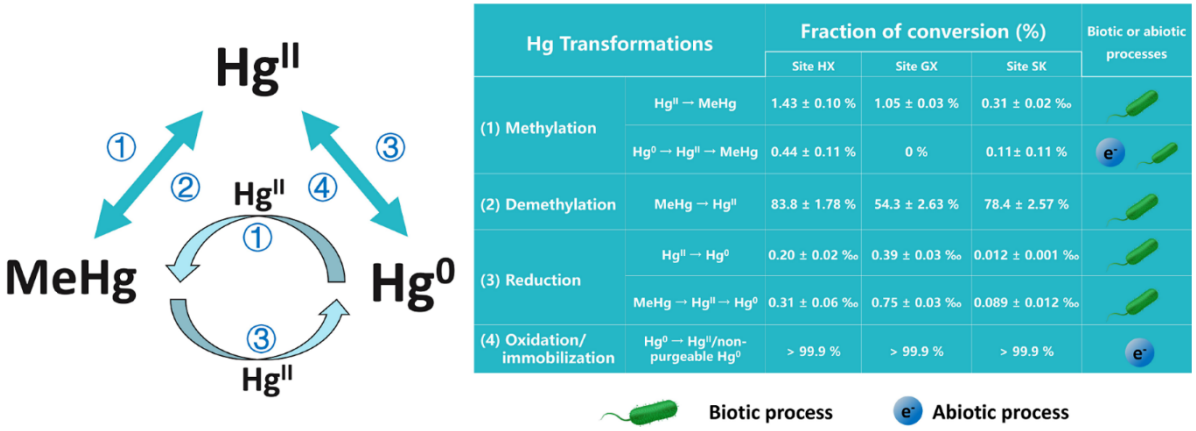

Hg Transformations		Fraction of conversion (%)			Biotic or abiotic processes
		Site HX	Site GX	Site SK	
(1) Methylation	$Hg^{II} \rightarrow MeHg$	1.43 ± 0.10 %	1.05 ± 0.03 %	0.31 ± 0.02 ‰	
	$Hg^0 \rightarrow Hg^{II} \rightarrow MeHg$	0.44 ± 0.11 %	0 %	0.11± 0.11 %	
(2) Demethylation	$MeHg \rightarrow Hg^{II}$	83.8 ± 1.78 %	54.3 ± 2.63 %	78.4 ± 2.57 %	
(3) Reduction	$Hg^{II} \rightarrow Hg^0$	0.20 ± 0.02 ‰	0.39 ± 0.03 ‰	0.012 ± 0.001 ‰	
	$MeHg \rightarrow Hg^{II} \rightarrow Hg^0$	0.31 ± 0.06 ‰	0.75 ± 0.03 ‰	0.089 ± 0.012 ‰	
(4) Oxidation/ immobilization	$Hg^0 \rightarrow Hg^{II}$/non-purgeable Hg^0	> 99.9 %	> 99.9 %	> 99.9 %	

Biotic process　Abiotic process

图 3-23 稻田土壤中 Hg 形态转化过程及其转化率

第 4 章 铁氧化物-有机质复合体系控制稻田土壤中新沉降汞的地球化学形态分馏

4.1 本章引言

汞与大部分重金属污染物不同，其能够以气态单质汞的形态长期存在于大气中，并进行长距离传输（冯新斌等，2009；Ariya et al., 2015）。正是由于 Hg 的这一特性，即使在一些人迹罕至的偏远地区，如北欧或者北美的高纬度湖泊中，也发现鱼体 Hg 含量严重超标的现象（Lucotte et al., 1999）。因此，Hg 的大气沉降是表生生态系统不可忽视的 Hg 源之一。近年来，国外学者针对这部分新沉降 Hg 在陆地生态系统的生物地球化学过程展开了大量研究（Hintelmann et al., 2002; Branfireun et al., 2005; Paterson et al., 2006; Harris et al., 2007; Orihel et al., 2008; Oswald et al., 2014; Blanchfield et al., 2021），发现新沉降的 Hg（简称为“新”Hg）较土壤中原本存在的 Hg（简称为“老”Hg）更易于被甲基化。在水生生态系统中，有学者也发现新沉降的 Hg 在被甲基化后，更易于在水生生物体中积累与富集（Paterson et al., 2006; Harris et al., 2007; Orihel et al., 2008）。课题组前期在稻田生态系统展开的研究也发现了类似的现象，即通过大气沉降进入稻田土壤的“新”Hg 比“老”Hg 更易于被甲基化，并在水稻中进行富集（Meng et al., 2010, 2011; Zhao et al., 2016; Ao et al., 2020）。然而，究竟是什么原因导致“新”Hg 和“老”Hg 在甲基化过程中存在差异，尚不清楚。众所周知，Hg 的生物有效性是影响 Hg 甲基化过程的重要因素之一（Hsu-Kim et al., 2013），而新沉降 Hg 在稻田土壤中的生物有效性受土壤理化性质的影响。特别是，稻田土壤中存在大量的有机质（Rolfhus et al., 2015）、铁/锰氧化物（O'Connor et al., 2019）、不同形态硫（Skyllberg, 2008）以及黏土矿物（Zhu et al., 2012）均控制着新沉降 Hg 的地球化学形态分馏过程（Geochemical Fractionation）；具体表现为控制新沉降 Hg 在不同地球化学形态之间的分配与再分布。因此，深入研究新沉降 Hg 在稻田土壤中的地球化学形态分馏过程是了解其甲基化及其潜在环境风险的必要前提。基于此，本研究采用单一富集稳定汞同位素示踪技术，通过添加 ^{200}Hg 示踪剂模拟稻田土壤中沉降的“新”Hg，以期明确“新”Hg在不同地球化学形态之间的分配与再分布过程，并识别影响“新”Hg 地球化学形态分馏的主要地化因子。

4.2 材料与方法

4.2.1 研究区与实验设计

本实验在陕西省安康市旬阳县进行。研究期间，实验点位大气中气态单质汞（GEM）的浓度为 1.0（ng m^{-3}）至 9.0（ng m^{-3}）之间，均值为 4.8 ± 2.0（ng m^{-3}）。该 GEM 浓度仅略高于长白山全球本底站点（1.60 ± 0.51（ng m^{-3}）, Fu et al., 2012），而低于城市区域（如贵阳城区，10.2 ± 7.06（ng m^{-3}）, Fu et al., 2015）和汞污染区（如万山汞矿区，403 ± 388（ng m^{-3}）, Zhao et al., 2016a）。因此，本研究区的大气 Hg 沉降量较低，在水稻种植期间通过大气沉降进入稻田土壤的这部分 Hg 可以忽略不计。

本实验使用预净化后的 PVC 箱（长宽高：54 cm × 42 cm × 33 cm）在露天的情况下，进行水稻培养实验。培养实验用土采集自研究位点附近的稻田土壤（总汞 THg 浓度为 78.4 ± 4.6（μg kg^{-1}））。在培养箱中填入过 2 mm 筛网后的土壤 40 kg，使箱内土壤厚度大于 20 cm。加入一定量的灌溉水，以保持培养用土与田间土壤的持水量接近，灌溉水 THg 浓度为 1.37 ± 0.45（ng L^{-1}）。供试土壤的理化参数如表 4-1 所示。

表 1 供试土壤理化性质

理化性质	含量
总汞（THg）	75.29 ±5.91（μg kg^{-1}）
酸碱度（pH）	7.93
总有机碳（TOC）	1.03 ±0.04（%）
总氮（TN）	0.14 ±0.01（%）
碳氮比（C/N）	7.03 ±0.14
总硫（TS）	1.00 ±0.26（mg kg^{-1}）
总铁（TFe）	32.10 ±2.16（g kg^{-1}）
总锰（TMn）	0.40 ±0.01（g kg^{-1}）

本研究通过向稻田土壤添加单一富集稳定汞同位素（^{200}Hg），模拟通过大气沉降进入稻田土壤的“新”Hg（Hintelmann et al., 2002; Branfireun et al., 2005; Oswald et al., 2014; Blanchfield et al., 2021）。由于大气沉降中的 Hg 以氧化态的二价汞为主（Ariya et al., 2015; Fu et al., 2015），因此，添加入稻田土壤的 ^{200}Hg 为 $^{200}Hg^{2+}$。将购买自美国

ISOFLEX 公司的 ^{200}Hg（纯度 98.2 ± 0.15%）溶解于浓硝酸中（纯度≥ 99.9%），制备得到 $^{200}Hg(NO_3)_2$ 储备液。使用超纯水（Milli-Q，Millipore，美国）稀释 $^{200}Hg(NO_3)_2$ 储备液得到浓度为 12（mg Hg L^{-1}）的工作液，并使用 NaOH 将该工作液的 pH 值调至中性。将制备得到的 $^{200}Hg(NO_3)_2$ 工作液使用一次性注射器，少量多次地加入 PVC 培养箱中，并迅速混匀，成化 24 h。经测定，培养用土中加入的 $^{200}Hg^{2+}$ 示踪剂含量为 115.09 ± 0.36（μg kg^{-1}）。

选用水稻品种为当地常用的杂交稻，水稻秧苗在温室中育苗 30 天。移栽时，挑选 20 株长势接近的水稻秧苗以 10 cm × 10 cm 的间距，移入 PVC 培养箱中。水稻种植期间的灌溉水为自来水，并在水稻生长期间始终保持 3~5 cm 深的淹水状态。为减少外源化学物质添加所带来的扰动，在水稻培养期间未使用任何化肥或者农药。从水稻移栽至收获，共培养 110 天。

4.2.2 样品采集与预处理

在水稻移栽后的第 0 天、30 天、60 天、90 天和 110 天进行样品的采集。每次采样分别随机采集 3~5 个根际土壤样品（10~20 cm），填满全新的聚丙烯采样管（不留空气）。使用 Parafilm®封口膜密封采样管，以减少样品运输途中的氧化。密封后的土样保存于冷藏箱中，并在 24 小时之内运回至实验室。在实验室内，使用冷冻干燥机（FD-3-85D-MP，FTS，美国）将土壤样品冷冻干燥，并过 200 目筛网。另外，在采集土壤的同时，使用便携式汞蒸气分析仪（RA-915+，Lumex，俄罗斯）每隔 10 s 采集一个气态单质汞浓度数据，并连续测定 1 小时以上。

4.2.3 分析方法

（1）汞形态的连续提取

汞形态的连续提取法采用经过修订后的 Tessier 五步提取法（Tessier et al., 1979），分别使用硝酸镁（$Mg(NO_3)_2$）提取溶解与可交换态 Hg；使用醋酸钠（NaOAc）提取碳酸盐结合态 Hg；使用溶于醋酸的盐酸羟胺（$NH_2OH·HCl$）提取铁/锰氧化物结合态 Hg；使用双氧水（H_2O_2）提取有机质结合态 Hg；使用王水消解提取残渣态 Hg。

（2）土壤有机质的形态分级

土壤有机质组分可分为溶解性有机质（DOM）、腐殖酸（HA）、富里酸（FA）、黏土矿物结合态的腐殖酸（C-HA）以及黏土矿物结合态的富里酸（C-FA）（Carter and Gregorich, 2007）。其中 DOM 采用超纯水（Milli-Q®, Millipore, 美国）以土水比 1:10 提取（Jiang et al., 2017; Liu et al., 2021b）。土壤腐殖质（humus），包括 HA、FA、C-HA 和 C-FA 采用 NaOH 提取。首先，使用 0.5 M 盐酸去除土壤中无机碳组分（主要是碳酸盐碳），随后使用 0.5 M NaOH 提取土壤腐殖质；在提取液中加入 6 M HCl 酸化，此时 HA 沉淀，而仍然 FA 仍然存在于上清液中。通过离心分离上清液后 FA 后，使用 0.1 M NaOH 再次溶解棕色沉淀，得到 HA。C-HA 和 C-FA 的提取为在土壤残渣中加入去离子水并超声振荡 10 min，随后低温（4 ºC）静置 48 小时。分离 C-HA 和 C-FA 的方法同 HA 和 FA 一致。

（3）铁形态的连续提取

铁形态的连续提取采用 Poulton 和 Canfield （2005）的方法，将铁（氢）氧化物分为溶解和可交换态 Fe（Fe_{exch}）、碳酸盐结合态 Fe（Fe_{carb}）、易还原态 Fe（Fe_{ox1}）、可还原态 Fe（Fe_{ox2}）和磁铁矿 Fe（Fe_{mag}）以及黄铁矿 Fe（Fe_{py}）。其中典型的易还原态 Fe 包括水铁矿（ferrihydrite）和纤铁矿（lepidocrocite）；而典型的可还原态 Fe 包括针铁矿（goethite）和赤铁矿（hematite）。定义上述不同形态 Fe 之和为活性 Fe（$Fe_{HR} = \sum (Fe_{exch} + Fe_{carb} + Fe_{ox1} + Fe_{ox2} + Fe_{mag} + Fe_{py})$）。Claff等人（2010）和 Slotznick 等人（2020）采用纯矿物体系，借助非破坏性岩石磁性实验和 X 射线衍射技术验证了该形态分级方法的可靠性。

4.2.4 测定方法

使用电感藕合等离子体质谱（ICP-MS）（Agilent 7700x，美国）测定土壤样品中的总汞同位素（$T^{200}Hg$）含量；使用气相色谱-电感藕合等离子体质谱（GC-ICP-MS）测定土壤样品中的甲基汞同位素（$Me^{200}Hg$）含量。使用冷原子荧光光谱法（CVAFS）（Brooks Rand Model III，美国）测定水体样品中的 THg 浓度。使用便携式汞蒸气分析仪（RA-915+，Lumex，俄罗斯）测定 GEM 浓度。土壤中的 TOC 和 TN 采用元素分析仪（Vario MACRO cube，Elementar，德国）测定；土壤有机质不同组分（DOM、

HA、FA、C-HA 和 C-FA）中含碳量采用有机碳分析仪（InnovOx®，GE，美国）测定；土壤 DOM 的吸收光谱和荧光光谱特征采用荧光光谱仪（Aqualog®，Horiba，日本）进行测定。其中，紫外-可见吸收光谱扫描波长范围为 230~800 nm，扫描间隔为 1 nm。荧光光谱所用的激发波长范围为 230~450 nm，发射波长范围 250~600 nm，扫描信号积分时间为 3 s，光源为 150 W 无臭氧氙弧灯，系统自动校正瑞丽散射和拉曼散射。采用 Wilson 和 Xenopoulos （2009）以及 Murphy 等人（2010）介绍的方法进行内滤效应校正。不同形态 Fe 含量采用盐酸羟胺还原，菲啰嗪（ferrozine）显色的方法测定（Viollier et al., 2000）。其中由于黄铁矿 Fe 提取过程使用了强氧化剂，因此黄铁矿 Fe 与总铁（TFe）和总锰（TMn）均采用火焰原子吸收法（PinAAcle 900T，PerkinElmer，美国）测定。总硫（TS）使用可见光分光光度计在 420 nm 波长通过比浊法测定（Sörbo, 1987）。

4.2.5 计算方法与质量控制

环境中原本存在的 Hg 称为背景 Hg（Ambient Hg），其能够通过实际测定得到的 $T^{202}Hg$ 和 $Me^{202}Hg$ 以及 ^{202}Hg 的天然丰度计算得到，在本研究中指代“老”Hg；本研究人为添加的 ^{200}Hg 为汞同位素示踪剂，其能够通过测定得到的 ^{200}Hg 含量扣除环境中原本存在的 ^{200}Hg 得到，在本研究中指代“新”Hg（Mao et al., 2013; Meng et al., 2018）（计算方法如 2 章 2.2 节）。根据土壤 DOM 的吸收-荧光光谱，计算得到 $SUVA_{254}$、$a(355)$、$S_{275–295}$、荧光峰 A、C、B 和 T、腐殖化指数（HIX）、自生源指数（BIX）。其中 $SUVA_{254}$ 为 254 nm 波长下的吸光系数与 DOM 含量的比值，反映土壤 DOM 的芳香性强弱；$a(355)$ 为 355 nm 波长下的吸光系数，反映土壤 DOM 中有色 DOM（CDOM）的相对浓度；$S_{275–295}$ 为吸收光谱在 275 nm 至 295 nm 处的斜率，反映土壤 DOM 分子量的大小；荧光峰 A 为类腐殖质峰；荧光峰 C 为类富里酸峰、荧光峰 B 和 T 为类蛋白峰；HIX 反映土壤 DOM 的腐殖化程度；BIX 反映土壤 DOM 中来自内源有机质的初级生产力（Hansen et al., 2016; Jiang et al., 2017; Liu et al., 2019）。

本研究分别使用 GSS-5 和 ERMCC580 两种标准物质，进行样品分析时的质量控制。其中，GSS-5 在 THg 分析时的回收率为 109 ± 4.7 % (n = 8)，ERMCC580 在 MeHg 分析时的回收率为 92 ± 10.0 % (n = 10)，满足实验室质量控制的要求。测定连续提取不同形态 ^{200}Hg 之和与 $T^{200}Hg$ 质量平衡的回收率为 86 %至 108 %，表明本研究所用连

续提取法能够有效地对 Hg 的不同地球化学形态进行分级。

4.3 稻田土壤中有机质组分与铁形态的分布特征

自然环境中，不同组分有机质在 Hg 的生物地球化学循环中扮演着重要的角色（Xu et al., 2021），并且有机质结合态 Hg 是土壤中重要的 Hg 地球化学形态之一。因此，本研究对不同组分土壤有机质的含量以及土壤溶解性有机质的结构和组成特征进行了分析与讨论。如图 4-1 所示，在水稻生长期内，稻田土壤总有机质（SOM）含量不断下降（$p < 0.05$），而溶解性有机质（DOM）则不断上升（$p < 0.05$）。在水稻生长的第 60 至 110 天，稻田土壤腐殖质含量（包括腐殖酸 HA 和富里酸 FA）显著增加，然而于黏土矿物结合的腐殖类物质含量（如 C-HA 和 C-FA）表现出降低的趋势。为进一步了解水稻生长过程中土壤有机质组分的变化情况，本研究采用了吸收光谱和荧光光谱对土壤中 DOM 组分进行表征，反映 DOM 的结构与组成的变化。通过吸收光谱，CDOM 的相对含量在水稻生长过程中显著增加（$p < 0.05$）；而 $SUVA_{254}$（第 0 至 90 天，$p < 0.05$）和 $S_{275\text{-}295}$（第 60 至 90 天，$p < 0.05$）均在一定程度上呈现出减小的趋势。随着水稻的生长，稻田土壤 DOM 中类蛋白物质的含量（Peak B 和 Peak T）以及自养生产力（BIX）不断增加（$p < 0.05$）；与之对应的是稻田土壤 DOM 中腐殖质的不断消耗，表现为腐殖化程度的降低（HIX，$p < 0.05$）。

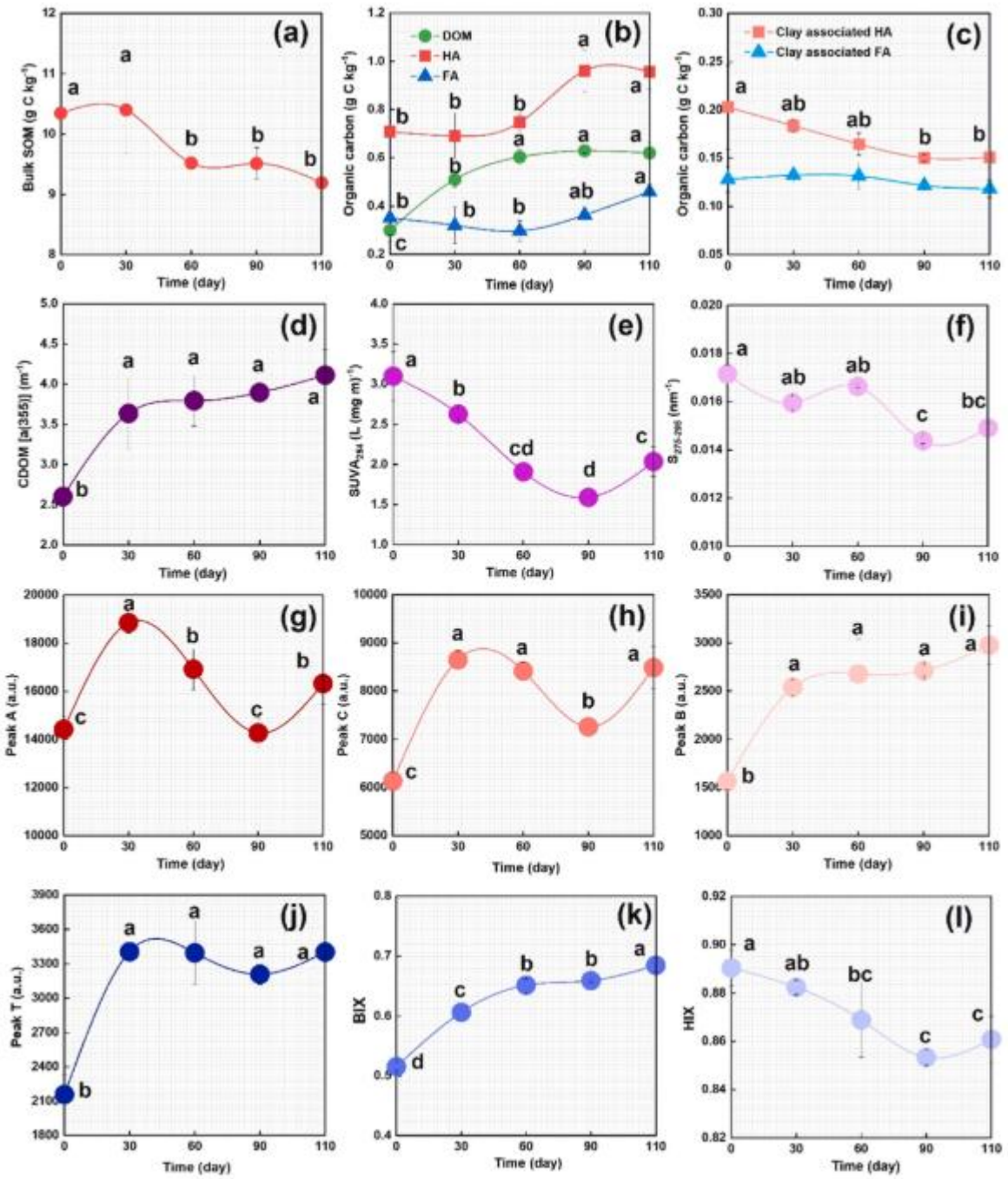

注：（a）土壤总有机质含量；（b）土壤溶解性有机质、腐殖酸和富里酸含量；（c）黏土矿物结合态腐殖酸与富里酸含量；图（d）至（l）均为土壤 DOM 的吸收与荧光光谱特征。其中，（d）为 CDOM 相对含量；（e）为 $SUVA_{254}$ 值；（f）为 $S_{275\text{-}295}$ 值；（g）为荧光峰 A 的强度；（h）荧光峰 C 的强度；（i）荧光峰 B 的强度；（j）荧光峰 T 的强度；（k）自生源指数 BIX；（l）腐殖化指数 HIX。不同小写字母表明在水稻生长周期内存在显著差异 ($p < 0.05$)

图 4-1 水稻生长期不同组分土壤有机质含量与土壤溶解性有机质光谱特征

除有机质以外，土壤中的铁/锰氧化物同样控制着 Hg 在环境中的归趋。在自然环境中，铁氧化物和锰氧化物通常相互依存，例如铁锰结核，且二者的环境行为较为相

似（Tessier et al., 1979; Liu C et al., 2021）。在本研究中，稻田土壤 TFe 含量（31.2 ± 0.8（g kg^{-1}））远高于 TMn 的含量（0.42 ± 0.01（g kg^{-1}））（图 4-2）；因此，本研究以 Fe 为例，研究不同形态 Fe 氧化物的分布与变化趋势，以反映铁/锰氧化物对 Hg 地球化学形态分馏的影响。

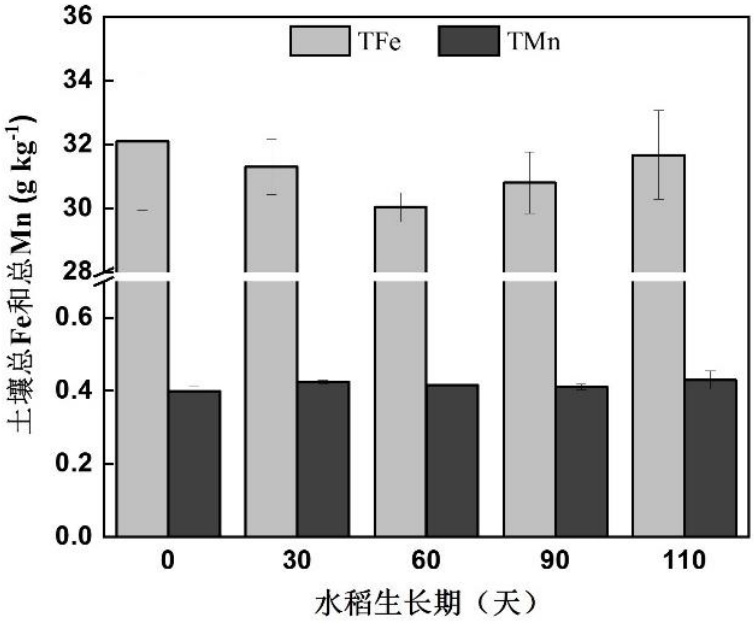

图 4-2 水稻生长期土壤总铁与总锰的含量

如表 4-1 所示，在水稻生长过程中，土壤活性 Fe（Fe_{HR}）含量以及 Fe_{HR} 占 TFe 的比例均保持相对稳定。在不同 Fe_{HR} 形态中，Fe_{ox2} 含量最高，其次分别为 Fe_{mag}、Fe_{ox1}、Fe_{py}、Fe_{carb}，而 Fe_{exch} 含量最低（$p < 0.05$）。尽管 Fe_{HR} 的总量相对稳定，但不同 Fe_{HR} 形态之间则表现出此消彼长的动态变化，例如在水稻生长过程中，土壤 Fe_{carb}、Fe_{ox1} 和 Fe_{py} 显著增加，而 Fe_{ox2} 和 Fe_{mag} 则显著降低（表 4-1），表现出 Fe_{ox2} 和 Fe_{mag} 向 Fe_{carb}、Fe_{ox1} 和 Fe_{py} 的转化。这说明，稻田土壤淹水期间，结晶型较好的铁氧化物向弱结晶型或者无定形态铁氧化物以及硫铁化物的转化过程。对土壤样品进行 X 射线衍射分析，未检出铁氧化物晶体结构，进一步说明结晶型铁氧化物在淹水的稻田土壤中向弱结晶型，甚至无定形铁氧化物的转化（Ratié et al., 2019; Bishop et al., 2020）。

表 4-1 水稻生长期稻田土壤中不同形态铁的含量

水稻生长期（天）	Fe_{HR} (g kg^{-1})	Fe_{exch} (mg kg^{-1})	Fe_{carb} (g kg^{-1})	Fe_{ox1} (g kg^{-1})	Fe_{ox2} (g kg^{-1})	Fe_{mag} (g kg^{-1})	Fe_{py} (g kg^{-1})
0	11.2 ±0.2ab	1.29 ±0.5	0.005 ±0.00c	0.37 ±0.03d	8.43 ±0.3a	1.77 ±0.1ab	0.59 ±0.03b
30	10.8 ±0.2b	1.20 ±0.2	0.067 ±0.01c	0.87 ±0.05c	7.34 ±0.4b	1.95 ±0.3a	0.60 ±0.04b
60	11.1 ±0.3ab	1.31 ±0.2	0.23 ±0.02b	1.19 ±0.06b	7.13 ±0.4bc	1.84 ±0.09ab	0.75 ±0.1ab
90	11.2 ±0.05a	1.37 ±0.2	0.45 ±0.04a	1.42 ±0.01a	7.01 ±0.03bc	1.65 ±0.02b	0.70 ±0.09ab
110	11.0 ±0.2ab	1.28 ±0.5	0.49 ±0.10a	1.45 ±0.05a	6.56 ±0.4c	1.66 ±0.1b	0.87 ±0.2a

注：活性 Fe（Fe_{HR}）；溶解与可交换态 Fe（Fe_{exch}）；碳酸盐结合态 Fe（Fe_{carb}）；易还原态 Fe（Fe_{ox1}）；可还原态 Fe（Fe_{ox2}）；磁铁矿 Fe（Fe_{mag}）；黄铁矿 Fe（Fe_{py}）。其中 Fe_{exch}、Fe_{carb}、Fe_{ox1}、Fe_{ox2}、Fe_{mag} 和 Fe_{py} 之和为活性 Fe（Fe_{HR}）。不同小写字母表明在水稻生长周期内存在显著差异 ($p < 0.05$)

4.4 稻田土壤中“新”汞与“老”汞的含量与赋存形态

稻田土壤中“新”Hg（$T^{200}Hg$）与“老”Hg（背景 THg）的总量在水稻生长期间无明显波动，其中 $T^{200}Hg$ 的含量为 104.04 ± 2.91（ng g^{-1}）至 120.65 ± 8.56（ng g^{-1}）；背景 THg 含量为 73.07 ± 4.29（ng g^{-1}）至 95.04 ± 17.12（ng g^{-1}）（图 4-3）。值得注意的是，本研究中用于模拟“新”Hg 的同位素示踪剂浓度与背景 Hg 含量接近，表明添加的汞同位素示踪剂能够有效反映真实稻田土壤中 Hg 环境行为（Hintelmann et al., 2002; Branfireun et al., 2005; Oswald et al., 2014）。“新”Hg 甲基化产生的甲基汞（$Me^{200}Hg$）含量范围分别为 0.019 ± 0.002（ng g^{-1}）至 0.49 ± 0.10（ng g^{-1}）；“老”Hg 产生的 MeHg（背景 MeHg）或土壤中原本存在的 MeHg 含量为 0.30 ± 0.07（ng g^{-1}）至 0.48 ± 0.05（ng g^{-1}）之间（图 4-3）。

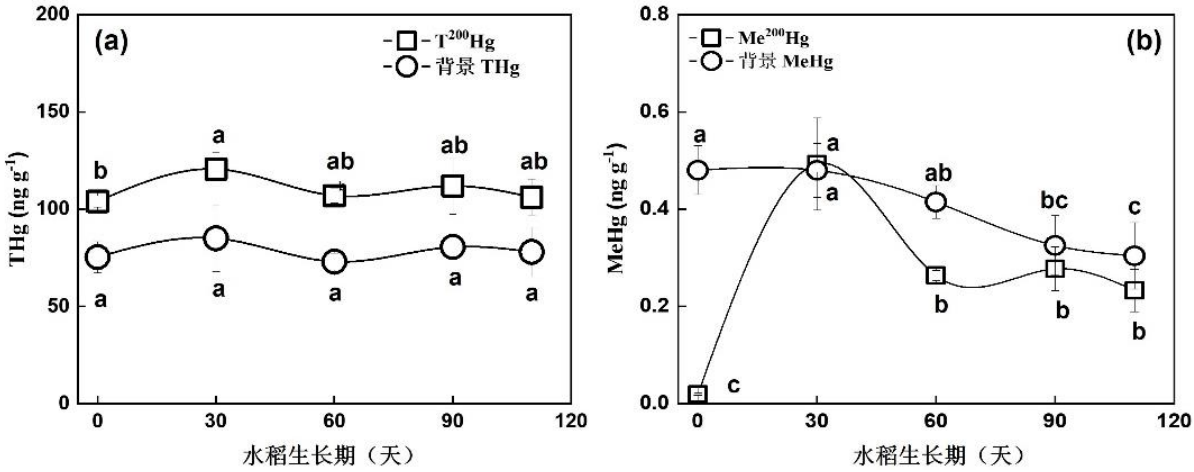

注：（a）THg 含量；（b）MeHg 含量。不同小写字母表明在水稻生长周期内存在显著差异 ($p < 0.05$)

图 4-3 水稻生长期内稻田土壤 THg 和 MeHg 的含量

在本研究中，“新”Hg 与“老”Hg 的总量（即 $T^{200}Hg$ 和背景 THg）在水稻生长期间无明显波动，其中 $T^{200}Hg$ 含量在 104.04 ± 2.91（ng g^{-1}）至 120.65 ± 8.56（ng g^{-1}）之间，背景 THg 含量在 73.07 ± 4.29（ng g^{-1}）至 95.04 ± 17.12（ng g^{-1}）之间（图 4-3）。值得注意的是，本研究中用于模拟“新”Hg 的同位素示踪剂浓度与背景 Hg 含量接近，表明添加的示踪剂能够有效反映真实稻田土壤中 Hg 环境行为（Hintelmann et al., 2002; Branfireun et al., 2005; Oswald et al., 2014）。“新”Hg 产生的 MeHg（$Me^{200}Hg$）与“老”Hg 产生的 MeHg 或土壤原有的 MeHg（背景 MeHg）含量范围分别为 0.019 ±

0.002（ng g^{-1}）至 0.49 ± 0.10（ng g^{-1}）和 0.30 ± 0.07（ng g^{-1}）至 0.48 ± 0.05（ng g^{-1}）之间（图 4-3）。

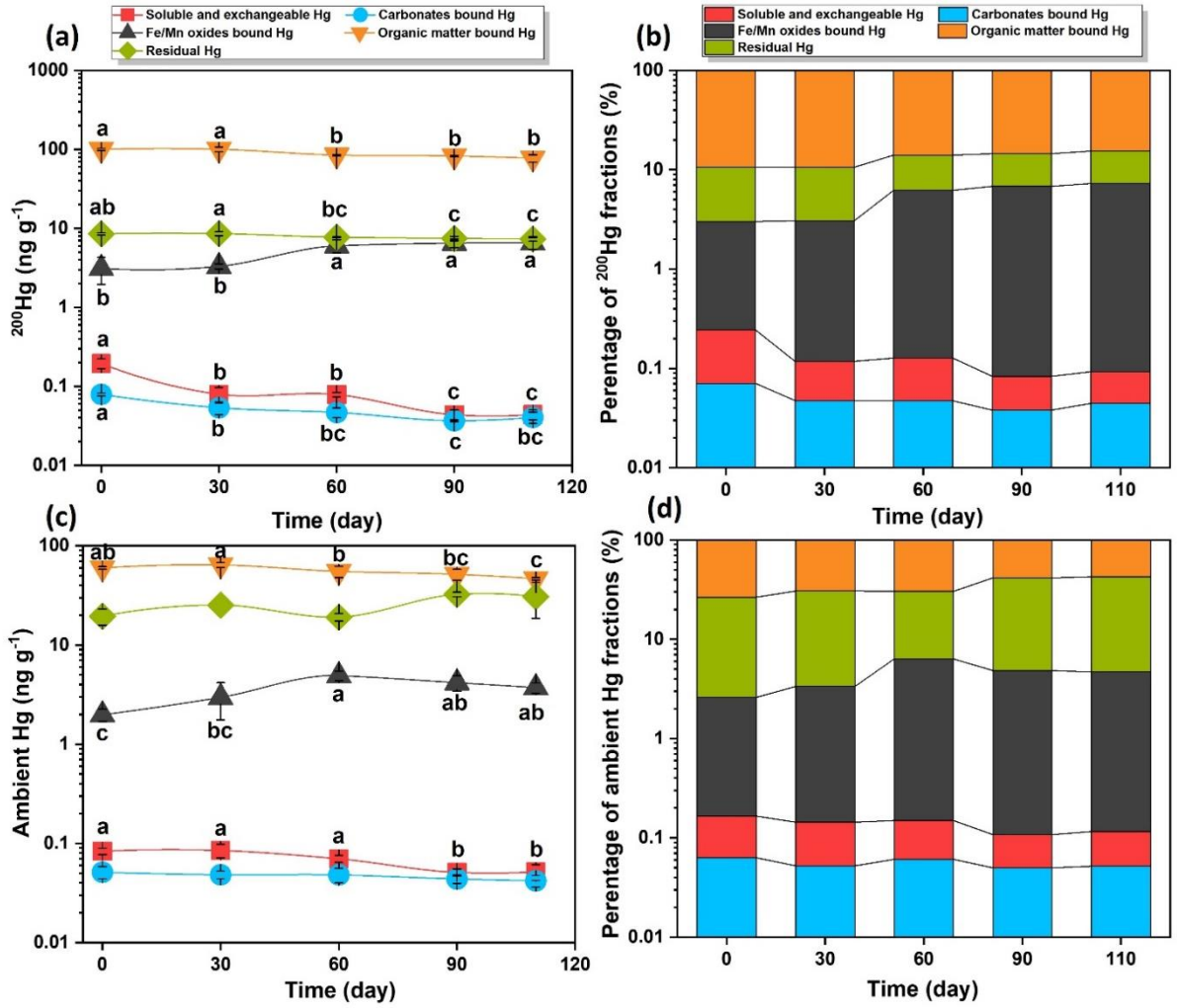

注：（a）不同地球化学形态 ^{200}Hg 的含量；（b）不同地球化学形态 ^{200}Hg 的占比；（c）不同地球化学形态背景 Hg 的含量；（d）不同地球化学形态背景 Hg 的占比。不同小写字母表明在水稻生长周期内存在显著差异 ($p < 0.05$)；无字母表示无显著性差异。

图 4-4 不同地球化学形态 Hg（^{200}Hg 和背景 Hg）的含量与占比

自“新”Hg 进入稻田土壤后（即添加 ^{200}Hg 后），绝大部分“新”Hg 与土壤有机质结合在一起，形成有机质结合态 ^{200}Hg，其占 T^{200}Hg 的 84.6~89.4 %；其次为残渣态 ^{200}Hg（7.6~8.1 %）、铁/锰氧化物结合态 ^{200}Hg（2.8~7.2 %）。溶解与可交换态 ^{200}Hg 和碳酸盐结合态 ^{200}Hg 所占的比例较小，仅为 0.05~0.17 %和 0.04~0.07%（图 4-4）。“老”Hg 在不同地球化学形态中的分布与“新”Hg 类似，但残渣态 Hg 占比为 23.9~37.9 %，显著高于“新”Hg 中残渣态 ^{200}Hg 的比例（$p < 0.01$）。此外，背景 Hg 中铁/锰氧化物结合态 Hg（2.4~6.2 %）和有机质结合态 Hg（57.4~73.5 %）的占比也均低于“新”Hg

（$p < 0.01$）。

在水稻生长期间，溶解与可交换态 ^{200}Hg、碳酸盐结合态 ^{200}Hg、有机质结合态 ^{200}Hg 以及残渣态 ^{200}Hg 的含量呈现出降低的趋势（$p < 0.05$）；而铁/锰氧化物结合态 ^{200}Hg 在第 30 至 60 天时表现出显著的增加，从 3.30 ± 0.24（ng g^{-1}）增至 6.01 ± 1.13（ng g^{-1}）（$p < 0.05$，图 4-4）。

4.5 稻田土壤中“新”汞在不同地球化学形态间的分配

土壤有机质不仅是“老”Hg，也是“新”Hg 最大的“汇”，且有机结合态 Hg 为稻田土壤中新沉降 Hg 最为主要的赋存形态。这一结果与贵州万山土法炼汞区稻田土壤类似，其有机质结合态 Hg 占总汞含量的 62 %（赵蕾，2016）。在贵州省贵阳市花溪区未受汞污染的背景区稻田土壤中，有机质结合态 Hg 占 THg 的比例可达 87.8 %（陆本琦等，2021）。可见，不同汞污染程度稻田土壤中，有机质结合态 Hg 均为 Hg 主要的地球化学形态，其潜在的原因主要有以下两个方面：（1）土壤有机质自身与 Hg^{2+}的结合能力较强；（2）土壤有机质通常与土壤颗粒物或土壤矿物形成有机无机复合体（Lalonde et al., 2012; Riedel et al., 2013），而较土壤矿物或颗粒物自身而言，这类有机无机复合体能够显著地增其对重金属的吸附与固定能力（Zhang et al., 2019），尤其是当复合体中含有带有机硫基团时（如巯基）（Skyllberg et al., 2006; Skyllberg, 2008）。另外，由于还原性硫的存在，新沉降 Hg 在进入稻田土壤后，通常会率先形成纳米颗粒态 HgS 或胶体态 HgS（Manceau et al., 2018），而土壤有机质对于这类亚稳态 Hg（纳米颗粒态 HgS 或胶体态 HgS）的稳定化起重要作用。有研究发现，在 DOM 存在的还原环境中，Hg 能够以 Hg-S-DOM 的三元复合体系的形式存在，且该复合体系显著地减缓了多核簇 HgS 结构的生长（Gerbig et al., 2011; Graham et al., 2012）。

传统认为，汞矿区残渣态 Hg 主要为 HgS（Yin et al., 2016），因此稻田土壤中淹水时硫酸盐还原产生的硫化物（HS^-）能够与新沉降的 Hg 形成稳定的 HgS 沉淀，从而不断增加残渣态 Hg 的含量。然而，本研究中残渣态 ^{200}Hg 仅占 $T^{200}Hg$ 的 7.6~8.1 %，这进一步表明新沉降 Hg 形成残渣态 HgS 的速率低于其与土壤有机质结合的速率，而有机质的存在正是 HgS 沉淀形成过程中的重要限速步骤（Gerbig et al., 2011; Graham et al., 2012; Hsu-Kim et al., 2013）。此外，由于本研究中 TS 的含量显著低于 SOM，且稻田土壤处于氧化还原环境更替的条件下，使得仅有少量的“新”Hg 转化成为残渣态 ^{200}Hg。

当“新”沉降的 Hg 进入稳定的土壤矿物晶格后（如硅酸盐晶格），这部分汞也会转变为残渣态 Hg（Tessier et al., 1979）。本研究由于较高的有机质结合态 ^{200}Hg 含量和较低的残渣态 ^{200}Hg 含量，说明新沉降 Hg 进入或者被置换进入矿物晶格的速率仍然低于其与有机质分子结合的速率。

除有机质结合态 Hg 和残渣态 Hg 以外，铁/锰氧化物结合态 Hg 是本研究中排列第三的“新”Hg 赋存形态。之前已有大量研究表明，土壤中的铁/锰氧化物对 Hg 具有较强的吸附能力（Bonnissel-Gissinger et al., 1999; Feyte et al., 2010）。然而，由于氧化还原条件变化所导致的铁/锰氧化物自身形态的改变，对铁/锰氧化物结合的“新”Hg 量表现出不断波动的趋势。由于新沉降 Hg 的形态通常以 Hg^{2+}为主，且用于模拟新沉降 Hg 的示踪剂是溶解态的 Hg^{2+}。因此，溶解与可交换态 Hg 应该为试验初期稻田土壤中“新”Hg 的主要赋存形态。然而，溶解与可交换态 ^{200}Hg 仅占 T^{200}Hg 的 0.05~0.17 %，表明稻田土壤中存在大量的 Hg 强结合位点（如表面络合位点），新沉降 Hg 在进入稻田土壤后会迅速与这类位点结合并被固定，并且在当前实验条件下，这类强结合位点尚未达到饱和。

4.6 稻田土壤中“新”汞在不同地球化学形态间的再分布

在水稻生长过程中，不同形态 ^{200}Hg 含量的动态变化体现了“新”Hg 在不同地球化学形态之间的再分布过程。本研究中，“新”Hg 在不同地球化学形态之间的再分布过程表现为从溶解与可交换态 ^{200}Hg、碳酸盐结合态 ^{200}Hg、有机质结合态 ^{200}Hg 和残渣态 ^{200}Hg 向铁/锰氧化物结合态 ^{200}Hg 的转化（图 4-4）。其中，溶解与可交换态 ^{200}Hg 和碳酸盐结合态 ^{200}Hg 的再分布过程主要发生于水稻种植初期，表明土壤对于这类活性较高的“新”Hg形态具有快速的固定作用。这类反应是由于固相或者胶体体系存在时，溶解态 ^{200}Hg 不稳定（Skyllberg et al., 2021），其可以在化学平衡热力学的作用下迅速达到平衡。

铁/锰氧化物结合态 ^{200}Hg、有机质结合态 ^{200}Hg 和残渣态 ^{200}Hg 的再分布则主要发生于水稻生长 30 天以后，表明即使溶解态 ^{200}Hg 能够迅速分配至固相体系中，但不同固相体系之间的再分布过程往往需要一定的时间。这一过程与热力学平衡不同，是受到氧化还原环境改变的驱动而进行的再平衡过程。在生物地球化学过程复杂多变的稻田土壤中（Kögel-Knabner et al., 2010），氧化还原环境改变驱动的化学再平衡过程是

“新”Hg在不同地球化学形态之间再分布的主导因素。例如，而土壤总有机质的降解（SOM 的降低）和 DOM 的增加（图 4-1）均与有机质结合态 ^{200}Hg 含量的降低存在耦合关系，表明在水稻生长过程中，有机质自身组分的改变会重新释放一部分与有机质结合的“新”Hg。另外，通过相关性分析发现，有机质结合态 ^{200}Hg 与 DOM 含量（Spearman's $r = -0.68$, $p < 0.01$）以及土壤 DOM 中内生源相关的信号（Peak B, Spearman's $r = -0.71$, $p < 0.01$; BIX, Spearman's $r = -0.82$, $p < 0.01$）显著负相关。上述共变化关系进一步说明，在水稻生长过程中，土壤有机质的微生物降解作用不可忽视（Liu, J. et al., 2021b），且该过程会释放一部分原本与有机质结合的“新”Hg。此外，水稻根际圈能够分泌大量的根际分泌物，这类根际分泌物通常为分子量较低的有机酸或者糖类物质。相比木质素以及一些大分子量或者芳香类化合物，这类小分子有机质更易于被微生物利用，因此可能对土壤原有的有机质矿化产生“激发效应”，从而进一步促进原本较为惰性的有机质被分解，从而进一步释放与有机质结合态的 Hg。有学者发现冻土退化引起的土壤有机质降解使得冻土区域重新成为 Hg 的“源”并产生潜在的 Hg 流失/释放风险（Mu et al., 2020）。

在本研究中，由于易还原态 Fe 与铁/锰氧化物结合态 ^{200}Hg 的提取剂一致，均为盐酸羟胺；因此，易还原态 Fe 含量的增加（表 4-1）以及铁/锰氧化物结合态 ^{200}Hg 含量的增加（图 4-4），表明更多的“新”Hg 重新分布至弱结晶态或者无定形态铁氧化物中，使得铁/锰氧化物在“新”Hg 的再分布过程中表现为“汇”的作用。尤其是在水稻生长期间，稻田土壤中 Fe 形态的转化规律为从结晶态 Fe 向弱结晶态或无定形态 Fe 的转化（Kappler et al., 2021; Huang et al., 2021）。有研究发现，弱结晶态或者无定形态 Fe 氧化物较结晶态 Fe 氧化物具有更大的比表面积，能够共沉淀或者吸附更多的“新”Hg（Tiffreau et al., 1995; Bao et al., 2021）。同时，弱结晶态或者无定形态 Fe 氧化物也是土壤中 DOM 的“汇”；反之，这类 Fe 氧化物通过与 DOM 形成 Fe-OM 复合体系又能够增强其自身的稳定性（Aiken et al., 2011；Lv et al., 2016）。目前，针对 Fe-OM 复合体系已经有学者展开了大量的研究（Wang et al., 2017; Chen et al., 2020; Zeng et al., 2020），然而其对于 Hg 环境行为的影响认识还比较有限，特别是氧化还原交替环境中 Fe-OM 复合体系对 Hg 的迁移转换以及生物有效性的影响还不明确，值得进一步研究（朱爱玲等，2019）。

残渣态 ^{200}Hg 在“新”Hg 的再分布过程中含量下降，表现出向其他形态的转化过

程。Li 等人（2022）报道，α-HgS 的溶解增加了 Hg 甲基化过程中生物有效性；此外，Liu 等人（2019）与 Wang 等人（2021）在间歇性淹水土壤中与泥炭土中发现，硫化物与单质硫形成的多硫化物能够与 HgS 中的 Hg 形成 Hg-多硫化物络合物，从而潜在地增加 HgS 的溶解度。因此，残渣态 Hg 中新生成 HgS 的再溶解可能是稻田土壤中残渣态 ^{200}Hg 下降的原因。

4.7 地球化学因子对“新”汞地球化学形态分馏的影响

为进一步揭示影响“新”Hg地球化学形态分馏的地化因子，本研究采用相关性分析结合线性回归分析，反映“新”Hg在不同地球化学形态中的赋存与地化因子的共变化关系（图 4-5）；采用偏最小二乘路径模型（PLS-PM），分析地化因子与不同地球化学形态“新”汞的因果关系（图 4-6）。

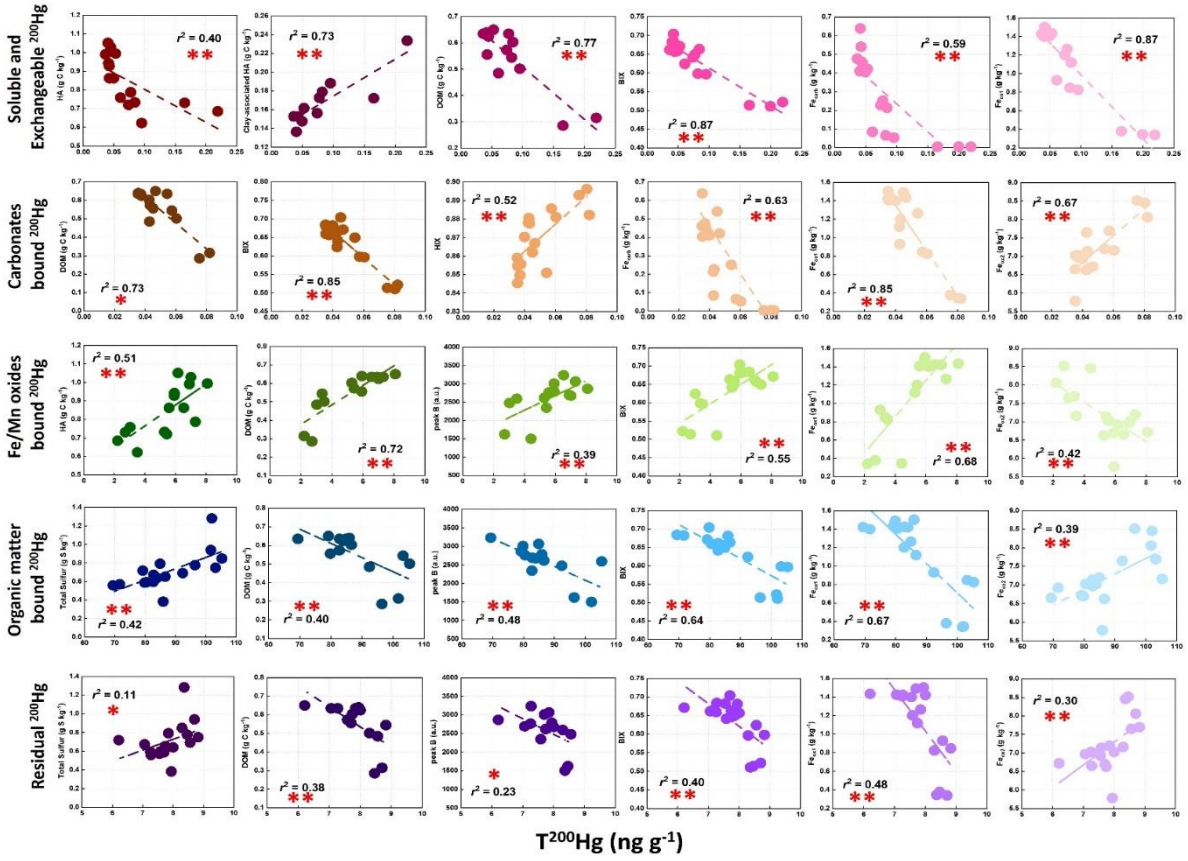

注：“*”与“**”分别表示显著（$p < 0.05$）与极显著（$p < 0.01$）相关。r^2 为决定线性回归的决定系数。

图 4-5 不同地球化学形态 ^{200}Hg 含量与不同地化因子的相关性

通过相关性分析发现，赋存在不同形态中的“新”Hg 含量与 DOM、a(355)、BIX、HIX、Fe_{carb}、Fe_{ox1} 和 Fe_{ox2} 均存在显著的相关关系（图 4-5），表明土壤 DOM 的含量与

结构特征以及铁氧化物对新沉降 Hg 在稻田土壤中的地球化学形态分馏存在显著影响。具体来说，铁/锰氧化物结合态 ^{200}Hg 与土壤 HA、DOM、类蛋白荧光峰（Peak B）以及自生源指数（BIX）显著正相关，表明铁氧化物与内源产生的有机质共同控制着新沉降 Hg 在稻田土壤中的分配与再分布过程。同时，有机质结合态 ^{200}Hg 与上述地化因子指标显著负相关，表明在水稻生长过程中，稻田土壤中存在弱结晶态或者无定形态铁氧化物-DOM 复合体。进一步结合有机质结合态 ^{200}Hg 以及铁/锰氧化物结合态 ^{200}Hg 的变化（图 4-4），我们推断一部分与有机质结合的“新”Hg 被释放后，重新被弱结晶态或者无定形态铁氧化物-DOM 复合体捕获，形成 Hg-Fe-DOM 的三元复合体系。有研究发现，As（Aftabtalab et al., 2022）、Cd（Du et al., 2018）和 Cr（Liao et al., 2020; Xia et al., 2020）也能够与 Fe-DOM 形成类似的三元复合体系。对于溶解与可交换态 ^{200}Hg 以及碳酸盐结合态 ^{200}Hg 而言，稻田土壤中的铁氧化物与有机质是这部分 Hg 的“汇”，其能够有效降低这部分 Hg 的活性。另外，溶解与可交换态 ^{200}Hg 以及碳酸盐结合态 ^{200}Hg 均与土壤 DOM 的 BIX 显著负相关，表明内源 DOM 的增加显著地降低了这部分活性 Hg 库的量。

除探讨“新”Hg形态与地化因子之间的共变化关系外，本研究还利用偏最小二乘路径模型（PLS-PM），分析地化因子与“新”Hg 形态的因果关系。PLS-PM 分析共设置四个潜变量，分别为（1）土壤化学性质，包含指标为土壤 TS、TFe、TMn、TN、pH 和 C/N；（2）土壤总有机质，包含指标为 SOM、HA、FA、C-FA 和 C-HA；（3）土壤 DOM，包含指标为 DOM 浓度、$SUVA_{254}$、$S_{275–295}$、Peak A、Peak B、BIX 和 HIX；（4）铁形态，包含指标为 Fe_{exch}、Fe_{carb}、Fe_{ox1}、Fe_{ox2} 和 Fe_{mag}。整个模型的解释度（GOF）在 0.57 至 0.60 之间，表明本研究所用模型能够较好地反映变量之间的因果关系。由图 4-6 所示，潜变量 DOM（路径系数-0.42）和铁形态（路径系数-0.39）是影响溶解与可交换 ^{200}Hg 的主要因素，而潜变量 DOM（路径系数-0.50）是影响碳酸盐结合态 ^{200}Hg 的主要因素。对于铁/锰氧化物结合态 ^{200}Hg 而言，潜变量 DOM 是最为重要的影响因素，路径系数达 0.86，表明 Fe-DOM 相互作用促进了“新”Hg 在铁/锰氧化物上的分配。相反的，潜变量铁形态是有机质结合态 ^{200}Hg 的重要影响因素（路径系数-0.43），表明土壤有机质与铁氧化物对新沉降 Hg 的竞争结合。一般来说，自然环境中有机质上的羧基或者酚羟基能够与铁氧化物上的羟基进行结合（Kleber et al., 2015; Bao et al., 2021）。因此，“新”Hg 与 Fe-OM 体系的结合存在两种方式：（1）“新”Hg 将铁

氧化物与有机质分子桥连在一起，形成 Fe-Hg-OM 复合物；（2）“新”Hg 与 Fe-OM 复合体结合，形成 Hg-OM-Fe 复合体系（Bao et al., 2021）。上述因果关系分析进一步表明，稻田土壤中新沉降的 Hg 与铁氧化物和 DOM 形成了三元复合体系对于新沉降汞的地球化学形态分馏扮演了重要的角色。

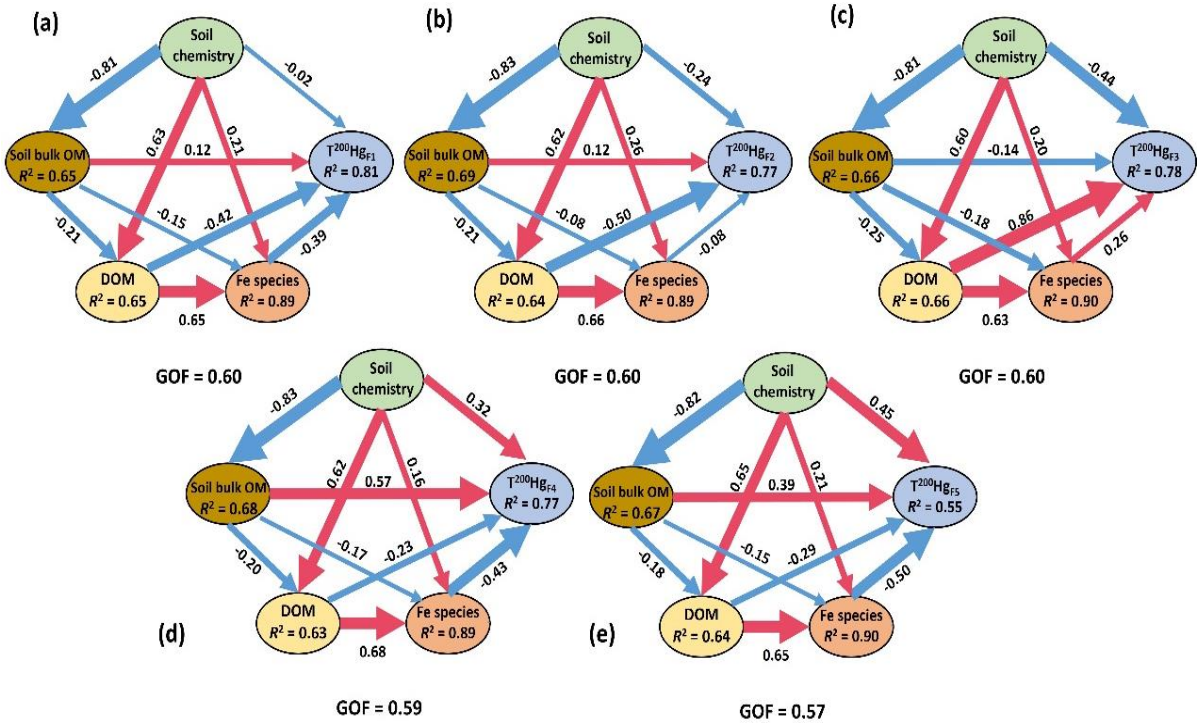

注：$^{200}Hg_{F1}$ 为溶解与可交换态 ^{200}Hg；$^{200}Hg_{F2}$ 为碳酸盐结合态 ^{200}Hg；$^{200}Hg_{F3}$ 为铁/锰氧化物结合态 ^{200}Hg；$^{200}Hg_{F4}$ 为有机质结合态 ^{200}Hg；$^{200}Hg_{F5}$ 为残渣态 ^{200}Hg。箭头上的数字为标准化的路径系数；R^2 为对应潜变量的解释度；GOF 为模型解释度。

图 4-6 偏最小二乘路径模型

4.8 环境启示

新沉降 Hg 在稻田土壤中的地球化学形态分馏过程决定了新沉降 Hg 的生物有效性，并进一步影响了新沉降 Hg 的环境风险。有学者通过对稻田土壤中“新”Cd 的环境行为研究发现，新进入稻田土壤的 Cd 能够迅速老化，表现为残渣态 Cd 的含量显著增加（Dong et al., 2021a, 2021b）。然而，本研究并未发现与之类似的老化过程，表明新沉降的 Hg 在进入稻田土壤后，仍具有较高的活性，这正好解释了高 Hg 沉降量区稻田土壤中即使土壤 THg 含量较低，也具有较高的 MeHg 含量（Meng et al., 2010, 2011; Zhao et al., 2016a）。另外，有机质结合态 ^{200}Hg 与 $Me^{200}Hg$ 含量显著相关，这暗示着除传统认为的溶解与可交换态 Hg 能够参与甲基化反应外，有机质结合态 Hg 可能也能够被甲

基化。因此，在评估大气沉降 Hg 的环境风险时，除溶解态 Hg 以外，其他形态的 Hg 也应该考虑在内。

4.9 本章小结

本部分内容采用单一富集稳定汞同位素示踪技术，明确了新沉降汞在进入稻田土壤后的在不同地球化学形态之间的分配及再分布过程。在稻田土壤中，“新”汞主要与土壤有机质结合在一起，以有机质结合态汞的形态存在，其次为残渣态汞、铁/锰氧化物结合态汞、溶解与可交换态汞和碳酸盐结合态汞。在水稻生长过程中，以溶解与可交换态汞、碳酸盐结合态汞、有机质结合态汞和残渣态汞形态存在的“新”汞向铁/锰氧化物结合态汞转化。微生物驱动的土壤有机质矿化作用以及氧化还原条件改变驱动的铁氧化物形态转化共同影响着稻田土壤中“新”汞的地球化学形态分馏。相关性分析与偏最小二乘路径模型分析得出，内源性有机质与弱结晶型或者无定形铁氧化物构成的复合体系控制着稻田土壤中新沉降汞的形态。除传统认为的溶解与可交换态汞外，有机质结合态汞也可能参与甲基化反应，为生物有效态汞。

第 5 章 主要结论

本文报告从铁硫循环的角度出发，通过三个工作探讨稻田生态系统中铁硫循环对汞生物地球化学过程的影响获得如下主要结论

（1）Nano-HgS 和 NOM-Hg(II)是稻田土壤中能够参与甲基化反应的汞形态，而≡FeS-Hg(II)几乎不能被甲基化，并且稻田土壤中新生成的 FeS 可能会显著降低 $Hg(NO_3)_2$ 的生物有效性（图 5-1）。在不同汞浓度梯度的稻田土壤中，汞甲基化率随汞浓度的增加而下降，并且，稻田土壤汞浓度梯度引起的甲基化速率的差异（10^3~10^4 倍）远远大于同一位点间不同汞形态之间的差异（1~5 倍）。此外，我们还发现，除了稻田土壤中汞的来源、土壤理化性质等因素外，不同位点间微生物群落结构及其活性的差异很可能是造成其甲基化速率存在巨大差异的主要原因。

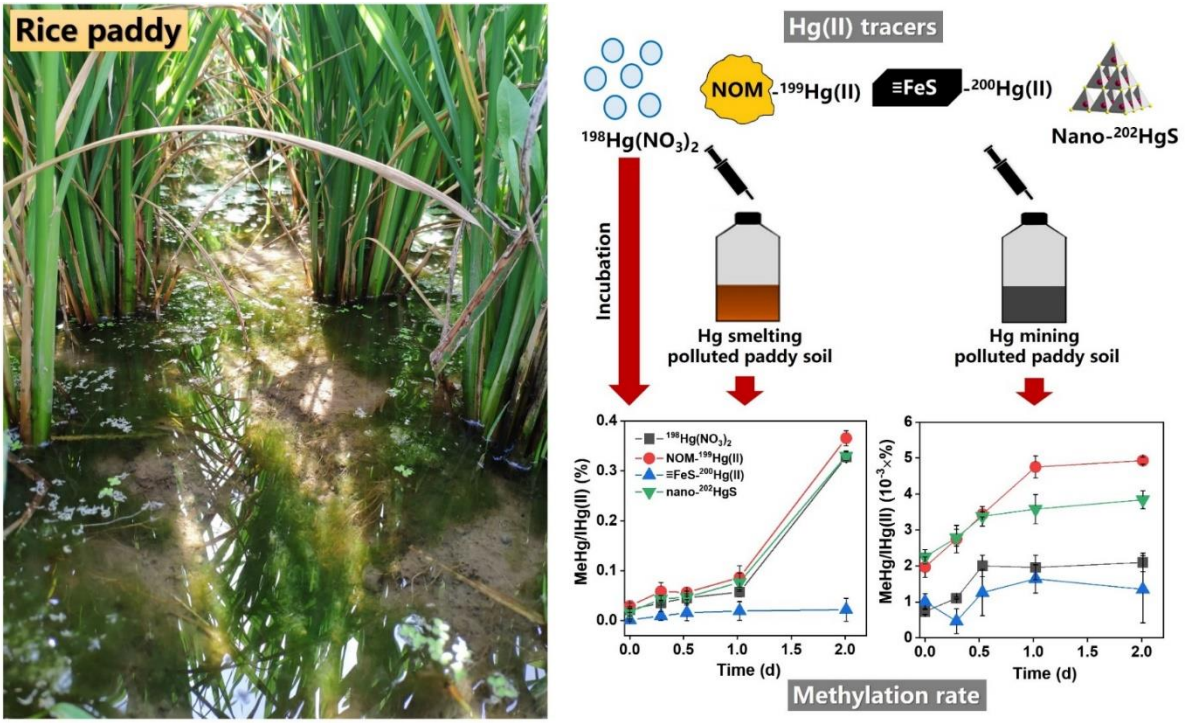

图 5-1 铁硫循环影响稻田土壤中参与甲基化反应的汞形态过程示意图

（2）除常规已知的无机汞甲基化和甲基汞去甲基化过程外，稻田土壤中还存在微生物介导的无机汞暗还原、零价汞的甲基化以及甲基汞的暗还原过程。在淹水的稻田土壤中，不同形态汞（Hg^{II}，MeHg 和 Hg^0）之间的相互转化并非独立过程，而是微生物介导的耦合过程。由于存在无机汞的微生物暗还原以及零价汞的甲基化过程，因此值得进一步关注稻田土壤中汞的氧化还原过程及其对净甲基汞积累的影响。外源硫输入对汞形态转化的影响机制存在两个方面，（1）影响参与汞形态转化的微生物群落结构和（2）影响汞的化学形态。本研究发现，土壤中硫输入主要通过影响微生物群落结构而进一步影响汞形态转化（图 5-2）。

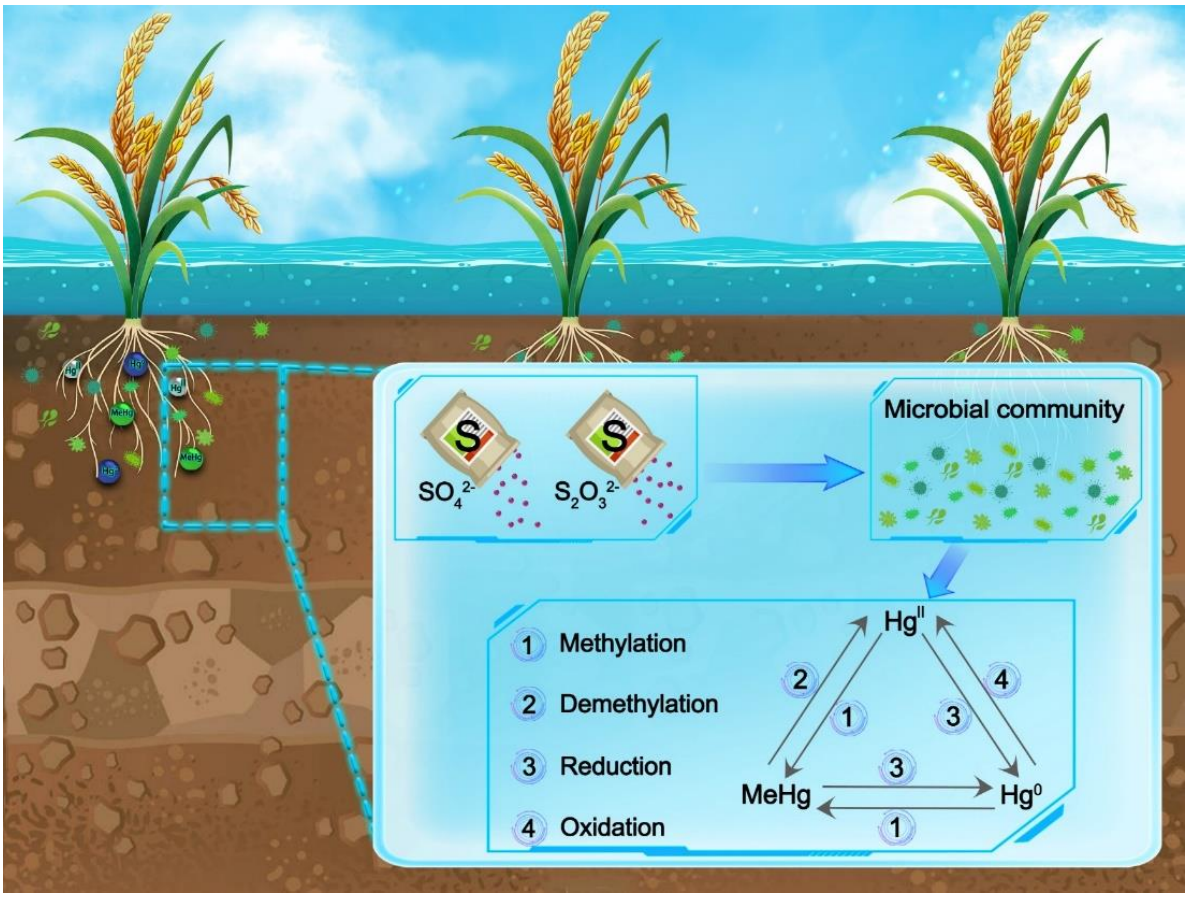

图 5-2 外源硫添加影响稻田土壤中汞形态转化过程示意图

（3）在稻田土壤中，“新”汞主要与土壤有机质结合在一起，以有机质结合态汞的形态存在，其次为残渣态汞、铁/锰氧化物结合态汞、溶解与可交换态汞和碳酸盐结合态汞。在水稻生长过程中，以溶解与可交换态汞、碳酸盐结合态汞、有机质结合态汞和残渣态汞形态存在的“新”汞向铁/锰氧化物结合态汞转化。微生物驱动的土壤有机质矿化作用以及氧化还原条件改变驱动的铁氧化物形态转化共同影响着稻田土壤中“新”汞的地球化学形态分馏，内源性有机质与弱结晶型或者无定形铁氧化物构成的复合体系控制着稻田土壤中新沉降汞的形态（图 5-3）。

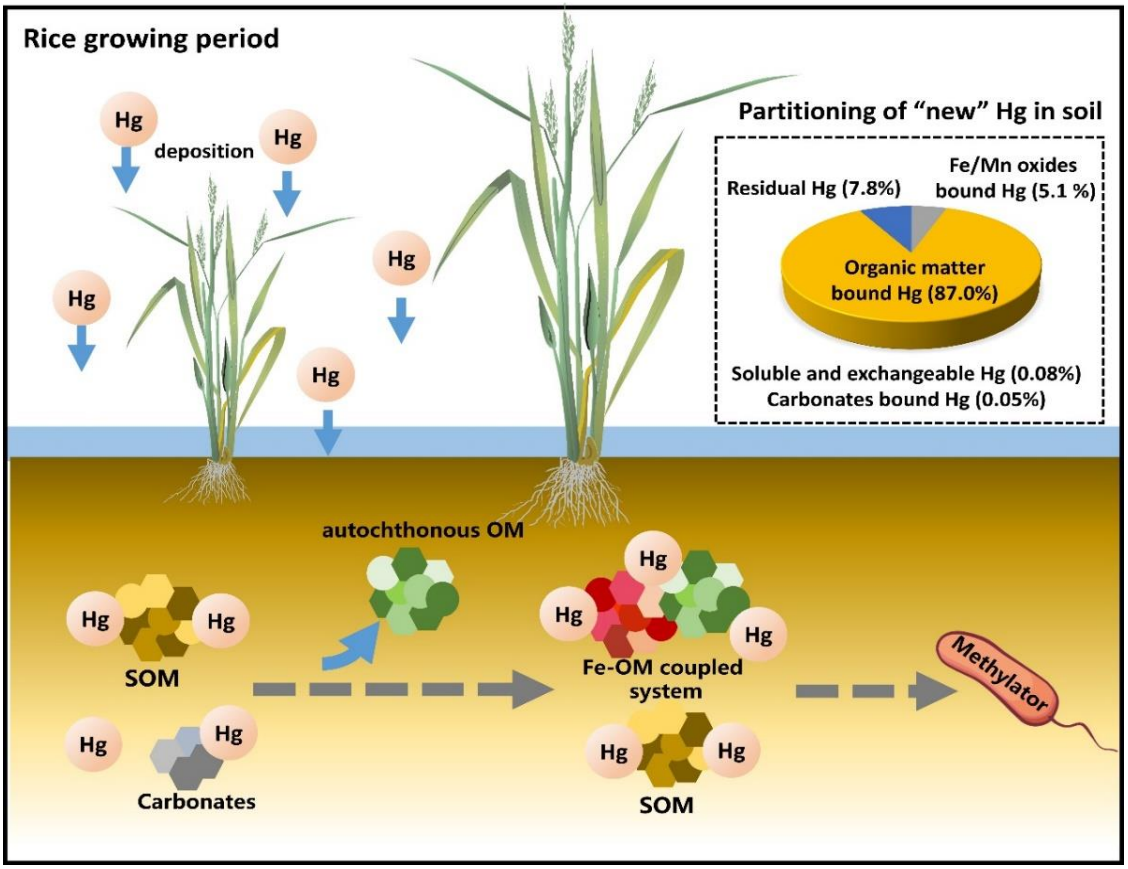

图 5-3 稻田土壤中“新”汞在不同地球化学形态之间的分配及再分布过程示意图

参考文献

冯新斌，仇广乐，付学吾，等，2009. 环境汞污染. 化学进展，21（2/3）：436-457.

冯新斌, 史健波, 李平, 阴永光, 江桂斌, 2020. 我国汞污染研究与履约进展. 中国科学院院刊. 35, 1344－1350.

胡海燕，仇广乐，冯新斌，等，2011. 汞的微生物甲基化研究进展. 生态学杂志，30：874－882.

谷成，钟寰，张慧玲，等，2017. 秸秆还田影响汞污染地区“稻田汞”环境行为的研究进展. 科学通报，62（24）：2717-2723.

凌倩倩，郭瑛瑛，梁勇，等，2020. 硫化汞纳米颗粒的微生物摄入及其在汞甲基化中的作用．环境化学，39(2) : 292-300.

刘金玲，丁振华, 2007. 汞的甲基化研究进展. 地球与环境，35（3）：215-222.

陆本琦，刘江，吕文强，等，2021. 汞矿区稻田土壤汞形态分布特征及对甲基化的影响. 矿物岩石地球化学通报，40（3）：690-698.

孟其义，钱晓莉，陈淼，等，2018. 稻田生态系统汞的生物地球化学研究进展. 生态学杂志，37（5）：1556－1573.

吴丰昌, 王立英, 黎文, 等，2008. 天然有机质及其在地表环境中的重要性. 湖泊科学，20（1）：1－12.

谢周清，孙立广，王新明，程邦波，2004. 北极大气中汞亏损与海冰演变. 极地研究，(3)：221－228

赵蕾，2016. 汞矿区稻田土壤中汞的分布特征及甲基化去甲基化速率研究. 博士学位论文（西南大学）.

朱爱玲，曹丹丹，陈颖，等，2019. 水环境中铁-汞耦合对汞生物地球化学循环的影响研究进展．环境化学，38（7）: 1431-1445.

Aftabtalab A, Rinklebe J, Shaheen SM, et al., 2022. Review on the interactions of arsenic, iron (oxy)(hydr)oxides, and dissolved organic matter in soils, sediments, and groundwater in a ternary system. Chemosphere, 286:131790.

Aiken GR, Hsu-Kim H, Ryan JN, 2011. Influence of dissolved organic matter on the environmental fate of metals, nanoparticles, and colloids. Environmental Science and Technology, 45: 3196–3201.

Ao M, Xu X, Wu Y, et al., 2020. Newly deposited atmospheric mercury in a simulated rice ecosystem in an active mercury mining region: High loading, accumulation, and availability. Chemosphere, 238: 124630.

Ariya PA, Amyot M, Dastoor A, et al., 2015. Mercury physicochemical and biogeochemical transformation in the atmosphere and at atmospheric interfaces: A review and future directions. Chemical Reviews, 115: 3760–3802.

Aslam, M. W.; Meng, B.; Abdelhafiz, M. A.; Liu, J.; Feng, X. Unravelling the Interactive Effect of Soil and Atmospheric Mercury Influencing Mercury Distribution and Accumulation in the Soil-Rice System. Sci. Total Environ. 2022, 803, 149967

Barkay T, Gillman M, Turner R, 1997. Effects of dissolved organic carbon and salinity on bioavailability of mercury. Applied and Environmental Microbiology, 63: 4267−4271

Bao Y, Bolan NS, Lai J, et al., 2021. Interactions between organic matter and Fe (hydr)oxides and their influences on immobilization and remobilization of metal(loid)s: A review.

Critical Reviews in Environmental Science and Technology.

Barkay, T.; Gu, B. Demethylation-The Other Side of the Mercury Methylation Coin: A Critical Review. ACS Environ. Au 2022, 2 (2), 77–97.

Begley,T. P.; Walts,A.E.; Walsh, C. T. Bacterial organomercurial lyase-overproduction, isolation, and characterization. Biochemistry 1986, 25 (22), 7186−7192.

Bishop ME, Dong H, Glasser P, et al., 2020. Microbially mediated iron redox cycling of subsurface sediments from Hanford Site, Washington State, USA. Chemical Geology, 546: 119643.

Biswas A, Brooks SC, Miller CL, et al., 2011. Bacterial growth phase influences methylmercury production by the sulfate-reducing bacterium Desulfovibrio Desulfuricans Nd132. Science of the Total Environment, 409: 3943–3948.

Blanchfield PJ, Rudd JWM, Hrenchuk LE, et al., 2021. Experimental evidence for recovery of mercury-contaminated fish populations. Nature, 601: 74–78.

Blum, J.D.; Bergquist, B.A. Reporting of variations in the natural isotopic composition of mercury. Anal. Bioanal. Chem. 2007, 388, 353–359

Bone, S.E., Bargar, J.R., Sposito, G., 2014. Mackinawite (FeS) reduces mercury(II) under sulfidic conditions. Environ. Sci. Technol. 48, 10681–10689.

Bonnissel-Gissinger P, Alnot M, Lickes JP, et al., 1999. Modeling the adsorption of mercury(II) on (hydr)oxides II: α-FeOOH (goethite) and amorphous silica. Journal of Colloid and Interface Science, 215: 313–322.

Bower, J., Savage, K.S., Weinman, B., Barnett, M.O., Hamilton, W.P., Harper, W.F., 2008. Immobilization of mercury by pyrite (FeS_2). Environ. Pollut. 156, 504–514.

Branfireun BA, Krabbenhoft DP, Hintelmann H, et al., 2005. Speciation and transport of newly deposited mercury in a boreal forest wetland: A stable mercury isotope approach. Water Resources Research, 41: 1–11.

Bravo AG, Cosio C, 2020. Biotic formation of methylmercury: A bio-physico-chemical conundrum. Limnology and Oceanography, 65: 1010–1027.

Bravo, A. G.; Bouchet, S.; Tolu, J.; Björn, E.; Mateos-Rivera, A.; Bertilsson, S. Molecular Composition of Organic Matter Controls Methylmercury Formation in Boreal Lakes. Nat. Commun. 2017, 8, 14255

Bravo, A. G.; Zopfi, J.; Buck, M.; Xu, J.; Bertilsson, S.; Schaefer, J. K.; Poté, J.; Cosio, C. Geobacteraceae Are Important Members of Mercury-Methylating Microbial Communities of Sediments Impacted by Waste Water Releases. ISME J. 2018, 12 (3), 802–812.

Carter MR, Gregorich EG, 2007. Soil Sampling and Methods of Analysis. CRC Press, Boca Raton, FL

Celo, V., Lean, D.R.S., Scott, S.L., 2006. Abiotic methylation of mercury in the aquatic environment. Science of the Total Environment, 368(1), 126–137

Chen C, Hall SJ, Thompson A, 2020. Iron-mediated organic matter decomposition in humid soils can counteract protection. Nature Communications, 11: 2255.

Choi, S.C., Bartha, R., 1993. Cobalamin-mediated mercury methylation by Desulfovibrio desulfuricans LS. Applied and Environmental Microbiology, 59, 290–295.

Chiasson-Gould SA, Blais JM, Poulain AJ, 2014. Dissolved organic matter kinetically controls mercury bioavailability to bacteria. Environmental Science and Technology, 48: 3153–

3161.

Christensen GA, Wymore AM, King AJ, et al., 2016. Development and Validation of Broad-range Qualitative and Clade-specific Quantitative Molecular Probes for Assessing Mercury Methylation in the Environment. Applied and Environmental Microbiology, 82: 6068–6078.

Claff SR, Sullivan LA, Burton ED, et al., 2010. A sequential extraction procedure for acid sulfate soils: Partitioning of iron. Geoderma, 155: 224–230.

Clarkson, T.W., 1997. The toxicology of mercury. Crit. Rev. Cl Lab. Sci. 34, 369–403.

Cline, J. D. Spectrophotometric Determination of Hydrogen Sulfide in Natural Waters. Limnol. Oceanogr. 1969, 454–458.

Coleman Wasik, J. K.; Mitchell, C. P. J.; Engstrom, D. R.; Swain, E. B.; Monson, B. A.; Balogh, S. J.; Jeremiason, J. D.; Branfireun, B. A.; Eggert, S. L.; Kolka, R. K.; Almendinger, J. E. Methylmercury Declines in a Boreal Peatland When Experimental Sulfate Deposition Decreases. Environ. Sci. Technol. 2012, 46 (12), 6663–6671.

Coleman Wasik, J. K.; Engstrom, D. R.; Mitchell, C. P. J. The Effects of Hydrologic Fluctuation and Sulfate Regeneration on Mercury Cycling in an Experimental Peatland. J. Geophys. Res. Biogeosciences 2015, 120 (9) 1697–1715.

Colombo, M. J.; Ha, J.; Reinfelder, J. R.; Barkay, T.; Yee, N. Oxidation of Hg(0) to Hg(II) by Diverse Anaerobic Bacteria. Chem. Geol. 2014, 363, 334–340.

Colombo, M. J.; Ha, J.; Reinfelder, J. R.; Barkay, T.; Yee, N. Anaerobic Oxidation of Hg(0) and Methylmercury Formation by Desulfovibrio Desulfuricans ND132. Geochim. Cosmochim. Acta 2013, 112, 166–177.

Compeau, G.C.; Bartha, R. Sufate-reducing bacteria: Principle methylators of mercury in anoxic estuarine sediments. Appl. Environ. Microbiol. 1985, 50, 498–502

Cui, L.; Feng, X.; Lin, C. J.; Wang, X.; Meng, B.; Wang, X.; Wang, H. Accumulation and Translocation of ^{198}Hg in Four Crop Species. Environ. Toxicol. Chem. 2014, 33 (2), 334–340

Cui, W.; Liu, G.; Bezerra, M.; Lagos, D. A.; Li, Y.; Cai, Y. Occurrence of Methylmercury in Rice-Based Infant Cereals and Estimation of Daily Dietary Intake of Methylmercury for Infants. J. Agric. Food Chem. 2017, 65, 9569–9578

Deonarine A, Hsu-Kim H, 2009. Precipitation of mercuric sulfide nanoparticles in NOM-containing water: Implications for the natural environment. Environmental Science and Technology, 43: 2368–2373.

Dong Q, Liu Y, Liu G, et al., 2021a. Aging and phytoavailability of newly introduced and legacy cadmium in paddy soil and their bioaccessibility in rice grain distinguished by enriched isotope tracing. Journal of Hazardous Materials, 417: 125998.

Dong Q, Liu Y, Liu G, et al., 2021b. Enriched isotope tracing to reveal the fractionation and lability of legacy and newly introduced cadmium under different amendments. Journal of Hazardous Materials, 403: 123975.

Driscoll, C.T., Mason, R.P., Chan, H.M., Jacob, D.J., Pirrone, N., 2013. Mercury as a global pollutant: Sources, pathways, and effects. Environmental Science & Technology, 47(10), 4967–4983.

Drott, A.; Björn, E.; Bouchet, S.; Skyllberg, U. Refining Thermodynamic Constants for Mercury(II)-Sulfides in Equilibrium with Metacinnabar at Sub-Micromolar Aqueous

Sulfide Concentrations. Environ. Sci. Technol. 2013, 47 (9), 4197–4203

Du H, Peacock CL, Chen W, et al., 2018. Binding of Cd by ferrihydrite organo-mineral composites: Implications for Cd mobility and fate in natural and contaminated environments. Chemosphere, 207: 404–412.

Eckley CS, Gilmour CC, Janssen S, et al., 2020. The assessment and remediation of mercury contaminated sites: A review of current approaches. Science of the Total Environment, 707: 136031.

Enescu M, Nagy KL, Manceau A, 2016. Nucleation of mercury sulfide by dealkylation. Scientific Reports, 6: 39359.

Feng, X.; Li, P.; Qiu, G.; Wang, S.; Li, G.; Shang, L.; Meng, B.; Jiang, H.; Bai, W.; Li, Z.; Fu, X. Human Exposure to Methylmercury through Rice Intake in Mercury Mining Areas, Guizhou Province, China. Environ. Sci. Technol. 2008, 42 (1), 326–332.

Feinberg, A.; Stenke, A.; Peter, T.; Hinckley, E. S.; Driscoll, C. T. Reductions in the Deposition of Sulfur and Selenium to Agricultural Soils Pose Risk of Future Nutrient Deficiencies. Commun. Earth Environ. 2021. 2, 101

Feyte S, Tessier A, Gobeil C, et al., 2010. In situ adsorption of mercury, methylmercury and other elements by iron oxyhydroxides and organic matter in lake sediments. Applied Geochemistry, 25: 984–995.

Fleming, E.J., Mack, E.E., Green, P.G., Nelson, D.C., 2006. Mercury methylation from unexpected sources: molybdate inhibited freshwater sediments and iron-reducing bacterium. Applied and Environmental Microbiology, 72, 457–464

Fu XW, Feng X, Shang LH, et al., 2012. Two years of measurements of atmospheric total gaseous mercury (TGM) at a remote site in Mt. Changbai area, Northeastern China. Atmospheric Chemistry and Physics, 12: 4215–4226.

Fu XW, Zhang H, Yu B, et al., 2015. Observations of atmospheric mercury in China: A critical review. Atmospheric Chemistry and Physics, 15: 9455–9476. Gai K, Hoelen TP, Hsu-Kim H, et al., 2016. Mobility of four common mercury species in model and natural unsaturated soils. Environmental Science and Technology, 50: 3342–3351.

Garcia, E., Poulain, A.J., Amyot, M., Ariya, P.A., 2005. Diel variations in photoinduced oxidation of Hg-0 in freshwater. Chemosphere, 59, 977−981.

Gårdfeldt, K., Munthe, J., Strömberg, D., Lindqvist, O., 2003. A kinetic study on the abiotic methylation of divalent mercury in the aqueous phase. The Science of the Total Environment, 304, 127–136.

Gerbig CA, Kim CS, Stegemeier JP, et al., 2011. Formation of nanocolloidal metacinnabar in mercury-DOM-sulfide systems. Environmental Science and Technology, 45: 9180–9187.

Gilmour CC, Bullock AL, McBurney A, et al., 2018. Robust mercury methylation across diverse methanogenic Archaea. MBio, 9: 1–13.

Gilmour CC, Podar M, Bullock AL, et al., 2013. Mercury methylation by novel microorganisms from new environments. Environmental Science and Technology, 47: 11810–11820.

Gilmour CC, Riedel GS, Ederington MC, et al., 1998. Methylmercury concentrations and production rates across a trophic gradient in the Northern Everglades. Biogeochemistry, 40: 327–345.

Gilmour, C. C.; Henry, E. A.; Ralph, M. Sulfate Stimulation of Mercury Methylation in

Freshwater Sediments. Environ. Sci. Technol. 1992, 26 (11), 2281–2287

Graham AM, Aiken GR, Gilmour CC, 2012. Dissolved organic matter enhances microbial mercury methylation under sulfidic conditions. Environmental Science and Technology, 46: 2715–2723.

Gray, J. E.; Hines, M. E.; Goldstein, H. L.; Reynolds, R. L. Mercury Deposition and Methylmercury Formation in Narraguinnep Reservoir, Southwestern Colorado, USA. Appl. Geochemistry 2014, 50, 82–90.

Grégoire, D. S.; Poulain, A. J. Shining Light on Recent Advances in Microbial Mercury Cycling. Facets 2018, 3 (1), 858–879.

Grégoire, D. S.; Lavoie, N. C.; Poulain, A. J. Heliobacteria Reveal Fermentation as a Key Pathway for Mercury Reduction in Anoxic Environments. Environ. Sci. Technol. 2018, 52 (7), 4145–4153.

Gu, B., Bian, Y., Miller, C.L., Dong, W., Jiang, X., Liang, L., 2011. Mercury reduction and complexation by natural organic matter in anoxic environments. Proc. Natl. Acad. Sci. 1–5.

Guo, Y.; Xiang, Y.; Liu, G.et al. 2023. “Trojan Horse” Type Internalization Increases the Bioavailability of Mercury Sulfide Nanoparticles and Methylation after Intracellular Dissolution. ACS Nano, 17 (3),1925–1934.

Hamelin, S., Amyot, M., Barkay, T., Wang, Y., Planas, D., 2011. Methanogens: Principal methylators of mercury in lake periphyton. Environmental Science & Technology, 45(18), 7693–7700.

Hammerschmidt, C.R., Lamborg, C.H., Fitzgerald, W.F., 2007. Aqueous phase methylation as a potential source of methylmercury in wet deposition. Atmospheric Environment, 41, 1663–1668

Han, Y.S., Kim, S.H., Chon, C.M., Kwon, S., Kim, J.G., Choi, H.W., Ahn, J.S., 2020. Effect of FeS on mercury behavior in mercury-contaminated stream sediment: A case study of Pohang Gumu Creek in South Korea. J. Hazard. Mater. 393, 122373.

Hansen AM, Kraus TEC, Pellerin BA, et al., 2016. Optical properties of dissolved organic matter (DOM): Effects of biological and photolytic degradation. Limnology and Oceanography, 61: 1015–1032.

Harris RC, Rudd JWM, Amyot M, et al., 2007. Whole-ecosystem study shows rapid fish-mercury response to changes in mercury deposition. Proceedings of the National Academy of Sciences of the United States of America, 104: 16586–16591.

Hinckley, E. L. S.; Crawford, J. T.; Fakhraei, H.; Driscoll, C. T. A Shift in Sulfur-Cycle Manipulation from Atmospheric Emissions to Agricultural Additions. Nat. Geosci. 2020, 13 (9), 597–604.

Hintelmann H, Evans RD, Villeneuve JY, 1995. Measurement of mercury methylation in sediments by using enriched stable mercury isotopes combined with methylmercury determination by gas chromatography-inductively coupled plasma mass spectrometry. Journal of Analytical Atomic Spectrometry, 10: 619–624.

Hintelmann H, Keppel-Jones K, Evans RD, 2000. Constants of mercury methylation and demethylation rates in sediments and comparison of tracer and ambient mercury availability. Environmental Toxicology and Chemistry, 19: 2204–2211.

Hintelmann H, Harris R, Heyes A, et al., 2002. Reactivity and mobility of new and old mercury

deposition in a boreal forest ecosystem during the first year of the METAALICUS study. Environmental Science and Technology, 36: 5034–5040.

Hsu-Kim H., Kucharzyk K. H., Zhang T. et al., 2013. Mechanisms regulating mercury bioavailability for methylating microorganisms in the aquatic environment: A critical review. Environ. Sci. Technol. 47, 2441–2456.

Hu, H.; Lin, H.; Zheng, W.; Tomanicek, S. J.; Johs, A.; Feng, X.; Elias, D. A.; Liang, L.; Gu, B. Oxidation and Methylation of Dissolved Elemental Mercury by Anaerobic Bacteria. Nat. Geosci. 2013, 6 (9), 751–754.

Huang J, Jones A, Waite TD, et al., 2021. Fe(II) redox chemistry in the environment. Chemical Reviews 121: 8161–8233.

Jeong HY, Klaue B, Blum JD, et al., 2007. Sorption of mercuric ion by synthetic nanocrystalline mackinawite (FeS). Environmental Science and Technology, 41: 7699–7705.

Jeremiason, J. D.; Engstrom, D. R.; Swain, E. B.; Nater, E. A.; Johnson, B. M.; Almendinger, J. E.; Monson, B. A.; Kolka, R. K. Sulfate Addition Increases Methylmercury Production in an Experimental Wetland. Environ. Sci. Technol. 2006, 40 (12), 3800–3806.

Jørgensen, B. B. The Sulfur Cycle of Freshwater Sediments: Role of Thiosulfate. Limnol. Oceanogr. 1990, 35 (6), 1329–1342.

Jørgensen, B. B.; Nelson, D. C. Sulfide Oxidation in Marine Sediments: Geochemistry meets microbiology. Geol. Soc. Am. Sp. Papers 2004, 379, 63–81.

Jiang, T., Wei, S.Q., Flanagan, D.C., Li, M.J., Li, X.M., Wang, Q., Luo, C., 2014. Effect of abiotic factors on the mercury reduction process by humic acids in aqueous systems. Pedosphere, 24, 125−136.

Jiang, T., Skyllberg, U., Wei, S.Q., Wang, D.Y., Lu, S., Jiang, Z.M., Flanagan, D.C., 2015. Modelling of the structure-specific kinetics of abiotic, dark reduction of Hg(II) complexed by O/N and S functional groups in humic acids while accounting for time-dependent structural rearrangement. Geochimica et Cosmochimica Acta, 154, 151–167.

Jiang T, Kaal J, Liang J, et al., 2017. Composition of dissolved organic matter (DOM) from periodically submerged soils in the Three Gorges Reservoir areas as determined by elemental and optical analysis, infrared spectroscopy, pyrolysis-GC-MS and thermally assisted hydrolysis and methylation. Science of the Total Environment, 603–604: 461–471.

Johs A, Eller VA, Mehlhorn TL, et al., 2019. Dissolved organic matter reduces the effectiveness of sorbents for mercury removal. Science of the Total Environment, 690: 410–416.

Jonsson S, Mazrui NM, Mason RP, 2016. Dimethylmercury formation mediated by inorganic and organic reduced sulfur surfaces. Scientific Reports, 6: 27958.

Jonsson S, Skyllberg U, Nilsson MB, et al., 2012. Mercury methylation rates for geochemically relevant HgII species in sediments. Environmental Science and Technology, 46: 11653–11659.

Kappler A, Bryce C, Mansor M, et al., 2021. An evolving view on biogeochemical cycling of iron. Nature Reviews Microbiology, 19: 360–374.

Kleber M, Eusterhues K, Keiluweit M, et al., 2015. Mineral-organic associations: Formation, properties, and relevance in soil environments. Advances in Agronomy, 130: 1–140.

Kim, M.K., Zoh, K.D., 2013. Effects of natural water constituents on the photo- decomposition of methylmercury and the role of hydroxyl radical. Science of the Total Environment, 449, 95–101.

Kögel-Knabner I, Amelung W, Cao Z, et al., 2010. Biogeochemistry of paddy soils. Geoderma, 157: 1–14.

Kwon, S. Y.; Selin, N. E.; Giang, A.; Karplus, V. J.; Zhang, D. Present and Future Mercury Concentrations in Chinese Rice: Insights from Modeling. Global Biogeochem. Cycles 2018, 437–462.

Lalonde K, Mucci A, Ouellet A, et al., 2012. Preservation of organic matter in sediments promoted by iron. Nature, 483: 198–200.

Landa, E.R. Retention of metallic mercury-vapor by soils. Geochim. Cosmochim. Acta 1987, 42, 1407–1411.

Lei, P.; Tang, C.; Wang, Y.; Wu, M.; Kwong, R. W. M.; Jiang, T.; Zhong, H. Understanding the Effects of Sulfur Input on Mercury Methylation in Rice Paddy Soils. Sci. Total Environ. 2021, 778, 146325.

Lemes, M., Wang, F.Y., 2009. Methylmercury speciation in fish muscle by HPLC-ICP-MS following enzymatic hydrolysis. Journal of Analytical Atomic Spectrometry, 24, 663–668

Li H, Li Y, Tang W, et al., 2022. Bioavailability and methylation of bulk mercury sulfide in paddy soils: New insights into mercury risks in rice paddies. Journal of Hazardous Materials, 424: 127394.

Li, X.; Tyl, C. E.; Kaiser, D. E.; Annor, G. A. Effect of Sulfur Fertilization Rates on Wheat (Triticum Aestivum L.) Functionality. J. Cereal Sci. 2019, 87, 292–300.

Li, Y.; Wang, Y.; Zhang, Q.; Hu, W.; Zhao, J.; Chen, Y.; Zhong, H.; Wang, G.; Zhang, Z.; Gao, Y. Elemental Sulfur Amendment Enhance Methylmercury Accumulation in Rice (Oryza Sativa L.) Grown in Hg Mining Polluted Soil. J. Hazard. Mater. 2019, 379, 120701.

Li, Y.; Lu, C.; Zhu, N.; Chao, J.; Hu, W.; Zhang, Z.; Wang, Y.; Liang, L.; Chen, J.; Xu, D.; Gao, Y.; Zhao, J. Mobilization and Methylation of Mercury with Sulfur Addition in Paddy Soil: Implications for Integrated Water-Sulfur Management in Controlling Hg Accumulation in Rice. J. Hazard. Mater. 2022, 430, 128447

Li YY, Zhao JT, Zhong H, et al., 2019. Understanding enhanced microbial MeHg production in mining-contaminated paddy soils under sulfate amendment: Changes in Hg mobility or microbial methylators? Environmental Science and Technology, 53: 1844–1852.

Liao P, Pan C, Ding W, et al., 2020. Formation and transport of Cr(III)-NOM-Fe colloids upon reaction of Cr(VI) with NOM-Fe(II) colloids at anoxic-oxic interfaces. Environmental Science and Technology, 54: 4256–4266.

Liem-Nguyen V, Jonsson S, Skyllberg U, et al., 2016. Effects of nutrient loading and mercury chemical speciation on the formation and degradation of methylmercury in estuarine sediment. Environmental Science and Technology, 50: 6983–6990.

Liem-Nguyen, V.; Skyllberg, U.; Björn, E. Methylmercury Formation in Boreal Wetlands in Relation to Chemical Speciation of Mercury(II) and Concentration of Low Molecular Mass Thiols. Sci. Total Environ. 2021, 755, 142666

Lin, H.; Morrell-Falvey, J. L.; Rao, B.; Liang, L.; Gu, B. Coupled Mercury-Cell Sorption, Reduction, and Oxidation on Methylmercury Production by Geobacter Sulfurreducens PCA. Environ. Sci. Technol. 2014, 48, 11969–11976.

Liu C, Massey MS, Latta DE, et al., 2021. Fe(II)-induced transformation of iron minerals in soil ferromanganese nodules. Chemical Geology, 559: 119901.

Liu, M.; Zhang, Q.; Cheng, M.; He, Y.; Chen, L.; Shen, H.; Zhang, W.; Tao, S.; Wang, X.; Zhang, H.; Cao, H. Rice Life Cycle-Based Global Mercury Biotransport and Human Methylmercury Exposure. Nat. Commun. 2019, 10, 5164

Liu J, Meng B, Poulain AJ, et al., 2021. Stable isotope tracers identify sources and transformations of mercury in rice (Oryza sativa L.) growing in a mercury mining area. Fundamental Research, 1: 259–268.

Liu J, Jiang T, Wang FY, et al., 2018. Inorganic sulfur and mercury speciation in the water level fluctuation zone of the Three Gorges Reservoir, China: The role of inorganic reduced sulfur on mercury methylation. Environmental Pollution, 237: 1112–1123.

Liu J, Liang J, Bravo AG, et al., 2021. Anaerobic and aerobic biodegradation of soil-extracted dissolved organic matter from the water-level-fluctuation zone of the Three Gorges Reservoir region, China. Science of the Total Environment, 764: 142857.

Liu J, Zhao L, Kong K, et al., 2022. Uncovering the Geochemical Fractionation of Newly Deposited Hg in Paddy Soil Using a Stable Isotope Tracer. Journal of Hazardous Materials, 433: 128752.

Liu, T.; Wang, J.; Feng, X.; Zhang, H.; Zhu, Z.; Cheng, S. Spectral Insight into Thiosulfate-Induced Mercury Speciation Transformation in a Historically Polluted Soil. Sci. Total Environ. 2019, 657, 938–944.

Liu YR, Johs A, Bi L, et al., 2018. Unraveling microbial communities associated with methylmercury production in paddy soils. Environmental Science and Technology, 52: 13110−13118.

Liu, Y.; Delgado-Baquerizo, M.; Bi, L.; Zhu, J.; He, J. Z. Consistent Responses of Soil Microbial Taxonomic and Functional Attributes to Mercury Pollution across China. Microbiome 2018, 183 (6), 1–12.

Lu, X.; Liu, Y.; Johs, A.; Zhao, L.; Wang, T.; Yang, Z.; Lin, H.; Elias, D. A.; Pierce, E. M.; Liang, L.; Barkay, T.; Gu, B. Anaerobic Mercury Methylation and Demethylation by Geobacter Bemidjiensis Bem. Environ. Sci. Technol. 2016, 50 (8), 4366–4373.

Lucotte M, Schetagne R, Therien N, et al., 1999. Mercury in the Biogeochemical Cycle: Natural Environments and Hydroelectric Reservoirs of Northern Québec (Canada). Springer, Berlin.

Lv J, Zhang S, Wang S, et al., 2016. Molecular-scale investigation with ESI-FT-ICR-MS on fractionation of dissolved organic matter induced by adsorption on iron oxyhydroxides. Environmental Science and Technology, 50: 2328–2336.

Manceau A, Wang JX, Rovezzi M, et al., 2018. Biogenesis of mercury-sulfur nanoparticles in plant leaves from atmospheric gaseous mercury. Environmental Science and Technology, 52: 3935–3948.

Marvin-DiPasquale, M.; Agee, J.; Mcgowan, C.; Oremland, R. S.; Thomas, M.; Krabbenhoft, D. Methyl-Mercury Degradation Pathways: A Comparison among Three Mercury-Impacted Ecosystems. Environ. Sci. Technol. 2000, 34 (23), 4908–4916

Mao, Y.; Li, Y.; Richards, J.; Cai, Y. Investigating Uptake and Translocation of Mercury Species by Sawgrass (Cladium Jamaicense) Using a Stable Isotope Tracer Technique. Environ. Sci. Technol. 2013, 47, 9678–9684.

Mazrui NM, Jonsson S, Thota S, et al., 2016. Enhanced availability of mercury bound to dissolved organic matter for methylation in marine sediments. Geochimica et Cosmochimica Acta, 194: 153–162.

Meng B, Feng XB, Qiu G, et al., 2014. Localization and speciation of mercury in brown rice with implications for Pan-Asian public health. Environmental Science and Technology, 48: 7974–7981.

Meng B, Feng X, Qiu G, et al., 2010. Distribution patterns of inorganic mercury and methylmercury in tissues of rice (Oryza Sativa L.) plants and possible bioaccumulation pathways. Journal of Agricultural and Food Chemistry, 58: 4951–4958.

Meng B, Feng X, Qiu G, et al., 2011. The process of methylmercury accumulation in rice (Oryza Sativa L.). Environmental Science and Technology, 45: 2711–2717.

Meng B, Li Y, Cui W, et al., 2018. Tracing the uptake, transport, and fate of mercury in Sawgrass (Cladium jamaicense) in the Florida Everglades using a multi-isotope technique. Environmental Science and Technology, 52: 3384–3391.

Merritt, K.A., Amirbahman, A., 2009. Mercury methylation dynamics in estuarine and coastal marine environments - A critical review. Earth- Science Reviews, 96 (1−2), 54−66

Mu C, Schuster PF, Abbott BW, et al., 2020. Permafrost degradation enhances the risk of mercury release on Qinghai-Tibetan Plateau. Science of the Total Environment, 708: 135127.

Murphy KR, Butler KD, Spencer RGM, et al., 2010. Measurement of dissolved organic matter fluorescence in aquatic environments: An interlaboratory comparison. Environmental Science and Technology, 44: 9405–9412.

O'Connor D, Hou D, Ok YS, et al., 2019. Mercury speciation, transformation, and transportation in soils, atmospheric flux, and implications for risk management: A critical review. Environmental International, 126: 747–761.

Olsen, T. A.; Muller, K. A.; Painter, S. L.; Brooks, S. C. Kinetics of Methylmercury Production Revisited. Environ. Sci. Technol. 2018, 52 (4), 2063–2070.

Orem, W.; Gilmour, C.; Axelrad, D.; Krabbenhoft, D.; Scheidt, D.; Kalla, P.; McCormick, P.; Gabriel, M.; Aiken, G. Sulfur in the South Florida Ecosystem: Distribution, Sources, Biogeochemistry, Impacts, and Management for Restoration. Crit. Rev. Environ. Sci. Technol. 2011, 41, 249–288.

Oremland, R.S.; Culbertson, C.W.; Winfrey, M. R. Methylmercury decomposition in sediments and bacterial cultures? involvement of methanogens and sulfate reducers in oxidative demethylation. Appl. Environ. Microbiol. 1991, 57, 130−137

Orihel DM, Paterson MJ, Blanchfield PJ, et al., 2008. Temporal changes in the distribution, methylation, and bioaccumulation of newly deposited mercury in an aquatic ecosystem. Environmental Pollution, 154: 77–88.

Oswald CJ, Heyes A, Branfireun BA, 2014. Fate and transport of ambient mercury and applied mercury isotope in terrestrial upland soils: Insights from the METAALICUS watershed. Environmental Science and Technology, 48: 1023–1031.

Paterson MJ, Blanchfield PJ, Podemski C, et al., 2006. Bioaccumulation of newly deposited mercury by fish and invertebrates: an enclosure study using stable mercury isotopes. Canadian Journal of Fisheries and Aquatic Sciences, 63: 2213–2224.

Pham AL, Morris A, Zhang T, et al., 2014. Precipitation of nanoscale mercuric sulfides in the

presence of natural organic matter: Structural properties, aggregation, and biotransformation. Geochimica et Cosmochimica Acta, 133: 204–215.

Piao H, Bishop PL, 2006. Stabilization of mercury-containing wastes using sulfide. Environmental Pollution, 139: 498–506.

Podar M, Gilmour CC, Brandt CC, et al., 2015. Global prevalence and distribution of genes and microorganisms involved in mercury methylation. Science Advances, 1: e1500675.

Poulain, A.J., Amyot, M., Findlay, D., Telor, S., Barkay, T., Hintelmann, H., 2004. Biological and photochemical production of dissolved gaseous mercury in a boreal lake. Limnology and Oceanography, 49, 2265−2275

Poulin, B. A.; Ryan, J. N.; Tate, M. T.; Krabbenhoft, D. P.; Hines, M. E.; Barkay, T.; Schaefer, J.; Aiken, G. R. Geochemical Factors Controlling Dissolved Elemental Mercury and Methylmercury Formation in Alaskan Wetlands of Varying Trophic Status. Environ. Sci. Technol. 2019, 53 (11), 6203–6213.

Poulton SW, Canfield DE, 2005. Development of a sequential extraction procedure for iron: implications for iron partitioning in continentally derived particulates. Chemical Geology, 214: 209–221. Parks JM, Johs A, Podar M, et al., 2013. The genetic basis for bacterial mercury methylation. Science, 339: 1332–1335.

Pu, Q.; Zhang, K.; Poulain, A. J.; Liu, J.; Zhang, R.; Abdelhafiz, M. A.; Meng, B.; Feng, X. Mercury Drives Microbial Community Assembly and Ecosystem Multifunctionality across a Hg Contamination Gradient in Rice Paddies. J. Hazard. Mater. 2022, 435, 129055.

Qian G, Sun DD, Tay JH, 2003. Immobilization of mercury and zinc in an alkali-activated slag matrix. Journal of Hazardous Materials, 101: 65–77.

Qin CY, Du BY, Yin RS, et al., 2020. Isotopic fractionation and source appointment of methylmercury and inorganic mercury in a paddy ecosystem. Environmental Science and Technology, 54: 14334–14342.

Qiu GL, Feng XB, Li P, et al., 2008. Methylmercury accumulation in rice (Oryza Sativa L.) grown at abandoned mercury mines in Guizhou, China. Journal of Agricultural and Food Chemistry, 56: 2465–2468.

Qvarnström, J.; Frech, W. Mercury Species Transformations during Sample Pre-Treatment of Biological Tissues Studied by HPLC-ICP-MS. J. Anal. At. Spectrom. 2002, 17 (11), 1486–1491.

Ratié G, Vantelon D, Lot E, et al., 2019. Iron speciation at the riverbank surface in wetland and potential impact on the mobility of trace metals. Science of the Total Environment, 651: 443–455.

Ravichandran M, 2004. Interactions between mercury and dissolved organic matter - A review. Chemosphere, 55: 319–331.

Ravichandran M, Aiken G, Ryan J, et al., 1999. Inhibition of precipitation and aggregation of metacinnabar (mercuric sulfide) by dissolved organic matter isolated from the Florida Everglades. Environmental Science and Technology, 33: 1418−1423.

Regnell O, Watras CJ, 2018. Microbial mercury methylation in aquatic environments: A critical review of published field and laboratory studies. Environmental Science and Technology, 53: 4–19.

Riedel T, Zak D, Biester H, et al., 2013. Iron traps terrestrially derived dissolved organic matter

at redox interfaces. Proceedings of the National Academy of Sciences of the United States of America, 110: 10101–10105.

Rodríguez Martín-Doimeadios RC, Krupp E, Amouroux D, 2002. Application of isotopically labeled methylmercury for isotope dilution analysis of biological samples using gas chromatography/ICPMS. Analytical Chemistry, 74: 2505–2512.

Rolfhus KR, Hurley JP, Bodaly RA, et al., 2015. Production and retention of methylmercury in inundated boreal forest soils. Environmental Science and Technology, 49: 3482–3489.

Rothenberg SE, Feng XB, 2012. Mercury cycling in a flooded rice paddy. Journal of Geophysical Research: Biogeosciences, 117: 1–16.

Santana, M. M.; Dias, T.; Gonzalez, J. M.; Cruz, C. Transformation of Organic and Inorganic Sulfur– Adding Perspectives to New Players in Soil and Rhizosphere. Soil Biol. Biochem. 2021, 160, 108306.

Schartup, A. T.; Balcom, P. H.; Soerensen, A. L.; Gosnell, K. J.; Calder, R. S. D.; Mason, R. P.; Sunderland, E. M. Freshwater Discharges Drive High Levels of Methylmercury in Arctic Marine Biota. Proc. Natl. Acad. Sci. 2015, 112 (38), 11789–11794.

Schaefer, J. K.; Yagi, J.; Reinfelder, J. R.; Cardona, T.; Ellickson, K. M.; Tel-Or, S.; Barkay, T. Role of the Bacterial Organomercury Lyase (MerB) in Controlling Methylmercury Accumulation in Mercury-Contaminated Natural Waters. Environ. Sci. Technol. 2004, 38 (16), 4304–4311.

Schaefer, J. K.; Kronberg, R.-M.; Morel, F. M. M.; Skyllberg, U. Detection of a Key Hg Methylation Gene, HgcA , in Wetland Soils. Environ. Microbiol. Rep. 2014, 6, 441–447.

Schippers, A. Biogeochemistry of metal sulfide oxidation in mining environments, sediments, and soils. In: Amend, J.P., Edwards, K.J., Lyons, T.W. (Eds.), Sulfur Biogeochemistry: Past and Present. Geological Society of America, Boulder, Colorado, 2004.

Shi, L.; Richardson, D. J.; Wang, Z.; Kerisit, S. N.; Rosso, K. M.; Zachara, J. M.; Fredrickson, J. K. The Roles of Outer Membrane Cytochromes of Shewanella and Geobacter in Extracellular Electron Transfer. Environ. Microbiol. Rep. 2009, 1 (4), 220–227.

Skyllberg U, Drott A, 2010. Competition between disordered iron sulfide and natural organic matter associated thiols for mercury(II)-an EXAFS study. Environmental Science and Technology, 44: 1254–1259.

Skyllberg U, Persson A, Tjerngren I, et al., 2021. Chemical speciation of mercury, sulfur and iron in a dystrophic boreal lake sediment, as controlled by the formation of mackinawite and framboidal pyrite. Geochimica et Cosmochimica Acta, 294: 106–125.

Skyllberg U, 2008. Competition among thiols and inorganic sulfides and polysulfides for Hg and MeHg in wetland soils and sediments under suboxic conditions: Illumination of controversies and implications for MeHg net production. Journal of Geophysical Research: Biogeosciences, 113.

Skyllberg U, Bloom PR, Qian J, et al., 2006. Complexation of mercury (II) in soil organic matter: EXAFS evidence for linear two-coordination with reduced sulfur groups. Environmental Science and Technology, 40(13): 4174–4180

Slotznick SP, Sperling EA, Tosca NJ, et al., 2020. Unraveling the Mineralogical Complexity of Sediment Iron Speciation Using Sequential Extractions. Geochemistry Geophysics Geosystems, 21: e2019GC008666.

Slowey AJ, 2010. Rate of formation and dissolution of mercury sulfide nanoparticles: The dual

role of natural organic matter. Geochimica et Cosmochimica Acta, 74: 4693–4708.

Sörbo B, 1987. Sulfate: turbidmetric and nephelometric methods. Methods in Enzymology, 143: 3–6.

St. Louis, V. L.; Rudd, J. W. M.; Kelly, C. A. et al., 2004. The Rise and Fall of Mercury Methylation in an Experimental Reservoir. Environ. Sci. Technol. 38 (5), 1348–1358

Strickman, R. J.; Mitchell, C. P. J. Accumulation and Translocation of Methylmercury and Inorganic Mercury in Oryza Sativa: An Enriched Isotope Tracer Study. Sci. Total Environ. 2017, 574, 1415–1423.

Strickman, R. J.; Mitchell, C. P. J. Mercury Methylation in Stormwater Retention Ponds at Different Stages in the Management Lifecycle. Environ. Sci. Process. Impacts 2018, 20 (4), 595–606.

Sun, R.G., Wang, D.Y., Zhang, Y.T., Mao, W., Zhang, T., Ma, M., Zhang, C., 2013. Photodegradation of monomethylmercury in the presence of chloride ion. Chemosphere, 91, 1471–1476.

Sun, R.G., Wang, D.Y., Mao, W., Ma, M., Zhang, C., Jiang, T., 2015. Diurnal characteristics of migration and transformation of mercury and effects of nitrate in Jialing River, Chongqing, China. Chemosphere, 119(2), 634–641.

Tessier A, Campbell PGC, Bisson M, 1979. Sequential Extraction Procedure for the Speciation of Particulate Trace Metals. Analytical Chemistry, 51: 844–851.

Tian L, Guan W, Ji Y, et al., 2021. Microbial methylation potential of mercury sulfide particles dictated by surface structure. Nature Geosciences, 14: 409–416.

Tiffreau C, Lützenkirchen J, Behra P, 1995. Modeling the adsorption of mercury(II) on (Hydr)oxides: I. Amorphous iron oxide and α-quartz. Journal of Colloid and Interface Science, 172: 82–93.

Todorova, S. G.; Driscoll, C. T.; Matthews, D. A.; Effler, S. W.; Hines, M. E.; Henry, E. A. Evidence for Regulation of Monomethyl Mercury by Nitrate in a Seasonally Stratified, Eutrophic Lake. Environ. Sci. Technol. 2009, 43 (17), 6572–6578.

Tuominen, L.; Kairesalo, T.; Hartikainen, H. Comparison of Methods for Inhibiting Bacterial Activity in Sediment. Appl. Environ. Microbiol. 1994, 60, 3454−3457

Ullrich, S.M., Tanton, T.W., Abddrashitova, S.A., 2001. Mercury in the Aquatic Environment: A Review of Factors Affecting Methylation. Critical Reviews in Environmental Science and Technology, 31(3):241–293.

Vázquez-Rodríguez, A.; Hansel, C. M.; Zhang, T.; Lamborg, C.; Santelli, C. M.; Webb, S.; Brooks, S. Microbial- and Thiosulfate-Mediated Dissolution of Mercury Sulfide Minerals and Transformation to Gaseous Mercury. Front. Microbiol. 2015, 6, 596.

Viollier E, Inglett PW, Hunter K, et al., 2000. The ferrozine method revisited: Fe(II)/Fe(III) determination in natural waters. Applied Geochemistry, 15: 785–790.

Wang B, Zhong S, Bishop K, et al., 2021. Biogeochemical influences on net methylmercury formation proxies along a peatland chronosequence. Geochimica et Cosmochimica Acta, 308: 188–203.

Wang, F.Y., Zhang, J.Z., 2013. Mercury contamination in aquatic ecosystems under a changing environment: implications for the Three Gorges Reservoir. Chinese Science Bulletin, 58, 141–149.

Wang JX, Feng XB, Anderson CWN, et al., 2012. Remediation of mercury contaminated sites

– A review. Journal of Hazardous Materials, 221–222: 1–18.

Wang, J.; Feng, X.; Anderson, C. W. N.; Wang, H.; Wang, L. Thiosulphate-Induced Mercury Accumulation by Plants: Metal Uptake and Transformation of Mercury Fractionation in Soil - Results from a Field Study. Plant Soil 2014, 375, 21–33.

Wang, J.; Feng, X.; Anderson, C. W. N.; Wang, H.; Zheng, L.; Hu, T. Implications of Mercury Speciation in Thiosulfate Treated Plants. Environ. Sci. Technol. 2012, 46 (10), 5361–5368.

Wang, J.; Shaheen, S. M.; Jing, M.; Anderson, C. W. N.; Swertz, A. C.; Wang, S. L.; Feng, X.; Rinklebe, J. Mobilization, Methylation, and Demethylation of Mercury in a Paddy Soil under Systematic Redox Changes. Environ. Sci. Technol. 2021, 55 (14), 10133–10141

Wang M, Li Y, Zhao D, et al., 2020. Immobilization of mercury by iron sulfide nanoparticles alters mercury speciation and microbial methylation in contaminated groundwater. Chemical Engineering Journal, 381: 122664.

Wang X, Ye ZH, Li B, et al., 2014. Growing rice aerobically markedly decreases mercury accumulation by reducing both Hg bioavailability and the production of MeHg. Environmental Science and Technology, 48: 1878–1885.

Wang, Y.; Li, Y.; Liu, G.; Wang, D.; Jiang, G.; Cai, Y. Elemental Mercury in Natural Waters: Occurrence and Determination of Particulate Hg(0). Environ. Sci. Technol. 2015, 49(16), 9742–9749

Wang, Y.; Wei, Z.; Zeng, Q.; Zhong, H. Amendment of Sulfate with Se into Soils Further Reduces Methylmercury Accumulation in Rice. J. Soils Sediments 2016, 16 (12), 2720–2727

Wang Y, Wang H, He J, et al., 2017. Iron-mediated soil carbon response to water-table decline in an alpine wetland. Nature Communications, 8: 1–9.

West J, Graham AM, Liem-Nguyen V, et al., 2020. Dimethylmercury degradation by dissolved sulfide and mackinawite. Environmental Science and Technology, 54: 13731–13738.

Wiatrowski, H.A., Das, S., Kukkadapu, R., Ilton, E.S., Barkay, T., Yee, N., 2009. Reduction of Hg(II) to Hg(0) by magnetite. Environmental Science & Technology, 43(14), 5307−5313.

Wilson HF, Xenopoulos MA, 2009. Effects of agricultural land use on the composition of fluvial dissolved organic matter. Nature Geosciences, 2: 37–41.

Wolfenden S, Charnock JM, Hilton J, et al., 2005. Sulfide species as a sink for mercury in lake sediments. Environmental Science and Technology, 39: 6644–6648.

Wu QQ, Hu HY, Meng B, et al., 2020. Methanogenesis is an important process in controlling MeHg concentration in rice paddy soils affected by mining activities. Environmental Science and Technology, 54: 13517–13526.

Xia X, Yang J, Yan Y, et al., 2020. Molecular sorption mechanisms of Cr(III) to organo-ferrihydrite coprecipitates using synchrotron-based EXAFS and STXM techniques. Environmental Science and Technology, 54: 12989–12997.

Xiang, Y.; Guo, Y.; Liu, G.; Liu, Y.; Song, M.; Shi, J.; Hu, L.; Yin, Y.; Cai, Y.; Jiang, G. Particle-Bound Hg(II) Is Available for Microbial Uptake as Revealed by a Whole-Cell Biosensor. Environ. Sci. Technol. 2022, 56, 6754–6764.

Xu Y, He T, Wu P, et al., 2021. Fulvic acid: A key factor governing mercury bioavailability in a polluted plateau wetland. Water Research, 205: 117652.

Yin, D.; He, T.; Yin, R.; Zeng, L. Effects of Soil Properties on Production and Bioaccumulation of Methylmercury in Rice Paddies at a Mercury Mining Area, China. J. Environ. Sci. 2018, 68, 194–205

Yin RS, Gu C, Feng XB, et al., 2016. Distribution and geochemical speciation of soil mercury in wanshan Hg mine: Effects of cultivation. Geoderma, 272: 32–38.

Yuan, D.; Wang, G.; Hu, C.; Zhou, S.; Clough, T. J.; Wrage-Mönnig, N.; Luo, J.; Qin, S. Electron Shuttle Potential of Biochar Promotes Dissimilatory Nitrate Reduction to Ammonium in Paddy Soil. Soil Biol. Biochem. 2022, 172, 108760.

Zeng Q, Huang L, Ma J, et al., 2020. Bio-reduction of ferrihydrite-montmorillonite-organic matter complexes: Effect of montmorillonite and fate of organic matter. Geochimica et Cosmochimica Acta, 276: 327–344.

Zhao L, Anderson CWN, Qiu GL, et al., 2016a. Mercury methylation in paddy soil: Source and distribution of mercury species at a Hg mining area, Guizhou Province, China. Biogeosciences, 13: 2429–2440.

Zhao L, Qiu GL, Anderson CWN, et al., 2016b. Mercury methylation in rice paddies and its possible controlling factors in the Hg mining area, Guizhou Province, southwest China. Environmental Pollution, 215: 1–9.

Zhang, H.; Feng, X.; Larssen, T.; Qiu, G.; Vogt, R. D. In Inland China, Rice, rather than Fish, Is the Major Pathway for Methylmercury Exposure. Environ. Health Perspect. 2010, 118 (9), 1183–1188

Zhang, H.; Feng, X.; Larssen, T.; Shang, L.; Li, P. Bioaccumulation of Methylmercury versus Inorganic Mercury in Rice (Oryza Sativa L.) Grain. Environ. Sci. Technol. 2010, 44 (12), 4499–4504

Zhang, H., Lindberg, S.E., 2001. Sunlight and iron(III)-induced photochemical production of dissolved gaseous mercury in freshwater. Environmental Science & Technology, 35(5), 928−935.

Zhang L, Wu S, Zhao L, et al., 2019. Mercury sorption and desorption on organo-mineral particulates as a source for microbial methylation. Environmental Science and Technology, 53: 2426–2433.

Zhang T, Kim B, Levard C, et al., 2012. Methylation of mercury by bacteria exposed to dissolved, nanoparticulate, and microparticulate mercuric sulfides. Environmental Science and Technology, 46: 6950–6958.

Zhang T, Kucharzyk KH, Kim B, et al., 2014. Net methylation of mercury in estuarine sediment microcosms amended with dissolved, nanoparticulate, and microparticulate mercuric sulfides. Environmental Science and Technology, 48: 9133–9141.

Zhang, Y.; Liu, Y. R.; Lei, P.; Wang, Y. J.; Zhong, H. Biochar and Nitrate Reduce Risk of Methylmercury in Soils under Straw Amendment. Sci. Total Environ. 2018, 619–620, 384–390.

Zhang Z, Si R, Lv J, et al., 2020. Effects of extracellular polymeric substances on the formation and methylation of mercury sulfide nanoparticles. Environmental Science and Technology, 54: 8061–8071.

Zheng, W.; Liang, L.; Gu, B. Mercury Reduction and Oxidation by Reduced Natural Organic Matter in Anoxic Environments. Environ. Sci. Technol. 2012, 46, 292–299.

Zhou XQ, Hao YY, Gu B, et al., 2020. Microbial communities associated with methylmercury

degradation in paddy soils. Environmental Science and Technology, 54: 7952–7960.

Zhou, X.; Qu, X.; Yang, Z.; Zhao, J.; Hao, Y.; Feng, J.; Huang, Q.; Liu, Y. Increased Water Inputs Fuel Microbial Mercury Methylation in Upland Soils. J. Hazard. Mater. 2022, 439, 129578.

Zhu W, Song Y, Adediran GA, et al., 2018. Mercury transformations in resuspended contaminated sediment controlled by redox conditions, chemical speciation and sources of organic matter. Geochimica et Cosmochimica Acta, 220: 158–179.

Zhu Y, Ma LQ, Gao B, et al., 2012. Transport and interactions of kaolinite and mercury in saturated sand media. Journal of Hazardous Materials, 213–214: 93–99.

Zopfi, J.; Böttcher, M. E.; Jørgensen, B. B. Biogeochemistry of Sulfur and Iron in Thioploca-Colonized Surface Sediments in the Upwelling Area of Central Chile. Geochim. Cosmochim. Acta 2008, 72 (3), 827–843.

致 谢

时光如逝，上一次我完成这样一本 100 多页的论文还是我的博士学位论文，那一次我用了整整 5 年的时间；这一次同样是 100 多页的报告，我仅仅用了 3 年的时间，这也许是我的成长，但感觉更像是一切都变得更快了。从博士毕业以来，仿佛我身边的一切都像按下了快进按钮，原本可以走路抵达的目的地，现在如果不跑两步可能就会被远远地甩在身后。3 年的时间原本足以让我们完成初中的学习，亦或是高中的学习。但是，现在感觉 3 年的时间也不过转瞬即逝，只有抓住了每一天，才能让时间过得稍微慢一点。

博士刚毕业那时，我仍然是迷茫的，缺少勇气的。身边去过地化所的同学一直讲述着在地化所学习的艰辛、导师的严厉以及繁重的试验，让我明知地化所就是汞研究工作者应该去的“圣地”，却害怕着它。所以，我希望回到加拿大，希望回到我熟悉的地方，和我熟悉的人相处，不愿意离开我自己的舒适圈。但是，我非常庆幸，疫情让我跳出了我的舒适圈，让我首先说服自己开启了新的生活。于是，我开启了这 3 年的时光，可以说，最终同样是 100 多页的报告或者论文，在地化所博士后的这 3 年，我所收获的成长远远超过了我读博的那 5 年。

回首这充实的 3 年时光，我首先希望感谢的就是我的博士后导师，孟博老师。3 年前的一个傍晚，在韬哥的引荐下，孟老师在我不知要何去何从时，毫不犹豫地给我了来地化所继续学习的机会。让当时仍然在原地徘徊的我，瞬间找到了工作的方向，也找回了被疫情磨去的信心。在我来到地化所，开展博士后工作后，孟老师更是给予了我百分之二百的支持和鼓励，对我论文细致入微地修改、对我基金文本逐字逐句地把关、对我独身一人在贵阳生活上的关心与照顾。虽然孟老师是我的合作导师，但在平日的工作和生活中，他更像是师兄、长兄和亲密的合作者。感谢孟老师！

我还要感谢我的“师爷”冯老师，试问每一个来地化所学习和工作汞研究工作者谁不是慕您的名而来呢？由衷地说，由于冯老师在我心目中的地位过于的高，让我不敢和冯老师走的很近，让我心存畏惧。但是，这 3 年以来，我逐渐地发现我之前的担忧和畏惧完全是多余的。冯老师和我们徒子徒孙们相处时，是那么地亲切，没有丝毫的距离感。同时，我也发现我更加的敬佩冯老师。冯老师领导的汞课题组是非常庞大的课题组，每位老师带领的小组都有自己独立的研究方向，但是每次年终汇报工作时我都能感觉到冯老师对每一个研究方向都运筹帷幄，并且始终站在研究前沿。即使我短短几分钟的汇报，冯老师也能够从中挖掘出研究亮点与不足，让作为年轻科研工作

者的我深深地感受到了大科学家的魅力。

除冯老师外，我还要感谢汞课题组的每一位老师。来地化所之前，这些老师的名字还停留在我读过的文献中，现在各位老师从文献中，书本中来到了我的工作和生活中。他们和孟老师一样，都像我的师兄师姐一般，无私地给予了我非常多的帮助。感谢付学吾老师、李平老师、商立海老师、闫海鱼老师、张华老师、王建旭老师、姚珩老师、尤纳斯老师、胡海燕老师，王宝林老师，赵之玲老师，当然还有我的广义师兄、训哥、巍哥、辉哥、康哥！同样也感谢环境室的其他老师，感谢刘承帅老师当初为我夫人也提供博后的位置、感谢尹主任不厌其烦地给我签字、感谢廖鹏老师对我工作的关心和指导，同样也感谢罗维均老师、宁增平老师、刘意章老师、杨海全老师的热情洋溢，让我的工作总是充满了正能量。

特别的感谢给我的“战友”们，感谢孟老师小组中的每一位成员对我无死角地帮助和关心。强哥作为我们的技术担当，将微生物这个武器武装到了每一个人；坤哥作为我们的大哥，有担当有作为，值得每一个人学习；陈吉作为我们的大总管，工作细致入微，为我们提供了坚实的保障；谦朔和东哥作为实验室的后起之秀，未来可期；宏姐作为课题组的卷王，虽然卷大家也为大家带来了不少笑料。同样的感谢送给湛哥、嘉嫣、小邴，以及已经离开的陆本琦、黎珊、孔坤、马超和穆哈。

额外要感谢的是我之前的老师们，感谢张进忠老师、王飞越老师、王定勇老师，以及韬哥。是你们对我之前的培养，让我有了今天更好的成长。特别是韬哥，3 年前，是韬哥给孟老师拨通了电话，随后我来到了地化所，明天我的出站答辩韬哥又来带我离开贵阳，也算有始有终，希望这 3 年没有给韬哥丢脸。

最后的感谢献给我的家人，感谢父母以及岳父岳母对我的理解，我能感受到 30 好几岁的人一家三口分居三地时来自长辈的焦虑；感谢我的爱人黄容，3 年来我们坚守异地，为了更好地相聚；也感谢我的女儿，目前来说我还不是称职的父亲，因为给你的陪伴寥寥可数，希望在后面的日子里，我能陪着你健康快乐地成长！

现在，地化所对我来说已经变成了新的舒适圈，又到了需要我跳出舒适圈，迎接新生活，新挑战的时候了！谢谢你，地化所！

刘江

2023 年 8 月 22 日夜

作者简历及博士后期间发表的学术论文

作者简历：

刘江，男，1989 年 10 月出生于甘肃省兰州市。

2008 年 9 月——2012 年 6 月，在兰州财经大学，资源环境与城乡规划管理专业获得理学学士学位。

2012 年 9 月——2019 年 6 月，在西南大学，农业资源与环境专业获得农学博士学位。

2016 年 9 月——2018 年 9 月，在加拿大曼尼托巴大学，地质与环境学院进行博士研究生联合培养。

2019 年 6 月——2020 年 6 月，在西南大学天然有机质实验室，从事科研助理工作。

2020 年 6 月——2023 年 8 月，在中国科学院地球化学研究所，从事博士后研究工作。

主持项目：

1. 国家自然科学基金委青年项目“铁氧化物/铁硫化物-溶解性有机质体系对稻田土壤汞甲基化过程的影响（42107442）”，2022-2024 年。
2. 贵州省科技厅基础研究计划（自然科学类）项目“喀斯特区域汞胁迫下稻田土壤甲烷排放与汞环境归趋的互作研究”，2023-2025 年。

博士后期间发表的论文：

Liu J., Chen J., Poulain A.J., Pu Q., Hao Z.D., Meng B*., Feng X.B. (2023) Mercury and sulfur redox cycling affect methylmercury levels in rice paddy soils across a contamination gradient. ***Environmental Science & Technology*** 57, 8149–8160.

Liu J., Zhao L*., Kong K., Abdelhafiz M., Tian S.Y., Jiang T., Meng B*., Feng X.B. (2022) Uncovering geochemical fractionation of the newly deposited Hg in paddy soil using a stable isotope tracer. ***Journal of Hazardous Materials*** 433, 128752.

Liu J., Lu B., Poulain A. J., Zhang R., Zhang T., Feng X.B., Meng B*. (2022) The underappreciated role of natural organic matter bond Hg(II) and nanoparticulate HgS as substrates for methylation in paddy soils across a Hg concentration gradient. ***Environmental Pollution*** 112075.

Liu J., Meng B*., Poulain A. J., Meng Q., Feng X.B*. (2021) Stable isotope tracers identify sources and transformations of mercury in rice (Oryza sativa L.) growing in a mercury mining area. ***Fundamental Research*** 1, 259–268.

Zhang, R., Aris-brosou, S., Storck, V., **Liu, J.**, Abdelhafi, M.A., Feng, X., Meng, B*., Poulain, A.J*. (2023). Mining-impacted rice paddies select for Archaeal methylators and reveal a putative (Archaeal) regulator of mercury methylation. ***ISME Communications*** 1–13.

Abdelhafiz M.A., **Liu J.**, Jiang T., Pu Q., Wajahat M., Zhang K., Meng B*., Feng X.B. (2023). DOM influences Hg methylation in paddy soils across a Hg contamination gradient. ***Environmental Pollution*** 322, 121237.

Pu Q., Zhang K., Poulain A J., **Liu J.,** Zhang R., Abdelhafiz M A., Meng B*., Feng X.B. (2022). Mercury drives microbial community assembly and ecosystem multifunctionality across a Hg contamination gradient in rice paddies. ***Journal of Hazardous Materials*** 435, 129055

Aslam M. W., Meng B*., Abdelhafiz M. A., **Liu J.** and Feng X.B. (2022) Unravelling the interactive effect of soil and atmospheric mercury influencing mercury distribution and accumulation in the soil-rice system. ***Science of the Total Environment*** 803, 149967

后附与本报告内容相关的已发表学术论文

Environmental Pollution 292 (2022) 118321

Contents lists available at ScienceDirect

Environmental Pollution

journal homepage: www.elsevier.com/locate/envpol

The underappreciated role of natural organic matter bond Hg(II) and nanoparticulate HgS as substrates for methylation in paddy soils across a Hg concentration gradient

Jiang Liu [a], Benqi Lu [a,b], Alexandre J. Poulain [c], Rui Zhang [c], Tong Zhang [d], Xinbin Feng [a,e], Bo Meng [a,*]

[a] State Key Laboratory of Environmental Geochemistry, Institute of Geochemistry, Chinese Academy of Sciences, Guiyang, 550081, China
[b] University of Chinese Academy of Sciences, Beijing, 100049, China
[c] Biology Department, University of Ottawa, 30 Marie Curie, Ottawa, ON, K1N 6N5, Canada
[d] College of Environmental Science and Engineering, Ministry of Education Key Laboratory of Pollution Processes and Environmental Criteria, Tianjin Key Laboratory of Environmental Remediation and Pollution Control, Nankai University, Tianjin, 300350, China
[e] Center for Excellence in Quaternary Science and Global Change, Chinese Academy of Sciences, Xi'an, 710061, China

ARTICLE INFO

Keywords:
Mercury
Mercury species
Methylation
Demethylation
Rice paddy

ABSTRACT

Rice consumption is the major pathway for human methylmercury (MeHg) exposure in inland China, especially in mercury (Hg) contaminated regions. MeHg production, a microbially driven process, depends on both the chemical speciation of inorganic divalent mercury, Hg(II), that determines Hg bioavailability for methylation. Studies have shown that Hg(II) speciation in contaminated paddy soils is mostly controlled by natural organic matter and sulfide levels, which are typically thought to limit Hg mobility and bioavailability. Yet, high levels of MeHg are found in rice, calling for reconsideration of the nature of Hg species bioavailable to methylators in paddy soils. Here, we conducted incubation experiments using a multi-isotope tracer technique including $^{198}Hg(NO_3)_2$, natural organic matter bond Hg(II) (NOM-^{199}Hg(II)), ferrous sulfide sorbed Hg(II) (≡FeS-^{200}Hg(II)), and nanoparticulate mercuric sulfide (nano-^{202}HgS), to investigate the relative importance of geochemically diverse yet relevant Hg(II) species on Hg methylation in paddy soils across a Hg concentration gradient. We show that methylation rates for all Hg(II) species tested decreased with increasing Hg concentrations, and that methylation rates using NOM-^{199}Hg(II) and nano-^{202}HgS as substrates were similar or greater than rates obtained using the labile $^{198}Hg(NO_3)_2$ substrate. ≡FeS-^{200}Hg(II) yielded the lowest methylation rate in all sites, and thus the formation of FeS is likely a sink for labile $^{198}Hg(NO_3)_2$ in sulfide-rich paddy soils. Moreover, the variability in the methylation data for a given site (1 to 5-fold variation depending on the Hg species) was smaller than what was observed across the Hg concentration gradient (10^3–10^4 fold variation between sites). These findings emphasize that at broad spatial scales, site-specific characteristics, such as microbial community structure, need to be taken into consideration, alongside the nature of the Hg substrate available for methylation, to determine net MeHg production. This study highlights the importance of developing site-specific strategies for remediating Hg pollution.

1. Introduction

Mercury (Hg) compounds are toxic pollutants, in which methylmercury (MeHg) can be bioaccumulated and biomagnified along the food chains posing potential threat to human health. It is generally accepted that fish consumption is the major exposure pathway of MeHg worldwide (Clarkson et al., 1993). Recently, however, rice (*Oryza sativa* L.) was identified as a bio-accumulator plant of MeHg (Qiu et al., 2008; Zhang et al., 2010a; Meng et al., 2010, 2011, 2014). As a result, rice consumption was shown to be the dominant MeHg exposure route to residents in inland China, especially in Hg contaminated regions (Feng et al., 2008; Zhang et al., 2010b; Li et al., 2012). Moreover, Hg contaminated rice remains a global issue affecting countries other than China, as MeHg contaminated rice has been reported previously in many

* Corresponding author.
E-mail address: mengbo@vip.skleg.cn (B. Meng).

https://doi.org/10.1016/j.envpol.2021.118321
Received 10 August 2021; Received in revised form 7 September 2021; Accepted 7 October 2021
Available online 8 October 2021

places including Indonesia (Krisnayanti et al., 2012), India (Lenka et al., 1992), Pakistan (Aslam et al., 2020) and Philippines (Appleton et al., 2006). Importantly, all of these countries are main rice exporters in the world, which therefore make dietary exposure of MeHg through rice a global challenge (Liu et al., 2019). Previous studies confirmed that MeHg in rice was originated from *in-situ* methylation of inorganic Hg in paddy soils (Meng et al., 2010, 2014; Zhao et al., 2016b; Qin et al., 2020; Liu et al., 2021a). As a typical ephemeral wetland, the submerged paddy soil is an ideal habitat for Hg methylating microorganisms carrying *hgc*AB genes (Gilmour et al., 2013; Parks et al., 2013; Podar et al., 2015; Liu et al., 2018). Accordingly, paddy soil has long been considered as a "hotspot" for Hg methylation (Rothenberg and Feng, 2012).

Multiple biological, physical and chemical factors determine net Hg methylation, including microbial community structure and function, Hg speciation, temperature, pH, redox, or natural organic matter (NOM) quality and quantity (Bravo and Cosio, 2020; Regnell and Watras, 2018). Among those factors, the speciation and bioavailability of Hg is considered one of the most important factors controlling net MeHg production (Hsu-kim et al., 2013; Wang et al., 2014; Regnell and Watras, 2018; Li et al., 2019; Liang et al., 2021; Liu et al., 2021b). The chemical nature of the Hg species bioavailable for Hg methylation is diverse and complex, ranging from inorganic to organic-bound Hg (Hsu-kim et al., 2013). Of particular interest in the context of rice paddies (Zhao et al., 2016a, b) are possibly Hg species formed by association with dissolved inorganic ligands (*e.g.*, HS^- (Jonsson et al., 2012; Liem-Nguyen et al., 2016; Zhu et al., 2018)), dissolved organic matter (DOM) (Jonsson et al., 2012; Liem-Nguyen et al., 2016; Mazrui et al., 2016; Zhu et al., 2018), sulfides (as nanosized Hg particles) (Zhang et al., 2012, 2014; Tian et al., 2021), and ferrous sulfide sorbed Hg(II) (Jonsson et al., 2012). However, the bioavailability and relative contribution of each Hg species to net Hg methylation, especially in Hg contaminated paddy soils remain unknown. Identifying the most relevant chemical species of Hg bioavailable for methylation in rice paddy soils has significant implications for remediation strategies.

To fill these knowledge gaps, we conducted a 2-day slurry incubation experiments jointly with a multi-isotope technique. Hg species including $^{198}Hg(NO_3)_2$, NOM bond $^{199}Hg(II)$, FeS sorbed $^{200}Hg(II)$, nanoparticulate ^{202}HgS and $Me^{198}Hg$ were prepared to trace methylation rates of geochemically relevant Hg(II) species and demethylation rate of MeHg over a Hg concentration gradient in paddy soils. The objectives of this study were: (1) to identify the bioavailability and methylation rates of Hg species in paddy soils, and (2) to determine the influence of a Hg concentration gradients on Hg methylation/demethylation. We expect these results to provide a theoretical basis for remediation of Hg polluted paddy soil and scientific guidance for risk assessment of Hg pollution in Hg mining area.

2. Materials and methods

2.1. Site description and sampling

Submerged soil and corresponding overlying water samples were collected from three paddy fields in Guizhou province, China from August 13th to 15th, 2019 during the cultivation of rice (50–60 days after the rice was planted, heading stage of rice growing). This period was chosen because relatively high net MeHg production and Hg methylation rates were found in our previous studies (Zhao et al., 2016a, b). Two rice paddy fields are located in Wanshan Hg mining area (WSHM, 109°07′-109°24' E, 27°24′-27°38' N; Fig. 1a) as Hg-contaminated sites, including an artisanal Hg smelting site (Gouxi, GX) and an abandoned Hg mining site (Sikeng, SK). GX and SK are typical Hg contaminated sites in WSHM, showing different Hg sources,

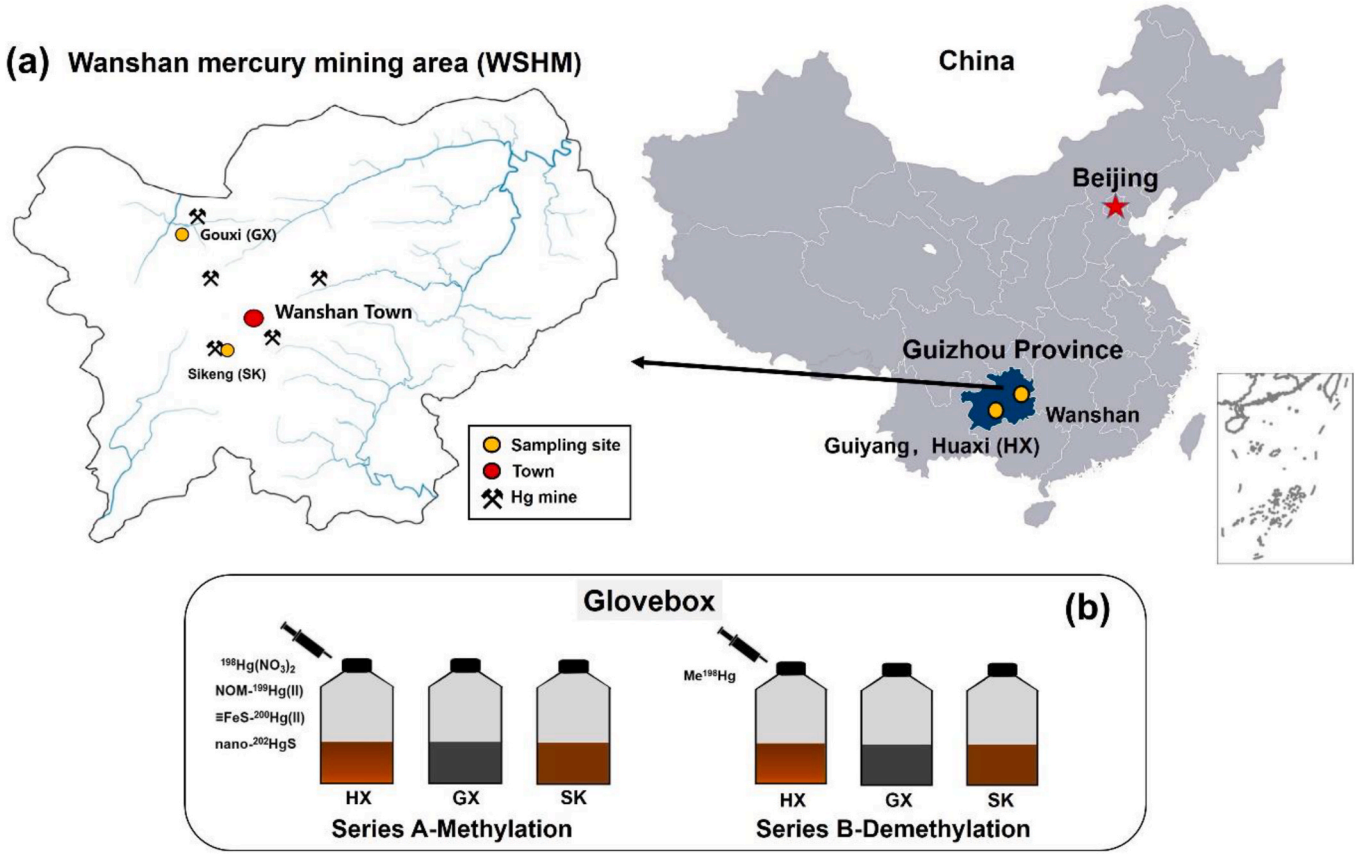

Fig. 1. Sampling sites (a) and illustration of the incubation design (b). HX, GX, and SK represent the slurries prepared by Gouxi, Sikeng, and Huaxi paddy soils, respectively.

contamination levels, and soil Hg fractions (Meng et al., 2010; Zhao et al., 2016a, b; Wu et al., 2020). In artisanal Hg smelting site (GX), the paddy fields were contaminated by atmospheric Hg deposition due to the high gaseous Hg in the air from previous smelting activities (Zhao et al., 2016b). In abandoned Hg mining site (SK), mining wastes and tailings remain to be the dominant Hg source, and therefore insoluble mercuric sulfide (*e.g.*, metacinnabar) is the major Hg fraction. One more paddy field is located in Huaxi district of Guiyang City (HX) as the non-Hg polluted control. The climate of Huaxi is similar to the WSHM area, but no Hg sources were found in this area (Fig. 1a). Soil types for these three sites are the same of hydragric anthrosols originate from gleyic cambisol (IUSS, 2006).

Surface layer of submerged soils (1–5 cm) were collected into 500 mL pre-cleaned polypropylene (PP) bottles (Thermo Scientific, Nalgene®, USA) without any headspace. Three submerged soils were collected at each site. Overlying water samples (1–3 cm above the soil-water interface) were collected using a 250 mL acid-precleaned syringes, and then transferred into PP bottle. All PP bottles filled with samples were sealed by Parafilm® and double bagged in ziplock bags separately in case of any cross-contamination. Samples were transported in coolers with ice packs to the lab within 24 h, and stored at 3–4 °C in the dark until further laboratory processing.

2.2. Preparation and characterization of isotope-enriched Hg species

Isotope-enriched inorganic Hg tracers (^{198}Hg (95.3 ± 0.15 %), ^{199}Hg (92.6 ± 0.15 %), ^{200}Hg (98.2 ± 0.15 %) and ^{202}Hg (99.2 ± 0.15 %)) and MeHg tracer (Me^{198}Hg) were used to trace inorganic Hg methylation and MeHg demethylation rates, respectively. Inorganic Hg tracers were purchased from ISOFLEX (USA). Four geochemically relevant Hg(II) species were synthesized in this study to trace the methylation, simultaneously, including (1) Hg(II) in nitrate solution (^{198}Hg(NO$_3$)$_2$), (2) natural organic matter (NOM) bond Hg(II) (NOM-^{199}Hg(II)), (3) ferrous sulfide sorbed Hg(II) (≡FeS-^{200}Hg(II)), and (4) nanoparticulate mercuric sulfide (nano-^{202}HgS). ^{198}Hg(NO$_3$)$_2$ was prepared by dissolve ^{198}Hg^0 in nitric acid (≥99.9 %, trace metals basis) (20 μg mL^{-1} and 1 μg mL^{-1}). NOM-^{199}Hg(II) (2.95 μg Hg mL^{-1}) was synthesized by using Suwannee River NOM (SRNOM) (International Humic Substances Society, HISS) in a glovebox (PLAS-LABS, USA). After the mixing of standard NOM and ^{199}Hg(II), the stock solution was homogenized by ultrasonication for few seconds and then equilibrated for 5 days at 4 °C (Jonsson et al., 2012). Ferrous sulfide (FeS(s)) was synthesized by dissolving Fe(NH$_4$)$_2$(SO$_4$)$_2$ and Na$_2$S·9H$_2$O in deoxygenated Milli-Q water in the glovebox ([FeS(s)] = 14.9 mg mL^{-1}). The reaction was left overnight and the newly formed FeS(s) was washed three times to remove residual sulfide (S(-II), the sum of [H$_2$S], [HS$^-$], and [S^{2-}]). ^{200}Hg(II) was added to deoxygenated Milli-Q® water (Millipore, USA) containing 0.1 g FeS(s) to form ≡FeS-^{200}Hg (II) ([≡FeS-^{200}Hg(II)] = 23.8 μg Hg mL^{-1}) (Jonsson et al., 2012). Nanoparticulate HgS was prepared by freshly dissolved N$_2$S·9H$_2$O and ^{202}Hg(II) stock ([nano-^{202}HgS] = 10.03 μg mL^{-1}). Suwannee River humic acid (HISS) (10 mg C L^{-1}) dissolved in 0.1 M NaNO$_3$ and 4 mM sodium 4-(2-hydroxyethyl) piperazine-1-ethanesulfonate (HEPES) buffer (pH 7.5) were used to stabilize nanoparticles (*i.e.*, mitigate the aggregation) (Zhang et al., 2012). The suspension was aged in the glovebox at room temperature for one week and then double filtered to a particle size <0.1 μm (Zhang et al., 2012). Me^{198}HgNO$_3$ was prepared by the methylcobalamin method (Rodríguez Martín-Doimeadios et al., 2002). Stock of Me^{198}Hg (3.77 μg mL^{-1}) was diluted into two working solutions (37.7 ng mL^{-1} and 3.77 ng mL^{-1}) to spike to Hg contaminated and the control microcosms.

Stock solutions for the prepared Hg species are shown in Fig. A1. The presence and the elemental composition of synthesized ≡FeS-^{200}Hg(II) and nano-^{202}HgS were characterized by the transmission electron microscopy (TEM) (Tecnai G2 F20 S-TWIN, FEI, USA). Droplets from particle stock solutions were deposited on a carbon-coated copper grid, and the excess liquid was wiped by Kimwipes. The particles were examined at 200 KeV after the air drying of the grid. Elemental composition of these particles were characterized by the equipped energy dispersive X-ray spectroscopy (EDX) (EDAX, USA) with TEM. Images of ≡FeS-^{200}Hg(II) and nano-^{202}HgS as well as their elemental compositions are shown in Fig. A.2 and Fig. A.3.

2.3. Incubation experiments

Anaerobic incubation of rice paddy slurries using serum bottles was conducted in an oxygen-free (filled by N$_2$) glovebox (PLAS-LABS, USA). The details in preparation of slurries is described in Text A.1. Two series of incubation were setup simultaneously, Hg tracers of ^{198}Hg(NO$_3$)$_2$, NOM-^{199}Hg(II), ≡FeS-^{200}Hg(II), and nano-^{202}HgS were spiked in Series A to trace the inorganic Hg methylation during the incubation. MeHg tracer (Me^{198}HgNO$_3$) was spiked in Series B to trace the MeHg demethylation (illustrated by Fig. 1b). The spiked concentrations of inorganic Hg and MeHg tracers are 10 % and 100 % of background total Hg (THg) and MeHg in rice paddies, respectively (Gilmour et al., 1998; Zhao et al., 2016a; Wu et al., 2020). It is noteworthy that the amounts of nitrate (NO_3^-, added as Hg(NO$_3$)$_2$) added in the incubation systems are too low to influence the reduction reactions (*e.g.*, sulfate reduction and iron reduction).

After the spike of isotope-enriched Hg tracers, serum bottles were then capped with butyl rubber stoppers, aluminium seals and incubated at room temperature for 2 days in dark (covered with aluminium foil) (96 bottles were setup in total, 48 bottles for each series and 16 bottles for each site). Three random replicates were withdrawn in both series A and B at 0, 0.25, 0.5, 1.0 and 2 days, respectively. Slurries (30 mL) used for pH, total sulfide ([S(-II)), sulfate (measures as water-soluble sulfate, SO_4^{2-}), [Fe^{2+}], [Fe^{3+}] and water-soluble soil organic carbon (WSOC) analyzes were destructively subsampled into 50 mL polypropylene (PP) tubes (JET, BIOFIL, China). Slurry samples used for DNA extraction was subsampled in 1.5 mL sterile cryogenic tubes (Thermo Scientific, Nalgene®, USA) and then stored at −80 °C. The remaining slurries used for Hg isotope analysis were acidified by 1 mL 6 N HCl and frozen at −20 °C immediately to stop the methylation and demethylation. All the subsampling was conducted in the glovebox (PLAS-LABS, USA).

2.4. Analytical methods

Isotope-enriched MeHg species (*i.e.*, Me^{198}Hg, Me^{199}Hg, Me^{200}Hg, Me^{201}Hg and Me^{202}Hg) were analyzed by using a gas chromatography inductively coupled plasma mass spectrometry (GC-ICP-MS, Agilent 7700×, Agilent Technologies Inc., USA) system following the ethylation-purge-trap method (Gilmour et al., 1998; Hintelmann et al., 1995, 2000). More details related to isotope-enriched MeHg extraction and measurement can be found in our previous studies (Zhao et al., 2016a; Wu et al., 2020; Lu et al., 2021). Isotope-enriched THg was determined by using ICP-MS (Agilent 7700×, Agilent Technologies Inc., USA) system following aqua regia digestion. Details for the procedures of THg digestion are described in Supplementary Material (Text A.2). Additionally, DNA in the original paddy soils were extracted (9 samples in total, three for each site). 16S rRNA gene amplicon high throughput sequencing was conducted to identified the diversity and richness of bacterial communities (details can be found in Text A.3). Quantitative PCR (qPCR) for *hgc*AB genes was performed by using ORNL-HgcAB-uni-F/R primer and clade-specific *hgc*A in *Deltaproteobacteria* (ORNL-Delta-HgcA-F/R). More details related to primers and PCR conditions are shown in Text A.4. Measurement of soil pH, SO_4^{2-}/S(-II), Fe^{2+}/Fe^{3+}, water-soluble soil organic carbon, mineralogy characters (XRD), as well as geochemical properties of background paddy soils including soil texture, ammonium nitrogen (NH_4^+-N), nitrate nitrogen (NO_3^--N) and porewater chemistry are introduced in the Supplementary Material (Text A.5).

2.5. Data analysis and QA/QC

Formation of isotope-enriched $Me^{198}Hg$, $Me^{199}Hg$, $Me^{200}Hg$ and $Me^{202}Hg$ was used to indicate the methylation of inorganic Hg tracers. Decrease of $Me^{198}Hg$ was used to show the demethylation of MeHg tracers. Production of MeHg from added isotope-enriched Hg(II) tracers and MeHg demethylation from added $Me^{198}Hg$ tracers were calculated as MeHg/Hg(II) (%) and MeHg demethylation (%). Methylation rate constant (K_m, d^{-1}) and demethylation rate constant (K_d, d^{-1}) were also calculated. All the details related to calculation are shown in Text A.6. It is noted that Hg isotope fractionation occurs in some biogeochemical processes (*e.g.*, methylation, demethylation and photoreduction) (Bergquist and Blum, 2007; Kritee et al., 2009; Janssen et al., 2016), whereas these isotope fractionations could be neglected in isotope-enriched Hg tracer spiked studies (Mao et al., 2013; Meng et al., 2018). Statistics were performed using SPSS 23.0 (IBM®, IL, USA) and Origin Pro 2018 (OriginLab®, MA, USA). Normality of datasets was assessed by Shapiro-Wilk test. T-test and One-way ANOVA with Duncan's post-hoc test were used for normal distributed datasets; Mann-Whitney *U* test and Kruskal-Wallis one-way ANOVA test were used for non-normal distributed datasets. Statistical significance (p) was declared at <0.05 (2-tailed).

Certified reference material (CRM) of ERM-CC580 (Estuarine sediment from European Reference Materials, [MeHg] = 75.5 ± 3.7 μg kg^{-1}) was used for quality control during measurement; the recoveries for CRM ranged from 99 % to 125 %, with an average of 111 ± 8.86 %. In addition, isotope-enriched THg (*i.e.*, sum of spiked inorganic Hg tracers and methylated MeHg) was measured at beginning and the end of the incubation to show the recovery of the spiked Hg tracers (Fig. A.4). The recoveries ranged from 93.5 % to 107 %, with an average of 100.0 ± 3.59 % (n = 40), indicating losses or contamination of isotope-enriched Hg was negligible during incubation processes. Method detection limit (3σ) for isotope-enriched MeHg isotopes, Fe^{2+} and S(-II) were 0.013 ng L^{-1}, 0.045 mg L^{-1} and 4.16 μg L^{-1}, respectively.

3. Results

3.1. Methylation of different Hg(II) tracers in paddy soil microcosms

Methylmercury production from added isotopic Hg(II) species (MeHg/Hg(II) in %) and corresponding methylation rate constant (K_m) within the incubation periods are shown in Fig. 2. All Hg(II) tracer species except ≡FeS-^{200}Hg(II) yielded significant MeHg production over time (Fig. 2a–c). Overall, isotope-enriched MeHg/Hg(II) decreased by several orders of magnitude over the contamination gradient (from HX to GX to SK sites, with increasing THg concentrations from HX to SK) (Fig. 2a–c); MeHg/Hg(II) ranged 2–5 % for HX, 0.3–0.35 % for GX and 0.002–0.005 % for SK. The same trend was observed for the K_m calculated between each time points (Fig. 2d–f). Depending on the site, we observed differences in the nature of the Hg species yielding the greatest MeHg production corrected for Hg(II) substrate levels.

At the control site (HX; [THg] = 0.27 mg kg^{-1}, Table A.1), the greatest MeHg production (shown as MeHg/Hg(II)) was observed for $^{198}Hg(NO_3)_2$ (4.85 ± 0.13 %) followed by NOM-^{199}Hg(II), nano-^{200}HgS and ≡FeS-^{200}Hg(II) (p < 0.05, Fig. 2a). At the intermediate contamination site (GX; [THg] = 3.34 mg kg^{-1}, Table A.1), NOM-^{199}Hg(II) yielded the highest MeHg production with $^{198}Hg(NO_3)_2$ and nano-^{200}HgS yielding comparable MeHg production at the end of the incubation period (p < 0.05, Fig. 2b). Finally, at the most contaminated site (SK; [THg] = 48.93 mg kg^{-1}), NOM-^{199}Hg(II) was the species yielding the greatest MeHg production followed by nano-^{200}HgS (p < 0.05, Fig. 2c). For the control (HX) and most contaminated (SK) site samples, MeHg production increased over time to eventually reach a plateau (Fig. 2a and c). Interestingly, in Gouxi (GX) microcosms, MeHg

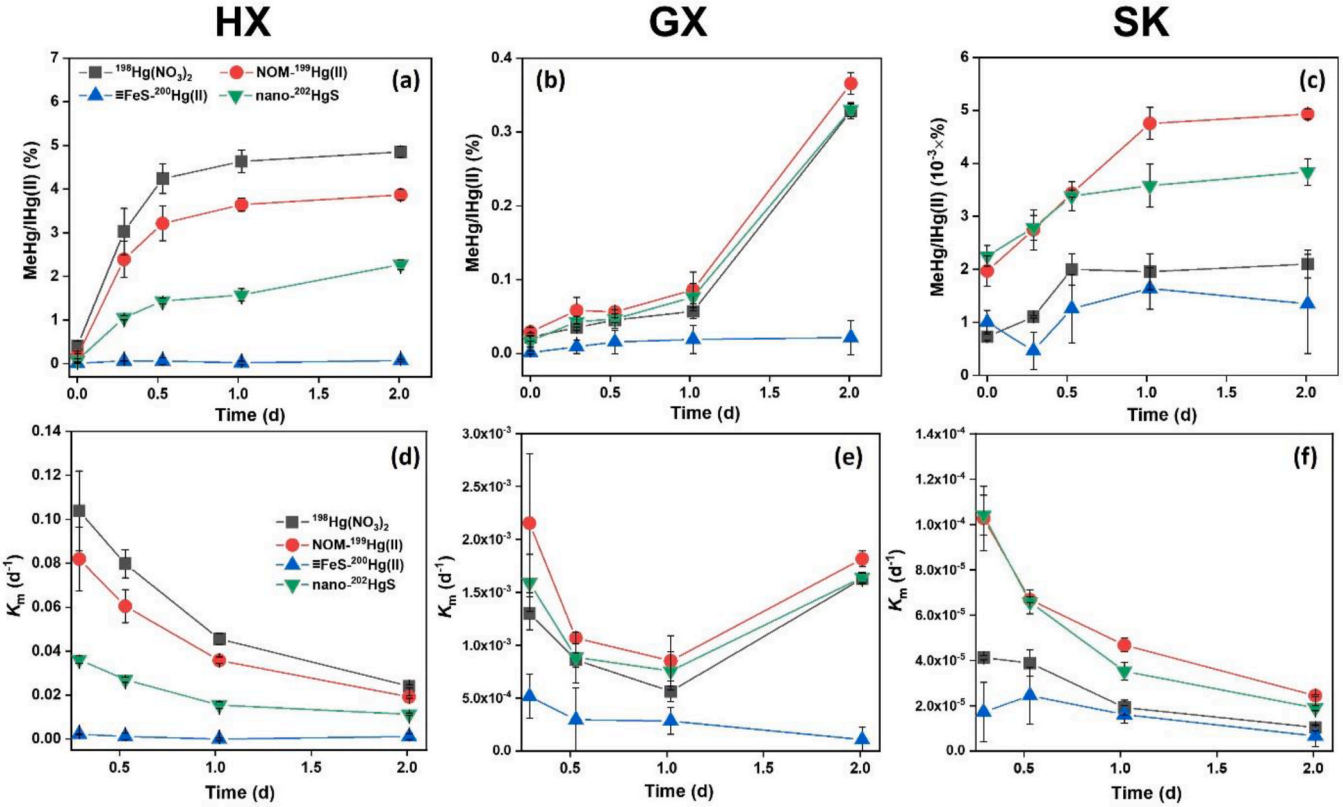

Fig. 2. Methylmercury production (MeHg/Hg(II), a, b and c) and methylation rate constant (K_m, d, e and f) as a function of time for different Hg(II) tracers in three microcosms. Huaxi (HX), Gouxi (GX), and Sikeng (SK). NOM-^{199}Hg(II) represents natural organic matter bond Hg(II); ≡FeS-^{200}Hg(II) represents mackinawite adsorbed Hg (II); and nano-^{202}HgS represents nanoparticulate HgS. Error bars indicate the standard deviation (±SD) for replicates (n = 3).

production was low for the first day and rapidly increased afterwards (Fig. 2a).

Methylation rate constants (K_m) were typically greater at the beginning of all experiments and subsequently decreased over time, which is consistent with pure culture experiments (Gilmour et al., 2018). At the control site (HX) and for the most contaminated site (SK), all K_m decreased over the first day and continued to do so afterwards (Fig. 2d and f). At GX, the artisanal Hg mining site exhibiting intermediate [THg], K_m for all species tested (except ≡FeS-^{200}Hg(II)) increased during the second day of the incubation to reach values similar to what was observed at the beginning of the experiment (Fig. 2e).

Using ≡FeS-^{200}Hg(II) as a substrate yielded significantly lower MeHg production than for the other Hg(II) species (*i.e.*, $^{198}Hg(NO_3)_2$, NOM-^{199}Hg(II), and nano-^{202}HgS) in GX and HX ($p < 0.05$). Concentrations of isotope-enriched MeHg and ambient MeHg are shown in Fig. A.5 and Fig. A.6, respectively. It can be seen that the concentrations of isotope-enriched MeHg are about 10 % of the ambient MeHg, suggesting proper amount of Hg(II) isotopes were added in this study. On one hand, the calculation of excess of MeHg isotopes (*i.e.*, isotope-enriched MeHg) could be biased by high ambient MeHg concentrations; on the other hand, an excessive amount of isotope-enriched Hg tracer may inhibit Hg methylation (Jonsson et al., 2012).

3.2. Demethylation of MeHg tracer in paddy soil microcosms

The greatest demethylation was observed at the most contaminated site, SK (Fig. 3). At the end of incubation, 44.26 ± 6.79 %, 47.03 ± 6.45 %, 80.99 ± 3.86 %, of spiked Me^{198}Hg was demethylated in the HX, GX, and SK and microcosms, respectively (Fig. 3a and Fig. A.5d). In SK and HX microcosms, K_d decreased gradually from 2.28 ± 0.18 d^{-1} and 1.38 ± 0.17 d^{-1} to 0.84 ± 0.12 d^{-1} ($p < 0.05$) and 0.31 ± 0.04 d^{-1} ($p < 0.05$), respectively. K_d in the GX microcosms decreased rapidly within half of a day (from 1.03 ± 0.59 d^{-1} to 0.33 ± 0.06 d^{-1}, $p > 0.05$), and then remained stable (Fig. 3b).

3.3. Dynamics of sulfur, iron and dissolved organic carbon in methylation assay

Concentrations of Fe^{2+}, Fe^{3+}, and S(-II) in the liquid phase of fresh slurries and SO_4^{2-} (*i.e.*, water-soluble SO_4^{2-}), soil dissolved organic carbon (*i.e.*, water-soluble SOC, WSOC) in freeze dried slurries were determined to reveal the dynamics of major electron acceptors/donors during methylation incubation (Fig. A.7). Higher Fe concentrations (both Fe^{2+} and Fe^{3+}) were observed in SK microcosms than those in GX and HX microcosms ($p < 0.05$). Variation trends of Fe^{2+} and Fe^{3+} in SK microcosms suggest a rapid (within one day) Fe^{3+} reduction accompanied by Fe^{2+} formation (Fig. A.7a and A.7b). Significant Fe reduction in GX microcosms occurred at the later period of incubation (second day of incubation), whereas Fe reduction in HX microcosms are not likely happened due to the relative stable concentrations of both Fe^{2+} and Fe^{3+} (Fig. A.7a and A.7b).

Sulfide concentrations in GX and HX microcosms are relative stable with only some minor fluctuations during incubation (Fig. A.7c). Higher S(-II) concentration was observed at the initial period of SK microcosms, and then decreased continuously (from 67.1 ± 3.7 μg L^{-1} to 22.7 ± 3.7 μg L^{-1}, $p < 0.05$). The consumption of S(-II) and Fe^{2+} in SK microcosms during incubation are likely the formation of FeS. Higher SO_4^{2-} during incubation were observed in SK microcosms (936 ± 61.4 mg kg^{-1}) than those in HX (491 ± 4.3 mg kg^{-1}) and GX microcosms (551 ± 47.3 mg kg^{-1}) ($p < 0.05$, Fig. A.7d). Slight decreases of SO_4^{2-} were found in SK microcosms during the first day of incubation ($p > 0.05$), whereas increases of SO_4^{2-} were observed in GX microcosms ($p < 0.05$). Concentrations of SO_4^{2-} in HX microcosms were stable during the entire incubation period. The water-soluble soil organic carbon (WSOC) content remained constant throughout the duration of the incubation experiments (Fig. A.7e) but its value decreased from SK (2.38 ± 0.12 g kg^{-1}), to HX (1.42 ± 0.12 g kg^{-1}), to GX (0.77 ± 0.05 g kg^{-1}).

3.4. Bacterial community analysis and quantification of hgcA genes

Overall, a total of 16,027 features (ASVs) were recovered, from which 61 bacterial phyla (2 unclassified), 170 classes (39 unclassified), 364 orders (114 unclassified), 598 families (260 unclassified), 1009 genera (464 unclassified) were determined across the 9 samples. Despite the vast richness of the microbial communities, 16S rRNA gene amplicon sequencing showed that all samples appeared to be dominated by bacteria from phyla *Proteobacteria*, *Acidobacteria*, *Chloroflexi* and *Bacteroidetes*, which represent more than 70 % of relative abundance across all samples. Meanwhile, the dominating classes were *Gammaproteobacteria*, *Deltaproteobacteria, Subgroup_6*, *Anaerolinae*, *Bacteroidia*, and *Alphaproteobacteria*, together representing more than 60 % of the relative abundance in all samples (Fig. A.8). Alpha diversity indices including Shannon and Chao1 were determined for the 9 samples (*i.e.*, 3 samples for each site) (Table A.2). In spite of non-significant differences of the

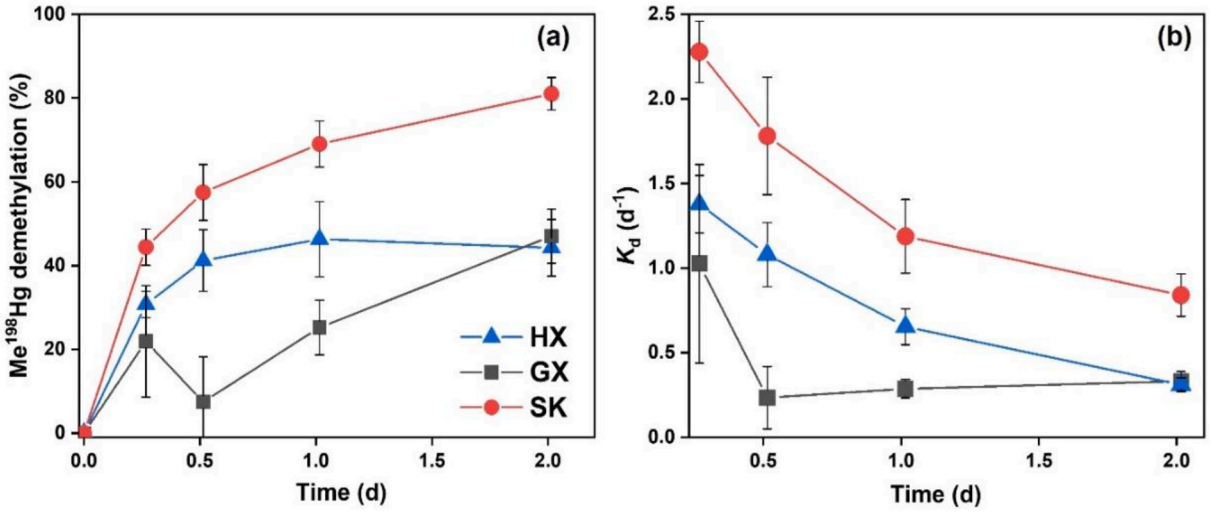

Fig. 3. MeHg demethylation (a) and demethylation rate constant (K_d) as a function of time in three microcosms. MeHg demethylation was represented by the variations of ^{198}MeHg demethylation (% of initial). HX, GX, and SK indicate three paddy soils collected from Gouxi, Sikeng, and Huaxi, respectively. Error bars are the standard deviation (±SD) for three replicates ($n = 3$).

two indices between sites (Shannon: Kruskal-Wallis chi-squared = 2.62, df = 2, p = 0.27; Chao1: Kruskal-Wallis chi-squared = 1.69, df = 2, p = 0.43), HX and GX exhibited similar results for the two indices, whereas SK showed the lowest values, potentially suggesting an inhibitory effect of high THg concentration on the microbial community structure. Regarding the beta diversity, unconstrained principal coordinate analysis (PCoA) of weighted and unweighted UniFrac distance metrices were conducted at the species level to assess microbial community structure differences across samples (Fig. A.9). Samples from the same site tend to cluster together (PCoA plots, Fig. A.9), and the permutational multivariate analysis of variance (PERMANOVA) tests showed that samples are more closely related to each other within a given site, rather than across sites (Fig. A.9 and Table A.3).

*hgc*AB gene cluster is an essential determinant for Hg(II) methylation (Parks et al., 2013). To test whether variations in MeHg production across sites may be associated with corresponding changes in the abundance of this gene cluster, we used qPCR targeting *hgc*A and *hgc*B (Livak and Schmittgen, 2001 and Text A.4). Using the ORNL-*hgc*AB-uniF/R primer sets, we observed that HX exhibited the highest relative *hgc*AB copy number, whereas SK exhibited the lowest (Fig. A.10a). However, when using a clade-specific primer set (*i.e.*, ORNL-Delta-*hgc*A) that target only *hgc*A from *deltaproteobacteria*, GX site samples exhibited the highest abundance (Fig. A.10b).

4. Discussion

4.1. Importance of NOM-Hg(II) and nano-HgS methylation in paddy soils

It is generally accepted that the presence of NOM will decrease the bioavailability of Hg and inhibit MeHg formation in aquatic environments (Barkay et al., 1997; Ravichandran, 2004) due to the formation of large macromolecular and hydrophilic Hg-NOM complexes (Hsu-kim et al., 2013; Chiasson-Gould et al., 2014). However, results of this study showed that NOM-^{199}Hg(II) was readily methylated at all three sites, and even yielding more MeHg than the other species as [THg] concentrations increased over the contamination gradient (Fig. 2 and Fig. A.11).

The water-soluble soil organic carbon (WSOC) content did not appear to control MeHg production nor degradation for the various sites, which may suggest that microbes were not limited by an organic substrate to conduct MeHg transformation. In fact, the presence of naturally occurring NOM at all site may have interacted with the various Hg species used, possibly affecting the outcome of the incubation experiments. Indeed, previous work has found that Hg(II) bound to humic acid showed a higher mobility than dissolved Hg(II)-Cl/-OH complexes, Hg(0) and HgS nanoparticles in a leaching experiment (Gai et al., 2016) and the equilibrium of Hg(II) with NOM reduced Hg(II) partition onto solid phases (Johs et al., 2019). High and comparable K_m values obtained for ^{201}Hg(NO$_3$)$_2$ and NOM-^{202}Hg(II) used as substrate in methylation experiments were also reported in an incubation study using Nätraån estuarine sediment (Zhu et al., 2018). Furthermore, evidence for NOM-Hg(II) (SRNOM, the same NOM with this study) uptake by Hg methylators was documented in pure cultures of *Desulfovibrio desulfuricans* ND132, showing comparable bioavailability of Hg(II) and SRNOM-Hg(II) (indicated by similar net MeHg production) (Biswas et al., 2011). Together, literature data coupled with our experimental work support the high mobility and accessibility of NOM-^{199}Hg(II) that can be microbially methylated in rice paddy soils. We recognize that the role of NOM on Hg mobility and bioavailability depends not only on its concentration, but also on its quality and physical chemical properties. For instance, Hg bound to hydrophobic NOM was confirmed to have higher methylation rate than transphilic NOM bond Hg (Moreau et al., 2015). Clearly, additional information needs to be collected on the properties and compositions of the NOM present in rice paddy soil across this contamination gradient to obtain a more complete picture of its role.

Nanoparticulate HgS is commonly found in either anoxic or oxic environments (Enescu et al., 2016; Manceau et al., 2018; Zhang et al., 2020). More importantly, active methylation of nanoparticulate HgS have been shown in previous studies (Zhang et al., 2012, 2014; Zhang et al., 2020; Deonarine and Hsu-Kim, 2009; Slowey, 2010; Gerbig et al., 2011; Graham et al., 2012; Tian et al., 2021). The particle size of nanoparticulate HgS determines its bioavailability, in which lower particle size (i.e., with shorter aging time) typically yields more MeHg production (Zhang et al., 2012). In this study, the particle size of prepared nano-^{202}HgS was ~10 nm (aged for one week) (Fig. S3b), which was similar to the nano-HgS made by Zhang et al. (2012) (3.2 to about 20 nm, aged from 16 h to one week). Zhang et al. (2014) also reported comparable MeHg production in nano-HgS (aged for 16 h) and dissolved Hg-S amended freshwater sediment microcosms, which further support the bioavailability of the nano-HgS used in this study. In a most recent study, methylation potential of nano-HgS was found independent with surface area but dependent with surface structure of nanoparticulate Hg (Tian et al., 2021). Although high methylation rates of nano-^{202}HgS were found (Fig. 2), the role of NOM in forming nano-^{202}HgS should not be neglected. In addition to binding with Hg, dissolved organic matter (DOM, dissolved fractions of NOM) could either slow the aggregation of HgS particles in sulfidic environments or promote the dissolution of HgS (s), and both processes could accumulate nanoparticulate HgS (Slowey, 2010; Gerbig et al., 2011; Graham et al., 2012; Ravichandran et al., 1999; Pham et al., 2014). Besides DOM, extracellular polymeric substances (EPS) derived from *D. desulfuricans* ND132 was also found to play a role similar to DOM and mitigating the aggregation of nanoparticulate HgS (Zhang et al., 2020).

4.2. The role of FeS on Hg methylation in paddy soils

Previous study performed using groundwater documented that FeS particles, even in nano scale, showed high Hg selectivity, fast sorption kinetics and high sorption capacity, and therefore limited Hg methylation (Wang et al., 2020). In addition, formation of FeS may be a dominant process controlling the bioavailability of Hg in paddy soils. In a previous study, Skyllberg et al. (2021) reported that the formation of mackinawite (FeS) controls the chemical speciation of Hg in boreal lake sediment. Similarly, in this study, a rapid reduction of Fe^{3+} and a relatively high S(-II) concentration at the beginning of the incubation (*i.e.*, within a half day) in SK microcosms (Fig. A.7a and A.7c) are likely to form amorphous or weakly crystalline FeS(s), which could easily have co-precipitated the added ^{198}Hg(NO$_3$)$_2$ tracer. Currently, no published works have compared the adsorption capacities of FeS(s), nano-HgS(s) or NOM for Hg(II) in paddy slurries, and great uncertainties remains (such as the log *K* of NOM and Hg(II) (varied over 26 orders of magnitude, Ravichandran, 2004) and re-adsorption of Hg(II) by HgS(s) (Jiang et al., 2016)). Through this study, an implication could be given that FeS may show higher influence on the bioavailability of Hg(II) in methylation than NOM and nano-HgS(s). Moreover, the newly formed FeS(s) could either sorb ^{198}Hg(NO$_3$)$_2$ through surface complexation or catalyze HgS formation through Fe-Hg replacement (Wolfenden et al., 2005; Jeong et al., 2007; Skyllberg and Drott, 2010). Besides, high sulfide concentrations may facilitate abiotic demethylation of both monomethylmercury (Jonsson et al., 2016) and dimethylmercury (West et al., 2020), which further explained higher demethylation of MeHg in SK microcosms than those in GX and HX microcosms.

However, the low bioavailability of ≡FeS-Hg(II) (both added ≡FeS-^{200}Hg(II) tracer and ≡FeS absorbed ^{198}Hg(NO$_3$)$_2$) in this study is inconsistent with Jonsson et al. (2012), who found a comparable bioavailability of ≡FeS-Hg(II) and NOM-Hg(II) in estuary sediment, which is likely attributed to the dissolution or desorption of Hg from solids in methylation (Jonsson et al., 2012, 2014). Instead of Hg dissolution or desorption form solids, ligand exchange of Hg on the cell surface and particles could also make Hg bound to solids bioavailable (Zhang et al., 2019). Therefore, more work is required to reveal the dynamics of solid (*e.g.*, FeS and FeS$_2$) in paddy soils and their effects on

Hg methylation.

4.3. Influence of Hg contamination gradient on methylation and demethylation rates in paddy soils

As previously described, MeHg production and methylation rate decreased over the increasing contamination gradient. One striking aspect of our finding is that the variability in the methylation data for a given site (1 to 5-fold variation depending on the Hg species) is far smaller than what was observed across the contamination gradient (10^3–10^4 fold variation between HX, GX and SK), emphasizing that, at broad spatial scales, site-specific characteristics have a greater effect on net [MeHg] than solely considering the nature of the Hg substrate available for methylation (Fig. 4).

Several environmental variables can explain this large variation. Such variables could be i) source of Hg contamination and Hg speciation, ii) soil physical-chemical properties unique to each sites, iii) variations in the microbial community structure and functions associated with Hg methylation and iv) demethylation process. We discuss each of these variables hereafter, starting with the source of Hg contamination and Hg speciation at each site.

- No mercury contamination sources were found at control site (i.e., HX). The relative high THg concentration in HX (0.27 ± 0.10 mg kg^{-1}, Table A.1) than the regional background (0.058 mg kg^{-1}) is because Guizhou province in China located in the circum-Pacific mercuriferous belt (Qiu et al., 2008), which shows high geological background of Hg. Methylation rate at HX site reproduced data from Jonsson et al. (2012) obtained in estuarine sediments, with the kinetics of Hg(II) methylation fitted by a first-order kinetic model (Fig. A.12a) (K_m could be fitted by a simple exponential model (Fig. A.12b)). This suggested that 1) the bioavailability of Hg species in paddy soils from control site is similar to those in estuarine sediments (ordered as: Hg(II) complexed with dissolved inorganic ligands (*e.g.*, $Hg(NO_3)_2$) > NOM bond Hg > nanoparticulate HgS > FeS adsorbed Hg), and that 2) methylation is faster at the initial period (within one day in this study).
- Gouxi (GX) site is contaminated by artisanal Hg smelting activities and showed high Hg^0 concentrations in ambient air (Zhao et al., 2016a). A greater accessibility and availability of the newly deposited Hg to methylators was reported by Zhao et al. (2016a), which explained the highest MeHg concentration (4.16–9.93 μg kg^{-1}) and MeHg/THg ratio (0.19 %) in GX site (Table A.1). In addition, organic-bound Hg (H_2O_2 extracted) was found as one of the dominant Hg species in GX soils through a sequential extraction (1.30 mg kg^{-1} and 40.0 % for THg, Table A.4). According to the higher K_m of NOM-^{199}Hg(II) (Fig. 2a) and the larger pool of organic-bound Hg in GX soil, we can speculate that the high MeHg concentrations in GX soils may result from the methylation of some yet undefined organic-bound Hg species. Moreover, more "new" Hg input through atmospheric deposition may result a large proportion of newly formed nano-HgS (Manceau et al., 2018), which was reported more bioavailable for biotic methylation than aged nano-HgS (Tian et al., 2021).
- Sikeng was the site with the highest background THg concentration ([THg] = 35.11–59.96 mg kg^{-1}, Table A.1) and showed the lowest K_m for all Hg(II) tracers ($p < 0.05$). Mining wastes and tailings from the long-historic Hg mining activities are the primary sources of Hg in paddy soils at SK site (Qiu et al., 2008). Studies from both sequential extraction and X-ray absorption near-edge structure spectroscopy (XANES) consistently showed that the major Hg species in paddy soil from abandoned Hg mining area were β-HgS (67.4–72 %, Yin et al., 2016) and a poorly defined residual Hg (77.3 %, Table A.4; Lu et al., 2021). Due to the potential partitioning onto solid phases, the methylation rate of $^{198}Hg(NO_3)_2$ tracer was lower than expected in SK microcosms (Fig. 2b and e). As we discussed above, the rapid formation of FeS(s) may explain the lower bioavailability of $^{198}Hg(NO_3)_2$. In addition, Hg in NOM-^{199}Hg(II) and nano-^{202}HgS were pre-equilibrated with NOM and NOM-sulfide prior to their addition to the microcosms, therefore limiting the influence from solid phase partition post spike. The successfully fitted methylation kinetics of NOM-^{199}Hg(II) and nano-^{202}HgS in SK microcosms also support this hypothesis (Fig. A.13).

It is unlikely that large variations in methylation (10^3–10^4 fold) across sites were caused by different soil properties. Indeed, soil physicochemical properties among three paddy fields were similar due to the same geological background (the Karst region in southwest China). As mentioned above, all three soils were all of a hydragric anthrosols type with similar textures (*i.e.*, clay loam for HX and GX, loam for SK,

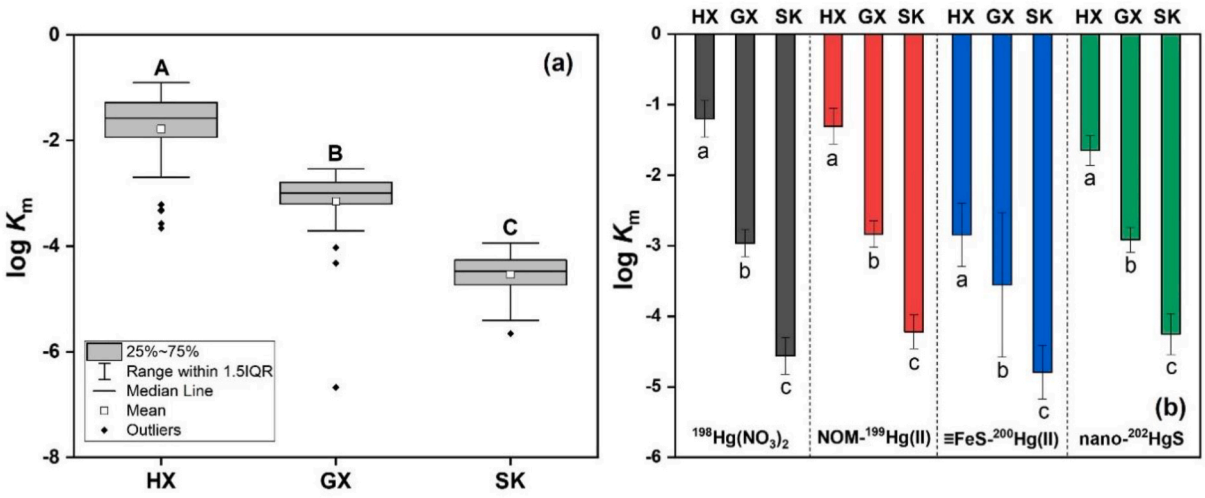

Fig. 4. Log-transformed methylation rate constants. (a) Four Hg(II) tracers grouped log K_m; (b) average log K_m for different Hg(II) tracers. HX, GX, and SK represent three paddy soils collected from Huaxi, Gouxi, and Sikeng, respectively. NOM-^{199}Hg(II) represents natural organic matter bond Hg(II); ≡FeS-^{200}Hg(II) represents mackinawite adsorbed Hg(II); and nano-^{202}HgS represents nanoparticulate HgS. In panel (a), different capital letters indicate the differences of four tracers combined log K_m among three sites are significant ($p < 0.05$); n for each box is 48. In panel (b), error bars indicate the standard deviation (±SD) for all K_m collected over the duration of the incubation (4 time points per 3 replicates; $n = 12$); different lowercase letters in each Hg(II) tracer indicate significant differences of log K_m among three sites ($p < 0.05$).

Table A.1). Moreover, soil pH (7.51–7.53) between sites are comparable. Finally, similar XRD patterns (Fig. A.14) of these soils further suggested comparable soil properties in terms of geology.

Net MeHg concentration is largely driven by microbial processes, whether it is for methylation or demethylation. Mercury is a toxic metal and we can expect its toxicity to strongly shape the structure and function of microbial community at each sites; this is also true for other variables affecting the mining landscape. The goal of our experiments was to test for the role of different Hg species suspected to have variable bioavailability to methylators. In light of the variation observed across large spatial scale, we attempted to test whether the microbial community structures were different at the three sites using 16S rRNA gene amplicon sequencing as well as quantitative PCR to evaluate the abundance of *hgcAB* genes involved in Hg methylation.

Principal coordinate analysis (PCoA) showed a good separation of the microbial community structures from the three paddy soils (HX, GX, and SK), indicating that the bacterial community structures were different (Fig. A.9). The contamination gradient may be responsible for these differences (Wu et al., 2020; Eckley et al., 2020). The possible toxicity of Hg at SK would also partially explain the lower microbial diversity (see Table A.2 for α-diversity from 16S rRNA sequencing). SK also exhibited the lowest abundance of *hgc*AB and *Deltaproteobacteria hgc*A determined using qPCR (Fig. A.10) when compared to GX and HX. These data suggest that variation in the microbial community structure and function at each site may be associated with the differences we observed in the methylation data (both net MeHg concentration (Table A.1) and overall methylation rate constant (Fig. 4a)). Unfortunately, we cannot identify the mechanistic drivers of such differences using solely 16S rRNA gene amplicon data. We have collected a large metagenomic dataset over the Hg contamination gradient that we are currently exploring and which results will be reported in another study.

Demethylation is a parallel factor and contributing net MeHg production together with methylation especially in rice paddies (Wu et al., 2020; Zhou et al., 2020). In this study, high MeHg demethylation and K_d were observed in the most Hg contaminated paddy soil (i.e., SK, Fig. 3). Together, the lower methylation rate and higher demethylation rate at SK, likely explain the lower relative MeHg levels in the paddy soils from SK when compared with GX and HX (Table A.1). It is also worth to hypothesize that paddy soil with high total Hg concentration may facilitate biotic demethylation of MeHg. Therefore, more works are needed to understand the community variations of MeHg demethylators across a Hg concentration gradient.

4.4. Implications for Hg contaminated rice paddy soil remediation

Several methods have been developed to remediate soils affected by Hg contamination (Wang et al., 2012; Eckley et al., 2020). However, most of these approaches focus on what are traditionally considered bioavailable Hg species (*i.e.*, soluble and exchangeable Hg) with the greatest methylation potential (Qian et al., 2003; Piao et al., 2006). In this study, however, methylation rates obtained from NOM-Hg(II) and nano-HgS were comparable to those obtained with the mostly labile Hg $(NO_3)_2$. Findings from this study indicate that Hg substrates for methylation could be more diverse than previously thought, highlighting the importance of NOM bound Hg(II) and HgS nanoparticles in rice paddy soils, especially growing studies have been pointed out that the prediction of MeHg production by using aqueous Hg species alone is not sufficient in different systems (Jonsson et al., 2012; Zhang et al., 2012, 2014; Mazrui et al., 2016). Moreover, a previous study already confirmed the large nanoparticulate HgS pool in the plants and soils of the Wanshan mining area (Manceau et al., 2018), further supporting the bioavailable Hg pool is various at these sites. Accordingly, remediation strategies cannot simply consider the presence of NOM and sulfide as sufficient to develop a robust remediation strategy. Rather, a comprehensive evaluation of Hg speciation used in combination with a multi-pronged approach is likely needed for *in-situ* remediation.

5. Conclusion

Natural organic matter bond Hg(II) and nanoparticulate mercuric sulfide were found have similar or higher methylation rate than that of $Hg(NO_3)_2$ through a multi-isotope tracer spiked rice paddy microcosm study, highlighting the high bioavailability of these Hg(II) species in paddy soils. Low methylation rates of ferrous sulfide sorbed Hg(II) were found independent with Hg concentration gradients (i.e., different sites) and the formation of FeS may reduce the bioavailability of Hg(II) in methylation. Methylation rates for all Hg(II) species tested decreased with increasing Hg concentrations and the variability in the methylation data for a given site (1 to 5-fold variation depending on the Hg(II) species) was smaller than what was observed across the mercury concentration gradient (10^3–10^4 fold variation between sites). Findings of this study emphasized that at broad spatial scales, site-specific characteristics, such as microbial community structure, need to be taken into consideration, alongside the nature of the Hg substrate available for methylation, to determine net MeHg production in paddy soils. However, the chemical speciation of the Hg species bioavailable for Hg methylation is very complicated, and far to be fully understood. Thus, further work is needed to uncover the Hg dynamics in rice paddy ecosystem, including 1) the coupling relationship among sulfur, iron, and Hg cycling, 2) the roles of natural organic matter on the bioavailability and methylation of Hg, and 3) the biogeochemical processes and the environmental fate of HgS nanoparticles in rice paddy ecosystem.

Author statement

Jiang Liu: Data curation; Formal analysis; Visualization; Writing – original draft. Benqi Lu: Data curation; Formal analysis; Investigation. Alexandre J. Poulain: Writing – review & editing; Formal analysis. Rui Zhang: Data curation; Formal analysis. Tong Zhang: Writing – review & editing. Xinbin Feng: Conceptualization; Funding acquisition; Writing – review & editing. Bo Meng: Conceptualization; Funding acquisition; Methodology; Project administration; Supervision; Writing – review & editing.

Declaration of competing interest

The authors declare that they have no known competing financial interests or personal relationships that could have appeared to influence the work reported in this paper.

Acknowledgements

The authors would like to acknowledge the support of the National Natural Science Foundation of China (41931297, 42022024), CAS "Light of West China" program, and the State Key Laboratory of Environmental Geochemistry (SKLEG2019707). We thank Chen J., Li S., Kong K. and Dr. Aslam M.W., for the help in sample collection and measurement. We thank Dr. Pu Q. for the help in data processing of 16S rRNA gene amplicon sequencing. We also would like to thank Dr. Meng Y. for XRD analysis.

Appendix A. Supplementary data

Supplementary data to this article can be found online at https://doi.org/10.1016/j.envpol.2021.118321.

References

Appleton, J.D., Weeks, J.M., Calvez, J.P., Beinhoff, C., 2006. Impacts of mercury contaminated mining waste on soil quality, crops, bivalves, and fish in the Naboc River area, Mindanao, Philippines. Sci. Total Environ. 354, 198–211.

Aslam, M.W., Ali, W., Meng, B., Abrar, M.M., Lu, B., Qin, C., Zhao, L., Feng, X.B., 2020. Mercury contamination status of rice cropping system in Pakistan and associated health risks. Environ. Pollut. 263, 114625.

Barkay, T., Gillman, M., Turner, R., 1997. Effects of dissolved organic carbon and salinity on bioavailability of mercury. Appl. Environ. Microbiol. 63, 4267–4271.
Bergquist, B.A., Blum, J.D., 2007. Mass-dependent and -independent fractionation of Hg isotopes by photoreduction in aquatic systems. Science 318, 417–420.
Biswas, A., Brooks, S.C., Miller, C.L., Mosher, J.J., Yin, X.L., Drake, M.M., 2011. Bacterial growth phase influences methylmercury production by the sulfate-reducing bacterium *Desulfovibrio Desulfuricans Nd132*. Sci. Total Environ. 409, 3943–3948.
Bravo, A.G., Cosio, C., 2020. Biotic formation of methylmercury: a bio – physico – chemical conundrum. Limnol. Oceanogr. 65, 1010–1027.
Chiasson-Gould, S.A., Blais, J.M., Poulain, A.J., 2014. Dissolved organic matter kinetically controls mercury bioavailability to bacteria. Environ. Sci. Technol. 48, 3153–3161.
Clarkson, T.W., 1993. Mercury: major issues in environmental health. Environ. Health Perspect. 100, 31–38.
Deonarine, A., Hsu-Kim, H., 2009. Precipitation of mercuric sulfide nanoparticles in NOM-containing water: implications for the natural environment. Environ. Sci. Technol. 43, 2368–2373.
Eckley, C.S., Gilmour, C.C., Janssen, S., Luxton, T.P., Randall, P.M., Whalin, L., Austin, C., 2020. The assessment and remediation of mercury contaminated sites: a review of current approaches. Sci. Total Environ. 707, 136031.
Enescu, M., Nagy, K.L., Manceau, A., 2016. Nucleation of mercury sulfide by dealkylation. Sci. Rep. 6, 39359.
Feng, X.B., Li, P., Qiu, G.L., Wang, S.F., Li, G.H., Shang, L.H., Meng, B., Jiang, H.M., Bai, W.Y., Li, Z.G., Fu, X.W., 2008. Human exposure to methylmercury through rice intake in mercury mining areas, Guizhou Province, China. Environ. Sci. Technol. 42, 326–332.
Gai, K., Hoelen, T.P., Hsu-Kim, H., Lowry, G.V., 2016. Mobility of four common mercury species in model and natural unsaturated soils. Environ. Sci. Technol. 50, 3342–3351.
Gerbig, C.A., Kim, C.S., Stegemeier, J.P., Ryan, J.N., Aiken, G.R., 2011. Formation of nanocolloidal metacinnabar in mercury-DOM-sulfide systems. Environ. Sci. Technol. 45, 9180–9187.
Gilmour, C.C., Bullock, A.L., McBurney, A., Podar, M., Elias, D.A., 2018. Robust mercury methylation across diverse methanogenic Archaea. mBio 9, 1–13.
Gilmour, C.C., Podar, M., Bullock, A.L., Graham, A.M., Brown, S.D., Somenahally, A.C., Johs, A., Hurt, R.A., Bailey, K.L., Elias, D.A., 2013. Mercury methylation by novel microorganisms from new environments. Environ. Sci. Technol. 47, 11810–11820.
Gilmour, C.C., Riedel, G.S., Ederington, M.C., Bell, J.T., Benoit, J.M., Gill, G.A., Stordal, M.C., 1998. Methylmercury concentrations and production rates across a trophic gradient in the Northern Everglades. Biogeochemistry 40, 327–345.
Graham, A.M., Aiken, G.R., Gilmour, C.C., 2012. Dissolved organic matter enhances microbial mercury methylation under sulfidic conditions. Environ. Sci. Technol. 46, 2715–2723.
Hsu-kim, H., Kucharzyk, K.H., Zhang, T., Deshusses, M.A., 2013. Mechanisms regulating mercury bioavailability for methylating microorganisms in the aquatic environment: a critical review. Environ. Sci. Technol. 47, 2441–2456.
IUSS Working Group WRB, 2006. World reference base for soil resources. In: World Soil Resources Reports, vol. 103. FAO, Rome.
Janssen, S.E., Barkay, T., Reinfelder, J.R., 2016. Fractionation of mercury stable isotopes during microbial methylmercury production by iron- and sulfate-reducing bacteria. Environ. Sci. Technol. 50, 8077–8083.
Jeong, H.Y., Klaue, B., Blum, J.D., Hayes, K.F., 2007. Sorption of mercuric ion by synthetic nanocrystalline mackinawite (FeS). Environ. Sci. Technol. 41, 7699–7705.
Jiang, P., Li, Y., Liu, G., Yang, G., Lagos, L., Yin, Y., Gu, B., Jiang, G., Cai, Y., 2016. Evaluating the role of re-adsorption of dissolved Hg^{2+} during cinnabar dissolution using isotope tracer technique. J. Hazard. Mater. 317, 466–475.
Johs, A., Eller, V.A., Mehlhorn, T.L., Brooks, S.C., Harper, D.P., Mayes, M.A., Pierce, E. M., Peterson, M.J., 2019. Dissolved organic matter reduces the effectiveness of sorbents for mercury removal. Sci. Total Environ. 690, 410–416.
Jonsson, S., Mazrui, N.M., Mason, R.P., 2016. Dimethylmercury formation mediated by inorganic and organic reduced sulfur surfaces. Sci. Rep. 6, 27958.
Jonsson, S., Skyllberg, U., Nilsson, M.B., Lundberg, E., Andersson, A., Björn, E., 2014. Differentiated availability of geochemical mercury pools controls methylmercury levels in estuarine sediment and biota. Nat. Commun. 5, 4624.
Jonsson, S., Skyllberg, U., Nilsson, M.B., Westlund, P., Shchukarev, A., Lundberg, E., Björn, E., 2012. Mercury methylation rates for geochemically relevant Hg^{II} species in sediments. Environ. Sci. Technol. 46, 11653–11659.
Krisnayanti, B.D., Anderson, C.W.N., Utomo, W.H., Feng, X.B., Handayanto, E., Mudarisna, N., Ikram, H., Khususiah, 2012. Assessment of environmental mercury discharge at a four-year- old artisanal gold mining area on Lombok Island, Indonesia. J. Environ. Monit. 14, 2598–2670.
Kritee, K., Barkay, T., Blum, J.D., 2009. Mass dependent stable isotope fractionation of mercury during mer mediated microbial degradation of monomethylmercury. Geochem. Cosmochim. Acta 73, 1285–1296.
Lenka, M., Panda, K.K., Panda, B.B., 1992. Monitoring and assessment of mercury pollution in the vicinity of a chloralkali plant. IV. Bioconcentration of mercury in in situ aquatic and terrestrial plants at Ganjam, India. Arch. Environ. Contam. Toxicol. 22, 195–202.
Li, P., Feng, X.B., Yuan, X.B., Chan, H.M., Qiu, G.L., Sun, G.X., Zhu, Y.G., 2012. Rice consumption contributes to low level methylmercury exposure in southern China. Environ. Int. 49, 18–23.
Li, Y.Y., Zhao, J.T., Zhong, H., Wang, Y., Li, H., Li, Y., Jiang, T., Zhang, Z., Gao, Y., Chai, Z., 2019. Understanding enhanced microbial MeHg production in mining-contaminated paddy soils under sulfate amendment: changes in Hg mobility or microbial methylators? Environ. Sci. Technol. 53, 1844–1852.
Liang, L., Xi, F., Tan, W., Meng, X., Hu, B., Wang, X., 2021. Review of organic and inorganic pollutants removal by biochar and biochar-based composites. Biochar 3, 255–281.
Liem-Nguyen, V., Jonsson, S., Skyllberg, U., Nilsson, M.B., Andersson, A., Lundberg, E., Björn, E., 2016. Effects of nutrient loading and mercury chemical speciation on the formation and degradation of methylmercury in estuarine sediment. Environ. Sci. Technol. 50, 6983–6990.
Liu, J., Meng, B., Poulain, A.J., Meng, Q.Y., Feng, X.B., 2021a. Stable isotope tracers identify sources and transformations of mercury in rice (Oryza sativa L.) growing in a mercury mining area. Fundam. Res. 1, 259–268.
Liu, M., Zhang, Q., Cheng, M., He, Y., Chen, L., Shen, H., Zhang, W., Tao, S., Wang, X., Zhang, H., Cao, H., 2019. Rice life cycle-based global mercury biotransport and human methylmercury exposure. Nat. Commun. 10, 5164.
Liu, X.L., Pang, H., Liu, X.W., Li, Q., Zhang, N., Mao, L., Qiu, M., Hu, B., Yang, H., Wang, X., 2021b. Orderly porous covalent organic frameworks-based materials: superior adsorbents for pollutants removal from aqueous solutions. Innovation 2, 100076.
Liu, Y.R., Johs, A., Bi, L., Lu, X., Hu, H., Sun, D., He, J.Z., Gu, B.H., 2018. Unraveling microbial communities associated with methylmercury production in paddy soils. Environ. Sci. Technol. 52, 13110–13118.
Livak, K.J., Schmittgen, T.D., 2001. Analysis of relative gene expression data using real-time quantitative PCR and the $2^{-\Delta\Delta CT}$ method. Methods 25, 402–408.
Lu, B.Q., Liu, J., Lv, W.Q., Li, S., Feng, X.B., Meng, B., 2021. Distribution characteristics of mercury occurrences in the paddy soil of Hg mining area and its effect on mercury methylation. Bull. Mineral Petrol. Geochem. 40, 1–9 (In Chinese).
Manceau, A., Wang, J.X., Rovezzi, M., Glatzel, P., Feng, X.B., 2018. Biogenesis of mercury-sulfur nanoparticles in plant leaves from atmospheric gaseous mercury. Environ. Sci. Technol. 52, 3935–3948.
Mao, Y., Li, Y., Richards, J., Cai, Y., 2013. Investigating uptake and translocation of mercury species by Sawgrass (*Cladium jamaicense*) using a stable isotope tracer technique. Environ. Sci. Technol. 47, 9678–9684.
Mazrui, N.M., Jonsson, S., Thota, S., Zhao, J., Mason, R.P., 2016. Enhanced availability of mercury bound to dissolved organic matter for methylation in marine sediments. Geochem. Cosmochim. Acta 194, 153–162.
Meng, B., Feng, X.B., Qiu, G., Anderson, C.W.N., Wang, J., Zhao, L., 2014. Localization and speciation of mercury in brown rice with implications for Pan-Asian public health. Environ. Sci. Technol. 48, 7974–7981.
Meng, B., Feng, X.B., Qiu, G.L., Cai, Y., Wang, D.Y., Li, P., Shang, L.H., Sommar, J., 2010. Distribution patterns of inorganic mercury and methylmercury in tissues of rice (Oryza Sativa L.) plants and possible bioaccumulation pathways. J. Agric. Food Chem. 58, 4951–4958.
Meng, B., Feng, X.B., Qiu, G.L., Liang, P., Li, P., Chen, C., Shang, L.H., 2011. The process of methylmercury accumulation in rice (Oryza Sativa L.). Environ. Sci. Technol. 45, 2711–2717.
Meng, B., Li, Y., Cui, W., Jiang, P., Liu, G., Wang, Y., Richards, J., Feng, X., Cai, Y., 2018. Tracing the uptake, transport, and fate of mercury in Sawgrass (Cladium jamaicense) in the Florida Everglades using a multi-isotope technique. Environ. Sci. Technol. 52, 3384–3391.
Moreau, J.W., Gionfriddo, C.M., Krabbenhoft, D.P., Ogorek, J.M., DeWild, J.F., Aiken, G. R., Roden, E.E., 2015. The effect of natural organic matter on mercury methylation by *Desulfobulbus Propionicus 1pr3*. Front. Microbiol. 6, 1389.
Parks, J.M., Johs, A., Podar, M., Bridou, R., Hurt, R.A., Smith, S.D., Tomanicek, S.J., Qian, Y., Brown, S.D., Brandt, C.C., Palumbo, A.V., Smith, J.C., Wall, J.D., Elias, D. A., Liang, L., 2013. The genetic basis for bacterial mercury methylation. Science 339, 1332–1335.
Pham, A.L., Morris, A., Zhang, T., Ticknor, J., 2014. Precipitation of nanoscale mercuric sulfides in the presence of natural organic matter: structural properties, aggregation, and biotransformation. Geochem. Cosmochim. Acta 133, 204–215.
Piao, H., Bishop, P.L., 2006. Stabilization of mercury-containing wastes using sulfide. Environ. Pollut. 139, 498–506.
Podar, M., Gilmour, C.C., Brandt, C.C., Soren, A., Brown, S.D., Crable, B.R., Palumbo, A. V., Somenahally, A.C., Elias, D.A., 2015. Global prevalence and distribution of genes and microorganisms involved in mercury methylation. Sci. Adv. 1, e1500675.
Qian, G., Sun, D.D., Tay, J.H., 2003. Immobilization of mercury and zinc in an alkali-activated slag matrix. J. Hazard. Mater. 101, 65–77.
Qin, C.Y., Du, B.Y., Yin, R.S., Meng, B., Fu, X.W., Li, P., Zhang, L., Feng, X.B., 2020. Isotopic fractionation and source appointment of methylmercury and inorganic mercury in a paddy ecosystem. Environ. Sci. Technol. 54, 14334–14342.
Qiu, G.L., Feng, X.B., Li, P., Wang, S.F., Li, G.H., Shang, L.H., Fu, X.W., 2008. Methylmercury accumulation in rice (Oryza Sativa L.) grown at abandoned mercury mines in Guizhou, China. J. Agric. Food Chem. 56, 2465–2468.
Ravichandran, M., 2004. Interactions between mercury and dissolved organic matter - a review. Chemosphere 55, 319–331.
Ravichandran, M., Aiken, G., Ryan, J., Reddy, M., 1999. Inhibition of precipitation and aggregation of metacinnabar (mercuric sulfide) by dissolved organic matter isolated from the Florida Everglades. Environ. Sci. Technol. 33, 1418–1423.
Regnell, O., Watras, C.J., 2018. Microbial mercury methylation in aquatic environments: a critical review of published field and laboratory studies. Environ. Sci. Technol. 53, 4–19.
Rodríguez Martín-Doimeadios, R.C., Krupp, E., Amouroux, D., Donard, O.F.X., 2002. Application of isotopically labeled methylmercury for isotope dilution analysis of biological samples using gas chromatography/ICPMS. Anal. Chem. 74, 2505–2512.
Rothenberg, S.E., Feng, X.B., 2012. Mercury cycling in a flooded rice paddy. J. Geophys. Res. Biogeosciences 117, 1–16.

Skyllberg, U., Drott, A., 2010. Competition between disordered iron sulfide and natural organic matter associated thiols for mercury(II)-an EXAFS study. Environ. Sci. Technol. 44, 1254–1259.
Skyllberg, U., Persson, A., Tjerngren, I., Kronberg, R., Drott, A., Meili, M., Björn, E., 2021. Chemical speciation of mercury, sulfur and iron in a dystrophic boreal lake sediment, as controlled by the formation of mackinawite and framboidal pyrite. Geochem. Cosmochim. Acta 294, 106–125.
Slowey, A.J., 2010. Rate of formation and dissolution of mercury sulfide nanoparticles: the dual role of natural organic matter. Geochem. Cosmochim. Acta 74, 4693–4708.
Tian, L., Guan, W., Ji, Y., He, X., Chen, W., Alvarez, P.J.J., Zhang, T., 2021. Microbial methylation potential of mercury sulfide particles dictated by surface structure. Nat. Geosci. 14, 409–416.
Wang, J., Feng, X.B., Anderson, C.W.N., Xing, Y., Shang, L., 2012. Remediation of mercury contaminated sites – a review. J. Hazard. Mater. 221–222, 1–18.
Wang, M., Li, Y., Zhao, D., Zhuang, L., Yang, G., Gong, Y., 2020. Immobilization of mercury by iron sulfide nanoparticles alters mercury speciation and microbial methylation in contaminated groundwater. Chem. Eng. J. 381, 122664.
Wang, X., Ye, Z.H., Li, B., Huang, L.N., Meng, M., Shi, J.B., Jiang, G.B., 2014. Growing rice aerobically markedly decreases mercury accumulation by reducing both Hg bioavailability and the production of MeHg. Environ. Sci. Technol. 48, 1878–1885.
West, J., Graham, A.M., Liem-Nguyen, V., Jonsson, S., 2020. Dimethylmercury degradation by dissolved sulfide and mackinawite. Environ. Sci. Technol. 54, 13731–13738.
Wolfenden, S., Charnock, J.M., Hilton, J., Livens, F.R., Vaughan, D.J., 2005. Sulfide species as a sink for mercury in lake sediments. Environ. Sci. Technol. 39, 6644–6648.
Wu, Q.Q., Hu, H.Y., Meng, B., Wang, B.L., Poulain, A.J., Zhang, H., Liu, J.L., Bravo, A.G., Bishop, K., Bertilsson, S., Feng, X.B., 2020. Methanogenesis is an important process in controlling MeHg concentration in rice paddy soils affected by mining activities. Environ. Sci. Technol. 54, 13517–13526.
Yin, R.S., Gu, C., Feng, X.B., Hurley, J.P., Krabbenhoft, D.P., Lepak, R.F., Zhu, W., Zheng, L., Hu, T., 2016. Distribution and geochemical speciation of soil mercury in wanshan Hg mine: effects of cultivation. Geoderma 272, 32–38.
Zhao, L., Anderson, C.W.N., Qiu, G.L., Meng, B., Wang, D.Y., Feng, X.B., 2016a. Mercury methylation in paddy soil: source and distribution of mercury species at a Hg mining area, Guizhou Province, China. Biogeosciences 13, 2429–2440.
Zhao, L., Qiu, G.L., Anderson, C.W.N., Meng, B., Wang, D.Y., Shang, L.H., Yan, H.Y., Feng, X.B., 2016b. Mercury methylation in rice paddies and its possible controlling factors in the Hg mining area, Guizhou Province, southwest China. Environ. Pollut. 215, 1–9.
Zhang, H., Feng, X.B., Larssen, T., Qiu, G.L., Vogt, R.D., 2010a. In inland China, rice, rather than fish, is the major pathway for methylmercury exposure. Environ. Health Perspect. 118, 1183–1188.
Zhang, H., Feng, X.B., Larssen, T., Shang, L.H., Li, P., 2010b. Bioaccumulation of methylmercury versus inorganic mercury in rice (Oryza Sativa L.) grain. Environ. Sci. Technol. 44, 4499–4504.
Zhang, L., Wu, S., Zhao, L., Lu, X., Pierce, E.M., Gu, B., 2019. Mercury sorption and desorption on organo-mineral particulates as a source for microbial methylation. Environ. Sci. Technol. 53, 2426–2433.
Zhang, T., Kim, B., Levard, C., Reinsch, B.C., Lowry, G.V., Deshusses, M.A., Hsu-Kim, H., 2012. Methylation of mercury by bacteria exposed to dissolved, nanoparticulate, and microparticulate mercuric sulfides. Environ. Sci. Technol. 46, 6950–6958.
Zhang, T., Kucharzyk, K.H., Kim, B., Deshusses, M.A., Hsu-Kim, H., 2014. Net methylation of mercury in estuarine sediment microcosms amended with dissolved, nanoparticulate, and microparticulate mercuric sulfides. Environ. Sci. Technol. 48, 9133–9141.
Zhang, Z., Si, R., Lv, J., Ji, Y., Chen, W., Guan, W., Cui, Y., Zhang, T., 2020. Effects of extracellular polymeric substances on the formation and methylation of mercury sulfide nanoparticles. Environ. Sci. Technol. 54, 8061–8071.
Zhou, X.Q., Hao, Y.Y., Gu, B., Feng, J., Liu, Y., Huang, Q., 2020. Microbial communities associated with methylmercury degradation in paddy soils. Environ. Sci. Technol. 54, 7952–7960.
Zhu, W., Song, Y., Adediran, G.A., Jiang, T., Reis, A.T., Pereira, E., Skyllberg, U., Björn, E., 2018. Mercury transformations in resuspended contaminated sediment controlled by redox conditions, chemical speciation and sources of organic matter. Geochem. Cosmochim. Acta 220, 158–179.

Environmental Science & Technology

pubs.acs.org/est

Article

Mercury and Sulfur Redox Cycling Affect Methylmercury Levels in Rice Paddy Soils across a Contamination Gradient

Jiang Liu, Ji Chen, Alexandre J. Poulain, Qiang Pu, Zhengdong Hao, Bo Meng,* and Xinbin Feng

Cite This: *Environ. Sci. Technol.* 2023, 57, 8149−8160

Read Online

ACCESS | Metrics & More | Article Recommendations | Supporting Information

ABSTRACT: Methylmercury (MeHg) contamination in rice via paddy soils is an emerging global environmental issue. An understanding of mercury (Hg) transformation processes in paddy soils is urgently needed in order to control Hg contamination of human food and related health impacts. Sulfur (S)-regulated Hg transformation is one important process that controls Hg cycling in agricultural fields. In this study, Hg transformation processes, such as methylation, demethylation, oxidation, and reduction, and their responses to S input (sulfate and thiosulfate) in paddy soils with a Hg contamination gradient were elucidated simultaneously using a multi-compound-specific isotope labeling technique ($^{200}Hg^{II}$, $Me^{198}Hg$, and $^{202}Hg^{0}$). In addition to Hg^{II} methylation and MeHg demethylation, this study revealed that microbially mediated reduction of Hg^{II}, methylation of Hg^{0}, and oxidative demethylation−reduction of MeHg occurred under dark conditions; these processes served to transform Hg between different species (Hg^{0}, Hg^{II}, and MeHg) in flooded paddy soils. Rapid redox recycling of Hg species contributed to Hg speciation resetting, which promoted the transformation between Hg^{0} and MeHg by generating bioavailable Hg^{II} for fuel methylation. Sulfur input also likely affected the microbial community structure and functional profile of Hg^{II} methylators and, therefore, influenced Hg^{II} methylation. The findings of this study contribute to our understanding of Hg transformation processes in paddy soils and provide much-needed knowledge for assessing Hg risks in hydrological fluctuation-regulated ecosystems.

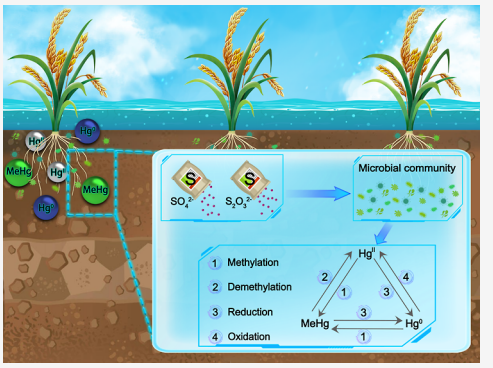

KEYWORDS: *Hg transformation, sulfur amended, paddy soil, multi-compound-specific isotope labeling*

1. INTRODUCTION

Over the last few decades, mercury (Hg) cycling in hydrological fluctuation-regulated ecosystems (e.g., wetlands, hydroelectric reservoirs, and paddy soils) has gained extensive attention. This is because, in these ecosystems, inorganic Hg is more readily transformed into toxic and bioaccumulative methylmercury (MeHg), as compared to other ecosystem types.[1−7] As a type of wetland, rice paddy fields play an important role in human MeHg exposure, especially in Hg-contaminated areas.[8,9] This is because rice (*Oryza sativa* L.) bioaccumulates MeHg[10,11] and paddy soil is a unique source of MeHg in rice.[12−16] Since rice is a staple food for a large proportion of the population worldwide, MeHg-contaminated rice and the resulting MeHg exposure risks are recognized as a global issue.[17−19] Therefore, a comprehensive understanding of the biogeochemical cycling of Hg in paddy soils is urgently required.

The transformation of Hg species in rice paddy ecosystems plays a vital role in Hg bioaccumulation and associated human exposure risks. Of particular importance are Hg methylation, demethylation, reduction, and oxidation; most of these processes are predominantly mediated by microorganisms.[20] Existing studies have mostly focused on methylation and demethylation,[3,4,21,22] with little attention paid to the reduction and oxidation processes. Thus, at present, we have an incomplete picture of Hg cycling in rice paddy soils. How redox processes affect (de)methylation remains unclear. Furthermore, most existing studies have only investigated bulk concentration changes in Hg species in rice paddies, with little study of interconversion processes.[3,4,23,24] Again, this has limited our understanding of net MeHg production mechanisms. Several studies have spiked stable Hg isotope tracers into rice paddy systems to simultaneously trace different transformation processes, including methylation and demethylation,[3,4,22,25] partitioning and redistribution,[26] and rice plant uptake and translocation.[15,27,28] However, only Hg^{II} or MeHg tracers have been applied to date, and only isotopic signals of THg or MeHg were measured in these studies. As a result, the redox processes of Hg in rice paddy systems have not yet been precisely traced.

Received: April 10, 2023
Revised: May 5, 2023
Accepted: May 5, 2023
Published: May 17, 2023

Wetlands are vital to the coupled biogeochemical cycles of Hg and sulfur (S).[29] On the one hand, sulfate reduction to sulfide and sulfide re-oxidation control the speciation and bioavailability of Hg by forming Hg−S compounds.[29−31] Recent studies have confirmed that the bioavailability of Hg substrates in methylation is determined not only by the formation of dissolved Hg−S complexes [e.g., $Hg(SH)_2$, HgS_2H^-, HgS_2^{2-}, $Hg(SR)_2$, etc.][30,31] but also by the intracellular dissolution of HgS nanoparticles.[25,32−34] On the other hand, sulfate reduction mediated by microorganisms is an important pathway for Hg methylation in natural environments.[35] For the reasons above, S input, especially atmospheric S deposition, is recognized as a major controlling factor in the production of MeHg.[36−39] More recently, however, a shift from atmospheric deposition to agricultural addition was reported as a new influencer of S cycling, and the role of S fertilizers in Hg transformation in agricultural fields was highlighted.[40] In the United States, agricultural S application exceeded ∼3.3 Tg yr^{-1} in 2017 (equal to ∼39.8 kg S ha^{-1} yr^{-1}),[40] and this number is projected to increase due to the decline in atmospheric S deposition and resulting S deficiencies in agricultural soils.[41] In China, where SO_2 emissions have declined from 21.85 Tg S yr^{-1} in 2011 to 3.18 Tg S yr^{-1} in 2021,[42] increasing application of S fertilizers has been reported.[43] Together, these estimates suggest that agricultural S additions are on par with atmospheric S deposition.[40] Therefore, S-regulated Hg transformation in agricultural fields (e.g., paddy soils) requires more attention. To date, limited studies have examined S input-influenced Hg transformation in paddy soils, with both promotion and inhibition of Hg^{II} methylation reported.[44−47] Most of these studies were based on bulk Hg concentration measurements, with little investigation of the precise transformation processes of Hg. Moreover, S species with different valent states determine the redox cycling of S and, thus, influence Hg transformation.[29] Accordingly, the role of different S species in Hg transformation is expected to be differential.

Here, a multi-compound-specific isotope labeling technique was employed together with sulfate and thiosulfate amendments of paddy soil to track Hg methylation, demethylation, oxidation, and reduction, simultaneously. Hg isotope labeling ($^{200}Hg^{II}$, $Me^{198}Hg$, and $^{202}Hg^0$) and geochemical and microbial approaches were combined to reveal Hg transformation in paddy soils and the underlying biogeochemical mechanisms. In addition to MeHg, isotopic signals of Hg^0 were determined, providing a more integrated understanding of Hg methylation, demethylation, oxidation, and reduction in paddy soils. In particular, the Hg transformation mechanisms were addressed in this study, especially S-regulated Hg transformation in paddy soils. Knowledge gained from this study can contribute to an improved understanding of Hg biogeochemistry in hydrological fluctuation-regulated ecosystems.

2. MATERIALS AND METHODS

2.1. Sample Collection. Rice paddy soil (surface soil, 1−5 cm) and overlying water samples were collected from three paddy fields. The first was an abandoned Hg mining site (SK, E 109°12′38″, N 27°31′2″) and the second was an artisanal Hg smelting site (GX, E 109°11′30″, N 27°33′50″) in the Wanshan Hg mining area (Wanshan District, Tongren City, Guizhou Province, China). The third was a control site in a rural area close to Guiyang City in Guizhou Province (HX, E 106°31′28″, N 26°25′20″). More detailed descriptions of the sampling sites are provided in Text S1 in the Supporting Information.

2.2. Preparation of Hg Isotope Tracers. Multi-compound-specific Hg isotope tracers, including the inorganic divalent Hg tracer ($^{200}Hg^{II}$), methyl-Hg tracer ($Me^{198}Hg$), and elemental Hg tracer ($^{202}Hg^0$), were used to trace Hg methylation (i.e., from $^{200}Hg^{II}$ to $Me^{200}Hg$ and from $^{202}Hg^0$ to $Me^{202}Hg$), MeHg demethylation (i.e., $Me^{198}Hg$ losses), Hg reduction (i.e., from $^{200}Hg^{II}$ to $^{200}Hg^0$ and from $Me^{198}Hg$ to $^{198}Hg^0$), and Hg oxidation/immobilization (i.e., $^{202}Hg^0$ losses). The preparation details are presented in Text S2.

2.3. Incubation Experiment Design. Serum bottles (100 mL, borosilicate glass bottle) were used for the anaerobic incubation experiment in an oxygen-free glovebox (PLAS-LABS, USA). Paddy soil and overlying water were mixed in the glovebox to prepare incubation slurries from each site, as described by Wu et al.[22] and Liu et al.[25] (see Text S3). Each homogenized slurry (30 mL) was weighed into a serum bottle. The moisture content of the prepared slurries (SK, GX and HX) was around 75% (Text S3). Four treatments, including sulfate (Na_2SO_4) and thiosulfate ($Na_2S_2O_3$) addition treatments as well as an autoclaved treatment (121 °C for 30 min) and a control treatment, were prepared. The same amount of S (equivalent to 2 mg of S) was added to each of the incubation bottles for the two S treatments. The dosage of exogenous S was similar to the total S content of paddy soils from Wanshan (∼200 mg kg^{-1}, ref 48). Isotope-enriched $^{200}Hg^{II}$, $Me^{198}Hg$, and $^{202}Hg^0$ tracers were spiked into all incubation bottles; the spiking dosage of Hg tracers depended on the ambient Hg concentration at each site (Table S1). Then, the incubation bottles were immediately sealed and gently shaken to mix the tracers and slurries. They were then covered with aluminum foil. The total period of incubation was 48 h (at 25 °C in the glovebox), and three random bottles (triplicates for each site and each treatment) were destructively sampled at 0 h, 12, 24, and 48 h. However, due to the periods of incubation, bottle preparation, and subsampling, the actual time series for purgeable Hg^0 was 2, 14, 26, and 50 h, and for MeHg, it was 4, 18, 28, and 52 h (see Text S4.1). After incubation, the isotope-enriched Hg^0 species ($^{198}Hg^0$, $^{200}Hg^0$, and $^{202}Hg^0$), MeHg species ($Me^{198}Hg$, $Me^{200}Hg$, and $Me^{202}Hg$), redox couples (HS^-/SO_4^{2-}, NO_3^-/NH_4^+, and Fe^{2+}/Fe^{3+}), and the concentration and optical properties (i.e., UV−vis absorption and fluorescence spectra) of water extracted soil dissolved organic matter (DOM) were determined. Genomic DNA was extracted for the quantification of functional genes that encode Hg and S transformations (*hgc*A, *mer*A, *mer*B, *dsr*B, and *sox*B). Hg-methylating microbial communities were identified by *hgcA* gene amplicon sequencing and metagenomic analysis, and the sequence data were deposited in the National Centre for Biotechnology Information (NCBI, https://www.ncbi.nlm.nih.gov/), with accession numbers PRJNA950218 and PRJNA950935, respectively. More details on the subsampling and measurements are provided in Text S4. The primers used for quantitative PCR are listed in Table S2.

2.4. Data Analysis. Ambient Hg refers to the Hg that is naturally present in the soil, and isotope-enriched Hg (^{198}Hg, ^{200}Hg, and ^{202}Hg) refers to Hg from the spiked tracers.[49,50] Mass-bias corrected signals of ambient Hg and Hg tracers were calculated using a simplified approach due to the negligible differences as compared to the matrix-based signal deconvolution approach[51] (Figure S1). Details related to the signal calculation and comparison methods can be found in Text S5.

https://doi.org/10.1021/acs.est.3c02676
Environ. Sci. Technol. 2023, 57, 8149−8160

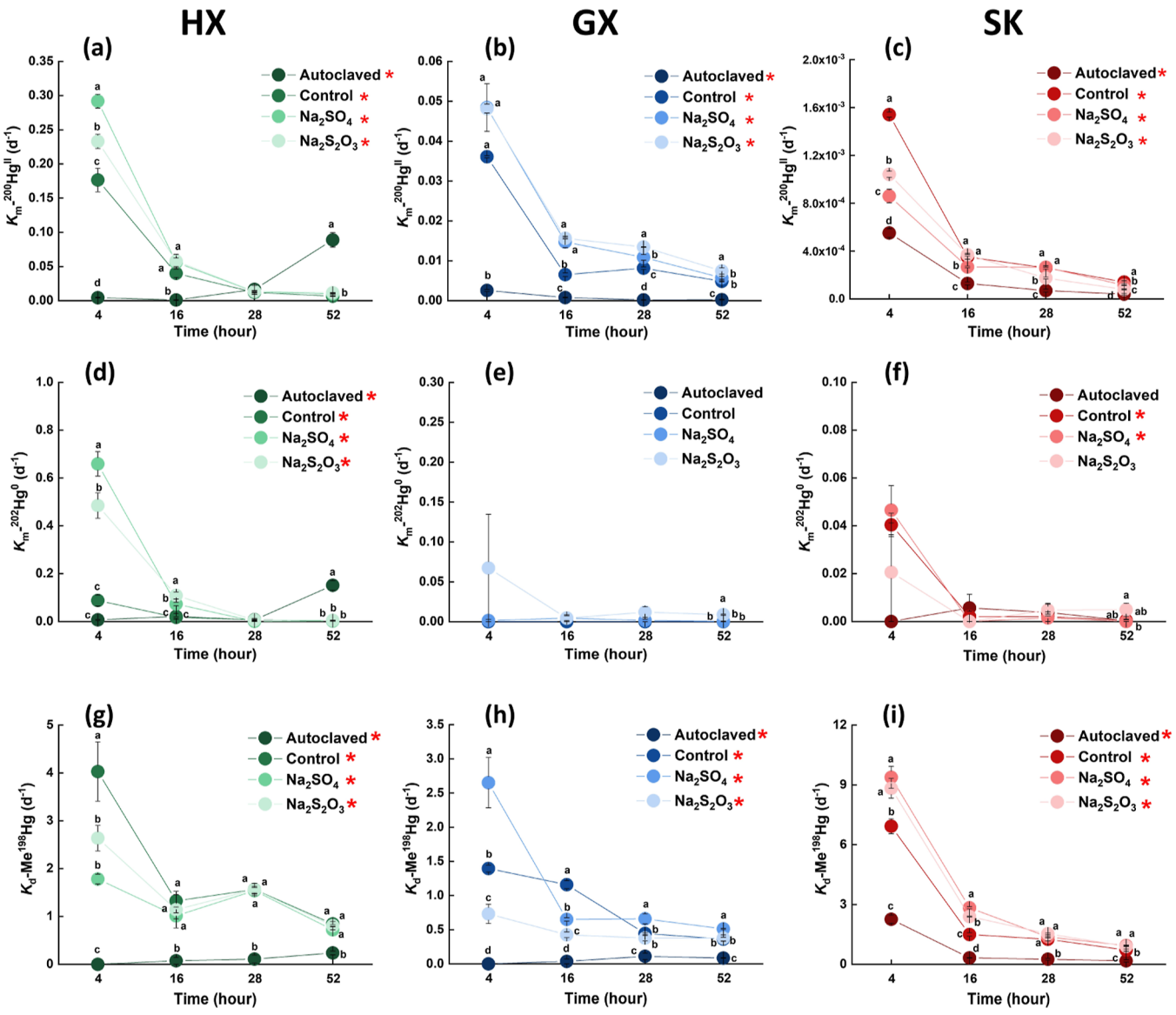

Figure 1. Methylation rate constants for $^{200}Hg^{2+}$ [K_m-$^{200}Hg^{2+}$, (a−c)], methylation rate constants for $^{202}Hg^0$ [K_m-$^{202}Hg^0$, (d−f)], and demethylation rate constants for $Me^{198}Hg$ [K_d-$Me^{198}Hg$, (g−i)] as a function of time at the three sites (HX, GX, and SK) across the different treatments. Error bars indicate the standard error (±SE) for replicates (n = 3). Different lowercase letters indicate that the differences between the treatments at each time point are significant (one-way ANOVA $p < 0.05$). Missing lowercase letters indicate no significant difference between treatments. "*" after the legend suggests that the differences within each treatment at different times are significant (t-test $p < 0.05$).

The concentrations of generated Me^iHg and $^iHg^0$ (i = 198, 200, and 202) were quantified by external calibrations[50] (Figure S2). The methylation rate constants [K_m-$^{200}Hg^{II}$ (d^{-1}) and K_m-$^{202}Hg^0$ (d^{-1})], demethylation rate constant [K_d-$Me^{198}Hg$ (d^{-1})], and volatilization rate constants [K_v-$Me^{198}Hg$ (d^{-1}) and K_v-$^{200}Hg^{II}$ (d^{-1})] were calculated from [Me^iHg], [$^iHg^0$] (i = 198, 200, and 202), and the amounts of spiked Hg tracers using an irreversible pseudo-first-order model.[52] Meanwhile, the ratios of produced MeHg to spiked inorganic Hg tracers [$Me^{200}Hg/^{200}Hg^{II}$ (%) and $Me^{202}Hg/^{202}Hg^0$ (%)], the ratio of MeHg losses to spiked MeHg tracer [$Me^{198}Hg$ demethylation (%)], and the ratios of produced purgeable Hg^0 to spiked Hg tracers [$^{200}Hg^0/^{200}Hg^{2+}$ (%) and $^{198}Hg^0/Me^{198}Hg$ (%)] were also obtained. The calculation details and assumptions made for the irreversible pseudo-first-order model are shown in Text S6. It should be noted that linear approximations may underestimate the rate constants in Hg transformation due to the presence of reversible reactions (e.g., demethylation),[53] adsorption, and precipitation of spiked Hg tracers.[54] Therefore, the rate constants obtained from this study may not be suitable for comparison with other works using different approaches. Similarly, using the measured purgeable Hg^0 may underestimate Hg^{II} reduction due to the potential existence of non-purgeable Hg^0 (e.g., immobilized by solid phases).[55,56] However, all purgeable Hg^0 was produced from Hg reduction; therefore, Hg volatilization was used in this study to represent Hg reduction.

2.5. QA/QC and Statistics. The certified reference material (CRM) ERM-CC580 was used, and the MeHg recovery measurement for CRM ranged from 76.2 to 108.4%, with an average of 85.2 ± 9.07% (n = 26), which is comparable with previous studies.[7,16,22,25,46,49] Duplicates were added every 10 samples during measurement, and the relative standard

https://doi.org/10.1021/acs.est.3c02676
Environ. Sci. Technol. 2023, 57, 8149−8160

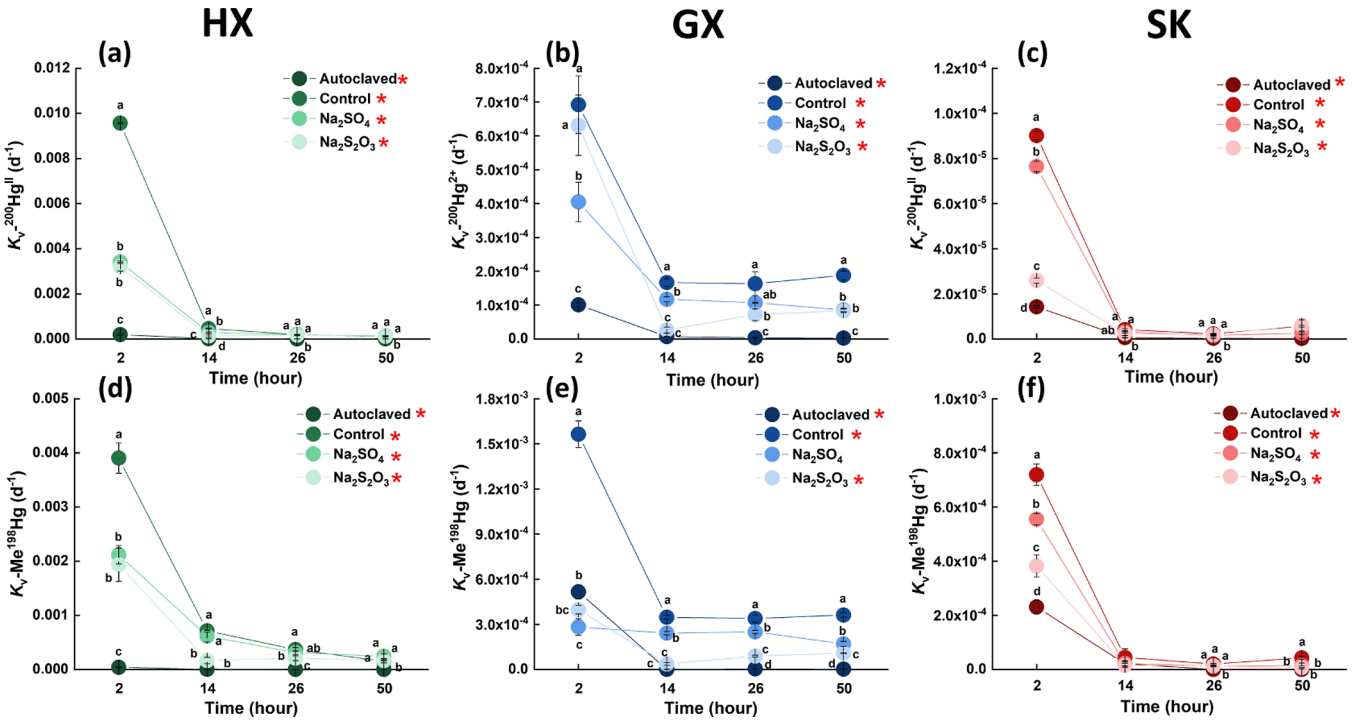

Figure 2. Volatilization rate constants for $^{200}Hg^{II}$ [K_v-$^{200}Hg^{II}$, (a–c)] and $Me^{198}Hg$ [K_v-$Me^{198}Hg$, (d–f)] as a function of time at the three sites (HX, GX, and SK) across the different treatments. Error bars indicate the standard error (±SE) for replicates (n = 3). Different lowercase letters indicate that the differences between the treatments at each time point are significant (one-way ANOVA $p < 0.05$). "*" after the legend indicates that the differences within each treatment at different times are significant (t-test $p < 0.05$).

deviation (RSD %) of duplicates is <10%. The instrument detection limits for Hg by using inductively coupled plasma–mass spectrometry is 10 pg. Data are presented as the mean ± standard error (SE). Group differences were assessed by t-tests and one-way ANOVA with Duncan's post hoc test using SPSS 23.0 (IBM, IL, USA). Statistical significance (p) was set at <0.05 (two-tailed).

3. RESULTS

3.1. Variations in Major Redox Couples and Soil DOM. Redox couples (HS^-–SO_4^{2-}, NH_4^+–NO_3^-, and Fe^{2+}–Fe^{3+}) were measured to show the redox conditions during incubation. The concentrations of NH_4^+ in the liquid phases of all paddy slurries were 2–3 orders of magnitude higher than those of NO_3^-; the highest NO_3^- concentrations were observed in the autoclaved treatments (Figure S3). Higher Fe^{2+} percentages in total Fe (Fe^{2+} + Fe^{3+}) were found in the two S treatments, as compared to the control treatment, at all sites ($p < 0.05$, Figure S4). Similar distribution patterns of SO_4^{2-} were found in the Na_2SO_4 and $Na_2S_2O_3$ treatments at sites HX and SK (Figure S5). The concentrations of sulfide (HS^-) at all sites were 3 orders of magnitude lower than those of SO_4^{2-} (Figure S5). It is noted that some large variations of Fe^{2+}, Fe^{3+}, and NO_3^- were observed in the autoclaved samples, and proper explanations are in the Text S7. The concentrations of soil DOM (represented by dissolved organic carbon, DOC) varied across the different sites ($p < 0.05$, Figure S6) but were similar among the different treatments at a given site ($p > 0.05$, Figure S6). UV–vis absorption and fluorescence spectra were used to characterize the compositional structure of DOM. Similarly, for almost all spectral indices [i.e., $SUVA_{254}$, $S_{275-295}$, a(355), fluorescence peaks, HIX, and BIX], there were no differences among the treatments (Figure S7). The only differences were as follows. First, higher intensities of fluorescence peak A ($p < 0.05$, Figure S7d) and peak C ($p < 0.05$, Figure S7e) were observed in the S addition treatments (i.e., both Na_2SO_4 and $Na_2S_2O_3$ treatments) as compared to the control at site SK. Second, at site GX, lower intensities of fluorescence peak B ($p < 0.05$, Figure S7f) and peak T ($p < 0.05$, Figure S7g) were observed in the S addition treatments as compared to the control.

3.2. Copy Numbers of the *hgcA*, *merA*, *merB*, *dsrB*, and *soxB* Genes and Hg-Methylating Communities. Copies of the *mer* operon (*merA* and *merB*) were below the detection limit in all treatments at all sites [real-time threshold cycle (C_T) > 31]. Significantly lower copies of *hgcA*, *dsrB*, and *soxB* were found in the autoclaved samples compared to the other treatments ($p < 0.05$, Figure S8). At site GX, the control treatment exhibited more *hgcA* genes than the two S treatments ($p < 0.05$, Figure S8b), while the opposite trend was observed at site SK ($p < 0.05$, Figure S8c). A distribution pattern similar to that of *hgcA* was found for *dsrB* at sites GX and SK (Figure S8e,f). More copies of the *soxB* gene in the $Na_2S_2O_3$ treatment were observed at the three sites, as compared to those in the Na_2SO_4 treatment ($p < 0.05$, Figure S8g–i). The *hgcA* gene amplicon sequencing revealed that the relative abundances of sulfate-reducing bacterium (SRB) methylators (i.e., SRB carrying the *hgcA* gene) in the S addition treatments at sites HX and GX were 1.04–1.56 and 1.27–1.82 times higher than that in the control, respectively ($p > 0.05$). The identified major SRB methylators were *Peptococcaceae*, *Desulfovibrionaceae*, and *Desulfobulbaceae* (Figure S9b). The search of the metagenomic data for homologues of *hgcA* revealed more SRB methylators in the S addition treatments than in the control at site HX (23.5% higher in

https://doi.org/10.1021/acs.est.3c02676
Environ. Sci. Technol. 2023, 57, 8149–8160

sulfate treatment and 17.5% higher in thiolsulfate treatment, Figure S9d).

3.3. Methylation of $^{200}Hg^{II}$ and $^{202}Hg^{0}$. The methylation rate constants, K_m-$^{200}Hg^{II}$ (d^{-1}) and K_m-$^{202}Hg^{0}$ (d^{-1}), show the methylation of spiked $^{200}Hg^{II}$ and $^{202}Hg^{0}$, respectively (Figure 1). The variation trend in K_m-$^{200}Hg^{II}$ was the same at all sites, with a sharp decrease from 4 to 16 h and a slight decrease thereafter; the autoclaved treatment at site HX was the only exception. However, the ranges of K_m-$^{200}Hg^{II}$ among the study sites differed greatly. The highest values of K_m-$^{200}Hg^{II}$ at sites HX, GX, and SK were all observed at the 4th h, with values of 0.29 ± 0.01 d^{-1} (in the Na_2SO_4 treatment, $p < 0.05$, Figure 1a), 0.048 ± 0.006 d^{-1} (in both the Na_2SO_4 and $Na_2S_2O_3$ treatments, $p < 0.05$, Figure 1b), and 0.0015 ± 0.00002 d^{-1} (in the control treatment, $p < 0.05$, Figure 1c), respectively. The ratios of produced $Me^{200}Hg$ to spiked $^{200}Hg^{II}$ [$Me^{200}Hg/^{200}Hg^{II}$ (%)] and the $Me^{200}Hg$ concentrations during incubation are shown in Figures S10 and S11, respectively. The S treatments yielded more production of $Me^{200}Hg$ than the control treatment at sites HX and GX ($p < 0.05$, Figure S11), and significantly higher $Me^{200}Hg$ was observed in the $Na_2S_2O_3$ treatment at site GX than in the Na_2SO_4 treatment (at the 52nd h, $p < 0.05$, Figure S11b).

The formation of $Me^{202}Hg$ from spiked $^{202}Hg^{0}$ reflects the methylation of $^{202}Hg^{0}$. At site HX, the highest K_m-$^{202}Hg^{0}$ was found at the 4th h in the Na_2SO_4 treatment (0.66 ± 0.05 d^{-1}, $p < 0.05$), followed by the $Na_2S_2O_3$ treatment (0.49 ± 0.05 d^{-1}, $p < 0.05$) and then the control and autoclaved treatments ($p < 0.05$, Figure 1a). Correspondingly, 10.98 ± 0.85 and 8.08 ± 0.89% of spiked $^{202}Hg^{0}$ were transformed to $Me^{202}Hg$ in the Na_2SO_4 and $Na_2S_2O_3$ treatments, respectively, at site HX (Figure S10d). At sites GX and SK, more $Me^{202}Hg$ was produced in the $Na_2S_2O_3$ treatment than in the other treatments (1.90 ± 0.17% for GX and 1.07 ± 0.59% for SK, $p < 0.05$, Figure S10e,f).

3.4. Demethylation of $Me^{198}Hg$. All $Me^{198}Hg$ tracers yielded significant degradation over time, except in the autoclaved treatments (Figure 1). At site HX, there were no significant differences in K_d-$Me^{198}Hg$ among the control, Na_2SO_4, and $Na_2S_2O_3$ treatments across the whole time series, with the exception of K_d-$Me^{198}Hg$ in the control treatment (4.03 ± 0.62 d^{-1}) at the 4th h. At sites GX and SK, the S-amended treatments yielded higher K_d-$Me^{198}Hg$ values than the control treatment at the end of incubation (the Na_2SO_4 treatment in GX and both the Na_2SO_4 and $Na_2S_2O_3$ treatments in SK) ($p < 0.05$, Figure 1h,i). Although demethylation of $Me^{198}Hg$ was also observed in the autoclaved treatments, it was significantly lower than that observed in the other treatments ($p < 0.05$, Figures S11d–f), suggesting that microbially mediated demethylation of MeHg is predominant in paddy soils.

3.5. Reduction of $^{200}Hg^{II}$ and Formation of $^{198}Hg^{0}$ from $Me^{198}Hg$. The volatilization rate constants, K_v-$^{200}Hg^{II}$ (d^{-1}) and K_v-$Me^{198}Hg$ (d^{-1}), show the formation of purgeable $^{200}Hg^{0}$ and $^{198}Hg^{0}$ by the reduction of spiked $^{200}Hg^{II}$ and $Me^{198}Hg$, respectively (Figure 2). Significantly higher amounts of purgeable $^{200}Hg^{0}$ and $^{198}Hg^{0}$ were detected in the non-autoclaved treatments than in the autoclaved samples at all sites (Figure S12). However, the ratios of produced purgeable $^{200}Hg^{0}$ and $^{198}Hg^{0}$ to spiked Hg tracers [$^{200}Hg^{0}/^{200}Hg^{II}$ (%) and $^{198}Hg^{0}/Me^{198}Hg$ (%)] were 1–2 orders of magnitude lower than those of $Me^{200}Hg/^{200}Hg^{II}$ (%) and $Me^{198}Hg$ demethylation (%) (Figures S10 and S13). In the initial period (2 h), K_v-$^{200}Hg^{II}$ in the control treatment was higher than those of the S-amended treatments (Na_2SO_4 and $Na_2S_2O_3$) at all sites ($p < 0.05$, except K_v-$^{200}Hg^{II}$ at site GX, Figure 2). Lower purgeable $^{200}Hg^{0}$ in the S treatments, as compared to the control treatment, was found at site GX across the entire study period ($p < 0.05$, Figure S12b) and at site HX in the first 14 h of incubation ($p < 0.05$, Figure S12a).

Similar to K_v-$^{200}Hg^{II}$, K_v-$Me^{198}Hg$ in the control treatment at the 2nd h was significantly higher than those of the S treatments at all sites ($p < 0.05$, Figure 2). However, a comparable purgeable $^{198}Hg^{0}$ mass was found between the control and S treatments across most of the incubation period at sites HX and SK (Figure S12d,f). Less purgeable $^{198}Hg^{0}$ mass was observed in the $Na_2S_2O_3$ treatment than the Na_2SO_4 treatment at site GX ($p < 0.05$, Figure S12e). It should be noted that some production of $^{198}Hg^{0}$ may be from $^{198}Hg^{II}$ reduction instead of from $Me^{198}Hg$ because the purity of our synthesized $Me^{198}Hg$ was 83.2%, which means that 16.8% of $^{198}Hg^{II}$ remained in the synthesized $Me^{198}Hg$. Therefore, the formation of $^{198}Hg^{0}$ only from $Me^{198}Hg$ was recalibrated according to the purity of $Me^{198}Hg$ and the fraction of conversion from $^{200}Hg^{II}$ to $^{200}Hg^{0}$ (Text S8). By subtracting $^{198}Hg^{0}$ originating from $^{198}Hg^{II}$, we found that 86.4 ± 11.6, 89.4 ± 10.4, and 97.1 ± 3.4% of $^{198}Hg^{0}$ were from $Me^{198}Hg$ at sites HX, GX, and SK, respectively. This confirms the transformation of $Me^{198}Hg$ to $^{198}Hg^{0}$. Thus, the recalibration procedure is necessary for accurately tracing the reduction of synthesized MeHg tracers; this has been ignored in previous studies.

3.6. Oxidation or Immobilization of $^{202}Hg^{0}$. The losses of spiked $^{202}Hg^{0}$ through purging suggest that purgeable $^{202}Hg^{0}$ is transformed to non-purgeable ^{202}Hg. Both oxidation and immobilization are responsible for the formation of non-purgeable ^{202}Hg. Rapid depletion of purgeable $^{202}Hg^{0}$ occurred in this study; more than 99.9% of spiked $^{202}Hg^{0}$ could not be purged out within 2 h (Figure S13g–i). S amendments significantly decreased the masses of purgeable $^{202}Hg^{0}$ at sites HX and GX when compared with the control treatment ($p < 0.05$, Figure S12g,h).

4. DISCUSSION

4.1. Mercury Transformation in Paddy Soils. Signals of isotope-enriched Hg tracers in the control and autoclaved treatments showed transformations (i.e., methylation, demethylation, reduction, and oxidation/immobilization) between different Hg species (Hg^{II}, MeHg, and Hg^{0}) in paddy soils.

Significantly lower $Me^{200}Hg$ production (Figures S10 and S11) in the autoclaved treatments compared to the other treatments suggests that abiotic methylation, if present at all, is negligible in paddy soils. Methylation of Hg^{II} (K_m-$^{200}Hg^{II}$) decreased by orders of magnitude over the Hg contamination gradient ([THg]: HX (0.15 ± 0.003 mg kg^{-1}) < GX (17.2 ± 1.7 mg kg^{-1}) < SK (609 ± 7 mg kg^{-1})), which is consistent with our previous findings.[22,25] Microbially mediated processes are likely the cause,[22,25] because (i) there were no differences in the soil texture and structure between the sites and (ii) Hg selective pressure can reshape the microbial community structure of paddy soils, altering the abundance of methylators or microbial helpers (e.g., syntrophic microorganisms) that support methylators.[57,58] Moreover, a lower concentration but more aromatic DOM (i.e., lower DOC but higher $SUVA_{254}$) was observed at site SK, as compared to sites HX and GX ($p <$

https://doi.org/10.1021/acs.est.3c02676
Environ. Sci. Technol. 2023, 57, 8149–8160

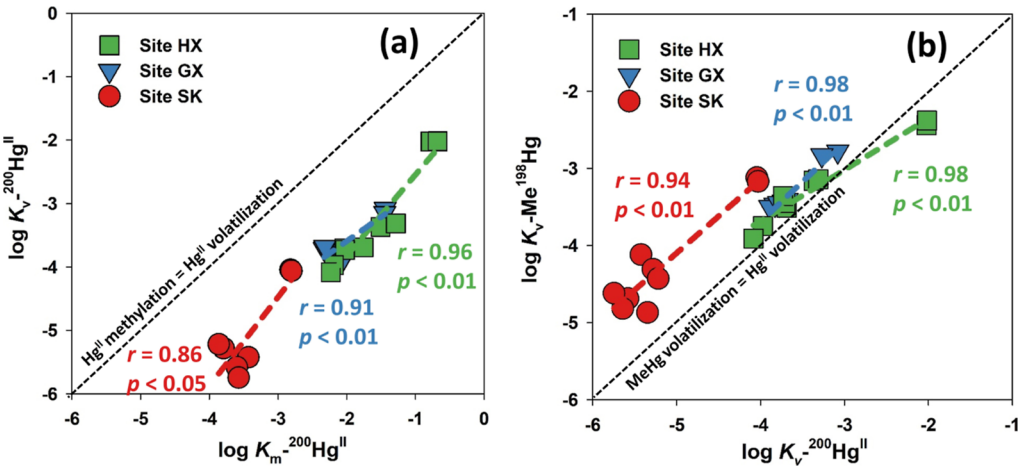

Figure 3. log K_m-$^{200}Hg^{II}$ vs log K_v-$^{200}Hg^{II}$ (a) and log K_v-$^{200}Hg^{II}$ vs log K_v-$Me^{198}Hg$ (b) at the three sites (HX, GX, and SK) in the control treatment. Dashed lines represent the 1:1 line between two variables.

0.05, Figures S6 and S7). This implies that DOM with a high humification degree inhibits microbially mediated Hg^{II} methylation. This is also supported by the observed negative correlations between K_m-$^{200}Hg^{II}$ and the humic-like characters of the DOM at all sites ($r = -0.58$ and $p < 0.05$ for K_m-$^{200}Hg^{II}$ vs peak A, $r = -0.75$ and $p < 0.01$ for K_m-$^{200}Hg^{II}$ vs peak C, and $r = -0.77$ and $p < 0.01$ for K_m-$^{200}Hg^{II}$ vs $SUVA_{254}$, Table S3). Typically, DOM with a lower molecular weight, less humic substances, and more autochthonous sources (e.g., low-molecular-weight organic acids, proteins, and sugars) can more readily fuel microbially mediated Hg^{II} methylation, as compared to highly aromatic or humic substances.[59]

Active methylation of $^{200}Hg^{II}$ (Figures 1a, S10a, and S11a) and increasing copies of the *hgcA* gene (Figure S8) were observed in the autoclaved treatment at site HX at the end of the period of incubation. This suggests potential microbial succession unaccounted for after autoclaving. An uncertain effect of autoclaving on the inhibition of bacterial activity has previously been reported, which is consistent with this observation.[22,60] A spread-plate experiment was conducted using autoclaved samples to test the activity of microorganisms (Text S9). No countable colony-forming units were identified, suggesting that the microorganisms responsible for the increase in the *hgcA* signal in the autoclaved samples are nonculturable with the selected growth medium. Moreover, we observed a significant correlation between methylation using either $^{200}Hg^{II}$ or $^{202}Hg^{0}$ as the substrate in the autoclaved treatment at site HX (Figure S14). This implies that both $^{202}Hg^{0}$ and $^{200}Hg^{II}$ can be methylated and their methylation processes are highly correlated. This is not surprising because Hg^{0} can be methylated after oxidation[61] in cultures of *Desulfovibrio desulfuricans* ND132[62,63] and *Geobacter sulfurreducens* PCA.[63,64] In this study, less than 0.1% of spiked $^{202}Hg^{0}$ was recovered as purgeable $^{202}Hg^{0}$ during incubation (i.e., dominated by non-purgeable ^{202}Hg, Figure S12g–i). The rapid formation of non-purgeable ^{202}Hg from spiked $^{202}Hg^{0}$ implies the rapid oxidization or solid-phase immobilization of $^{202}Hg^{0}$ in paddy soil slurries. Non-purgeable Hg^{0} can be present as Hg^{0} or Hg^{II} associated with particles.[56] However, with the presence of natural organic matter[65,66] and some anaerobic bacteria,[62,63] Hg^{0} can easily be oxidized to Hg^{II}. In particular, several recent studies have reported that particulate-bound Hg^{II} can also act as a bioavailable substrate fueling methylation.[67,68] Previously, Colombo et al.[62] and Hu et al.[63] reported the biotic oxidation of Hg^{0} through pure culture studies. The current results demonstrated that abiotic reactions likely dominate the oxidization of spiked $^{202}Hg^{0}$ due to the lower purgeable $^{202}Hg^{0}$ masses recovered from the autoclaved treatments, as compared to the other treatments ($p < 0.5$, Figure S12g–i). In this study, the spiked $^{202}Hg^{0}$ in paddy soils was likely oxidized to $^{202}Hg^{II}$ and then microbially methylated. Accordingly, both biotic oxidation[61−64] and abiotic oxidation[65,66] of Hg^{0} will provide Hg^{II} fuel for methylation. This observation supports the hypothesis that rapid redox recycling of Hg species contributes to Hg speciation resetting, forming bioavailable Hg^{II} at methylation sites.[69]

In addition to the coupled reactions of oxidization and methylation of Hg^{0} in paddy soils, the reduction of Hg^{II} was also co-varied with the methylation of Hg^{II}, as indicated by the significant correlation between log K_m-$^{200}Hg^{II}$ and log K_v-$^{200}Hg^{II}$ in the control treatment (Figure 3a). Historically, it was assumed that reduction competes with methylation for bioavailable Hg^{II} substrates; however, this view is rapidly changing, as Hg^{0} has been shown to be capable of serving as a substrate for methylation.[62,63] In this microcosm study, competition between methylation and reduction was also not observed due to the co-variation between K_m-$^{200}Hg^{II}$ and K_v-$^{200}Hg^{II}$ (Figure 3a). Lu et al.[70] identified a *merA*- and *merB*-containing iron-reducing bacterium capable of simultaneously methylating Hg^{II} and generating Hg^{0} through reductive demethylation of MeHg in anoxic conditions. Here, no significant correlation was observed between $^{200}Hg^{II}$ methylation (shown as K_m-$^{200}Hg^{II}$ or $Me^{200}Hg/^{200}Hg^{II}$ %) and $Me^{198}Hg$ demethylation (shown as K_d-$Me^{198}Hg$ and $Me^{198}Hg$ demethylation %), and the *merA* and *merB* genes were below the detection limit. This suggests that reductive demethylation of newly formed $Me^{200}Hg$ (via the *mer* operon) is not the likely mechanism responsible for the correlation between $^{200}Hg^{II}$ methylation and reduction. Rather, other pathways, such as the involvement of c-type cytochromes in Hg^{II} reduction[63] and/or photoheterotrophic or fermentative Hg^{II} reduction,[71] may exist in paddy soils. The former process depends on extracellular electron transfer, whereas the latter depends on the presence of fermentable carbon sources in the dark or stimulation of bacterial phototrophy in the presence of light.[69,71,72] However, the reduction of $^{200}Hg^{II}$ was 1−2 orders of magnitude lower

https://doi.org/10.1021/acs.est.3c02676
Environ. Sci. Technol. 2023, 57, 8149−8160

than the methylation of $^{200}Hg^{II}$ (Figures 3a, S11, and S12), suggesting a predominant role of methylation when compared with the reduction of Hg^{II} in paddy soils. It is also possible that the newly produced $^{200}Hg^0$ is rapidly re-oxidized to $^{200}Hg^{II}$ prior to being methylated to $Me^{200}Hg$ (i.e., avoiding the purge). This quick redox recycling step may favor $^{200}Hg^0$ accessibility and availability to methylators. As a result, rapid anoxic redox cycling, further away from the air/water interface, may maintain a pool of bioavailable Hg^{II}, albeit small, that sustains methylation. Nevertheless, over a large scale or long term, Hg reduction and its subsequent evasion may still contribute to the removal of Hg from rice paddy soils and, therefore, limit the formation of MeHg, especially in uncontaminated paddy soils (i.e., Hg^{II} methylation is constrained by the THg concentration). Therefore, it is critical to tease apart the importance of these two pathways for the proper management of paddy systems.

In this study, purgeable $^{198}Hg^0$ was detected from the spiked $Me^{198}Hg$ (Figure S12d−f), whereas the ratio of purgeable $^{198}Hg^0$ to the spiked $Me^{198}Hg$ ($^{198}Hg^0/Me^{198}Hg$ %) was 3−4 orders of magnitude lower than the $Me^{198}Hg$ demethylation % (Figures S10 and S13). The copy numbers of the *mer* operon genes (*merA* and *merB*), which mediate reductive demethylation,[73,74] were below the detection limit in the control treatment. In the absence of a broad-range *mer* operon (i.e., involved in both MeHg degradation and Hg^{II} reduction), *mer*-independent oxidative demethylation (OD) may be a significant mechanism underlying MeHg degradation in paddy soils.[75] Oxidative demethylation is a nonspecific co-metabolic process producing Hg^{II} and CO_2 and is commonly observed in anoxic conditions.[74,76] In this study, the correlations between K_v-$Me^{198}Hg$ and K_v-$^{200}Hg^{II}$ (Figure 3b) and between purgeable $^{198}Hg^0$ and $^{200}Hg^0$ (Figure S15) suggest that the formation of purgeable $^{198}Hg^0$ from $Me^{198}Hg$ is a two-step reaction: $Me^{198}Hg$ is oxidatively demethylated to $^{198}Hg^{II}$ and then reduced to $^{198}Hg^0$, likely using a pathway similar to $^{200}Hg^{II}$ reduction. The data points were located close to the log K_v-$Me^{198}Hg$: log K_v-$^{200}Hg^{II}$ = 1:1 line (Figure 3b), further supporting the control of $Me^{198}Hg$ degradation by mechanisms similar to or closely associated with $^{198}Hg^{II}$ reduction. Moreover, significant correlations were observed between the purgeable $^{200}Hg^0$ and $^{202}Hg^0$ masses at all sites (Figure S15), implying that the formation of Hg^0 from spiked $^{200}Hg^{II}$, $Me^{198}Hg$, and $^{202}Hg^0$ tracers is the same as Hg^{II} reduction. This further highlights that the formation of Hg^{II} may be a precondition for subsequent methylation and reduction. In addition, significant correlations between humic-like characters of DOM (i.e., humic-like compounds indicated by peak A and peak C and aromaticity indicated by $SUVA_{254}$) and K_v (i.e., both K_v-$Me^{198}Hg$ and K_v-$^{200}Hg^{II}$) were observed but were absent with K_d-$Me^{198}Hg$ (Table S3). This implies that humic fractions of soil DOM inhibited Hg^{II} reduction. This is the major mechanism explaining the inhibited transformation of MeHg to Hg^0 by humified DOM.

Partitioning of Fe between solid and aqueous phases plays a role in Hg transformation. This was evidenced by the significant correlations between the aqueous Fe concentration (i.e., Fe^{2+}+Fe^{3+}) and K_m-$^{200}Hg^{II}$ or K_v-$^{200}Hg^{II}$ in this study (Table S4). Research has demonstrated that reductive dissolution of Fe(oxyhydr)oxides may increase the bioavailability of previously adsorbed Hg^{II}.[24,26] However, the recrystallization from Fe(oxyhydr)oxides to Fe−S solids (e.g., FeS and FeS_2) may largely decrease the bioavailability of the released Hg^{II} from Fe(oxyhydr)oxides.[25,29] The influence of redox cycling of Fe in aqueous phases (Fe^{2+}−Fe^{3+} couple) on Hg transformation was absent in this microcosm study. More research on Fe redox cycling in both solid and aqueous phases, and its influence on Hg transformation, is needed in the future.

4.2. Role of Sulfate and Thiosulfate in Hg Transformation in Paddy Slurries. The influences of S addition on Hg methylation/demethylation were not only dependent on the S species but also on the study site (Figures 1 and 2, S11, and S12). The roles of S species in different Hg transformation processes raise two questions: (i) how does the S input influence Hg transformation in paddy soils? and (ii) do sulfate and thiosulfate affect the abovementioned processes to the same extent? These two questions are addressed below.

4.2.1. Hg Speciation Change- vs Microbial-Driven Hg Transformation under S Input Conditions. The bioavailability of Hg and the microbial community are recognized as important factors determining biotic Hg cycling in the natural environment.[20,77] However, it is still not clear whether S-dependent Hg transformation is regulated by Hg speciation (or mobility/bioavailability) or by changes in the microbial community structure and function in response to S species amendments. Recently, Li et al.[21] and Lei et al.[47] reported that an increase in Hg mobility, rather than changes in the structure and functional profiles of microbial methylators, triggers an enhancement of Hg methylation in S-amended paddy soils. Here, Hg speciation and the microbial community were found to play different roles in Hg methylation in S-treated paddy soils with different Hg contamination levels.

At sites (HX and GX) with low and moderate [THg] levels, opposing influences of S addition on Hg methylation and reduction were observed; the addition of Na_2SO_4 and $Na_2S_2O_3$ increased the formation of $Me^{200}Hg$ but decreased the formation of $^{200}Hg^0$ from $^{200}Hg^{II}$ ($p < 0.05$, Figures 1, 2, and S10−S13). If the bioavailability of Hg is increased, it is expected that S addition would promote Hg^{II} methylation and reduction synchronously, especially given the presence of the co-varied methylation and reduction of Hg^{II} as discussed above (Figure 3a). Despite the very limited experimental evidence, the uptake of Hg^{II} species by Hg methylators and Hg reducers is assumed to be comparable. In our previous study, SRBs were confirmed to be the dominant Hg^{II} methylators at site HX and one of the Hg^{II} methylators at site GX.[22] Here, both Na_2SO_4 and $Na_2S_2O_3$ provided SO_4^{2-}, thus fueling the SRB following oxidization or disproportionation of $S_2O_3^{2-}$.[78−80] Therefore, the SRB-mediated Hg^{II} methylation at sites HX and GX was likely promoted. In particular, higher SO_4^{2-} concentrations ($p < 0.05$, Figure S5a) and copy numbers of the *dsrB* gene ($p < 0.05$, Figure S8d) in the S treatments compared to the control treatment were identified at site HX. At site GX, however, S addition significantly reduced the abundance of the *dsrB* gene ($p < 0.05$, Figure S8e), and this was closely correlated with *hgcA* gene copies (Figure S16). This implies that in addition to SRB, other microorganisms are also involved in Hg^{II} methylation, and SO_4^{2-} might be a limiting factor for methylation at site GX.[22] In addition, more SRB methylators were observed in the S addition treatments compared to the control at sites HX and GX through either *hgcA* gene amplicon sequencing or metagenomic analysis (Figure S9), which provides direct evidence that the activity of SRB methylators was promoted by adding both sulfate and thiolsulfate. Among all the identified SRB methylators, *Desulfomonile* is likely a key SRB genus associate with Hg^{II} methylation at sites HX and GX

https://doi.org/10.1021/acs.est.3c02676
Environ. Sci. Technol. 2023, 57, 8149−8160

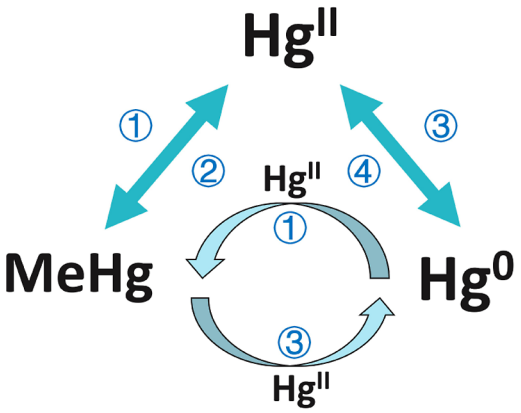

Hg Transformations		Fraction of conversion (%)			Biotic or abiotic processes
		Site HX	Site GX	Site SK	
(1) Methylation	$Hg^{II} \rightarrow MeHg$	1.43 ± 0.10 %	1.05 ± 0.03 %	0.31 ± 0.02 ‰	
	$Hg^{0} \rightarrow Hg^{II} \rightarrow MeHg$	0.44 ± 0.11 %	0 %	0.11± 0.11 %	e⁻
(2) Demethylation	$MeHg \rightarrow Hg^{II}$	83.8 ± 1.78 %	54.3 ± 2.63 %	78.4 ± 2.57 %	
(3) Reduction	$Hg^{II} \rightarrow Hg^{0}$	0.20 ± 0.02 ‰	0.39 ± 0.03 ‰	0.012 ± 0.001 ‰	
	$MeHg \rightarrow Hg^{II} \rightarrow Hg^{0}$	0.31 ± 0.06 ‰	0.75 ± 0.03 ‰	0.089 ± 0.012 ‰	
(4) Oxidation/ immobilization	$Hg^{0} \rightarrow Hg^{II}$/non-purgeable Hg^{0}	> 99.9 %	> 99.9 %	> 99.9 %	e⁻

Biotic process Abiotic process

Figure 4. Schematic diagram illustrating Hg cycling in paddy soils and transformation rates of each process. Fractions of conversion are from Figures S10 and S13.

under S addition, due to its significant co-variation with log K_m-$^{200}Hg^{II}$ (Figure S17).

Inhibition of $^{200}Hg^{II}$ reduction under S addition at sites HX and GX ($p < 0.05$, Figures 2 and S12) could be interpreted in two ways. (i) S addition promotes both Hg^{II} and Hg^0 methylation. The rapid redox cycling of Hg^0 makes it a bioavailable substrate for methylation (discussed above) which, therefore, reduces the amount of purgeable Hg^0. (ii) Exogenous S addition may break the balance between Hg^{II} methylators (i.e., SRB) and Hg^{II} reducers, thereby reducing the activity of Hg^{II} reducers. However, the communities of Hg^{II} reducers in this study remain unknown (i.e., *merA*-independent reducers), and more research is needed.

At the most contaminated site (SK, with the highest [THg]), Hg^{II} methylation and reduction were hampered, whereas demethylation of MeHg was promoted in the S-treated paddy soils when compared with the control treatment at site SK (Figures 1, 2, S11, and S12). It should be noted that a much higher NO_3^- concentration (1−3 orders of magnitude higher than those at sites HX and GX) was observed in the autoclaved treatment compared to the other treatments at site SK ($p < 0.05$, Figure S1c). This suggests that significant dissimilatory reduction of NO_3^- occurred in the presence of microorganisms.[81] The reduction of a large amount of NO_3^- may deplete electron donors for Hg^{II} methylation (e.g., sulfate reduction, iron reduction, and methanogenesis processes) and Hg^{II} reduction,[82−84] as evidenced by the higher SO_4^{2-} ($p < 0.05$, Figure S5) and lower Fe^{2+} ($p < 0.05$, Figure S6) concentrations at the end of incubation when compared with sites HX and GX. In addition, our previous work revealed that methanogens are involved in MeHg formation at site SK.[22] In this study, among the community of Hg methylators, higher relative abundances of *Methanothrix* and *Methanoregula*, carrying *hgcA* genes, were observed at site SK as compared to sites HX and GX (Figure S9c). Therefore, adding SO_4^{2-} will bring more competition for substrates between SRB and methanogens. In particular, the formation of CH_4 is thermodynamically more difficult than the reduction of SO_4^{2-} (i.e., a lower Eh is required).[85] In the matter of MeHg demethylation, promotion of SRB by the addition of SO_4^{2-} sources may facilitate SRB-mediated OD, since SRB is one of the major players in OD,[74,86] and OD was the dominant pathway for MeHg degradation in this study. The role of DOM in Hg transformation among different treatments is limited, due to the comparable optical properties for most of the indices (Figure S6). It is worth mentioning that consumption of protein-like compounds under the S addition treatments was observed at site GX (lower peak *B* and peak *T* than control, $p < 0.05$, Figure S6e,f). This partly explains the promoted activity of microorganisms (e.g., SRB) under sulfate and thiosulfate addition because the protein-like substances could be utilized preferentially by microorganisms.[87]

The evidence discussed above suggests that the increased production of MeHg is likely attributed to the facilitated activity of Hg^{II} methylators under the exogenous S input. Hg transformations are more sensitive to microorganisms involved in S cycling than Hg speciation changes regulated by reduced S species. S amendments affect the microbial community structure and functional profile of Hg methylators by directly supplying metabolic substrates (i.e., SO_4^{2-} for SRB) or amplifying the competition for metabolic substrates.

4.2.2. Sulfate vs Thiosulfate. Sulfate is a terminal electron acceptor, and thiosulfate is one of the major intermediates in S redox cycling.[78,80,88,89] In this study, the rates and magnitudes of Hg transformations in the S treatments were dependent on the S species (i.e., SO_4^{2-} and $S_2O_3^{2-}$).

Previous studies have reported that Hg^{II} can bind with $S_2O_3^{2-}$ and form bioavailable Hg−S_2O_3 complexes [e.g., $Hg(S_2O_3)_2^{2-}$ and $Hg(S_2O_3)_3^{4-}$],[90−93] which may be the mechanism underlying $Na_2S_2O_3$ addition-promoted methylation. However, the current results appear to suggest a different scenario. We suspect that the added $S_2O_3^{2-}$ was unstable and readily transformed into SO_4^{2-} rather than forming Hg−S_2O_3 complexes; this is evidenced by the similar SO_4^{2-} concentrations to those in the Na_2SO_4 treatment (Figure S5a−c). Furthermore, our modeling exercise (Visual MINTEQ, Text S10) predicted that the speciation of Hg^{II} was dominated by Hg-sulfide complexes [e.g., HgS_2H^-, $Hg(SH)_2^0$, and HgS_2^{2-}, Figure S18]; Hg−S_2O_3 complexes, if present at all, were negligible when sulfides were present in the paddy soils. In addition to Hg speciation changes, the prolonged supply of SO_4^{2-} to Hg^{II} methylators in the $Na_2S_2O_3$ treatment is probably another mechanism for the enhanced Hg^{II} methylation. Rapid depletion of SO_4^{2-} was found in the Na_2SO_4 treatment. However, in the $Na_2S_2O_3$ treatment, $S_2O_3^{2-}$ and its acid decomposition products (i.e., SO_3^{2-} and S^0)[79] involved in

https://doi.org/10.1021/acs.est.3c02676
Environ. Sci. Technol. 2023, 57, 8149−8160

disproportionation also continuously supplied SO_4^{2-}. These reactions are considered to be typical inorganic fermentations and are independent of external reductants or oxidants.[94] In the current study, the formation of SO_4^{2-} at site GX was slower than at sites HX and SK, suggesting that the oxidation of $S_2O_3^{2-}$ was likely concomitant with the reduction of SO_4^{2-} in the $Na_2S_2O_3$ and Na_2SO_4 treatments, respectively (Figure S5b). Moreover, higher abundances of S-oxidizing bacteria (*soxB* gene) were observed in the $Na_2S_2O_3$ treatments than the Na_2SO_4 treatments. In particular, copies of the *soxB* gene were negatively correlated with $[HS^-]$ at site GX ($r = -0.87$ and $p < 0.01$), which further confirms the capability of $S_2O_3^{2-}$ to replenish SO_4^{2-} through S oxidation (Figure S8g–i). This highlights that the role of S-oxidizing bacteria in SRB-mediated Hg methylation should be given more attention. In summary, the mechanisms of $S_2O_3^{2-}$- and SO_4^{2-}-regulated Hg^{II} methylation are partly different. Both can enhance SO_4^{2-} supply for Hg^{II} methylation, albeit at different rates. Therefore, the kinetics of SO_4^{2-} production or microbial SO_4^{2-} utilization influenced by the $S_2O_3^{2-}$ input can more likely explain the greater formation of MeHg in the $Na_2S_2O_3$ treatment. This deserves further study in the future. Although this study was not able to provide evidence as to how Hg speciation changes influence Hg methylation under S addition, this should not be ignored, especially in redox-fluctuation paddy soils.

5. ENVIRONMENTAL IMPLICATIONS

In addition to the widely accepted Hg^{II} methylation and MeHg demethylation, this study provides direct evidence of Hg^{II} reduction, Hg^0 oxidation/immobilization, Hg^0 methylation, and the formation of Hg^0 from MeHg in paddy soils (Figure 4). These processes are biotically mediated, with only one exception being that Hg^0 oxidation/immobilization is mainly mediated by abiotic processes. The finding that dark reduction of Hg^{II} occurs through a biotically mediated process in paddy soils further highlights the role of microbial reduction of Hg^{II} in this environmental media. Interestingly, Hg^0 from the dark reduction of Hg^{II} can be methylated upon re-oxidation. The comparable K_m-$^{202}Hg^0$ and K_m-$^{200}Hg^{II}$ values further imply the rapid redox recycling of Hg species, fueling methylation. The transformation of MeHg to Hg^0 is attributed to oxidative demethylation coupled with reduction, instead of reductive demethylation (RD), in flooded paddy soils; RD may occur during the drying period (air-exposed) of rice-growing in paddy soils.[74] These findings highlight that (i) biotically mediated dark reduction of Hg^{II} followed by re-oxidation is also a source of Hg^{II} methylation in flooded paddy soils; this has been largely overlooked previously in redox fluctuating environments; and (ii) transformation processes for different Hg species (Hg^0, Hg^{II}, and MeHg) in paddy soils are closely associated with each other. In addition to Hg^{II} reduction and methylation as mentioned above, MeHg may also be a source of Hg^0 emission into the atmosphere through oxidative demethylation and then reduction. This highlights the continuous and dynamic nature of Hg transformation in paddy soils.

Sulfate reduction and the formation of reduced S species (sulfide, elemental sulfur, polysulfides, etc.) have long been considered as factors influencing Hg transformation due to the role of the SRB in Hg^{II} methylation[38,89] and speciation changes of Hg.[29−31] However, this study implies that the oxidation of reduced S species by S-oxidizing bacteria is also an important process in Hg^{II} methylation. The likely mechanisms are (i) to provide more sulfate and (ii) to change the rate of sulfate supply in sulfate reduction. Therefore, SRB-mediated Hg^{II} methylation is not only influenced by the quantity of sulfate but also controlled by the kinetics of sulfur species transformations, warranting additional work to fully explore their connection to Hg methylation.

■ ASSOCIATED CONTENT

Supporting Information

The Supporting Information is available free of charge at https://pubs.acs.org/doi/10.1021/acs.est.3c02676.

Additional descriptions of sampling sites and sample collection; preparation of Hg tracers; preparation of paddy slurry; subsampling and measurements; calculation for ambient and isotope-enriched Hg signals; fraction of conversion and corresponding rate constants in Hg transformation; explanation for Fe^{2+}, Fe^{3+}, and NO_3^- variations; recalculation of produced $^{198}Hg^0$ from $Me^{198}Hg$; spread-plate experiment; MINTEQ modeling; amounts of spiked Hg tracers; primers used in qPCR; correlation between optical properties of DOM and Hg transformation rate constants; correlation between Fe species and Hg transformation rate constants; comparison of matrix-based deconvolution approach and the simplified approach; quality control for the external standard method; concentrations of NO_3^-/NH_4^+, Fe^{2+}/Fe^{3+}, SO_4^{2-}/HS^-, and DOC; optical properties of DOM; copy numbers of *hgcA*, *dsrB*, and *soxB* genes; mercury-methylating communities; concentrations of $Me^{198}Hg$, $Me^{200}Hg$, and $Me^{202}Hg$; masses of purgeable $^{198}Hg^0$, $^{200}Hg^0$, and $^{202}Hg^0$; ratio of produced MeHg or Hg^0 from spiked Hg tracers; log K_m-$^{200}Hg^{II}$ versus log K_m-$^{202}Hg^0$; log *hgcA* versus log *dsrB*; correlations among purgeable $^{198}Hg^0$, $^{200}Hg^0$, and $^{202}Hg^0$ masses; log K_m-$^{200}Hg^{II}$ versus relative abundance of SRB methylators; and speciation of Hg^{II} (PDF)

■ AUTHOR INFORMATION

Corresponding Author

Bo Meng − *State Key Laboratory of Environmental Geochemistry, Institute of Geochemistry, Chinese Academy of Sciences, Guiyang 550002, China;* orcid.org/0000-0002-7827-8673; Phone: +86-851-84396920; Email: mengbo@vip.skleg.cn; Fax: +86-851-85891721

Authors

Jiang Liu − *State Key Laboratory of Environmental Geochemistry, Institute of Geochemistry, Chinese Academy of Sciences, Guiyang 550002, China*

Ji Chen − *State Key Laboratory of Environmental Geochemistry, Institute of Geochemistry, Chinese Academy of Sciences, Guiyang 550002, China; College of Chemical Engineering, Huaqiao University, Xiamen 361021, China;* orcid.org/0000-0002-3385-1149

Alexandre J. Poulain − *Biology Department, University of Ottawa, Ottawa ON K1N 6N5, Canada;* orcid.org/0000-0002-0488-3993

Qiang Pu − *State Key Laboratory of Environmental Geochemistry, Institute of Geochemistry, Chinese Academy of Sciences, Guiyang 550002, China*

Zhengdong Hao − *State Key Laboratory of Environmental Geochemistry, Institute of Geochemistry, Chinese Academy of*

Sciences, Guiyang 550002, China; University of Chinese Academy of Sciences, Beijing 100049, China

Xinbin Feng − *State Key Laboratory of Environmental Geochemistry, Institute of Geochemistry, Chinese Academy of Sciences, Guiyang 550002, China;* orcid.org/0000-0002-7462-8998

Complete contact information is available at: https://pubs.acs.org/10.1021/acs.est.3c02676

Notes

The authors declare no competing financial interest.

■ ACKNOWLEDGMENTS

This research was supported by the National Natural Science Foundation of China (42022024, 41931297, 41921004, and 42107442), the CAS "Light of West China" program, Guizhou Provincial 2020 Science and Technology Subsidies (no GZ2020SIG), and the Guizhou Provincial Natural Science Foundation (Qian- Ke-He-Ji-Chu ZK [2023] Yi ban 474). We thank Kun Zhang for his help in the sample analysis. We also thank Dr. Tao Jiang, Siqi Zhang, and Sihua Zhu, all from Southwest University, for their valuable help in DOM analysis and discussion about the manuscript revision.

■ REFERENCES

(1) St. Louis, V. L.; Rudd, J. W. M.; Kelly, C. A.; Bodaly, R. A. D.; Paterson, M. J.; Beaty, K. G.; Hesslein, R. H.; Heyes, A.; Majewski, A. R. The Rise and Fall of Mercury Methylation in an Experimental Reservoir. *Environ. Sci. Technol.* **2004**, *38*, 1348−1358.

(2) Schartup, A. T.; Balcom, P. H.; Soerensen, A. L.; Gosnell, K. J.; Calder, R. S. D.; Mason, R. P.; Sunderland, E. M. Freshwater Discharges Drive High Levels of Methylmercury in Arctic Marine Biota. *Proc. Natl. Acad. Sci. U.S.A.* **2015**, *112*, 11789−11794.

(3) Zhao, L.; Anderson, C. W. N.; Qiu, G.; Meng, B.; Wang, D.; Feng, X. Mercury Methylation in Paddy Soil: Source and Distribution of Mercury Species at a Hg Mining Area, Guizhou Province, China. *Biogeosciences* **2016**, *13*, 2429−2440.

(4) Zhao, L.; Qiu, G.; Anderson, C. W. N.; Meng, B.; Wang, D.; Shang, L.; Yan, H.; Feng, X. Mercury Methylation in Rice Paddies and Its Possible Controlling Factors in the Hg Mining Area, Guizhou Province, Southwest China. *Environ. Pollut.* **2016**, *215*, 1−9.

(5) Liu, J.; Jiang, T.; Wang, F.; Zhang, J.; Wang, D.; Huang, R.; Yin, D.; Liu, Z.; Wang, J. Inorganic Sulfur and Mercury Speciation in the Water Level Fluctuation Zone of the Three Gorges Reservoir, China: The Role of Inorganic Reduced Sulfur on Mercury Methylation. *Environ. Pollut.* **2018**, *237*, 1112−1123.

(6) Liem-Nguyen, V.; Skyllberg, U.; Björn, E. Methylmercury Formation in Boreal Wetlands in Relation to Chemical Speciation of Mercury(II) and Concentration of Low Molecular Mass Thiols. *Sci. Total Environ.* **2021**, *755*, 142666.

(7) Zhou, X.; Qu, X.; Yang, Z.; Zhao, J.; Hao, Y.; Feng, J.; Huang, Q.; Liu, Y. Increased Water Inputs Fuel Microbial Mercury Methylation in Upland Soils. *J. Hazard. Mater.* **2022**, *439*, 129578.

(8) Feng, X.; Li, P.; Qiu, G.; Wang, S.; Li, G.; Shang, L.; Meng, B.; Jiang, H.; Bai, W.; Li, Z.; Fu, X. Human Exposure to Methylmercury through Rice Intake in Mercury Mining Areas, Guizhou Province, China. *Environ. Sci. Technol.* **2008**, *42*, 326−332.

(9) Zhang, H.; Feng, X.; Larssen, T.; Qiu, G.; Vogt, R. D. In Inland China, Rice, Rather than Fish, Is the Major Pathway for Methylmercury Exposure. *Environ. Health Perspect.* **2010**, *118*, 1183−1188.

(10) Qiu, G.; Feng, X.; Li, P.; Wang, S.; Li, G.; Shang, L.; Fu, X. Methylmercury Accumulation in Rice (*Oryza Sativa L.*) Grown at Abandoned Mercury Mines in Guizhou, China. *J. Agric. Food Chem.* **2008**, *56*, 2465−2468.

(11) Zhang, H.; Feng, X.; Larssen, T.; Shang, L.; Li, P. Bioaccumulation of Methylmercury versus Inorganic Mercury in Rice (Oryza Sativa L.) Grain. *Environ. Sci. Technol.* **2010**, *44*, 4499−4504.

(12) Meng, B.; Feng, X.; Qiu, G.; Cai, Y.; Wang, D.; Li, P.; Shang, L.; Sommar, J. Distribution Patterns of Inorganic Mercury and Methylmercury in Tissues of Rice (*Oryza Sativa L.*) Plants and Possible Bioaccumulation Pathways. *J. Agric. Food Chem.* **2010**, *58*, 4951−4958.

(13) Meng, B.; Feng, X.; Qiu, G.; Liang, P.; Li, P.; Chen, C.; Shang, L. The Process of Methylmercury Accumulation in Rice (*Oryza Sativa L.*). *Environ. Sci. Technol.* **2011**, *45*, 2711−2717.

(14) Aslam, M. W.; Meng, B.; Abdelhafiz, M. A.; Liu, J.; Feng, X. Unravelling the Interactive Effect of Soil and Atmospheric Mercury Influencing Mercury Distribution and Accumulation in the Soil-Rice System. *Sci. Total Environ.* **2022**, *803*, 149967.

(15) Liu, J.; Meng, B.; Poulain, A. J.; Meng, Q.; Feng, X. Stable Isotope Tracers Identify Sources and Transformations of Mercury in Rice (*Oryza Sativa L.*) Growing in a Mercury Mining Area. *Fundam. Res.* **2021**, *1*, 259−268.

(16) Qin, C.; Du, B.; Yin, R.; Meng, B.; Fu, X.; Li, P.; Zhang, L.; Feng, X. Isotopic Fractionation and Source Appointment of Methylmercury and Inorganic Mercury in a Paddy Ecosystem. *Environ. Sci. Technol.* **2020**, *54*, 14334−14342.

(17) Cui, W.; Liu, G.; Bezerra, M.; Lagos, D. A.; Li, Y.; Cai, Y. Occurrence of Methylmercury in Rice-Based Infant Cereals and Estimation of Daily Dietary Intake of Methylmercury for Infants. *J. Agric. Food Chem.* **2017**, *65*, 9569−9578.

(18) Kwon, S. Y.; Selin, N. E.; Giang, A.; Karplus, V. J.; Zhang, D. Present and Future Mercury Concentrations in Chinese Rice: Insights from Modeling. *Global Biogeochem. Cycles* **2018**, *32*, 437−462.

(19) Liu, M.; Zhang, Q.; Cheng, M.; He, Y.; Chen, L.; Zhang, H.; Cao, H.; Shen, H.; Zhang, W.; Tao, S.; Wang, X. Rice Life Cycle-Based Global Mercury Biotransport and Human Methylmercury Exposure. *Nat. Commun.* **2019**, *10*, 5164.

(20) Bravo, A. G.; Cosio, C. Biotic Formation of Methylmercury: A Bio-Physico-Chemical Conundrum. *Limnol. Oceanogr.* **2020**, *65*, 1010−1027.

(21) Li, Y.; Zhao, J.; Zhong, H.; Wang, Y.; Li, H.; Li, Y.-F.; Liem-Nguyen, V.; Jiang, T.; Zhang, Z.; Gao, Y.; et al. Understanding Enhanced Microbial MeHg Production in Mining- Contaminated Paddy Soils under Sulfate Amendment: Changes in Hg Mobility or Microbial Methylators? *Environ. Sci. Technol.* **2019**, *53*, 1844−1852.

(22) Wu, Q.; Hu, H.; Meng, B.; Wang, B.; Poulain, A. J.; Zhang, H.; Liu, J.; Bravo, A. G.; Bishop, K.; Bertilsson, S.; Feng, X. Methanogenesis Is an Important Process in Controlling MeHg Concentration in Rice Paddy Soils Affected by Mining Activities. *Environ. Sci. Technol.* **2020**, *54*, 13517−13526.

(23) Rothenberg, S. E.; Feng, X. Mercury Cycling in a Flooded Rice Paddy. *J. Geophys. Res.: Biogeosci.* **2012**, *117*, 1−16.

(24) Wang, J.; Shaheen, S. M.; Jing, M.; Anderson, C. W. N.; Swertz, A. C.; Wang, S. L.; Feng, X.; Rinklebe, J. Mobilization, Methylation, and Demethylation of Mercury in a Paddy Soil under Systematic Redox Changes. *Environ. Sci. Technol.* **2021**, *55*, 10133−10141.

(25) Liu, J.; Lu, B.; Poulain, A. J.; Zhang, R.; Zhang, T.; Feng, X.; Meng, B. The Underappreciated Role of Natural Organic Matter Bond Hg(II) and Nanoparticulate HgS as Substrates for Methylation in Paddy Soils across a Hg Concentration Gradient. *Environ. Pollut.* **2022**, *292*, 118321.

(26) Liu, J.; Zhao, L.; Kong, K.; Abdelhafiz, M. A.; Tian, S.; Jiang, T.; Meng, B.; Feng, X. Uncovering geochemical fractionation of the newly deposited Hg in paddy soil using a stable isotope tracer. *J. Hazard. Mater.* **2022**, *433*, 128752.

(27) Cui, L.; Feng, X.; Lin, C. J.; Wang, X.; Meng, B.; Wang, X.; Wang, H. Accumulation and Translocation of ^{198}Hg in Four Crop Species. *Environ. Toxicol. Chem.* **2014**, *33*, 334−340.

(28) Strickman, R. J.; Mitchell, C. P. J. Accumulation and Translocation of Methylmercury and Inorganic Mercury in *Oryza*

Sativa: An Enriched Isotope Tracer Study. *Sci. Total Environ.* **2017**, *574*, 1415−1423.
(29) Skyllberg, U.; Persson, A.; Tjerngren, I.; Kronberg, R.; Drott, A.; Meili, M.; Bjorn, E. Chemical Speciation of Mercury, Sulfur and Iron in a Dystrophic Boreal Lake Sediment, as Controlled by the Formation of Mackinawite and Framboidal Pyrite. *Geochim. Cosmochim. Acta* **2021**, *294*, 106−125.
(30) Drott, A.; Björn, E.; Bouchet, S.; Skyllberg, U. Refining Thermodynamic Constants for Mercury(II)-Sulfides in Equilibrium with Metacinnabar at Sub-Micromolar Aqueous Sulfide Concentrations. *Environ. Sci. Technol.* **2013**, *47*, 4197−4203.
(31) Liem-Nguyen, V.; Skyllberg, U.; Nam, K.; Björn, E. Thermodynamic Stability of Mercury(II) Complexes Formed with Environmentally Relevant Low-Molecular-Mass Thiols Studied by Competing Ligand Exchange and Density Functional Theory. *Environ. Chem.* **2017**, *14*, 243−253.
(32) Zhang, T.; Kucharzyk, K. H.; Kim, B.; Deshusses, M. A.; Hsu-Kim, H. Net Methylation of Mercury in Estuarine Sediment Microcosms Amended with Dissolved, Nanoparticulate, and Microparticulate Mercuric Sulfides. *Environ. Sci. Technol.* **2014**, *48*, 9133−9141.
(33) Tian, L.; Guan, W.; Ji, Y.; He, X.; Chen, W.; Alvarez, P. J. J.; Zhang, T. Microbial methylation potential of mercury sulfide particles dictated by surface structure. *Nat. Geosci.* **2021**, *14*, 409−416.
(34) Guo, Y.; Xiang, Y.; Liu, G.; Chen, Y.; Liu, Y.; Song, M.; Li, Y.; Shi, J.; Hu, L.; Yin, Y.; Cai, Y.; Jiang, G. Trojan Horse" Type Internalization Increases the Bioavailability of Mercury Sulfide Nanoparticles and Methylation after Intracellular Dissolution. *ACS Nano* **2023**, *17*, 1925−1934.
(35) Compeau, G. C.; Bartha, R. Sulfate-Reducing Bacteria: Principal Methylators of Mercury in Anoxic Estuarine Sediment. *Appl. Environ. Microbiol.* **1985**, *50*, 498−502.
(36) Gilmour, C. C.; Henry, E. A.; Mitchell, R. Sulfate Stimulation of Mercury Methylation in Freshwater Sediments. *Environ. Sci. Technol.* **1992**, *26*, 2281−2287.
(37) Jeremiason, J. D.; Engstrom, D. R.; Swain, E. B.; Nater, E. A.; Johnson, B. M.; Almendinger, J. E.; Monson, B. A.; Kolka, R. K. Sulfate Addition Increases Methylmercury Production in an Experimental Wetland. *Environ. Sci. Technol.* **2006**, *40*, 3800−3806.
(38) Coleman Wasik, J. K.; Mitchell, C. P. J.; Engstrom, D. R.; Swain, E. B.; Monson, B. A.; Balogh, S. J.; Jeremiason, J. D.; Branfireun, B. A.; Eggert, S. L.; Kolka, R. K.; Almendinger, J. E. Methylmercury Declines in a Boreal Peatland When Experimental Sulfate Deposition Decreases. *Environ. Sci. Technol.* **2012**, *46*, 6663−6671.
(39) Coleman Wasik, J. K.; Engstrom, D. R.; Mitchell, C. P. J.; Swain, E. B.; Monson, B. A.; Balogh, S. J.; Jeremiason, J. D.; Branfireun, B. A.; Kolka, R. K.; Almendinger, J. E. The Effects of Hydrologic Fluctuation and Sulfate Regeneration on Mercury Cycling in an Experimental Peatland. *J. Geophys. Res.: Biogeosci.* **2015**, *120*, 1697−1715.
(40) Hinckley, E. L. S.; Crawford, J. T.; Fakhraei, H.; Driscoll, C. T. A Shift in Sulfur-Cycle Manipulation from Atmospheric Emissions to Agricultural Additions. *Nat. Geosci.* **2020**, *13*, 597−604.
(41) Feinberg, A.; Stenke, A.; Peter, T.; Hinckley, E.-L. S.; Driscoll, C. T.; Winkel, L. H. E. Reductions in the Deposition of Sulfur and Selenium to Agricultural Soils Pose Risk of Future Nutrient Deficiencies. *Commun. Earth Environ.* **2021**, *2*, 101.
(42) National Bureau of Statistics of China. *China Statistical Yearbook*, 2021.
(43) Li, X.; Tyl, C. E.; Kaiser, D. E.; Annor, G. A. Effect of Sulfur Fertilization Rates on Wheat (*Triticum Aestivum L.*) Functionality. *J. Cereal Sci.* **2019**, *87*, 292−300.
(44) Wang, Y.; Wei, Z.; Zeng, Q.; Zhong, H. Amendment of Sulfate with Se into Soils Further Reduces Methylmercury Accumulation in Rice. *J. Soils Sediments* **2016**, *16*, 2720−2727.
(45) Li, Y.; Wang, Y.; Zhang, Q.; Hu, W.; Zhao, J.; Chen, Y.; Zhong, H.; Wang, G.; Zhang, Z.; Gao, Y. Elemental Sulfur Amendment Enhance Methylmercury Accumulation in Rice (*Oryza Sativa L.*) Grown in Hg Mining Polluted Soil. *J. Hazard. Mater.* **2019**, *379*, 120701.
(46) Li, Y.; Lu, C.; Zhu, N.; Chao, J.; Hu, W.; Zhang, Z.; Wang, Y.; Liang, L.; Chen, J.; Xu, D.; Gao, Y.; Zhao, J. Mobilization and Methylation of Mercury with Sulfur Addition in Paddy Soil: Implications for Integrated Water-Sulfur Management in Controlling Hg Accumulation in Rice. *J. Hazard. Mater.* **2022**, *430*, 128447.
(47) Lei, P.; Tang, C.; Wang, Y.; Wu, M.; Kwong, R. W. M.; Jiang, T.; Zhong, H. Understanding the Effects of Sulfur Input on Mercury Methylation in Rice Paddy Soils. *Sci. Total Environ.* **2021**, *778*, 146325.
(48) Yin, D.; He, T.; Yin, R.; Zeng, L. Effects of Soil Properties on Production and Bioaccumulation of Methylmercury in Rice Paddies at a Mercury Mining Area, China. *J. Environ. Sci.* **2018**, *68*, 194−205.
(49) Mao, Y.; Li, Y.; Richards, J.; Cai, Y. Investigating Uptake and Translocation of Mercury Species by Sawgrass (*Cladium Jamaicense*) Using a Stable Isotope Tracer Technique. *Environ. Sci. Technol.* **2013**, *47*, 9678−9684.
(50) Meng, B.; Li, Y.; Cui, W.; Jiang, P.; Liu, G.; Wang, Y.; Richards, J.; Feng, X.; Cai, Y. Tracing the Uptake, Transport, and Fate of Mercury in Sawgrass (*Cladium Jamaicense*) in the Florida Everglades Using a Multi-Isotope Technique. *Environ. Sci. Technol.* **2018**, *52*, 3384−3391.
(51) Qvarnström, J.; Frech, W. Mercury Species Transformations during Sample Pre-Treatment of Biological Tissues Studied by HPLC-ICP-MS. *J. Anal. At. Spectrom.* **2002**, *17*, 1486−1491.
(52) Hintelmann, H.; Keppel-Jones, K.; Evans, D. Constants of mercury methylation and demethylation rates in sediments and comparison of tracer and ambient mercury availability. *Environ. Toxicol. Chem.* **2000**, *19*, 2204−2211.
(53) Jonsson, S.; Skyllberg, U.; Nilsson, M. B.; Westlund, P.; Shchukarev, A.; Lundberg, E.; Bjorn, E. Mercury Methylation Rates for Geochemically Relevant Hg^{II} Species in Sediments. *Environ. Sci. Technol.* **2012**, *46*, 11653−11659.
(54) Olsen, T. A.; Muller, K. A.; Painter, S. L.; Brooks, S. C. Kinetics of Methylmercury Production Revisited. *Environ. Sci. Technol.* **2018**, *52*, 2063−2070.
(55) Landa, E. R. The retention of metallic mercury vapor by soils. *Geochim. Cosmochim. Acta* **1978**, *42*, 1407−1411.
(56) Wang, Y.; Li, Y.; Liu, G.; Wang, D.; Jiang, G.; Cai, Y. Elemental Mercury in Natural Waters: Occurrence and Determination of Particulate Hg(0). *Environ. Sci. Technol.* **2015**, *49*, 9742−9749.
(57) Liu, Y.; Delgado-Baquerizo, M.; Bi, L.; Zhu, J.; He, J. Z. Consistent Responses of Soil Microbial Taxonomic and Functional Attributes to Mercury Pollution across China. *Microbiome* **2018**, *6*, 183−212.
(58) Pu, Q.; Zhang, K.; Poulain, A. J.; Liu, J.; Zhang, R.; Abdelhafiz, M. A.; Meng, B.; Feng, X. Mercury Drives Microbial Community Assembly and Ecosystem Multifunctionality across a Hg Contamination Gradient in Rice Paddies. *J. Hazard. Mater.* **2022**, *435*, 129055.
(59) Bravo, A. G.; Bouchet, S.; Tolu, J.; Björn, E.; Mateos-Rivera, A.; Bertilsson, S. Molecular Composition of Organic Matter Controls Methylmercury Formation in Boreal Lakes. *Nat. Commun.* **2017**, *8*, 14255.
(60) Tuominen, L.; Kairesalo, T.; Hartikainen, H. Comparison of Methods for Inhibiting Bacterial Activity in Sediment. *Appl. Environ. Microbiol.* **1994**, *60*, 3454−3457.
(61) Colombo, M. J.; Ha, J.; Reinfelder, J. R.; Barkay, T.; Yee, N. Oxidation of Hg(0) to Hg(II) by Diverse Anaerobic Bacteria. *Chem. Geol.* **2014**, *363*, 334−340.
(62) Colombo, M. J.; Ha, J.; Reinfelder, J. R.; Barkay, T.; Yee, N. Anaerobic Oxidation of Hg(0) and Methylmercury Formation by *Desulfovibrio Desulfuricans* ND132. *Geochim. Cosmochim. Acta* **2013**, *112*, 166−177.
(63) Hu, H.; Lin, H.; Zheng, W.; Tomanicek, S. J.; Johs, A.; Feng, X.; Elias, D. A.; Liang, L.; Gu, B. Oxidation and Methylation of Dissolved Elemental Mercury by Anaerobic Bacteria. *Nat. Geosci.* **2013**, *6*, 751−754.

https://doi.org/10.1021/acs.est.3c02676
Environ. Sci. Technol. 2023, 57, 8149−8160

(64) Lin, H.; Morrell-Falvey, J. L.; Rao, B.; Liang, L.; Gu, B. Coupled Mercury-Cell Sorption, Reduction, and Oxidation on Methylmercury Production by *Geobacter Sulfurreducens* PCA. *Environ. Sci. Technol.* **2014**, *48*, 11969−11976.
(65) Zheng, W.; Liang, L.; Gu, B. Mercury Reduction and Oxidation by Reduced Natural Organic Matter in Anoxic Environments. *Environ. Sci. Technol.* **2012**, *46*, 292−299.
(66) Poulin, B. A.; Ryan, J. N.; Tate, M. T.; Krabbenhoft, D. P.; Hines, M. E.; Barkay, T.; Schaefer, J.; Aiken, G. R. Geochemical Factors Controlling Dissolved Elemental Mercury and Methylmercury Formation in Alaskan Wetlands of Varying Trophic Status. *Environ. Sci. Technol.* **2019**, *53*, 6203−6213.
(67) Zhang, L.; Wu, S.; Zhao, L.; Lu, X.; Pierce, E. M.; Gu, B. Mercury Sorption and Desorption on Organo-Mineral Particulates as a Source for Microbial Methylation. *Environ. Sci. Technol.* **2019**, *53*, 2426−2433.
(68) Xiang, Y.; Guo, Y.; Liu, G.; Liu, Y.; Song, M.; Shi, J.; Hu, L.; Yin, Y.; Cai, Y.; Jiang, G. Particle-Bound Hg(II) Is Available for Microbial Uptake as Revealed by a Whole-Cell Biosensor. *Environ. Sci. Technol.* **2022**, *56*, 6754−6764.
(69) Grégoire, D. S.; Poulain, A. J. Shining Light on Recent Advances in Microbial Mercury Cycling. *Facets* **2018**, *3*, 858−879.
(70) Lu, X.; Liu, Y.; Johs, A.; Zhao, L.; Wang, T.; Yang, Z.; Lin, H.; Elias, D. A.; Pierce, E. M.; Liang, L.; Barkay, T.; Gu, B. Anaerobic Mercury Methylation and Demethylation by *Geobacter Bemidjiensis Bem*. *Environ. Sci. Technol.* **2016**, *50*, 4366−4373.
(71) Grégoire, D. S.; Lavoie, N. C.; Poulain, A. J. *Heliobacteria* Reveal Fermentation as a Key Pathway for Mercury Reduction in Anoxic Environments. *Environ. Sci. Technol.* **2018**, *52*, 4145−4153.
(72) Shi, L.; Richardson, D. J.; Wang, Z.; Kerisit, S. N.; Rosso, K. M.; Zachara, J. M.; Fredrickson, J. K. The Roles of Outer Membrane Cytochromes of *Shewanella* and *Geobacter* in Extracellular Electron Transfer. *Environ. Microbiol. Rep.* **2009**, *1*, 220−227.
(73) Begley, T. P.; Walts, A. E.; Walsh, C. T. Bacterial organomercurial lyase-overproduction, isolation, and characterization. *Biochemistry* **1986**, *25*, 7186−7192.
(74) Barkay, T.; Gu, B. Demethylation-The Other Side of the Mercury Methylation Coin: A Critical Review. *ACS Environ. Au* **2022**, *2*, 77−97.
(75) Zhou, X.; Hao, Y.; Gu, B.; Feng, J.; Liu, Y.; Huang, Q. Microbial Communities Associated with Methylmercury Degradation in Paddy Soils. *Environ. Sci. Technol.* **2020**, *54*, 7952−7960.
(76) Oremland, R. S.; Culbertson, C. W.; Winfrey, M. R. Methylmercury decomposition in sediments and bacterial cultures? involvement of methanogens and sulfate reducers in oxidative demethylation. *Appl. Environ. Microbiol.* **1991**, *57*, 130−137.
(77) Hsu-Kim, H.; Kucharzyk, K. H.; Zhang, T.; Deshusses, M. A. Mechanisms Regulating Mercury Bioavailability for Methylating Microorganisms in the Aquatic Environment: A Critical Review. *Environ. Sci. Technol.* **2013**, *47*, 2441−2456.
(78) Jørgensen, B. B. The Sulfur Cycle of Freshwater Sediments: Role of Thiosulfate. *Limnol. Oceanogr.* **1990**, *35*, 1329−1342.
(79) Schippers, A. Biogeochemistry of metal sulfide oxidation in mining environments, sediments, and soils. In *Sulfur Biogeochemistry: Past and Present*; Amend, J. P., Edwards, K. J., Lyons, T. W., Eds.; Geological Society of America: Boulder, Colorado, 2004.
(80) Zopfi, J.; Böttcher, M. E.; Jørgensen, B. B. Biogeochemistry of Sulfur and Iron in Thioploca-Colonized Surface Sediments in the Upwelling Area off Central Chile. *Geochim. Cosmochim. Acta* **2008**, *72*, 827−843.
(81) Yuan, D.; Wang, G.; Hu, C.; Zhou, S.; Clough, T. J.; Wrage-Mönnig, N.; Luo, J.; Qin, S. Electron Shuttle Potential of Biochar Promotes Dissimilatory Nitrate Reduction to Ammonium in Paddy Soil. *Soil Biol. Biochem.* **2022**, *172*, 108760.
(82) Todorova, S. G.; Driscoll, C. T.; Matthews, D. A.; Effler, S. W.; Hines, M. E.; Henry, E. A. Evidence for Regulation of Monomethyl Mercury by Nitrate in a Seasonally Stratified, Eutrophic Lake. *Environ. Sci. Technol.* **2009**, *43*, 6572−6578.
(83) Strickman, R. J.; Mitchell, C. P. J. Mercury Methylation in Stormwater Retention Ponds at Different Stages in the Management Lifecycle. *Environ. Sci.: Processes Impacts* **2018**, *20*, 595−606.
(84) Zhang, Y.; Liu, Y. R.; Lei, P.; Wang, Y. J.; Zhong, H. Biochar and Nitrate Reduce Risk of Methylmercury in Soils under Straw Amendment. *Sci. Total Environ.* **2018**, *619−620*, 384−390.
(85) Kögel-knabner, I.; Amelung, W.; Cao, Z.; Fiedler, S.; Frenzel, P.; Jahn, R.; Kalbitz, K.; Kölbl, A.; Schloter, M. Biogeochemistry of Paddy Soils. *Geoderma* **2010**, *157*, 1−14.
(86) Marvin-DiPasquale, M.; Agee, J.; Mcgowan, C.; Oremland, R. S.; Thomas, M.; Krabbenhoft, D.; Gilmour, C. C. Methyl-Mercury Degradation Pathways: A Comparison among Three Mercury-Impacted Ecosystems. *Environ. Sci. Technol.* **2000**, *34*, 4908−4916.
(87) Liu, J.; Liang, J.; Bravo, A. G.; Wei, S.; Yang, C.; Wang, D.; Jiang, T. Anaerobic and Aerobic Biodegradation of Soil-Extracted Dissolved Organic Matter from the Water-Level-Fluctuation Zone of the Three Gorges Reservoir Region, China. *Sci. Total Environ.* **2021**, *764*, 142857.
(88) Orem, W.; Gilmour, C.; Axelrad, D.; Krabbenhoft, D.; Scheidt, D.; Kalla, P.; McCormick, P.; Gabriel, M.; Aiken, G. Sulfur in the South Florida Ecosystem: Distribution, Sources, Biogeochemistry, Impacts, and Management for Restoration. *Crit. Rev. Environ. Sci. Technol.* **2011**, *41*, 249−288.
(89) Santana, M. M.; Dias, T.; Gonzalez, J. M.; Cruz, C. Transformation of Organic and Inorganic Sulfur− Adding Perspectives to New Players in Soil and Rhizosphere. *Soil Biol. Biochem.* **2021**, *160*, 108306.
(90) Wang, J.; Feng, X.; Anderson, C. W. N.; Wang, H.; Wang, L. Thiosulphate-Induced Mercury Accumulation by Plants: Metal Uptake and Transformation of Mercury Fractionation in Soil - Results from a Field Study. *Plant Soil* **2014**, *375*, 21−33.
(91) Wang, J.; Feng, X.; Anderson, C. W. N.; Wang, H.; Zheng, L.; Hu, T. Implications of Mercury Speciation in Thiosulfate Treated Plants. *Environ. Sci. Technol.* **2012**, *46*, 5361−5368.
(92) Vázquez-Rodríguez, A.; Hansel, C. M.; Zhang, T.; Lamborg, C.; Santelli, C. M.; Webb, S.; Brooks, S. Microbial- and Thiosulfate-Mediated Dissolution of Mercury Sulfide Minerals and Transformation to Gaseous Mercury. *Front. Microbiol.* **2015**, *6*, 596.
(93) Liu, T.; Wang, J.; Feng, X.; Zhang, H.; Zhu, Z.; Cheng, S. Spectral Insight into Thiosulfate-Induced Mercury Speciation Transformation in a Historically Polluted Soil. *Sci. Total Environ.* **2019**, *657*, 938−944.
(94) Jørgensen, B. B.; Nelson, D. C. Sulfide Oxidation in Marine Sediments: Geochemistry meets microbiology. *Geol. Soc. Am. Sp. Papers* **2004**, *379*, 63−81.

https://doi.org/10.1021/acs.est.3c02676
Environ. Sci. Technol. 2023, 57, 8149−8160

Journal of Hazardous Materials 433 (2022) 128752

Contents lists available at ScienceDirect

Journal of Hazardous Materials

journal homepage: www.elsevier.com/locate/jhazmat

Research Paper

Uncovering geochemical fractionation of the newly deposited Hg in paddy soil using a stable isotope tracer

Jiang Liu [a], Lei Zhao [b,c,*], Kun Kong [a,d], Mahmoud A. Abdelhafiz [a,d,e], Shanyi Tian [f], Tao Jiang [a,g], Bo Meng [a,**], Xinbin Feng [a]

[a] State Key Laboratory of Environmental Geochemistry, Institute of Geochemistry, Chinese Academy of Sciences, Guiyang 550081, China
[b] School of Management Science, Guizhou University of Finance and Economics, Guiyang 550025, China
[c] Guizhou Key Laboratory of Big Data Statistical Analysis (No. [2019]5103), Guiyang 550025, China
[d] University of Chinese Academy of Sciences, Beijing 100049, China
[e] Geology Department, Faculty of Science, Al-Azhar University, Assiut 71524, Egypt
[f] Soil Ecology Lab, College of Resources and Environmental Sciences, Nanjing Agricultural University, Nanjing 210095, China
[g] Interdisciplinary Research Centre for Agriculture Green Development in Yangtze River Basin, Department of Environmental Sciences and Engineering, College of Resources and Environment, Southwest University, Chongqing 400716, China

HIGHLIGHTS

- Enriched Hg isotope was employed to simulate newly deposited Hg.
- Geochemical fractionation of newly deposited Hg in paddy soil was studied.
- Organic matter is the largest pool of newly deposited Hg in paddy soil.
- Transitions from OM-Hg to Fe/Mn oxide-Hg were observed in paddy soil.
- Coupling of Fe and DOM controlled the fate of newly deposited Hg.

GRAPHICAL ABSTRACT

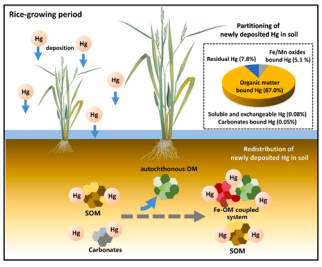

ARTICLE INFO

Editor: Lingxin Chen

Keywords:
Newly deposited Hg
Stable Hg isotope tracer
Geochemical fractionation
Paddy soil

ABSTRACT

The newly deposited mercury (Hg) is more readily methylated to methylmercury (MeHg) than native Hg in paddy soil. However, the biogeochemical processes of the newly deposited Hg in soil are still unknown. Here, a field experimental plot together with a stable Hg isotope tracing technique was used to demonstrate the geochemical fractionation (partitioning and redistribution) of the newly deposited Hg in paddy soils during the rice-growing period. We showed that the majority of Hg tracer (^{200}Hg, 115.09 ± 0.36 μg kg^{-1}) was partitioned as organic matter bound ^{200}Hg (84.6–89.4%), followed by residual ^{200}Hg (7.6–8.1%), Fe/Mn oxides bound ^{200}Hg (2.8–7.2%), soluble and exchangeable ^{200}Hg (0.05–0.2%), and carbonates bound ^{200}Hg (0.04–0.07%) in paddy soils. Correlation analysis and partial least squares path modeling revealed that the coupling of autochthonous dissolved organic matter and poorly crystalline Fe (oxyhydr)oxides played a predominant role in controlling the redistribution of the newly deposited Hg among geochemical fractions (i.e., fraction changes). The expected aging processes of the newly deposited Hg were absent, potentially explaining the high bioavailability of these Hg in paddy soil. This study implies that other Hg pools (e.g., organic matter bound Hg) should be considered instead of merely soluble Hg pools when evaluating the environmental risks of Hg from atmospheric depositions.

* Corresponding author at: School of Management Science, Guizhou University of Finance and Economics, Guiyang 550025, China.
** Corresponding author.
E-mail addresses: zl2047480664@mail.gufe.edu.cn (L. Zhao), mengbo@vip.skleg.cn (B. Meng).

https://doi.org/10.1016/j.jhazmat.2022.128752
Received 23 January 2022; Received in revised form 8 March 2022; Accepted 19 March 2022

1. Introduction

Methylmercury (MeHg), the organic form of mercury (Hg), is a broad public concern due to its neurotoxicity, bioaccumulation and biomagnification in food chains. In contrast to other heavy metal pollutants, elemental Hg, the vapor form of Hg could exist in the ambient air, and long-term transportation of this gaseous Hg was widely recoded (Ariya et al., 2015). Consequently, high Hg burdens in biota, especially at high trophic levels, were found in sparsely populated areas (e.g., high latitude lakes) due to the deposition of long-term transported Hg (Lucotte et al., 1999), and the deposition of atmospheric Hg was therefore considered an important Hg source for terrestrial ecosystems.

In recent decades, biogeochemical processes of the newly deposited Hg in terrestrial and aquatic environments have aroused great concerns (Blanchfield et al., 2021; Branfireun et al., 2005; Harris et al., 2007; Hintelmann et al., 2002; Orihel et al., 2008; Oswald et al., 2014; Paterson et al., 2006). A previous study reported that the newly deposited Hg had higher reactivities in reduction and volatilization than native Hg in soils (Hintelmann et al., 2002). Moreover, methylation of the newly deposited Hg was also found to be more active than native Hg in wetland systems (Branfireun et al., 2005) and boreal forest systems (Hintelmann et al., 2002). In a peatland of the Experimental Lakes Area (ELA) in Canada, 6% of newly introduced Hg (used to simulate the newly deposited Hg) was methylated within 24 h (Branfireun et al., 2005). Furthermore, research in aquatic systems documented that the newly deposited Hg is more prone to bioaccumulation in aquatic biota through the formation of MeHg (Harris et al., 2007; Orihel et al., 2008; Paterson et al., 2006).

Rice (*Oryza sativa* L.) is the most important staple food for world populations. In recent studies, however, rice was identified as a bioaccumulator for MeHg (Feng et al., 2011; Meng et al., 2010; Qiu et al., 2008), and health risks for rice-eating people in MeHg exposure were reported (Feng et al., 2008; Zhang et al., 2010). Furthermore, paddy soil, as an ephemeral artificial wetland, was identified as a hotspot of Hg methylation and the major source of MeHg accumulated in rice (Aslam et al., 2022; Liu et al., 2021a; Meng et al., 2010, 2011; Zhao et al., 2016a,b, 2020). Our previous studies confirmed that the newly deposited Hg is more readily methylated to MeHg and accumulates in rice than native Hg in soil (Meng et al., 2010, 2011). The higher bioavailability of the newly deposited Hg in paddy soil was further highlighted in the follow-up studies (Ao et al., 2020; Zhao et al., 2016a). However, the mechanisms behind this finding remain unclear. Therefore, new techniques and more works are urgently needed to uncover the divergent bioavailabilities of native Hg and the newly entered Hg (e.g., newly deposited), especially in Hg-sensitive ecosystems (e.g., rice paddies).

Bioavailability and other factors such as the activity of microorganisms and electron acceptors/donors, resulted in the net production of MeHg (Hsu-Kim et al., 2013) from the newly deposited Hg, which determined the environmental risks of Hg from atmospheric depositions. It is generally accepted that the speciation controls the bioavailability of Hg in biotically mediated methylation (Hsu-Kim et al., 2013; Jonsson et al., 2014; Liu et al., 2022). Typically, Hg speciation in dry or wet depositions is inorganic oxidized Hg (Hg(II)) due to the high deposition velocity (Ariya et al., 2015; Fu et al., 2015) and oxidation events (e.g., atmospheric Hg depletion events, AMDE) in high latitude areas (Schroeder et al., 1998). On the other hand, the speciation changes of the newly deposited Hg in soils are soil chemistry- and particulate-dependent and controlled by the presence of organic matter (Rolfhus et al., 2015), metal (oxyhydr)oxides (O'Connor et al., 2019), sulfur species (Skyllberg, 2008) and clay minerals (Zhu et al., 2012). All of these compounds, in particular, are highly related to the methylation process because they mediate the partitioning and redistribution of Hg among different geochemical fractions (referred to as geochemical fractionation). Therefore, investigating the geochemical fractionation of the newly deposited Hg is critical to understand the behaviors of the newly deposited Hg in methylation as well as corresponding environmental risks.

To fill all the knowledge gaps above, we spiked an isotope-enriched ^{200}Hg tracer to simulate the newly deposited Hg in paddy soils. In addition, the geochemical fractionation processes of spiked ^{200}Hg (i.e., referred to as the newly deposited Hg or "new" Hg) and native Hg (i.e., referred to as ambient Hg or "old" Hg) in paddy soil during the rice-growing period were studied. Furthermore, sequential extractions of Hg (both spiked and native Hg), iron (oxyhydr)oxides and soil organic matter fractions were conducted. The key objectives of this study were to (1) identify the partitioning of "new" Hg in different geochemical fractions in paddy soil, (2) determine the redistribution process of "new" Hg among geochemical fractions during the rice-growing period, and (3) reveal the key factors that potentially control the geochemical fractionation of "new" Hg in paddy soil.

2. Materials and methods

2.1. Study site and rice cultivation experiment

This study was carried out in a regional background area (low Hg concentration in soil and atmosphere), located in Xunyang County, Shannxi Province, China (109°23'24''E, 32°49'48''N). During the rice-growing period, the overall range of gaseous elemental mercury (GEM) at the study site was 1.0–9.0 ng m^{-3} (average 4.8 ± 2.0 ng m^{-3}, Fig. S1). Concentrations of GEM at the study site are slightly higher than the GEM of some remote forest areas (e.g., Mt. Changbai, China, [GEM] = 1.60 ± 0.51 ng m^{-3}, Fu et al., 2012) but lower than those in some urban areas (e.g., Guiyang City, China, [GEM] = 10.2 ± 7.06 ng m^{-3}, Fu et al., 2015) and Hg mining areas (e.g., Wanshan Hg mining area, China, [GEM] = 403 ± 388 ng m^{-3}, Zhao et al., 2016a). Accordingly, low Hg deposition from the atmosphere is expected, which provides ideal conditions when comparing the newly deposited Hg ($^{200}Hg^{2+}$ tracers) and ambient Hg in paddy soil. Therefore, an assumption was made that atmospheric Hg deposition into the experimental plot could be negligible during the rice-growing period.

A simulated rice paddy plot (precleaned polyvinyl chloride box, 54 cm × 42 cm × 33 cm) was set up to investigate the partitioning and redistribution of the newly deposited Hg in paddy soil during the rice-growing period. The soil used in the rice cultivation was collected from cropland (surface soil, 1–20 cm) with a total Hg concentration of 78.4 ± 4.6 μg kg^{-1}. Then, 40 kg pre-sieved soil (2 mm) was filled into the box with a soil depth of approximately 20 cm. Irrigation water (Hg concentration of 1.37 ± 0.45 ng L^{-1}) was added to reach the field moisture capacity. Other physical and chemical properties of the collected soil are shown in Table S1. Isotope-enriched ^{200}Hg ($^{200}Hg(NO_3)_2$), as an inorganic Hg tracer, was spiked into the experimental soil to simulate the newly deposited Hg (Blanchfield et al., 2021; Branfireun et al., 2005; Hintelmann et al., 2002; Oswald et al., 2014). The spiked ^{200}Hg tracer (purity of 98.2 ± 0.15%) was prepared by using $^{200}Hg^0$ (ISOFLEX, USA) according to the methods reported in our previous studies (Liu et al., 2021a, 2022; Meng et al., 2018). Specifically, a working solution of ^{200}Hg tracer (~12 mg Hg L^{-1}, diluted by using deionized water) was prepared to neutral pH and then evenly spiked at ten different positions in the soil of the experimental box. After spiking, the soil in the box was further mixed to homogenize the tracers, and then immediately covered with dark plastic lids (to reduce the potential losses of Hg isotopes) and aged for 24 h before transplanting rice seedlings. The concentration of spiked ^{200}Hg tracer in the studied soil before rice planting is 115.09 ± 0.36 μg kg^{-1}. Notably, oxidized Hg(II), instead of Hg(0), was used as the tracer, as Hg(II) is the dominant species in the atmospheric depositions (Ariya et al., 2015; Fu et al., 2015).

A rice cultivar (hybrid rice), widely grown in Shannxi Province was used in this study. Rice seedlings were pre-cultivated for 30 days. Twenty seedlings with similar biomass and plant height were transplanted to the experimental box with a space of 10 cm × 10 cm. The soil in the box was submerged by irrigation water, and the water level in

each plot was kept at 3–5 cm above the soil surface. Rice in the experimental box was cultivated for 110 days in the field (in an open environment). The water management measures for this study were the same as for local paddy fields (i.e., keep flooding since transplanted and drying from the day 90) to simulate the natural environment for rice-growing. To minimize the perturbation from exogenous chemicals, no fertilizers or pesticides were applied during the rice-growing period. Five sampling campaigns were conducted on the days 0, 30, 60, 90, and 110 after rice transplanting, and 3–5 soil samples from the root zone (10–20 cm depth) were collected into new polypropylene tubes (JET®, China) at each sampling without any headspace. Parafilm® was used to seal the tubes to avoid the potential oxidation during transportation. The collected soil samples were transported to the laboratory within 24 h in coolers with ice packs (~4 °C). Changes of soil physical and chemical properties were minimized. Soil samples were stored at − 20 °C before the freezing dried. The freezing dried (FD-3–85D-MP, FTS, USA) samples were sieved to 200 mesh before measurement. The concentration of GEM close to the experimental box was recorded every 10 s and continuously measured for > 1 h at each sampling in the field.

2.2. Analytical methods

2.2.1. Sequential extraction of Hg

The procedures for sequential extraction of Hg were modified from the method of Tessier et al. (1979). Five fractions were defined as soluble and exchangeable Hg ($Mg(NO_3)_2$ extracted), carbonates bound Hg (NaOAc extracted), Fe/Mn oxides bound Hg ($NH_2OH{\cdot}HCl$ in HAc extracted), organic matter bound Hg (H_2O_2 extracted), and residual Hg (digested by aqua-regia). The details of the extraction procedures are described in Tessier et al. (1979) and were pervasively used by Wang et al. (2011), Zhao (2016), and Li et al. (2019).

2.2.2. Isolation of soil organic matter (SOM) fractions

Soil organic matter was isolated as dissolved organic matter (DOM), humic acid (HA), fulvic acid (FA), clay-associated HA (C-HA), and clay-associated FA (C-FA) (Carter and Gregorich, 2007). DOM was extracted by distilled water (Milli-Q®, Millipore, USA) with a soil-water ratio (*w/v*) of 1:10 (Jiang et al., 2017; Liu et al., 2021b). The details of SOM isolation are shown in Text S1.

2.2.3. Sequential extraction of Fe (oxyhydr)oxides

Iron fractions were extracted as soluble and exchangeable Fe (Fe_{exch}), carbonates associated Fe (Fe_{carb}, siderite, and ankerite), easily reducible Fe oxides (Fe_{ox1}, ferrihydrite, and lepidocrocite), reducible Fe oxides (Fe_{ox2}, goethite, and hematite), magnetite Fe (Fe_{mag}), and pyrite Fe (Fe_{py}) (Text S2). The methods of Fe sequential extraction were established by Poulton and Canfield (2005) and verified by using rock magnetic and X-ray diffraction measurements of pure mineral extractions (Claff et al., 2010; Slotznick et al., 2020).

2.2.4. Measurements

The concentration of GEM was determined by using a portable Hg Vapor Analyzer (RA-915 +, Lumex, Russia). The isotope-enriched $T^{200}Hg$ in soil samples was digested by aqua-regia and determined by using ICP–MS (Agilent 7700 ×, Agilent Technologies Inc., USA) after BrCl oxidation, $SnCl_2$ reduction, and gold trap amalgamation. The method for the isotope-enriched ^{200}Hg after sequential extractions was the same as that for $T^{200}Hg$ after aqua-regia digestion. The isotope-enriched $Me^{200}Hg$ was determined by using gas chromatography (GC)-ICP-MS (Agilent 7700 ×, Agilent Technologies Inc., USA) after ethylation and trapped by Tenax (Brooks, USA) (Gilmour et al., 1998). More details related to the isotope-enriched ^{200}Hg measurements can be found in our previous work (Liu et al., 2021a, 2022). The total amount of organic carbon (TOC) and total nitrogen in soils were measured by an elemental analyzer (Vario MACRO cube, Elementar, Germany) after the removal of inorganic carbon through acidification. Concentrations of each SOM fraction (i.e., DOM, HA, FA, C-HA, C-FA) were determined by a total organic carbon analyzer (InnovOx®, GE, USA). Concentrations of bulk SOM and soil DOM are shown as TOC and DOC, respectively. The optical properties of DOM were characterized by UV–vis absorption and fluorescence spectra through Aqualog® absorption-fluorescence spectroscopy (Jobin Yvon, Horiba, Japan). UV–vis absorption spectra for liquid samples were scanned from 230 nm to 800 nm (1 nm interval). Emission-excitation matrices (EEMs) of fluorescence spectra for liquid samples were scanned from 250 nm to 600 nm for emission spectra and from 230 nm to 450 nm for excitation spectra. Inner-filter effects were corrected according to Wilson and Xenopoulos (2009) and Murphy et al. (2010). Fe in sequential extractions (except pyrite Fe) was reduced by 10% (*w/v*) $NH_2OH{\cdot}HCl$ and quantified by using the ferrozine assay (Viollier et al., 2000). The digestion methods of total Mn and S were the same as those of total Fe. Total Fe, pyrite Fe (nitrate acid extracted in sequential extraction), and total Mn were measured by a flame atomic absorption spectrophotometer (PinAAcle 900 T, PerkinElmer, USA). Total sulfur was measured by a turbidimetric method using a UV–Vis spectrophotometer (UV-5100B, METASH, China) at 420 nm (Sörbo, 1987). Soil pH was determined by a pH meter at a soil-water ratio of 1:2.5 (*w/v*). The X-ray diffraction (XRD) spectra for soil samples were scanned by an X-ray diffractometer (Empyrean, Panalytical, Netherlands) with Cu-K-α radiation from 5° to 60° using 0.025° steps. Soil mineral phases were retrieved by using MDI Jade 6 software (Materials Data Inc., USA).

2.3. Data analysis

Concentrations of ambient THg and MeHg (i.e., Hg that is naturally present in the soil samples) and the isotope-enriched $T^{200}Hg$ and $Me^{200}Hg$ (i.e., ^{200}Hg only from spiked tracer and the ambient ^{200}Hg was deducted) were calculated according to the method detailed in our previous work (Liu et al., 2021a, 2022; Meng et al., 2018). Hg isotope fractionations induced by natural processes were ignored in the isotope-enriched Hg tracer spike studies (Meng et al., 2018). Data analysis for the optical properties of soil DOM is shown in Text S3.

2.4. QA/QC and statistics

Certified reference materials (CRMs) of GSS-5 ([THg] = 290 ± 30 ng g^{-1}) and ERM-CC580 ([MeHg] = 75.5 ± 3.7 ng g^{-1}) were used. The recoveries in THg and MeHg measurements were 109 ± 4.7% (n = 8) and 92 ± 10.0% (n = 10), respectively. The recoveries of mass balance ([the sum of ^{200}Hg fractions] / [$T^{200}Hg$]) for sequential extraction of ^{200}Hg ranged from 86% to 108% (n = 5, Fig. S2). The recoveries of mass balance ([the sum of Hg fractions]/[THg]) for sequential extraction of Hg ranged from 73% to 96% (n = 5). The method detection limits (3σ) were 0.02 μg kg^{-1} for THg, 0.002 μg kg^{-1} for MeHg, and 0.03 μg kg^{-1} for Hg isotopes in soils samples. The relative standard deviation (RSD) for duplicates was less than 10%.

The differences in data sets that were normally distributed were assessed by t–test and one-way ANOVA with Duncan's post-hoc test using SPSS 23.0 (IBM®, IL, USA). The differences tests for nonnormally distributed datasets were accessed by Kruskal–Wallis one-way ANOVA. The statistical significance (p) was declared at < 0.05 (2-tailed). The partial least squares path modeling (PLS-PM) was conducted by using R software (version 4.1.2) that was equipped with the "plspm" package.

3. Results

3.1. The isotope-enriched ^{200}Hg and ambient Hg

Concentrations of the isotope-enriched $T^{200}Hg$ and ambient THg in paddy soil during the rice-growing period were stable, with various ranges of 104.04 ± 2.91–120.65 ± 8.56 ng g^{-1} and 73.07 ± 4.29–95.04 ± 17.12 ng g^{-1}, respectively (Fig. S3a). It is worth mentioning that the

concentrations of spiked $T^{200}Hg$ and ambient THg are comparable, indicating that the spiked isotope tracers in this study can reflect the practical situation of Hg fate in paddy soil (Branfireun et al., 2005; Hintelmann et al., 2002; Oswald et al., 2014).

Since the spiking of Hg isotope tracers into paddy soil, most parts of the spiked ^{200}Hg were partitioned into organic matter bound Hg (84.6–89.4% of $T^{200}Hg$), followed by residual ^{200}Hg (7.6–8.1% of $T^{200}Hg$), and then Fe/Mn oxides bound ^{200}Hg (2.8–7.2% of $T^{200}Hg$) (Kruskal–Wallis one-way ANOVA $p < 0.01$, Figs. 1a and b). Soluble and exchangeable ^{200}Hg (0.05–0.17% of $T^{200}Hg$) and carbonates bound ^{200}Hg (0.04–0.07% of $T^{200}Hg$) governed only a small proportion of $T^{200}Hg$ (Figs. 1a and b). A similar distribution pattern was found in the ambient Hg fractions (i.e., organic matter bound Hg > residual Hg > Fe/Mn oxides bound Hg > exchangeable Hg > carbonates bound Hg). Nevertheless, relatively higher residual Hg (23.9–37.9% of THg, Kruskal–Wallis one-way ANOVA $p < 0.01$) but lower Fe/Mn oxides bound Hg (2.4–6.2% of THg, paired samples t-test $p < 0.05$) and organic matter bound Hg (57.4–73.5% of THg, paired samples t-test $p < 0.01$) were observed for ambient Hg than those of spiked ^{200}Hg (Figs. 1c and d, Fig. S4).

During the rice-growing period, the decreases in soluble and exchangeable Hg (both ^{200}Hg and ambient Hg) ^{200}Hg, carbonates bound ^{200}Hg, organic matter bound Hg (both ^{200}Hg and ambient Hg), and residual ^{200}Hg were observed (one-way ANOVA $p < 0.05$, Figs. 1a and c, Figs. S5 and S6). The significant increases in Fe/Mn oxides bound ^{200}Hg were found from the day 30–60 (from 3.30 ± 0.24 ng g^{-1} to 6.01 ± 1.13 ng g^{-1}, one-way ANOVA $p < 0.05$, Fig. 1a and Fig. S5). The variations in $Me^{200}Hg$ and ambient MeHg during the rice-growing period are shown in the Fig. S3b and Text S4.

3.2. Soil organic matters and optical properties of soil DOM

Different soil organic matter fractions play key roles in regulating the fate of Hg (Xu et al., 2021). Moreover, organic matter bound Hg was identified as the largest pool for the newly deposited Hg in paddy soil (Fig. 1); therefore, soil organic matter fractions were investigated. As shown in Fig. 2, the decreases in total organic carbon (TOC, showing the concentration of bulk SOM) but increases in dissolved organic carbon (DOC, showing the concentration of soil DOM) in paddy soils were observed during the rice-growing period (one-way ANOVA $p < 0.05$). Soil humic substances were isolated as humic acid (HA), fulvic acid (FA), and clay-associated HA and FA. In detail, the significant increases in HA and FA were found from the day 60 to day 110 in paddy soil (Fig. 2b, one-way ANOVA $p < 0.05$), whereas the HA and FA associated with soil clays decreased (Fig. 2c, a significant difference was only found in C-HA, one-way ANOVA $p < 0.05$).

Both UV–vis absorption and fluorescence spectra were used to calculate the optical properties of soil DOM. Through UV–vis absorption

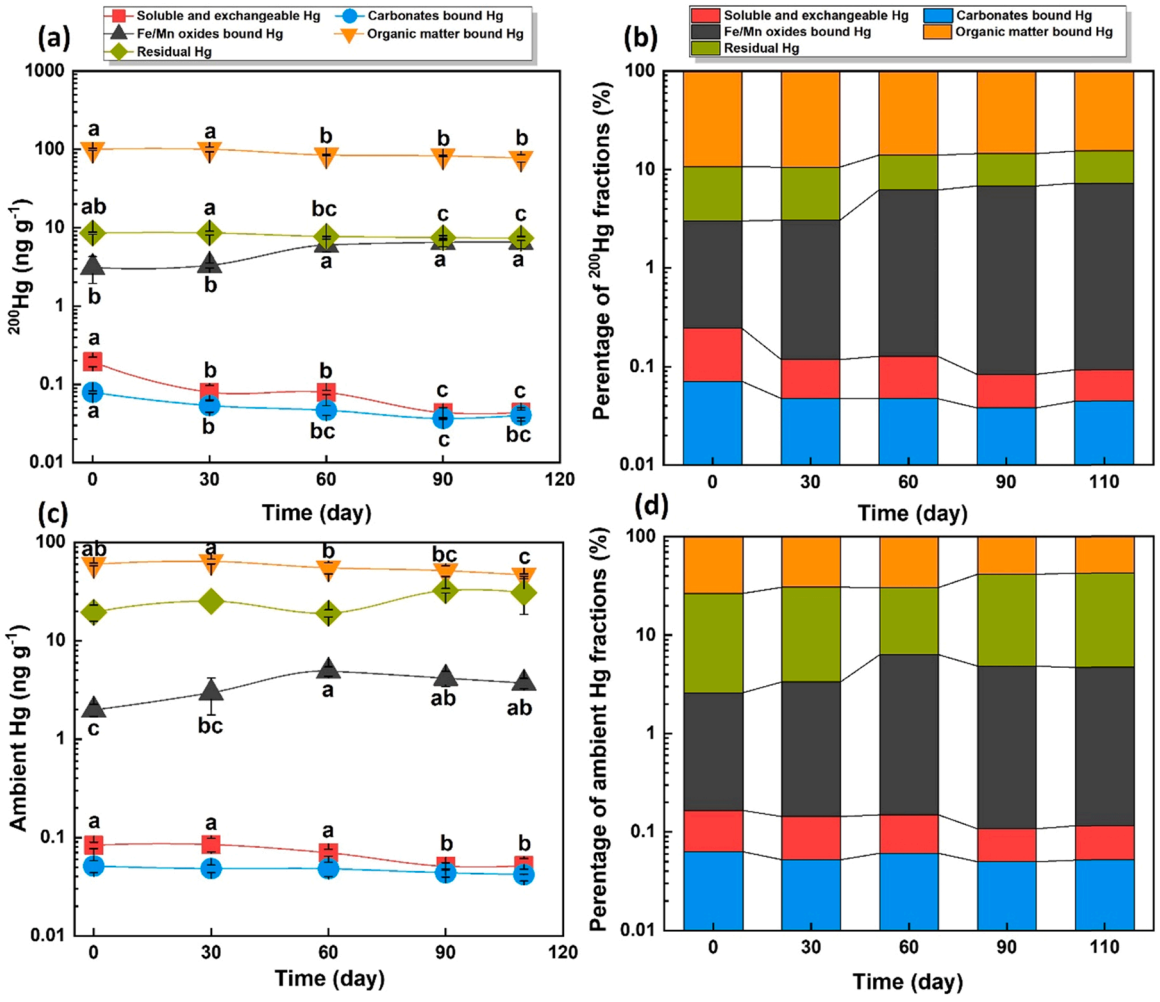

Fig. 1. Concentration and percentage of isotope-enriched ^{200}Hg (a and b) and ambient Hg (c and d) fractions in paddy soils during the rice-growing period. Different lowercase letters in line plots indicate that the differences in Hg concentration in paddy soils during the rice-growing period are significant through one-way ANOVA with Duncan's post-hoc test ($p < 0.05$). Data without lowercase letters suggest the difference is not significant. Error bars in line plots represent the standard deviation of three replicates (five replicates on day 110). All the units were presented by dry weight.

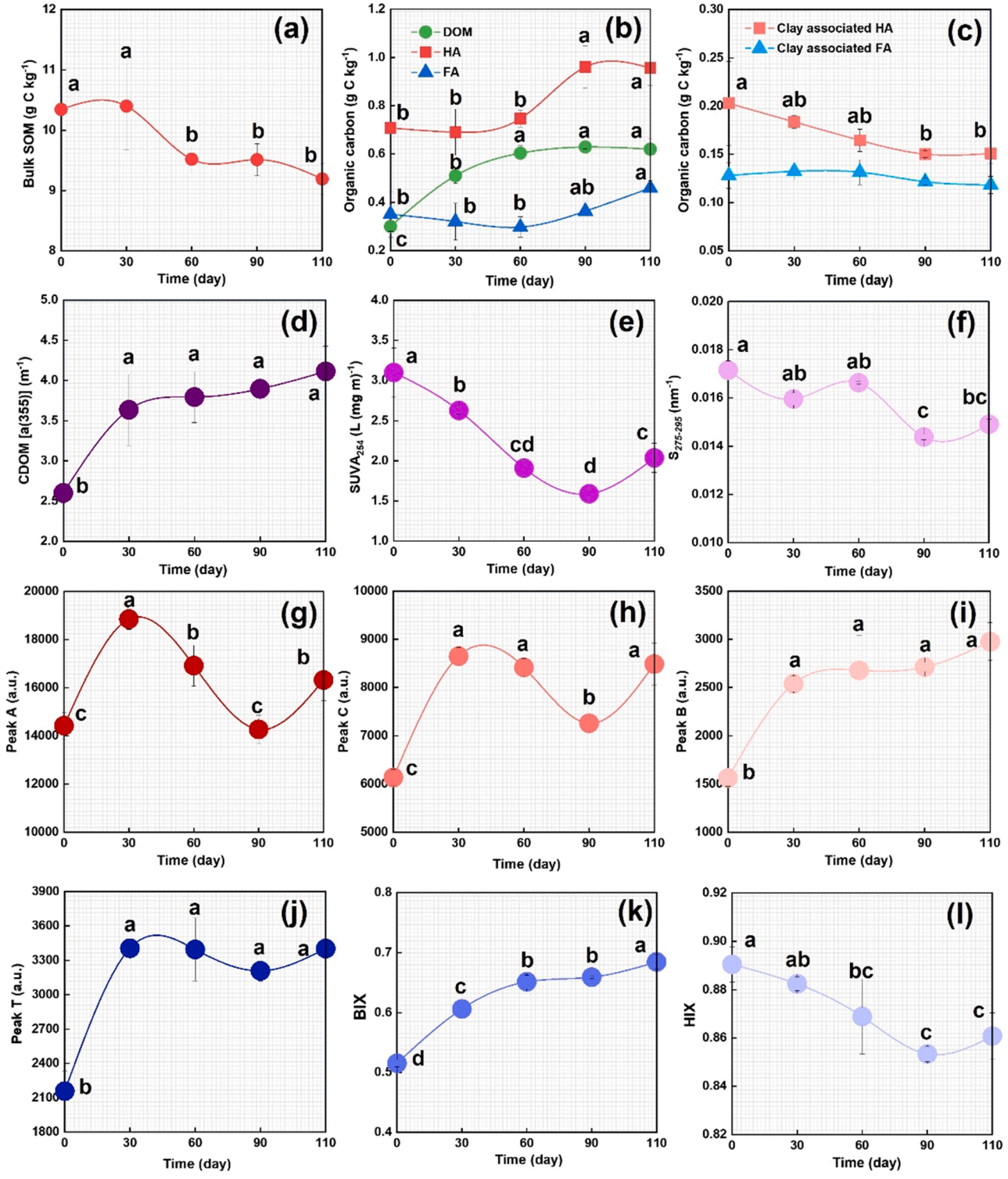

Fig. 2. Concentrations of bulk soil organic matter (SOM) (a), dissolved organic matter (DOM), humic acid (HA), fulvic acid (FA) (b), clay-associated HA and FA (c) and the optical properties of DOM (d-l) in paddy soils during the rice-growing period. Plots (d) to (f) are the properties from UV–vis absorption spectra of DOM, including the absorption coefficient at 355 nm (used to represent colored dissolved organic matter, $a(355)$) (d), specific UV absorbance at a wavelength of 254 nm ($SUVA_{254}$) (e), and spectral slope of 275–295 nm ($S_{275-295}$) (f). Plots (g) to (l) are the fluorescence compounds and calculated indices from EEM fluorescence spectra of DOC, including peak A (g), peak C (h), peak B (i), peak T (j), biological index (BIX) (k), and humification index (HIX) (l). Different lowercase letters indicate that the difference is significant through one-way ANOVA with Duncan's post-hoc test ($p < 0.05$). Data without lowercase letters suggest the difference is not significant. The error bar represents the standard deviation of three replicates (five replicates on day 110). All the units of mass were presented by dry weight.

spectra, increased signals of CDOM were found during the rice-growing period (Fig. 2d, one-way ANOVA $p < 0.05$), whereas the decreases in $SUVA_{254}$ (Fig. 2e, from the day 0 to day 90, one-way ANOVA $p < 0.05$) and $S_{275–295}$ (Fig. 2f, from the day 60 to day 90, one-way ANOVA $p < 0.05$) were observed. $SUVA_{254}$ increased after the decline from the first 90 days. Fluctuations of the intensities of fulvic-like (i.e., peak A, less humified) and humic-like compounds (i.e., peak C, more humified) and higher intensities of peak A than that of peak C were obtained (Figs. 2 g and h, one-way ANOVA $p < 0.05$). With the growth of rice, more signals of protein-like (or fresh-like) compounds (Figs. 2i and j, one-way ANOVA $p < 0.05$) and higher autotrophic productivity (shown as BIX, Fig. 2k, one-way ANOVA $p < 0.05$) values were found in soil DOM. Nevertheless, the humification degree, shown as HIX, decreased during the rice-growing period (Fig. 2l, one-way ANOVA $p < 0.05$).

3.3. Total Fe, Mn, and Fe fractions

In addition to organic matter bound Hg, Fe/Mn oxides bound Hg was also an important pool for the newly deposited Hg in paddy soil (Fig. 1). Typically, Fe and Mn coexist in soils such as ferromanganese nodules (Liu, C. et al., 2021c; Tessier et al., 1979), and the environmental behaviors of Fe and Mn oxides are quite similar. In this study, the concentration of total Fe (TFe, averaged 31.2 ± 0.8 g kg^{-1}) was more than 70 times higher than that of total Mn (TMn, averaged 0.42 ± 0.01 g kg^{-1}) during the rice-growing period (Fig. S7). Therefore, Fe fractions (i.e., Fe (oxyhydr)oxides) were further extracted to show the influences of Fe/Mn oxides on the fate of "new" Hg. During the rice-growing period, the percentage of highly reactive Fe (Fe_{HR}) in TFe in rice paddy soil was stable, and no significant variation was observed (Table 1). The largest Fe pool in Fe_{HR} is reducible Fe oxides (Fe_{ox2}, crystalline Fe oxides), followed by magnetite Fe, easily reducible Fe oxides, pyrite Fe, and carbonate-bound Fe. The significant increases in Fe_{carb} (one-way ANOVA $p < 0.05$), Fe_{ox1} (one-way ANOVA $p < 0.05$), and Fe_{py} (one-way ANOVA $p < 0.05$) were found in paddy soil during the rice-growing period (Table 1). Magnetite Fe decreased from the day 30 to the end of the experiment (one-way ANOVA $p < 0.05$), and Fe_{ox2} decreased during the whole rice-growing period (one-way ANOVA $p < 0.05$) (Table 1). Due to the relatively stable Fe_{HR} concentration and Fe_{HR}/TFe, the increases in Fe_{carb}, Fe_{ox1}, and Fe_{py} were offset by the decreases in Fe_{ox2} and Fe_{mag} (one-way ANOVA $p < 0.05$). No crystalline structures of Fe(oxyhydr)oxides were identified through XRD (Fig. S8), which may be attributed to the poor crystalline structures or the formation of micro/nanometric Fe(oxyhydr)oxides under redox conditions (Bishop et al., 2020; Ratié et al., 2019). More descriptions of ancillary data (soil pH, total sulfur, total nitrogen, and the C/N ratio) are shown in the Text S5 in the Supporting Information.

3.4. Relationships between the isotope-enriched ^{200}Hg and geochemical factors

Through the correlation analysis, all the isotope-enriched ^{200}Hg fractions (i.e., soluble and exchangeable ^{200}Hg, carbonates bound ^{200}Hg, Fe/Mn oxides bound ^{200}Hg, organic matter bound ^{200}Hg, and residual ^{200}Hg fractions) were significantly correlated with DOM, $a(355)$, BIX, HIX, Fe_{carb}, Fe_{ox1}, and Fe_{ox2} (Table 2). For example, Fe/Mn oxides bound to ^{200}Hg are highly co-varied with soil humic acid (Spearman's $r = 0.77$, $p < 0.01$, $r^2 = 0.51$), DOM (Spearman's $r = 0.91$, $p < 0.01$, $r^2 = 0.72$), protein-like fluorescence compounds (i.e., peak B, Spearman's $r = 0.76$, $p < 0.01$, $r^2 = 0.39$) and BIX (Spearman's $r = 0.67$, $p < 0.01$, $r^2 = 0.55$) (Fig. 3 and Table 2). It is noted that soil DOM is negatively correlated with soluble and exchangeable ^{200}Hg, carbonates bound ^{200}Hg, organic matter bound ^{200}Hg, and residual ^{200}Hg, but positively correlated with Fe/Mn oxides bound ^{200}Hg (Fig. 3). Similar tendency of correlations was also found in BIX and Fe_{ox1}.

Four latent variables, including soil chemistry (including total sulfur, total Fe, total Mn, total N, pH, and C/N ratio), soil bulk OM (including TOC, humic acid, fulvic acid, and clay-associated humic acid and fulvic acid), DOM (including DOC, $SUVA_{254}$, $S_{275–295}$, peak A, peak B, BIX, and HIX), and Fe species (including Fe_{exch}, Fe_{carb}, Fe_{ox1}, Fe_{ox2}, and Fe_{mag}), were input for partial least squares path modeling analysis. The goodness-of-fit (GOF) ranged from 0.57 to 0.60, showing a good model predictive value (Fig. 4). Through Fig. 4, DOM (path coefficient of −0.42) and Fe (oxyhydr)oxides (path coefficient of −0.39) are two major effects for soluble and exchangeable ^{200}Hg, whereas DOM (path coefficient of −0.50) is the major effect for carbonates bound ^{200}Hg (Figs. 4a and b). For Fe/Mn oxides bound ^{200}Hg, DOM showed the most considerable effect (path coefficient of 0.86, Fig. 4c). In addition to bulk SOM and DOM, Fe species also showed a high contribution (path coefficient of −0.43) to organic matter bound ^{200}Hg (Fig. 4d).

4. Discussions

4.1. Partitioning of "new" Hg in different geochemical fractions in paddy soil

Through sequential extraction, organic matter was identified as the largest sink of both newly spiked and ambient Hg in paddy soil (Fig. 1). This finding is consistent with our previous works in paddy soil at an artisanal Hg smelting site (i.e., Wanshan Hg mining area, [THg] = 3.2 ± 0.75 mg kg^{-1}, organic matter bound Hg could reach 62% of THg, Zhao, 2016) and in the background soil of urban areas (i.e., Huaxi, Guiyang City, [THg] = 0.25 ± 0.06 mg kg^{-1}, organic matter bound Hg could reach 87.8% of THg, Lu et al., 2021). These results highlighted that organic matter could be the largest pool for the Hg from atmosphere depositions. Soil organic matter is regarded as one of the most important Hg sinks due to (1) its high binding affinity with Hg and (2) its association with Hg-adsorbing particles (O'Connor et al., 2019). In particular, the majority of "new" Hg in the soil is partitioned into the solid phase (e.g., soil minerals) since deposition, and only a small fraction of the newly deposited Hg in the soil is present in the aqueous phase (e.g., porewater) (Jonsson et al., 2014). Furthermore, research has documented that soil minerals are often coated with organic matter (Lalonde et al., 2012; Riedel et al., 2013), and the adsorption behaviors of soil minerals for Hg are profoundly influenced by this organic matter (Zhang et al., 2019),

Table 1
Concentration of total Fe and various Fe pools in paddy soils during the rice-growing period.

Rice-growing period	TFe	Fe_{exch}	Fe_{carb}	Fe_{ox1}	Fe_{ox2}	Fe_{mag}	Fe_{py}	Fe_{HR}	Fe_{HR}/TFe
(day)	(g kg^{-1})	(mg kg^{-1})	(g kg^{-1})	(g kg^{-1})	(g kg^{-1})	(g kg^{-1})	(g kg^{-1})	(g kg^{-1})	(%)
0	32.1 ± 2.2	1.29 ± 0.5	0.005 ± 0.0004c	0.37 ± 0.03d	8.43 ± 0.3a	1.77 ± 0.1ab	0.59 ± 0.03b	11.2 ± 0.2ab	34.8 ± 1.8
30	31.3 ± 0.9	1.20 ± 0.2	0.067 ± 0.01c	0.87 ± 0.05c	7.34 ± 0.4b	1.95 ± 0.3a	0.60 ± 0.04b	10.8 ± 0.2b	35.5 ± 0.9
60	30.0 ± 0.5	1.31 ± 0.2	0.23 ± 0.02b	1.19 ± 0.06b	7.13 ± 0.4 bc	1.84 ± 0.09ab	0.75 ± 0.1ab	11.1 ± 0.3ab	36.3 ± 1.4
90	30.8 ± 1.0	1.37 ± 0.2	0.45 ± 0.04a	1.42 ± 0.01a	7.01 ± 0.03 bc	1.65 ± 0.02b	0.70 ± 0.09ab	11.2 ± 0.05a	36.8 ± 0.3
110	31.7 ± 1.4	1.28 ± 0.5	0.49 ± 0.10a	1.45 ± 0.05a	6.56 ± 0.4c	1.66 ± 0.1b	0.87 ± 0.2a	11.0 ± 0.2ab	34.5 ± 1.0

TFe is total Fe; Fe_{exch} is soluble and exchangeable Fe; Fe_{carb} is carbonates bound Fe; Fe_{ox1} is easily reducible Fe; Fe_{ox2} is reducible Fe; Fe_{mag} is magnetite Fe; Fe_{py} is pyrite Fe; Fe_{HR} is highly reactive Fe ($FeHR = \sum (Fe_{exch} + Fe_{carb} + Fe_{ox1} + Fe_{ox2} + Fe_{mag} + Fe_{py})$). Different lowercase letters in each column indicate that the differences in Fe concentrations in paddy soils at different rice-growing periods are significant through one-way ANOVA with Duncan's post-hoc test ($p < 0.05$). All the units of mass were presented by dry weight

Table 2
Correlation matrix between ^{200}Hg fractions and geochemical factors.

	Soluble and exchangeable ^{200}Hg	Carbonates bound ^{200}Hg	Fe/Mn oxides bound ^{200}Hg	Organic matter bound ^{200}Hg	Residual ^{200}Hg
TS	0.85**	0.80**		0.73**	0.55*
TFe					
TMn					
pH					
TOC				0.48*	
C/N					
HA	-0.85**		0.77**	-0.68**	-0.56*
FA	-0.58*				
C-HA	0.87**	0.84**		0.82**	0.72**
C-FA					
DOC	-0.67**	-0.55*	0.91**	-0.68**	-0.074**
a(355)	-0.73**	-0.57*	0.67*	-0.77**	-0.65*
$SUVA_{254}$	0.58*	0.58*	-0.87**		0.65*
$S_{275–295}$	0.70**		-0.79**	0.57*	0.52*
peak A					
peak B	-0.66*		0.76**	-0.71**	-0.60*
peak C					
peak T					
BIX	-0.86**	-0.65**	0.67**	-0.82**	-0.72**
HIX	0.76**	0.66**	-0.79**	0.61**	0.65**
Fe_{exch}					
Fe_{carb}	-0.94**	-0.66**	0.79**	-0.74**	-0.68**
Fe_{ox1}	-0.91**	-0.62**	0.79**	-0.74**	-0.71**
Fe_{ox2}	0.76**	0.68**	-0.61**	0.65**	0.68**
Fe_{mag}	0.58*			0.54*	
Fe_{py}	-0.52*		0.65**	-0.62**	-0.72**

Spearman's r was used as the correlation coefficient. "*" and "**" indicate that the correlations are significant at $p < 0.05$ and $p < 0.01$. Vacancies suggest that the correlations are not significant. Abbreviations: TS, total sulfur; TFe, total iron; TMn, total manganese, TOC, total organic carbon; C/N, carbon and nitrogen ratio; HA, humic acid; FA, fulvic acid; C-HA, clay-associated HA; C-FA, clay-associated FA; DOC, dissolved organic carbon; a(355), absorption coefficient at 355 nm; $SUVA_{254}$, specific UV absorbance at a wavelength of 254 nm; $S_{275–295}$, spectral slope of 275–295 nm; peaks A, B, C, and T, fluorescence compounds; BIX, biological index; HIX, humification index; Fe_{exch}, soluble and exchangeable Fe; Fe_{carb}, carbonate associated Fe; Fe_{ox1}, easily reducible Fe oxides; Fe_{ox2}, reducible Fe oxides; Fe_{mag}, magnetite Fe; Fe_{py}, pyrite Fe.

such as thiol ligands (-RSH) associated with the organic matter (Skyllberg et al., 2006; Skyllberg, 2008) under reduced conditions. As a result, the retention of "new" Hg by organo-minerals (i.e., organic matter-coated minerals) is an important reason that explains the high partitioning of the newly deposited Hg in organic matter. In addition, the formation and stabilization of nanoparticulate or colloidal HgS originating from "new" Hg are highly influenced by organic matter (Gerbig et al., 2011; Graham et al., 2012), and this Hg pool is commonly found in anoxic environments (e.g., paddy soil) and cannot be ignored (Manceau et al., 2018).

Traditionally, sulfides are the major sink of Hg in natural environments, especially in Hg mining areas (Yin et al., 2016). However, due to the lower amount of total sulfur than SOM (Fig. 2 a and Fig. S9) and the redox fluctuation (i.e., dry-wet alterations in paddy soils), the pool size of residual ^{200}Hg (typically HgS) only accounts for 7.6–8.1% of the T^{200}Hg pool. The unexpectedly low partitioning of "new" Hg into residual Hg suggests that the kinetics of Hg-soil organic matter binding are faster than the formation of HgS particles, which is consistent with previous studies showing that organic matter is the rate-limited factor for the aggregation of HgS clusters (Gerbig et al., 2011; Graham et al., 2012; Hsu-kim et al., 2013). Well-structured mineral lattices are also Hg sinks (forming residual Hg pools, Tessier et al., 1979); however, the entrance or replacement of Hg into those lattices (e.g., silicate lattices) is usually slower than binding with organic matter. This also supports the low partitioning of "new" Hg into residual Hg.

Metal oxides are also one of the sinks for trace metals in soil, and numerous studies have reported high adsorption capacities of Fe/Mn oxides for Hg (Bonnissel-Gissinger et al., 1999; Feyte et al., 2010). This explained that Fe/Mn oxides are the third pool of "new" Hg only to organic matter bound Hg and residual Hg (Fig. 1). However, this Hg pool varied with the oxide phase changes driven by redox alternations, which was supported by variations in Hg distribution (Fig. 1) and Fe(oxyhydr) oxide changes during the rice-growing period (Table 1).

The spiked ^{200}Hg into paddy soil is dissolved $^{200}Hg(NO_3)_2$; therefore, a large fraction of soluble and exchangeable Hg was excepted. However, the partitioning of "new" Hg into soluble and exchangeable Hg and carbonates bound Hg only accounts for a minor fraction (0.09–0.24%) of T^{200}Hg, suggesting that the strong binding sites (e.g., surface complexation sites, adsorption sites) for Hg are far from saturated in paddy soil and the newly deposited Hg will be immobilized immediately.

4.2. *Redistribution of "new" Hg among different geochemical fractions during the rice-growing period*

The redistribution of the newly deposited Hg among geochemical pools can be revealed by variations in different ^{200}Hg pools during the rice-growing period (Fig. 1a). In this study, transitions from soluble and exchangeable ^{200}Hg, carbonates bound ^{200}Hg, organic matter bound ^{200}Hg, and residual ^{200}Hg to Fe/Mn oxides bound ^{200}Hg were found (Fig. 3a). Redistribution of soluble and exchangeable ^{200}Hg and carbonates bound ^{200}Hg occurred initially after spiking with ^{200}Hg tracers, suggesting an immobilization process of these highly liable Hg pools. However, transitions of organic matter bound ^{200}Hg, Fe/Mn oxides bound ^{200}Hg and residual ^{200}Hg mainly occurred after 30 days. This suggests that although "new" Hg rapidly partitioned into the solid phase after deposition, the redistribution among these three Hg pools (i.e., Fe/Mn oxides bound Hg, organic matter bound Hg and residual Hg) took time to reach equilibrium. Two reasons may be explained for the redistribution of "new" Hg in environments: one is the thermodynamic equilibrium process of Hg in soil, and the other is the biogeochemical condition change-induced re-equilibrium process. The former is likely responsible for the decreases in soluble and exchangeable ^{200}Hg and carbonates bound ^{200}Hg because dissolved phases (e.g., soluble Hg) are not stable in the presence of colloids or solids (Skyllberg et al., 2021), which will be redistributed into colloids or solids rapidly. Nevertheless, the latter (i.e., re-equilibrium process) may play a dominant role in the redistribution of "new" Hg among geochemical pools due to the highly dynamic biogeochemistry of paddy soil (Kögel-Knabner et al., 2010).

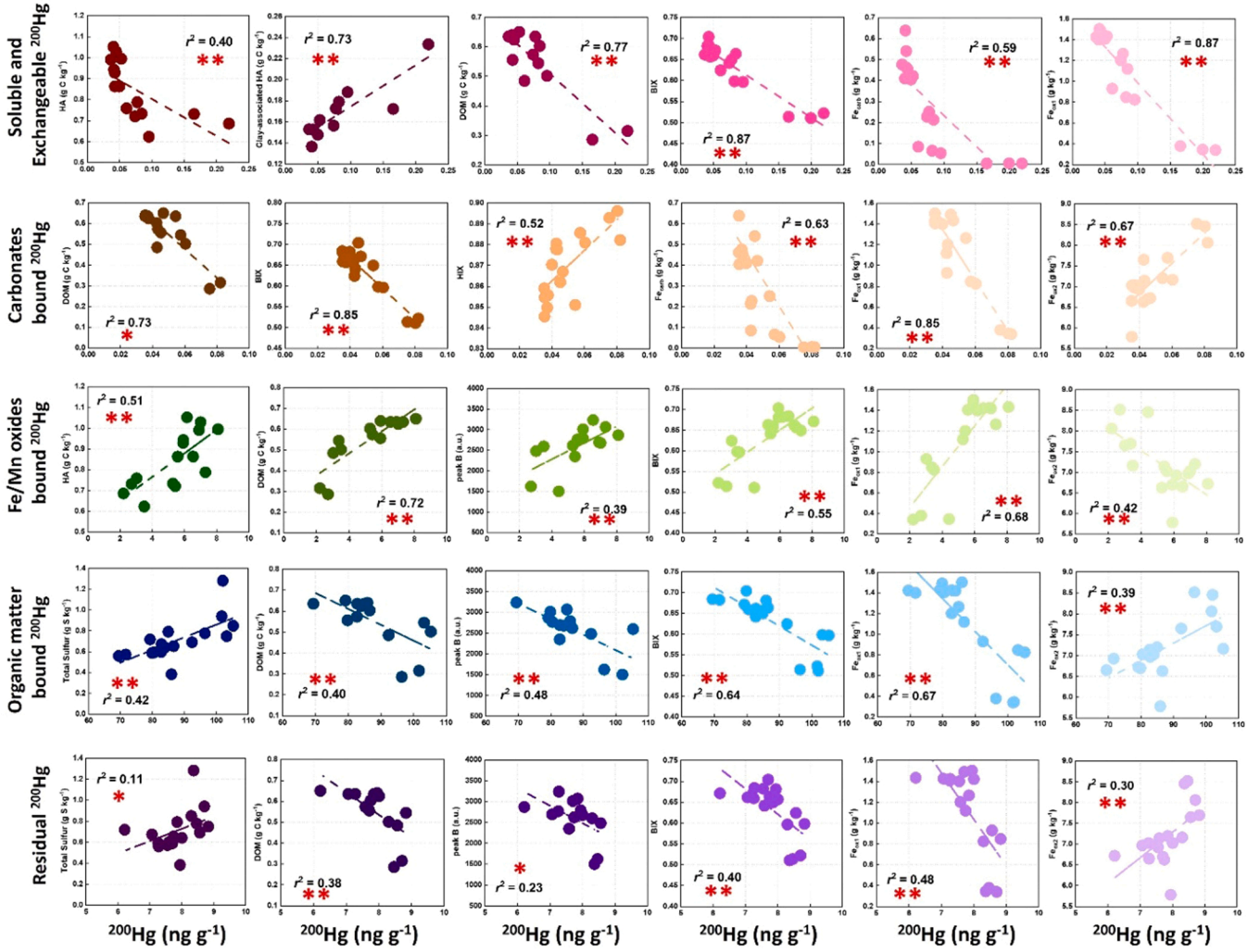

Fig. 3. Concentration of isotope enriched ^{200}Hg in different fractions versus various geochemical factors. r^2 is the determination coefficient from linear regression, "* " and "* *" suggest that the correlation between two variables is significant at $p < 0.05$ and $p < 0.01$. Abbreviations: HA is humic acid, DOM is dissolved organic matter, BIX is biological index, HIX is humification index, peak B is a fluorescence compound with protein-like character, Fe_{carb} is carbonate-associated Fe, Fe_{ox1} is easily reducible Fe oxides, and Fe_{ox2} is reducible Fe oxides. All the units of mass were presented by dry weight.

For example, changes in both the concentration and structural composition of soil organic matter (Fig. 2) coupled with the decreases in organic matter bound ^{200}Hg (Fig. 1a) indicate the release of "new" Hg from OM in paddy soil during the rice-growing period. Specifically, mineralization of SOM and production of dissolved OM fractions in this study were evidenced by the decreased TOC (Fig. 2a) and increased water-soluble organic carbon (Fig. 2b) during the rice-growing period. Moreover, significant negative correlations between organic matter bound to ^{200}Hg and the concentration of DOM (Spearman's $r = -0.68$, $p < 0.01$) and autochthonous signals of DOM (Peak B, Spearman's $r = -0.71, p < 0.01$; BIX, Spearman's $r = -0.82, p < 0.01$) can be found in Fig. 3. These findings demonstrate that mineralization of SOM and production of dissolved OM through microbial metabolism (Liu et al., 2021b), especially in the rhizosphere, could release "new" Hg from SOM. A similar result was reported in permafrost areas, in which OM decomposition induced by permafrost degradation posed a great risk to Hg release (Mu et al., 2020). Furthermore, the secretion of root exudates in the rhizosphere may have a priming effect on the mineralization of SOM in paddy soil (Du et al., 2020), which may also promote the release of Hg from SOM. It is noted that this study is not to discuss the absorption, translocation and bioaccumulation of Hg tracers in soil-rice systems. Therefore, the data for the isotope-enriched ^{200}Hg, and ambient Hg in rice tissues were not studied. However, translocation and transformation of Hg in rice plants were reported in a parallel work with similar experimental design but conducted at a different site (high GEM region) (Liu et al., 2021a).

An interesting finding of this study is that Fe/Mn oxides are sinks for the newly deposited Hg in redistribution. Due to the coexistence and similar environmental behaviors of Fe and Mn oxides (Liu, C. et al., 2021c; Tessier et al., 1979), as well as higher concentrations of total Fe than Mn in soils (Fig. S7). This study takes Fe oxides as an example to show the influence of Fe/Mn oxides on "new" Hg. Significant enrichment of ^{200}Hg was found in poorly crystalline or amorphous Fe species, which is supported by the increases in easily reducible Fe ($p < 0.05$, Table 1) and increases in Fe/Mn oxides bound ^{200}Hg ($p < 0.05$, Fig. 1a). This is because the extraction method of Fe/Mn oxides bound ^{200}Hg are the same as easily reducible Fe (i.e., $NH_2OH{\cdot}HCl$ in acetic acid), which is usually regarded as poorly crystalline or amorphous Fe (oxyhydr)oxides (Poulton and Canfield, 2005; Tessier et al., 1979). Variations in Fe species suggested the transition from well crystalline Fe (oxyhydr)oxides (e.g., goethite and hematite) to poorly crystalline Fe (oxyhydr)oxides (e.g., ferrihydrite) and then to Fe-S minerals (e.g., pyrite) in flooded paddy soil during the rice-growing period (Huang et al., 2021; Kappler et al., 2021). The studies have reported that poorly crystalline or amorphous Fe species are more active in co-precipitation or adsorption of free ^{200}Hg released from the organic matter due to the larger specific surface area

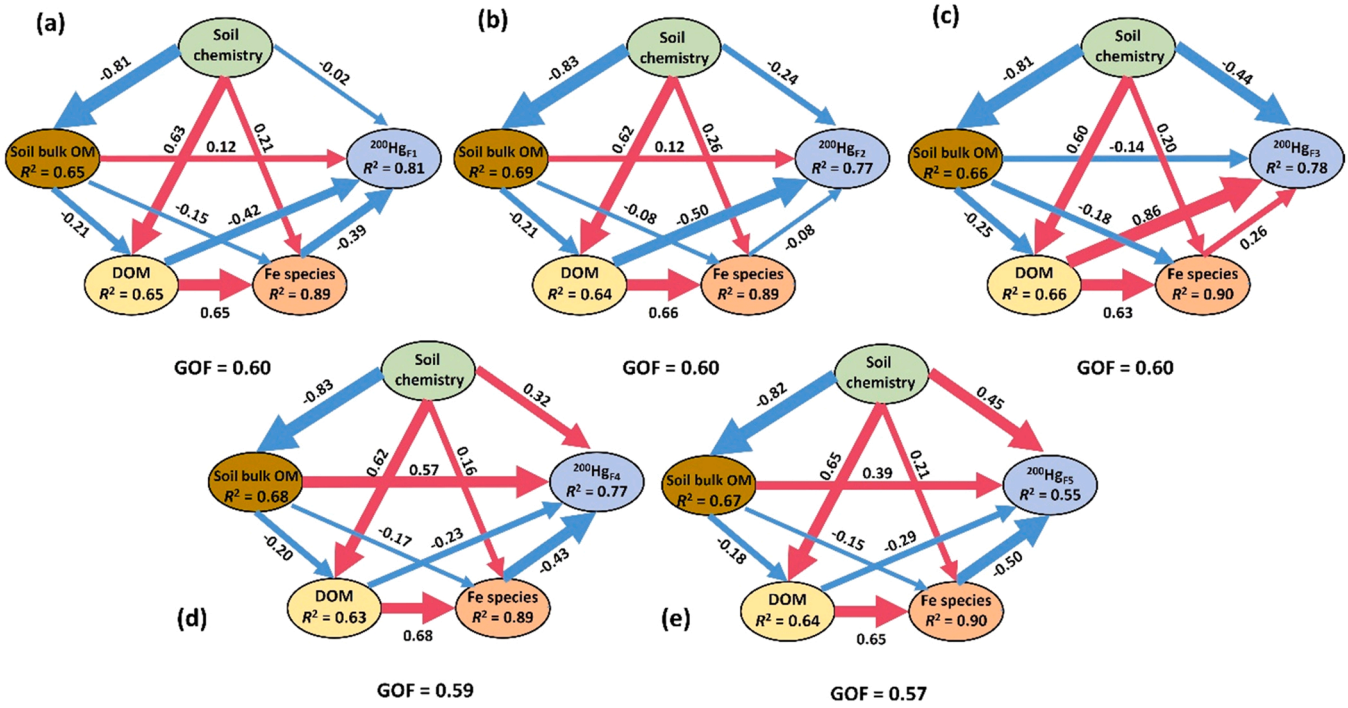

Fig. 4. Partial least squares path modeling (PLS-PM) showing the cascade relationships among soil chemistry, soil bulk organic matter, dissolved organic matter, iron species and the concentration of newly introduced Hg in different fractions in paddy soils. (a) Soluble and exchangeable ^{200}Hg; (b) carbonates bound ^{200}Hg; (c) Fe/Mn oxides bound ^{200}Hg; (d) organic matter bound ^{200}Hg; (e) residual ^{200}Hg. Red and blue arrows represent positive and negative flows of causality, respectively. The numbers on the arrows show standardized path coefficients. R^2 represents the variance of the dependent variable explained by the model. GOF represents goodness of fit.

and higher reactivity than well crystalline Fe (oxyhydr)oxides (Bao et al., 2021; Tiffreau et al., 1995). Furthermore, poorly crystalline or amorphous Fe (oxyhydr)oxides were found as a sink of DOM (Lv et al., 2016), and DOM, in return, could stabilize Fe (oxyhydr)oxides (Aiken et al., 2011). As a result, the formation of an Fe-OM (colloidal) system may coagulate Hg and affect the behaviors of the newly deposited Hg (Bao et al., 2021). However, more studies are needed to uncover the role of the Fe-OM system (Chen et al., 2020; Wang et al., 2017; Zeng et al., 2020) on the mobility and bioavailability of Hg in redox fluctuating environments. Significantly, although the total Mn concentration is lower than that of TFe, more studies are needed to study the role of Mn oxides on the fate of Hg, especially the immobilization of heavy metals by reduced sulfur coupled Mn oxides (Sun et al., 2020). Moreover, the interactions between Mn and DOM were also reported (Li et al., 2021).

It is noted that the pool of residual ^{200}Hg decreased in the redistribution of the newly deposited Hg during the rice-growing period. One possible explanation is that dissolution of the newly formed HgS (i.e., residual Hg) occurs in flooded soils. A study by Li et al. (2022) found that the dissolution of α-HgS increased the bioavailable Hg in methylation. In addition, the potential dissolution of bulk HgS induced by the formation of Hg-(poly)sulfide complexes was suggested in some periodically flooded soils (e.g., water-level fluctuation areas of reservoirs, Liu et al., 2018) and peatlands (Wang et al., 2021). However, the formation constants and measurement techniques for Hg-(poly)sulfides are still problematic.

4.3. Geochemical factors' control on partitioning and redistribution of "new" Hg in paddy soil

To unravel the controlling factors for the partitioning and redistribution of the newly deposited Hg in paddy soil, multiple analyses were applied. The correlation analysis coupled with linear regression was used to show the covariation of "new" Hg with different geochemical characteristics. Partial least squares path modeling was used to show causal relationships of the distribution pattern for the newly introduced Hg caused by various geochemical factors.

Through the correlation analysis, the significant correlations between all the isotope-enriched ^{200}Hg fractions and DOM, a(355), BIX, HIX, Fe_{carb}, Fe_{ox1}, and Fe_{ox2} (Table 2), suggesting influences of organic matter and Fe (oxyhydr)oxides on partitioning and redistribution of the newly deposited Hg. Specifically, correlations between Fe/Mn oxides bound to ^{200}Hg and soil humic acid, DOM, protein-like fluorescence compounds (peak B), and BIX (Table 2 and Fig. 3), suggested that Fe (oxyhydr)oxides are intimately linked with autochthonous OM (i.e., microbial sources) to control the partitioning and redistribution of "new" Hg in paddy soil. Similarly, opposite Spearman's r values (Spearman's $r < 0$, $p < 0.05$) were identified between those factors and OM bound ^{200}Hg (Table 2). Together with the variations of ^{200}Hg described above (i.e., the transition from organic matter bound ^{200}Hg to Fe/Mn oxides bound ^{200}Hg, Fig. 1a) and correlations here, we suggested that ^{200}Hg released from stable organic matter was recaptured by poorly crystalline Fe (oxyhydr)oxide-DOM associations during the rice-growing period and formed Hg-Fe-DOM ternary complexes. Similar ternary complexes were reported comprising different pollutants, such as As (Aftabtalab et al., 2022), Cd (Du et al., 2018), and Cr (Liao et al., 2020; Xia et al., 2020). Microbial-mediated mineralization of the recalcitrant organic matter may be the major reason for the losses of organic matter bound to ^{200}Hg because lower binding capacity and strength for Hg was found in less humified organic matter than in recalcitrant organic matter (Wang et al., 2022).

For liable Hg pools (i.e., soluble and exchangeable Hg and carbonates bound Hg), Fe (oxyhydr)oxides and organic matter are potential sinks and responsible for the aging/inactivation of "new" Hg due to their significant negative correlations (soluble and exchangeable ^{200}Hg versus humic acid, DOM, Fe_{carb} and Feo_{x1}; carbonates bound ^{200}Hg versus DOM, Fe_{carb} and Fe_{ox1}) (Table 2 and Fig. 3). Moreover, the negative covariations of soluble and exchangeable ^{200}Hg and carbonates bound ^{200}Hg with BIX indicate that increases in autochthonous DOM may

decrease the liable Hg pools, which further suggests that rhizosphere reactions and microbial metabolism could decrease the liable Hg pools. This finding is different from the traditional understanding that the formation of low molecular weight OM (e.g., low molecular weight organic acids) promotes the release of Hg to aqueous phases (Yin et al., 2018). Associations of Fe (oxyhydr)oxides-DOM are likely the reason (Bao et al., 2021).

The ternary system, Fe (oxyhydr)oxide-OM-newly deposited Hg, highlighted above was also evidenced by PLS-PM (Fig. 4). Specifically, considerable effect from DOM for Fe/Mn oxides bound ^{200}Hg, suggesting that Fe-OM interactions promote the distribution of "new" Fe(oxyhydr)oxides. In contrast, contributions from Fe species to organic matter bound ^{200}Hg implied competitive binding of ^{200}Hg between bulk SOM and Fe (oxyhydr)oxides during the rice-growing period. Typically, Fe (oxyhydr)oxides and OM often interact with each other in natural environments due to the strong binding ability between –COOH/phenolic –OH groups on OM and –OH groups on Fe (oxyhydr)oxides (Bao et al., 2021; Kleber et al., 2015). Two binding mechanisms of the newly deposited Hg by the Fe (oxyhydr)oxide-OM system were suggested: (1) ^{200}Hg act as a "bridge" connecting Fe (oxyhydr)oxides and OM to form Fe-^{200}Hg-OM associations, and (2) ^{200}Hg bind with OM associated with Fe (oxyhydr)oxides to form ^{200}Hg-OM-Fe associations (Bao et al., 2021).

The previous studies have reported that Fe-OM interactions showed significant influences on the fate of other heavy metals/metalloids (e.g., Cr, U, and As) (Al-Sid-Cheikh et al., 2015; Bao et al., 2021; Huang et al., 2021; Liao et al., 2020). This work further demonstrates that interactions between Fe(oxyhydr)oxides and DOM dominate the distribution of the newly deposited Hg in paddy soil.

4.4. Implication and prospects

The geochemical fractionation (i.e., partitioning and redistribution) of the newly deposited heavy metals into terrestrial systems determine their bioavailability and bioaccessibility, further determining the environmental risks for human exposure. The previous studies have reported that the newly introduced Cd in paddy soil rapidly aged from soluble Cd to residual Cd within 56 days through an in-lab incubation experiment, suggesting a significant aging process of Cd in paddy soil (Dong et al., 2021a, 2021b). However, similar aging processes of the newly deposited Hg in paddy soil were absent in this in situ plot experiment with a longer incubation time (i.e., 110 days). This finding partially explains why lower THg but higher MeHg was observed in the artisanal Hg mining site (i.e., contaminated by atmospheric deposited Hg) in previous studies (Meng et al., 2010, 2011; Zhao et al., 2016a). In particular, a significant correlation was observed between organic matter bound ^{200}Hg and Me^{200}Hg in this study (Spearman's $r = 0.57$, $p < 0.05$, from the day 30 to day 110). Similarly, high methylation rates of DOM-bound Hg in paddy soil were found in our previous work (Liu et al., 2022). The largest pool (i.e., organic matter bound Hg) of the newly deposited Hg in paddy soil may become a potential Hg substrate fueling methylation. Therefore, other Hg pools (e.g., organic matter bound Hg) instead of merely soluble and exchangeable Hg should be considered in evaluating the environmental risks of Hg deposited from the atmosphere. Moreover, this study provides a clue to environmental implications that highlight the role of the Fe-OM association in controlling the redistribution of "new" Hg in paddy soil. The releases and further redistribution of Hg in Fe (oxyhydr)oxide-DOM-Hg associations are likely to occur when the redox condition changes. For example, the degradation of OM or reductive dissolution of Fe(III) likely releases Hg (Bravo et al., 2018).

On the other hand, we should note that the study was conducted during one rice-growing period (110 days), and the geochemical fractionation or potential aging process of deposited Hg over a longer time scale remains unclear. Therefore, a long-term study of the dynamics of "new" Hg in wetland ecosystems is needed to better evaluate the environmental risks of Hg from atmospheric deposition, such as the Mercury Experiment to Assess Atmospheric Loading in Canada and the United States (METAALICUS) project (Blanchfield et al., 2021; Branfireun et al., 2005; Harris et al., 2007; Hintelmann et al., 2002; Oswald et al., 2014). Moreover, a more solid or direct evidence is needed to show the formation of Hg-Fe-DOM ternary systems, for example, by using nanoscale secondary ion mass spectrometry (NanoSIMS) (Al-Sid-Cheikh et al., 2015; Du et al., 2018) and scanning transmission X-ray microscopy (STXM) (Xia et al., 2020).

5. Conclusions

The isotope-enriched ^{200}Hg was applied to trace partitioning and redistribution of the newly deposited Hg in paddy soil during the rice-growing period. Soil organic matter is the largest sink of the newly deposited Hg in paddy soils, followed by residual Hg, Fe/Mn oxides bound Hg, soluble and exchangeable Hg, and carbonates bound Hg. In this study, 89.4% of Hg was rapidly distributed into the organic matter since it was deposited. During the rice-growing period, redistribution of the newly deposited Hg was identified from soluble and exchangeable Hg, carbonates bound Hg, organic matter bound Hg, and residual Hg to Fe/Mn oxides bound Hg. Geochemical fractionation of the newly deposited Hg in paddy soil is likely caused by (1) microbial-mediated mineralization of soil organic matter and (2) Fe phase changes from well crystalline Fe (oxyhydr)oxides to poorly crystalline Fe (oxyhydr)oxides and then Fe-S minerals. Correlation analyses jointly with partial least squares path modeling suggested that the coupling of autochthonous OM and poorly crystalline/amorphous Fe (oxyhydr)oxides plays a predominant role in controlling the speciation of "new" Hg in paddy soils. The decreases in the residual Hg pool from the newly deposited Hg were found in this study, suggesting the aging processes of conversion to a residue Hg from newly deposited Hg was absent in paddy soils during the rice-growing period. This study also implied that soluble and exchangeable Hg is not the only bioavailable Hg pool; other pools, for example, organic matter bound Hg, may also be methylated and should be considered.

Environmental implication

For the first trial, we successfully identified the fate of newly deposited Hg in paddy soils by using enriched stable Hg isotopes. We suggested that soluble and exchangeable Hg is not the only bioavailable Hg pool; other pools, for example, organic matter bound Hg, may also be methylated and should be considered. Our findings provide new information on the speciation and bioavailability of "new" Hg in paddy soils, which would help to improve our understanding of the biogeochemical cycling and environmental risks of newly deposited Hg, especially in sensitive ecosystems (e.g., rice paddies, wetlands, and reservoirs).

CRediT authorship contribution statement

Jiang Liu: Investigation, Data curation, Formal analysis, Writing – original draft. **Lei Zhao**: Investigation, Conceptualization, Funding acquisition; Writing – review & editing. **Kun Kong**: Investigation, Data curation. **Mahmoud A. Abdelhafiz:** Writing – review & editing. **Shanyi Tian**: Formal analysis, Writing – review & editing. **Tao Jiang**: Formal analysis, Writing – review & editing. **Bo Meng**: Project administration, Conceptualization, Supervision, Writing – review & editing. **Xinbin Feng:** Resources, Writing – review & editing.

Declaration of Competing Interest

The authors declare that they have no known competing financial interests or personal relationships that could have appeared to influence the work reported in this paper.

Acknowledgments

The authors would like to acknowledge the support of the National Natural Science Foundation of China (42163009, 41703130, 42107442), the Guizhou Provincial Natural Science Foundation (Qian-Ke-He-Ji-Chu ZK [2021]Zhong-Dian 041), the CAS "Light of West China" program, and the Opening Fund of the State Key Laboratory of Environmental Geochemistry (SKLEG2021201). We thank Qiyi Meng and Ji Chen for helps with sample collection and measurement. We thank Songbo Yao and Yuqin Wang, both from Southwest University, for important help in the analysis of natural organic matter and the establishment of PLS-PM. We would also like to thank Dr. Yong Meng for XRD analysis. Finally, we thank the editors and 11 anonymous reviewers for their constructive comments.

Appendix A. Supporting information

Supplementary data associated with this article can be found in the online version at doi:10.1016/j.jhazmat.2022.128752.

References

Aftabtalab, A., Rinklebe, J., Shaheen, S.M., Niazi, N.K., Moreno-Jiménez, E., Schaller, J., Knorr, K.H., 2022. Review on the interactions of arsenic, iron (oxy)(hydr)oxides, and dissolved organic matter in soils, sediments, and groundwater in a ternary system. Chemosphere 286. https://doi.org/10.1016/j.chemosphere.2021.131790.

Aiken, G.R., Hsu-kim, H., Ryan, J.N., 2011. Influence of dissolved organic matter on the environmental fate of metals, nanoparticles, and colloids. Environ. Sci. Technol. 3196–3201. https://doi.org/10.1021/es103992s.

Al-Sid-Cheikh, M., Pédrot, M., Dia, A., Guenet, H., Vantelon, D., Davranche, M., Gruau, G., Delhaye, T., 2015. Interactions between natural organic matter, sulfur, arsenic and iron oxides in compounds within riparian wetlands: NanoSIMS and X-ray adsorption spectroscopy evidences. Sci. Total Environ. 515–516, 118–128. https://doi.org/10.1016/j.scitotenv.2015.02.047.

Ao, M., Xu, X., Wu, Y., Zhang, C., Meng, B., Shang, L., Liang, L., Qiu, R., Wang, S., Qian, X., Zhao, L., Qiu, G., 2020. Newly deposited atmospheric mercury in a simulated rice ecosystem in an active mercury mining region: High loading, accumulation, and availability. Chemosphere 238, 124630. https://doi.org/10.1016/j.chemosphere.2019.124630.

Ariya, P.A., Amyot, M., Dastoor, A., Deeds, D., Feinberg, A., Kos, G., Poulain, A., Ryjkov, A., Semeniuk, K., Subir, M., Toyota, K., 2015. Mercury physicochemical and biogeochemical transformation in the atmosphere and at atmospheric interfaces: A review and future directions. Chem. Rev. 115, 3760–3802. https://doi.org/10.1021/cr500667e.

Aslam, M.W., Meng, B., Abdelhafiz, M.A., Liu, J., Feng, X., 2022. Unravelling the interactive effect of soil and atmospheric mercury influencing mercury distribution and accumulation in the soil-rice system. Sci. Total Environ. 803, 149967 https://doi.org/10.1016/j.scitotenv.2021.149967.

Bao, Y., Bolan, N.S., Lai, J., Wang, Y., Jin, X., Kirkham, M.B., Wu, X., Fang, Z., Zhang, Y., Wang, H., 2021. Interactions between organic matter and Fe (hydr)oxides and their influences on immobilization and remobilization of metal(loid)s: A review. Crit. Rev. Environ. Sci. Technol. https://doi.org/10.1080/10643389.2021.1974766.

Bishop, M.E., Dong, H., Glasser, P., Briggs, B.R., Pentrak, M., Stucki, J.W., 2020. Microbially mediated iron redox cycling of subsurface sediments from Hanford Site, Washington State, USA. Chem. Geol. 546, 119643 https://doi.org/10.1016/j.chemgeo.2020.119643.

Blanchfield, P.J., Rudd, J.W.M., Hrenchuk, L.E., Amyot, M., Babiarz, C.L., Beaty, K.G., Bodaly, R.A.D., Branfireun, B.A., Gilmour, C.C., Graydon, J.A., Hall, B.D., Harris, R. C., Heyes, A., Hintelmann, H., Hurley, J.P., Kelly, C.A., Krabbenhoft, D.P., Lindberg, S.E., Mason, R.P., Paterson, M.J., Podemski, C.L., Sandilands, K.A., Southworth St, G.R., Louis, V.L., Tate, L.S., Tate, M.T., 2021. Experimental evidence for recovery of mercury-contaminated fish populations. Nature 601, 74–78. https://doi.org/10.1038/s41586-021-04222-7.

Bonnissel-Gissinger, P., Alnot, M., Lickes, J.P., Ehrhardt, J.J., Behra, P., 1999. Modeling the adsorption of mercury(II) on (hydr)oxides II: α-FeOOH (goethite) and amorphous silica. J. Colloid Interface Sci. 215, 313–322. https://doi.org/10.1006/jcis.1999.6263.

Branfireun, B.A., Krabbenhoft, D.P., Hintelmann, H., Hunt, R.J., Hurley, J.P., Rudd, J.W. M., 2005. Speciation and transport of newly deposited mercury in a boreal forest wetland: A stable mercury isotope approach. Water Resour. Res. 41, 1–11. https://doi.org/10.1029/2004WR003219.

Bravo, A.G., Zopfi, J., Buck, M., Xu, J., Bertilsson, S., Schaefer, J.K., Poté, J., Cosio, C., 2018. Geobacteraceae are important members of mercury-methylating microbial communities of sediments impacted by waste water releases. ISME J. 12, 802–812. https://doi.org/10.1038/s41396-017-0007-7.

Carter, M.R., Gregorich, E.G., 2007. Soil Sampling and Methods of Analysis. CRC Press, Boca Raton, FL.

Chen, C., Hall, S.J., Thompson, A., 2020. Iron-mediated organic matter decomposition in humid soils can counteract protection. Nat. Commun. 11, 2255. https://doi.org/10.1038/s41467-020-16071-5.

Claff, S.R., Sullivan, L.A., Burton, E.D., Bush, R.T., 2010. A sequential extraction procedure for acid sulfate soils: Partitioning of iron. Geoderma 155, 224–230. https://doi.org/10.1016/j.geoderma.2009.12.002.

Dong, Q., Liu, Y., Liu, G., Guo, Y., Yang, Q., Shi, J., Hu, L., Liang, Y., Yin, Y., Cai, Y., Jiang, G., 2021a. Aging and phytoavailability of newly introduced and legacy cadmium in paddy soil and their bioaccessibility in rice grain distinguished by enriched isotope tracing. J. Hazard. Mater. 417, 125998 https://doi.org/10.1016/j.jhazmat.2021.125998.

Dong, Q., Liu, Y., Liu, G., Guo, Y., Yang, Q., Shi, J., Hu, L., Liang, Y., Yin, Y., Cai, Y., Jiang, G., 2021b. Enriched isotope tracing to reveal the fractionation and lability of legacy and newly introduced cadmium under different amendments. J. Hazard. Mater. 403, 123975 https://doi.org/10.1016/j.jhazmat.2020.123975.

Du, H., Peacock, C.L., Chen, W., Huang, Q., 2018. Binding of Cd by ferrihydrite organo-mineral composites: Implications for Cd mobility and fate in natural and contaminated environments. Chemosphere 207, 404–412. https://doi.org/10.1016/j.chemosphere.2018.05.092.

Du, L., Zhu, Z., Qi, Y., Zou, D., Zhang, G., Zeng, X., Ge, T., Wu, J., Xiao, Z., 2020. Effects of different stoichiometric ratios on mineralisation of root exudates and its priming effect in paddy soil. Sci. Total Environ. 743, 140808 https://doi.org/10.1016/j.scitotenv.2020.140808.

Feng, X., Li, P., Qiu, G., Wang, S., Li, G., Shang, L., Meng, B., Jiang, H., Bai, W., Li, Z., Fu, X., 2008. Human exposure to methylmercury through rice intake in mercury mining areas, Guizhou Province, China. Environ. Sci. Technol. 42, 326–332. https://doi.org/10.1021/es071948x.

Feyte, S., Tessier, A., Gobeil, C., Cossa, D., 2010. In situ adsorption of mercury, methylmercury and other elements by iron oxyhydroxides and organic matter in lake sediments. Appl. Geochem. 25, 984–995. https://doi.org/10.1016/j.apgeochem.2010.04.005.

Fu, X.W., Feng, X., Shang, L.H., Wang, S.F., Zhang, H., 2012. Two years of measurements of atmospheric total gaseous mercury (TGM) at a remote site in Mt. Changbai area, Northeastern China. Atmos. Chem. Phys. 12, 4215–4226. https://doi.org/10.5194/acp-12-4215-2012.

Fu, X.W., Zhang, H., Yu, B., Wang, X., Lin, C.J., Feng, X.B., 2015. Observations of atmospheric mercury in China: A critical review. Atmos. Chem. Phys. 15, 9455–9476. https://doi.org/10.5194/acp-15-9455-2015.

Gerbig, C.A., Kim, C.S., Stegemeier, J.P., Ryan, J.N., Aiken, G.R., 2011. Formation of nanocolloidal metacinnabar in mercury-DOM-sulfide systems. Environ. Sci. Technol. 45, 9180–9187. https://doi.org/10.1021/es201837h.

Gilmour, C.C., Riedel, G.S., Ederington, M.C., Bell, J.T., Benoit, J.M., Gill, G.A., Stordal, M.C., 1998. Methylmercury concentrations and production rates across a trophic gradient in the Northern Everglades. Biogeochemistry 40, 327–345. https://doi.org/10.1023/A:1005972708616.

Graham, A.M., Aiken, G.R., Gilmour, C.C., 2012. Dissolved organic matter enhances microbial mercury methylation under sulfidic conditions. Environ. Sci. Technol. 46, 2715–2723. https://doi.org/10.1021/es203658f.

Harris, R.C., Rudd, J.W.M., Amyot, M., Babiarz, C.L., Beaty, K.G., Blanchfield, P.J., Bodaly, R.A., Branfireun, B.A., Gilmour, C.C., Graydon, J.A., Heyes, A., Hintelmann, H., Hurley, J.P., Kelly, C.A., Krabbenhoft, D.P., Lindberg, S.E., Mason, R.P., Paterson, M.J., Podemski, C.L., Robinson, A., Sandilands, K.A., Southworth St., G.R., Louis, V., Tate, M.T., 2007. Whole-ecosystem study shows rapid fish-mercury response to changes in mercury deposition. Proc. Nati. Acad. Sci. U.S.A. 104, 16586–16591. https://doi.org/10.1073/pnas.0704186104.

Hintelmann, H., Harris, R., Heyes, A., Hurley, J.P., Kelly, C.A., Krabbenhoft, D.P., Lindberg, S., Rudd, J.W.M., Scott, K.J., St. Louis, V., 2002. Reactivity and mobility of new and old mercury deposition in a boreal forest ecosystem during the first year of the METAALICUS study. Environ. Sci. Technol. 36, 5034–5040. https://doi.org/10.1021/es025572t.

Hsu-kim, H., Kucharzyk, K.H., Zhang, T., Deshusses, M.A., 2013. Mechanisms regulating mercury bioavailability for methylating microorganisms in the aquatic environment: a critical review. Environ. Sci. Technol. 47, 2441–2456. https://doi.org/10.1021/es304370g.

Huang, J., Jones, A., Waite, T.D., Chen, Y., Huang, X., Rosso, K.M., Kappler, A., Mansor, M., Tratnyek, P.G., Zhang, H., 2021. Fe(II) redox chemistry in the environment. Chem. Rev. 121, 8161–8233. https://doi.org/10.1021/acs.chemrev.0c01286.

Jiang, T., Kaal, J., Liang, J., Zhang, Y., Wei, S., Wang, D., Green, N.W., 2017. Composition of dissolved organic matter (DOM) from periodically submerged soils in the Three Gorges Reservoir areas as determined by elemental and optical analysis, infrared spectroscopy, pyrolysis-GC-MS and thermally assisted hydrolysis and methylation. Sci. Total Environ. 603–604, 461–471. https://doi.org/10.1016/j.scitotenv.2017.06.114.

Jonsson, S., Skyllberg, U., Nilsson, M.B., Lundberg, E., Andersson, A., Björn, E., 2014. Differentiated availability of geochemical mercury pools controls methylmercury levels in estuarine sediment and biota. Nat. Commun. 5, 4624. https://doi.org/10.1038/ncomms5624.

Kappler, A., Bryce, C., Mansor, M., Lueder, U., Byrne, J.M., Swanner, E.D., 2021. An evolving view on biogeochemical cycling of iron. Nat. Rev. Microbiol. 19, 360–374. https://doi.org/10.1038/s41579-020-00502-7.

Kleber, M., Eusterhues, K., Keiluweit, M., Mikutta, C., Mikutta, R., Nico, P.S., 2015. Mineral-organic associations: Formation, properties, and relevance in soil environments. Adv. Agron. 130, 1–140. https://doi.org/10.1016/bs.agron.2014.10.005.

Kögel-Knabner, I., Amelung, W., Cao, Z., Fiedler, S., Frenzel, P., Jahn, R., Kalbitz, K., Kölbl, A., Schloter, M., 2010. Biogeochemistry of paddy soils. Geoderma 157, 1–14. https://doi.org/10.1016/j.geoderma.2010.03.009.

Lalonde, K., Mucci, A., Ouellet, A., Gélinas, Y., 2012. Preservation of organic matter in sediments promoted by iron. Nature 483, 198–200. https://doi.org/10.1038/nature10855.

Liao, P., Pan, C., Ding, W., Li, W., Yuan, S., Fortner, J.D., Giammar, D.E., 2020. Formation and transport of Cr(III)-NOM-Fe colloids upon reaction of Cr(VI) with NOM-Fe(II) colloids at anoxic − oxic interfaces. Environ. Sci. Technol. 54, 4256–4266. https://doi.org/10.1021/acs.est.9b07934.

Liu, J., Jiang, T., Wang, F., Zhang, J., Wang, D., Huang, R., Yin, D., Liu, Z., Wang, J., 2018. Inorganic sulfur and mercury speciation in the water level fluctuation zone of the Three Gorges Reservoir, China: the role of inorganic reduced sulfur on mercury methylation. Environ. Pollut. 237, 1112–1123. https://doi.org/10.1016/j.envpol.2017.11.045.

Liu, J., Liang, J., Bravo, A.G., Wei, S., Yang, C., Wang, D., Jiang, T., 2021b. Anaerobic and aerobic biodegradation of soil-extracted dissolved organic matter from the water-level-fluctuation zone of the Three Gorges Reservoir region, China. Sci. Total Environ. 764, 142857 https://doi.org/10.1016/j.scitotenv.2020.142857.

Liu, J., Lu, B., Poulain, A.J., Zhang, R., Zhang, T., Feng, X., Meng, B., 2022. The underappreciated role of natural organic matter bond Hg(II) and nanoparticulate HgS as substrates for methylation in paddy soils across a Hg concentration gradient. Environ. Pollut., 112075 https://doi.org/10.1016/j.envpol.2021.118321.

Liu, C., Massey, M.S., Latta, D.E., Xia, Y., Li, F., Gao, T., Hua, J., 2021c. Fe(II)-induced transformation of iron minerals in soil ferromanganese nodules. Chem. Geol. 559, 119901 https://doi.org/10.1016/j.chemgeo.2020.119901.

Liu, J., Meng, B., Poulain, A.J., Meng, Q., Feng, X., 2021a. Stable isotope tracers identify sources and transformations of mercury in rice (*Oryza sativa L.*) growing in a mercury mining area. Fundam. Res. 1, 259–268. https://doi.org/10.1016/j.fmre.2021.04.003.

Li, H., Li, Y., Tang, W., Liu, Y., Zheng, L., Xu, N., Li, Y.-F., Xu, D., Gao, Y., Zhao, J., 2022. Bioavailability and methylation of bulk mercury sulfide in paddy soils: New insights into mercury risks in rice paddies. J. Hazard. Mater. 424, 127394 https://doi.org/10.1016/j.jhazmat.2021.127394.

Li, H., Santos, F., Butler, K., Herndon, E., 2021. A critical review on the multiple roles of manganese in stabilizing and destabilizing soil organic matter. Environ. Sci. Technol. 55, 12136–12152. https://doi.org/10.1021/acs.est.1c00299.

Li, Y., Wang, Y., Zhang, Q., Hu, W., Zhao, J., Chen, Y., Zhong, H., Wang, G., Zhang, Z., Gao, Y., 2019. Elemental sulfur amendment enhance methylmercury accumulation in rice (*Oryza sativa* L.) grown in Hg mining polluted soil. J. Hazard. Mater. 379, 120701 https://doi.org/10.1016/j.jhazmat.2019.05.094.

Lucotte, M., Schetagne, R., Therien, N., Langlois, C., Tremblay, A., 1999. Mercury in the Biogeochemical Cycle: Natural Environments and Hydroelectric Reservoirs of Northern Québec (Canada). Springer, Berlin.

Lu, B.Q., Liu, J., Lv, W.Q., Li, S., Feng, X.B., Meng, B., 2021. Distribution characteristics of mercury occurrences in the paddy soil of Hg mining area and its effect on mercury methylation. Bull. Miner. Petrol. Geochem. 40, 1–9 (In Chinese with English abstract).

Lv, J., Zhang, S., Wang, S., Luo, L., Cao, D., Christie, P., 2016. Molecular-scale investigation with ESI-FT-ICR-MS on fractionation of dissolved organic matter induced by adsorption on iron oxyhydroxides. Environ. Sci. Technol. 50, 2328–2336. https://doi.org/10.1021/acs.est.5b04996.

Manceau, A., Wang, J., Rovezzi, M., Glatzel, P., Feng, X., 2018. Biogenesis of mercury-sulfur nanoparticles in plant leaves from atmospheric gaseous mercury. Environ. Sci. Technol. 52, 3935–3948. https://doi.org/10.1021/acs.est.7b05452.

Meng, B., Feng, X., Qiu, G., Cai, Y., Wang, D., Li, P., Shang, L., Sommar, J., 2010. Distribution patterns of inorganic mercury and methylmercury in tissues of rice (*Oryza sativa* L.) plants and possible bioaccumulation pathways. J. Agric. Food Chem. 58, 4951–4958. https://doi.org/10.1021/jf904557x.

Meng, B., Feng, X., Qiu, G., Liang, P., Li, P., Chen, C., Shang, L., 2011. The process of methylmercury accumulation in rice (*Oryza sativa* L.). Environ. Sci. Technol. 45, 2711–2717. https://doi.org/10.1021/es103384v.

Meng, B., Li, Y., Cui, W., Jiang, P., Liu, G., Wang, Y., Richards, J., Feng, X., Cai, Y., 2018. Tracing the uptake, transport, and fate of mercury in Sawgrass (*Cladium jamaicense*) in the Florida Everglades using a multi-isotope technique. Environ. Sci. Technol. 52, 3384–3391. https://doi.org/10.1021/acs.est.7b04150.

Murphy, K.R., Butler, K.D., Spencer, R.G.M., Stedmon, C.A., Boehme, J.R., Aiken, G.R., 2010. Measurement of dissolved organic matter fluorescence in aquatic environments: an interlaboratory comparison. Environ. Sci. Technol. 44, 9405–9412. https://doi.org/10.1021/es102362t.

Mu, C., Schuster, P.F., Abbott, B.W., Kang, S., Guo, J., Sun, S., Wu, Q., Zhang, T., 2020. Permafrost degradation enhances the risk of mercury release on Qinghai-Tibetan Plateau. Sci. Total Environ. 708, 135127 https://doi.org/10.1016/j.scitotenv.2019.135127.

O'Connor, D., Hou, D., Ok, Y.S., Mulder, J., Duan, L., Wu, Q., Wang, S., Tack, F.M.G., Rinklebe, J., 2019. Mercury speciation, transformation, and transportation in soils, atmospheric flux, and implications for risk management: A critical review. Environ. Int. 126, 747–761. https://doi.org/10.1016/j.envint.2019.03.019.

Orihel, D.M., Paterson, M.J., Blanchfield, P.J., Bodaly, R.A.D., Gilmour, C.C., Hintelmann, H., 2008. Temporal changes in the distribution, methylation, and bioaccumulation of newly deposited mercury in an aquatic ecosystem. Environ. Pollut. 154, 77–88. https://doi.org/10.1016/j.envpol.2007.12.030.

Oswald, C.J., Heyes, A., Branfireun, B.A., 2014. Fate and transport of ambient mercury and applied mercury isotope in terrestrial upland soils: Insights from the METAALICUS watershed. Environ. Sci. Technol. 48, 1023–1031. https://doi.org/10.1021/es404260f.

Paterson, M.J., Blanchfield, P.J., Podemski, C., Holger, H., Gilmour, C.C., Harris, R., Ogrinc, N., Rudd, J.W.M., Sandilands, K.A., 2006. Bioaccumulation of newly deposited mercury by fish and invertebrates: an enclosure study using stable mercury isotopes. Can. J. Fish. Aquat. Sci. 63, 2213–2224. https://doi.org/10.1139/f06-118.

Poulton, S.W., Canfield, D.E., 2005. Development of a sequential extraction procedure for iron: implications for iron partitioning in continentally derived particulates. Chem. Geol. 214, 209–221. https://doi.org/10.1016/j.chemgeo.2004.09.003.

Qiu, G.L., Feng, X.B., Li, P., Wang, S.F., Li, G.H., Shang, L.H., Fu, X.W., 2008. Methylmercury accumulation in rice (*Oryza sativa* L.) grown at abandoned mercury mines in Guizhou, China. J. Agric. Food Chem. 56, 2465–2468. https://doi.org/10.1021/jf073391a.

Ratié, G., Vantelon, D., Lot, E., Bihannic, I., Pierson-wickmann, A.C., Davranche, M., 2019. Iron speciation at the riverbank surface in wetland and potential impact on the mobility of trace metals. Sci. Total Environ. 651, 443–455. https://doi.org/10.1016/j.scitotenv.2018.09.143.

Riedel, T., Zak, D., Biester, H., Dittmar, T., 2013. Iron traps terrestrially derived dissolved organic matter at redox interfaces. Proc. Natl. Acad. Sci. U.S.A. 110, 10101–10105. https://doi.org/10.1073/pnas.1221487110.

Rolfhus, K.R., Hurley, J.P., Bodaly, R.A., Perrine, G., 2015. Production and retention of methylmercury in inundated boreal forest soils. Environ. Sci. Technol. 49, 3482–3489. https://doi.org/10.1021/es505398z.

Schroeder, W.H., Anlauf, K.G., Barrie, L.A., Lu, J.Y., Steffen, A., Schneeberger, D.R., Berg, T., 1998. Arctic springtime depletion of mercury. Nature 394, 331–332. https://doi.org/10.1038/28530.

Skyllberg, U., 2008. Competition among thiols and inorganic sulfides and polysulfides for Hg and MeHg in wetland soils and sediments under suboxic conditions: illumination of controversies and implications for MeHg net production. J. Geophys. Res.: Biogeosci. 113. https://doi.org/10.1029/2008JG000745.

Skyllberg, U., Bloom, P.R., Qian, J., Lin, C.M., Bleam, W.F., 2006. Complexation of mercury (II) in soil organic matter: EXAFS evidence for linear two-coordination with reduced sulfur groups. Environ. Sci. Technol. 40 (13), 4174–4180. https://doi.org/10.1021/es0600577.

Skyllberg, U., Persson, A., Tjerngren, I., Kronberg, R., Drott, A., Meili, M., Björn, E., 2021. Chemical speciation of mercury, sulfur and iron in a dystrophic boreal lake sediment, as controlled by the formation of mackinawite and framboidal pyrite. Geochim. Cosmochim. Acta 294, 106–125. https://doi.org/10.1016/j.gca.2020.11.022.

Slotznick, S.P., Sperling, E.A., Tosca, N.J., Miller, A.J., Clayton, K.E., van Helmond, N.A. G.M., Slomp, C.P., Swanson-Hysell, N.L., 2020. Unraveling the Mineralogical Complexity of Sediment Iron Speciation Using Sequential Extractions. e2019GC008666 Geochem. Geophys. Geosyst. 21. https://doi.org/10.1029/2019GC008666.

Sun, Q., Cui, P., Wu, S., Liu, C., Fan, T., Alves, M.E., Cheng, H., Huang, M., Zhou, D., Wang, Y., 2020. Role of reduced sulfur in the transformation of Cd(II) immobilized by δ-MnO_2. Environ. Sci. Technol. 54, 14955–14963. https://doi.org/10.1021/acs.est.0c02936.

Sörbo, B., 1987. Sulfate: turbidmetric and nephelometric methods. Method. Enzymol. 143, 3–6. https://doi.org/10.1016/0076-6879(87)43003-6.

Tessier, A., Campbell, P.G.C., Bisson, M., 1979. Sequential extraction procedure for the speciation of particulate trace metals. Anal. Chem. 51, 844–851 https://0003-2700/79/0351-0844$01.00/0.

Tiffreau, C., Lützenkirchen, J., Behra, P., 1995. Modeling the adsorption of mercury(II) on (Hydr)oxides: I. Amorphous iron oxide and α-quartz. J. Colloid Interface Sci. 172, 82–93. https://doi.org/10.1006/jcis.1995.1228.

Viollier, E., Inglett, P.W., Hunter, K., Roychoudhury, A.N., Cappellen, P.V., 2000. The ferrozine method revisited: Fe(II)/Fe(III) determination in natural waters. Appl. Geochem. 15, 785–790. https://doi.org/10.1016/S0883-2927(99)00097-9.

Wang, J., Feng, X., Anderson, C.W.N., Qiu, G., Ping, L., Bao, Z., 2011. Ammonium thiosulphate enhanced phytoextraction from mercury contaminated soil – Results from a greenhouse study. J. Hazard. Mater. 186, 119–127. https://doi.org/10.1016/j.jhazmat.2010.10.097.

Wang, Y., Liu, J., Liem-Nguyen, V., Tian, S., Zhang, S., Wang, D., Jiang, T., 2022. Binding strength of mercury (II) to different dissolved organic matter: the roles of DOM properties and sources. Sci. Total Environ. 807, 150979 https://doi.org/10.1016/j.scitotenv.2021.150979.

Wang, Y., Wang, H., He, J., Feng, X., 2017. Iron-mediated soil carbon response to water-table decline in an alpine wetland. Nat. Commun. 8, 1–9. https://doi.org/10.1038/ncomms15972.

Wang, B., Zhong, S., Bishop, K., Nilsson, M.B., Hu, H., Eklöf, K., Bravo, A.G., Åkerblom, S., Bertilsson, S., Björn, E., Skyllberg, U., 2021. Biogeochemical influences on net methylmercury formation proxies along a peatland chronosequence. Geochim. Cosmochim. Acta 308, 188–203. https://doi.org/10.1016/j.gca.2021.06.010.

Wilson, H.F., Xenopoulos, M.A., 2009. Effects of agricultural land use on the composition of fluvial dissolved organic matter. Nat. Geosci. 2, 37–41. https://doi.org/10.1038/ngeo391.

Xia, X., Yang, J., Yan, Y., Wang, J., Hu, Y., Zeng, X., 2020. Molecular sorption mechanisms of Cr(III) to organo-ferrihydrite coprecipitates using synchrotron-based EXAFS and STXM techniques. Environ. Sci. Technol. 54, 12989–12997. https://doi.org/10.1021/acs.est.0c02872.

Xu, Y., He, T., Wu, P., Yin, D., Shu, R., 2021. Fulvic acid: a key factor governing mercury bioavailability in a polluted plateau wetland. Water Res. 205, 117652 https://doi.org/10.1016/j.watres.2021.117652.

Yin, R., Gu, C., Feng, X., Hurley, J.P., Krabbenhoft, D.P., Lepak, R.F., Zhu, W., Zheng, L., Hu, T., 2016. Distribution and geochemical speciation of soil mercury in Wanshan

Hg mine: effects of cultivation. Geoderma 272, 32–38. https://doi.org/10.1016/j.geoderma.2016.03.003.
Yin, D., Wang, Y., Jiang, T., Qin, C., Xiang, Y., Chen, Q., Xue, J., Wang, D., 2018. Methylmercury production in soil in the water-level-fluctuating zone of the Three Gorges Reservoir, China: the key role of low-molecular-weight organic acids. Environ. Pollut. 235, 186–196. https://doi.org/10.1016/j.envpol.2017.12.072.
Zeng, Q., Huang, L., Ma, J., Zhu, Z., He, C., Shi, Q., Liu, W., Wang, X., Xia, Q., Dong, H., 2020. Bio-reduction of ferrihydrite-montmorillonite-organic matter complexes: Effect of montmorillonite and fate of organic matter. Geochim. Cosmochim. Acta 276, 327–344. https://doi.org/10.1016/j.gca.2020.03.011.
Zhang, H., Feng, X.B., Larssen, T., Qiu, G.L., Vogt, R.D., 2010. In inland China, rice, rather than fish, is the major pathway for methylmercury exposure. Environ. Health Perspect. 118, 1183–1188. https://doi.org/10.1289/ehp.1001915.
Zhang, L., Wu, S., Zhao, L., Lu, X., Pierce, E.M., Gu, B., 2019. Mercury sorption and desorption on organo-mineral particulates as a source for microbial methylation. Environ. Sci. Technol. 53, 2426–2433. https://doi.org/10.1021/acs.est.8b06020.
Zhao, L., 2016. Distribution patterns and methylation/demethylation rate of mercury in rice paddy in Hg mining area (ph. D. thesis). Southwest University (In Chinese with English abstract).
Zhao, L., Anderson, C.W.N., Qiu, G., Meng, B., Wang, D., Feng, X., 2016a. Mercury methylation in paddy soil: source and distribution of mercury species at a Hg mining area, Guizhou Province, China. Biogeosciences 13, 2429–2440. https://doi.org/10.5194/bg-13-2429-2016.
Zhao, L., Meng, B., Feng, X., 2020. Mercury methylation in rice paddy and accumulation in rice plant: a review. Ecotoxicol. Environ. Saf. 195, 110462 https://doi.org/10.1016/j.ecoenv.2020.110462.
Zhao, L., Qiu, G., Anderson, C.W.N., Meng, B., Wang, D., Shang, L., Yan, H., Feng, X., 2016b. Mercury methylation in rice paddies and its possible controlling factors in the Hg mining area, Guizhou Province, southwest China. Environ. Pollut. 215, 1–9. https://doi.org/10.1016/j.envpol.2016.05.001.
Zhu, Y., Ma, L.Q., Gao, B., Bonzongo, J.C., Harris, W., Gu, B., 2012. Transport and interactions of kaolinite and mercury in saturated sand media. J. Hazard. Mater. 213–214, 93–99. https://doi.org/10.1016/j.jhazmat.2012.01.061.